Improved Prediction Models for PCC Pavement Performance-Related Specifications, Volume I: Final Report

PUBLICATION NO. FHWA-RD-00-130

SEPTEMBER 2000

U.S. Department of Transportation
Federal Highway Administration

Research, Development, and Technology
Turner-Fairbank Highway Research Center
6300 Georgetown Pike
McLean, VA 22101-2296

FOREWORD

The development of performance-related specifications has long been a goal of the highway industry. Recently, prototype performance-related specifications for portland cement concrete paving were developed and field tested in several States. Using such specifications, a highway agency can upon construction predict the performance of a pavement and forecast the pavement's life-cycle costs. The benefits to the agency having such a capability can be significant.

This report is the first of two volumes. It describes research work to improve the performance prediction models that form the basis for the prototype performance-related specifications. As highway agencies use performance-related specifications and collect the resulting quality, cost, and performance data, it is expected the models will undergo even further improvements and increases in performance prediction accuracy. This report will be of interest to engineers concerned with quality assurance, specifications, and the construction of concrete pavements.

Sufficient copies of this report are being distributed to provide a minimum of two copies to each FHWA resource center and division office, and eight copies to each State highway agency. Direct distribution is being made to the division offices. Additional copies for the public are available from the National Technical Information Service (NTIS), 5285 Port Royal Road, Springfield, Virginia 22161.

T. Paul Teng, P.E.
Director, Office of Infrastructure
Research and Development

NOTICE

This document is disseminated under the sponsorship of the Department of Transportation in the interest of information exchange. The United States Government assumes no liability for its contents or use thereof. This report does not constitute a standard, specification, or regulation.

The United States Government does not endorse products or manufacturers. Trade and manufacturers' names appear in this report only because they are considered essential to the object of the document.

Technical Report Documentation Page

1. Report No.	2. Government Accession No.	3. Recipient's Catalog No.
FHWA-RD-00-130		

4. Title and Subtitle
IMPROVED PREDICTION MODELS FOR PCC PAVEMENT PERFORMANCE-RELATED SPECIFICATIONS, Volume I: Final Report

5. Report Date
September 2000

6. Performing Organization Code

7. Author(s)
T.E. Hoerner, M.I. Darter, L. Khazanovich, L. Titus-Glover, and K.L. Smith

8. Performing Organization Report No.

9. Performing Organization Name and Address
ERES Consultants (A Division of Applied Research Associates, Inc.)
505 W. University Avenue
Champaign, IL 61820-3915

10. Work Unit No. (TRAIS)
xxxx

11. Contract or Grant No.
DTFH61-97-C-00071

12. Sponsoring Agency Name and Address
Office of Engineering R&D
Federal Highway Administration
6300 Georgetown Pike
McLean, Virginia 22101-2296

13. Type of Report and Period Covered
Final Report
November 1997–April 2000

14. Sponsoring Agency Code

15. Supplementary Notes
FHWA Contracting Officer's Technical Representative (COTR): Peter A. Kopac, HRDI–12

16. Abstract

The current performance-related specifications (PRS) methodology has been under development by the Federal Highway Administration (FHWA) for several years and has now reached a level at which it can be implemented by State highway agencies. PRS for highway pavements depend heavily on performance prediction models to determine the impact of varying levels of construction quality. This study focused on the improvement of the key distress and smoothness prediction models used in the PRS for jointed plain concrete pavement (JPCP). Performance models for transverse joint faulting, transverse slab cracking, transverse joint spalling, and smoothness (International Roughness Index [IRI]) were evaluated and then improved substantially. This was accomplished using a comprehensive national database of JPCP performance data, along with sound statistical and engineering techniques. Performance model calibration guidelines were also developed so that a State can calibrate any of these models specifically to its pavement performance data.

The PaveSpec PRS demonstration software was upgraded to Version 3.0 under this study. Some of the specific improvements incorporated in PaveSpec 3.0 include: 1) incorporation of the improved distress indicator models, as well as the ability to calibrate or modify the default models, 2) sensitivity analysis capibilities, 3) expected pay charts, and 4) online help. Appendix A of this report contains a complete updated PaveSpec User's Guide.

This volume is the first of two volumes. The other volume is:
FHWA-RD-00-131 Volume II: Appendix A—PaveSpec 3.0 User's Guide

17. Key Words
performance-related specifications, performance prediction, pavement distress, smoothness, concrete pavement, quality assurance, specifications, life-cycle costing, and pavement construction

18. Distribution Statement
No restrictions. This document is available to the public through the National Technical Information Service, Springfield, Virginia 22161.

19. Security Classif. (of this report)	20. Security Classif. (of this page)	21. No of Pages	22. Price
Unclassified	Unclassified	220	

Form DOT F 1700.7 (8-72) Reproduction of completed page authorized

TABLE OF CONTENTS

CHAPTER 1: INTRODUCTION 1

RECENT PROGRESS IN PRS DEVELOPMENT 1
PROJECT OBJECTIVES AND SCOPE 4
RESEARCH APPROACH 4
SEQUENCE OF REPORT 6

CHAPTER 2: EVALUATION OF DISTRESS INDICATOR MODELS AND POTENTIAL DATA SOURCES 7

INTRODUCTION 7
STEP 1—IDENTIFICATION OF AVAILABLE JPCP DISTRESS INDICATOR MODELS 8
STEP 2—IDENTIFICATION AND EVALUATION OF POTENTIAL DATA SOURCES 10
Identification of Required Data Types for Inclusion in the National PRS Database 10
Specific Data Elements Required by the Available Distress Indicator Models 11
Identification and Evaluation of Potential Data Sources 11
Availability of Required Data Elements in the Identified Potential Data Sources 20
STEP 3—SELECTION OF BEST-AVAILABLE DISTRESS INDICATOR MODELS 21
Transverse Joint Faulting Model 29
Transverse Fatigue Cracking Model 29
Transverse Joint Spalling Model 29
IRI Model 29
STEP 4—IDENTIFICATION OF SPECIFIC DATA SOURCES TO BE INCLUDED IN THE NATIONAL PRS DATABASE 30

CHAPTER 3: PROCEDURES USED TO VALIDATE/IMPROVE DISTRESS INDICATOR MODELS 31

INTRODUCTION 31
PREPARATION OF MODEL TYPE SPECIFIC DATA SETS 31
TECHNIQUES OF THE MODEL VALIDATION/IMPROVEMENT PROCESS 31
Engineering Assessment 32
Statistical Analyses 32
ACCEPTABILITY OF MODELS 37

TABLE OF CONTENTS (continued)

CHAPTER 4: TRANSVERSE JOINT FAULTING MODEL 39

INTRODUCTION 39
CURRENT PRS JPCP TRANSVERSE JOINT FAULTING MODEL 39
JPCP Transverse Joint Faulting (Not Including Percent Consolidation Around Dowels) 40
JPCP Transverse Joint Faulting (Including Percent Consolidation Around Dowels) 41
LIMITATIONS OF THE CURRENT PRS TRANSVERSE JOINT FAULTING MODEL 42
EXISTING JPCP TRANSVERSE JOINT FAULTING MODELS 43
SHRP P-020 JPCP Transverse Joint Faulting Model 43
FHWA RPPR 1997 JPCP Transverse Joint Faulting Model 46
ACPA JPCP Transverse Joint Faulting Model 48
FHWA NAPCOM JPCP Transverse Joint Faulting Model 49
LTPP Data Analysis Study JPCP Transverse Joint Faulting Model 50
Overview of Existing JPCP Transverse Joint Faulting Models 51
RECALIBRATION OF THE CURRENT JPCP TRANSVERSE JOINT FAULTING MODEL 51
Data Preparation 53
Statistical Tools for Regression and Optimization 55
Final JPCP Transverse Joint Faulting Model 55
MODEL VERIFICATION (SENSITIVITY ANALYSIS) 60
Effect of Material- and Design-Related Factors 60
Effect of Climatic Variables 66
SUMMARY 68

CHAPTER 5: JPCP TRANSVERSE FATIGUE CRACKING MODEL 71

INTRODUCTION 71
CURRENT PRS JPCP TRANSVERSE SLAB CRACKING MODEL 72
ATTEMPTED VALIDATION OF THE CURRENT PRS TRANSVERSE SLAB CRACKING MODEL 74
EXISTING JPCP TRANSVERSE SLAB CRACKING MODELS 75
NCHRP Project 1-26 JPCP Transverse Cracking Model 75
FHWA RPPR 1997 JPCP Transverse Cracking Model 79
Overview of Existing JPCP Transverse Cracking Models 82
IMPROVEMENT OF THE RPPR 1997 JPCP TRANSVERSE CRACKING MODEL 83
Data Preparation 85
Statistical Tools for Regression and Optimization 85

TABLE OF CONTENTS (continued)

Final JPCP Transverse Cracking Model 85
Procedure Used to Predict Fatigue Damage 88
MODEL VERIFICATION (SENSITIVITY ANALYSIS) 105
Effect of Material- and Design-Related Factors 105
Effect of Site-Related Factors 108
SUMMARY 112

CHAPTER 6: TRANSVERSE JOINT SPALLING MODEL 113

INTRODUCTION 113
CURRENT PRS JPCP TRANSVERSE JOINT SPALLING MODEL 113
Transverse Joint Spalling Baseline Model (Not Including Air Content) 114
Transverse Joint Spalling Model and Procedure (Including Air Content) 114
ATTEMPTED VALIDATION OF THE CURRENT PRS TRANSVERSE JOINT SPALLING MODEL 118
EXISTING JPCP TRANSVERSE JOINT SPALLING MODELS 121
SHRP P-020 JPCP Transverse Joint Spalling Model 121
LTPP Data Analysis JPCP Transverse Joint Spalling Model 122
CTL JPCP Transverse Joint Spalling Model 124
FHWA RPPR JPCP Transverse Joint Spalling Model 124
Overview of JPCP Transverse Joint Spalling Models 126
DEVELOPMENT OF A NEW JPCP TRANSVERSE JOINT SPALLING MODEL 127
Data Preparation 128
Selection of a Suitable JPCP Transverse Joint Spalling Prediction Model Form 130
Statistical Tools for Regression and Optimization 130
Final JPCP Transverse Joint Spalling Model 131
MODEL VERIFICATION (SENSITIVITY ANALYSIS) 132
Effect of Air Content 132
Effect of PCC Compressive Strength 134
Effect of Joint Sealant Type 134
Effect of PCC Slab Thickness 136
Effect of Total Air Freeze-Thaw Cycles 136
Effect of Water/Cement Ratio 137
SUMMARY 137

CHAPTER 7: IRI MODEL 139

INTRODUCTION 139
CURRENT PRS IRI MODEL 139

TABLE OF CONTENTS (continued)

ATTEMPTED VALIDATION OF THE CURRENT PRS IRI MODEL.....140
EXISTING JPCP IRI MODELS 142
SHRP P-020 JPCP IRI Models.....142
LTPP Data Analysis JPCP IRI Model.....144
FHWA RPPR JPCP IRI Model.....145
Overview of JPCP IRI Models.....145
DEVELOPMENT OF A NEW JPCP IRI MODEL 146
Data Preparation.....147
Selection of a Suitable JPCP IRI Prediction Model Form.....152
Statistical Tools for Regression and Optimization 154
Final JPCP IRI Model.....154
MODEL VERIFICATION (SENSITIVITY ANALYSIS).....155
Effect of Initial IRI.....155
Effect of Transverse Slab Cracking 157
Effect of Transverse Joint Spalling.....158
Effect of Transverse Joint Faulting.....159
Effect of Pavement Site Conditions.....159
SUMMARY 160

CHAPTER 8: DEVELOPMENT OF INITIAL SMOOTHNESS RELATIONSHIPS.....163

INTRODUCTION.....163
BACKGROUND 164
Initial Smoothness Testing 164
Smoothness Monitoring 166
PRELIMINARY INVESTIGATION—PAST STUDIES ON SMOOTHNESS RELATIONSHIPS.....167
Pennsylvania Transportation Institute Profilograph Calibration Study.....167
Arizona DOT Initial Smoothness Study 169
University of Texas Smoothness Specification Study.....169
Florida DOT Ride Quality Equipment Comparison Study.....170
Texas Transportation Institute Smoothness Testing Equipment Comparison Study 172
Summary of IRI–PI Relationships.....173
DETAILED INVESTIGATION—LTPP CORRELATION ANALYSIS.....174
LTPP Profile and Smoothness Data 176
Development and Application of Simulation Software 177
Data Analysis.....178
SUMMARY AND RECOMMENDATIONS 186

TABLE OF CONTENTS (continued)

CHAPTER 9: GUIDELINES FOR MODEL CALIBRATION AND DEVELOPMENT 189

INTRODUCTION 189
GUIDELINES FOR CALIBRATING AN EXISTING DISTRESS INDICATOR MODEL 189
Step 1—Compile the Calibration Data Set 190
Step 2—Compute Corresponding *Predicted* Values 191
Step 3—Plot Predicted vs. Measured Distress Values 191
Step 4—Statistical Analysis of Predicted vs. Measured Distress Values 192
Step 5—Determine Calibration Coefficients A and B 192
Step 6—Determine Calibrated Distress Values 192
Step 7—Plot Calibrated vs. Measured Distress Values 193
Step 8—Statistical Analysis of Calibrated vs. Measured Distress Values 193
GUIDELINES FOR DEVELOPING NEW DISTRESS INDICATOR MODELS 194
Distress Indicator Prediction Model Types 194
Basic Principles to Developing Improved Distress Indicator Prediction Models 195

CHAPTER 10: SUMMARY AND RECOMMENDATIONS 199

SUMMARY 199
Improved Performance Prediction Models 200
Investigation of Initial Smoothness Relationships 201
Distress Indicator Model Calibration Guidelines 201
Development of PaveSpec 3.0 202
RECOMMENDATIONS FOR FUTURE RESEARCH 202

REFERENCES 205

LIST OF FIGURES

Figure No.

1 Example of a plot of predicted versus actual data 33
2 Conceptual illustration of the difference between bias and precision 34
3 Example of the sensitivity of a JPCP cracking model to slab thickness. 37
4 Predicted versus measured transverse joint faulting (using the compiled validation data set). 44
5 Residual versus predicted transverse joint faulting (using the compiled validation data set) 44
6 Predicted versus measured faulting for the validated JPCP faulting model 60
7 Residual versus predicted faulting for the validated JPCP faulting model 61
8 Sensitivity of the final JPCP transverse joint faulting model to changes in dowel diameter 62
9 Sensitivity of the final JPCP transverse joint faulting model to changes in transverse joint spacing 63
10 Sensitivity of the final JPCP transverse joint faulting model to changes in base erodibility factor 63
11 Sensitivity of the final JPCP transverse joint faulting model to changes in dynamic modulus of subgrade reaction 64
12 Sensitivity of final validated JPCP joint faulting model to changes in base permeability 65
13 Sensitivity of the final JPCP transverse joint faulting model to changes in PCC slab thickness 65
14 Sensitivity of the final JPCP transverse joint faulting model to changes in PCC modulus of elasticity 66
15 Sensitivity of the final JPCP transverse joint faulting model to changes in percent consolidation of PCC around 25.4-mm (1-in) dowels 67
16 Sensitivity of the final JPCP transverse joint faulting model to changes in percent consolidation of PCC around 38.1-mm (1.5-in) dowels 67
17 Sensitivity of the final JPCP transverse joint faulting model to changes in precipitation 68
18 Sensitivity of the final JPCP transverse joint faulting model to changes in number of hot days 69
19 Predicted (equation 36) versus measured JPCP transverse slab cracking (using the compiled validation data set) 76
20 Residual versus predicted (equation 36) transverse JPCP slab cracking (using the compiled validation data set) 76
21 Predicted (RPPR 97 model) versus actual slab cracking (using the section-by-section temperature shift factors and gradient distributions) 84

LIST OF FIGURES (continued)

22 Predicted (RPPR 97 model) versus actual slab cracking (using regional temperature shift factors with section-by-section temperature gradient distributions) 84
23 Predicted (equation 55) versus measured JPCP transverse cracking 87
24 Residual versus predicted (equation 55) JPCP transverse cracking 87
25 Sensitivity of the final JPCP transverse slab cracking model to changes in PCC slab thickness 106
26 Sensitivity of the final JPCP transverse slab cracking model to changes in PCC flexural strength 106
27 Sensitivity of the final JPCP transverse cracking model to changes in modulus of elasticity 107
28 Sensitivity of the final JPCP transverse cracking model to changes in modulus of elasticity and corresponding changes in PCC flexural stiffness 107
29 Sensitivity of the final JPCP transverse slab cracking model to changes in PCC slab joint spacing 109
30 Sensitivity of the final JPCP transverse slab cracking model to changes in edge support 109
31 Sensitivity of the final JPCP transverse slab cracking model to changes in base type and bond condition 110
32 Sensitivity of the final JPCP transverse slab cracking model to changes in climate 111
33 Sensitivity of the final JPCP transverse slab cracking model to changes in dynamic k-value 111
34 Predicted (equation 83) versus measured JPCP transverse joint spalling (using the LTPP validation data set) 120
35 Residual versus predicted (equation 83) transverse joint spalling (using the LTPP validation data set) 121
36 Predicted (equation 97) versus measured spalling for the final JPCP transverse joint spalling model 133
37 Residual versus predicted (equation 97) spalling for the final JPCP transverse joint spalling model 133
38 Sensitivity of final JPCP joint spalling model to changes in PCC concrete air content (measured with air pressure meter) 134
39 Sensitivity of final JPCP joint spalling model to changes in PCC 28-day compressive strength 135
40 Sensitivity of final JPCP joint spalling model to changes in joint sealant type 135
41 Sensitivity of final JPCP joint spalling model to changes in PCC slab thickness 136
42 Sensitivity of final JPCP joint spalling model to changes in cumulative air freeze-thaw cycles 137
43 Sensitivity of final JPCP joint spalling model to changes in water-cement ratio 138

LIST OF FIGURES (continued)

44 Predicted (equation 99) versus measured JPCP IRI (using the LTPP validation data set) 141
45 Residual versus predicted (equation 99) JPCP IRI (using the LTPP validation data set) 142
46 Example of the linear model method used to backcast an initial IRI from time-series data 150
47 Initial IRI distribution for measured (SPS) and backcasted JPCP (GPS-3) data 151
48 Plot of estimated initial backcasted IRI versus section age for JPCP 152
49 Predicted (equation 108) versus measured IRI for the final JPCP IRI model 156
50 Residuals versus predicted (equation 108) IRI for the final JPCP IRI model 156
51 Sensitivity of the final JPCP IRI model to changes in initial IRI and percent cracked slabs 157
52 Sensitivity of the final JPCP IRI model to changes in percent joints spalled and initial IRI 158
53 Sensitivity of the final JPCP IRI model to changes in total joint faulting per km and initial IRI 159
54 Effect of freezing index on JPCP IRI after 30 years 160
55 Effect of subgrade percent passing 0.075-mm sieve on JPCP IRI after 30 years 161
56 Relationship between IRI and manually generated PI in PTI profilograph calibration study 168
57 Relationship between IRI and computer-generated PI in PTI profilograph calibration study 168
58 Correlation of IRI and PI in Arizona pavement smoothness study 170
59 IRI–$PI_{5\text{-mm}}$ ($PI_{0.2\text{-in}}$) correlations established in Florida's ride quality equipment study 171
60 IRI–$PI_{2.5\text{-mm}}$ ($PI_{0.1\text{-in}}$) and IRI–$PI_{0.0}$ correlations established in Florida's ride quality equipment study 172
61 Relationship between IRI and computer-simulated PI values in TTI equipment comparison study 173
62 Graphical illustration of documented IRI–$PI_{5\text{-mm}}$ ($PI_{0.2\text{-in}}$) smoothness relationships 175
63 Graphical illustration of documented IRI–$PI_{2.5\text{-mm}}$ ($PI_{0.1\text{-in}}$) smoothness relationships 175
64 Graphical illustration of documented IRI–$PI_{0.0}$ smoothness relationships 176
65 Graphical illustration of LTPP IRI–$PI_{5\text{-mm}}$ ($PI_{0.2\text{-in}}$) smoothness relationship 179
66 Graphical illustration of LTPP IRI–$PI_{2.5\text{-mm}}$ ($PI_{0.1\text{-mm}}$) smoothness relationship 180
67 Graphical illustration of LTPP IRI–$PI_{0.0}$ smoothness relationship 180
68 Graphical comparison of IRI–$PI_{5\text{-mm}}$ ($PI_{0.2\text{-in}}$) smoothness relationships 181
69 Graphical comparison of IRI–$PI_{2.5\text{-mm}}$ ($PI_{0.1\text{-in}}$) smoothness relationships 181
70 Graphical comparison of IRI–$PI_{0.0}$ smoothness relationships 182

LIST OF FIGURES (continued)

71 Comparison of IRI–$PI_{5\text{-mm}}$ ($PI_{0.2\text{-in}}$) relationships for different filter types and settings 184
72 Comparison of IRI–$PI_{2.5\text{-mm}}$ ($PI_{0.1\text{-in}}$) relationships for different filter types and settings 185
73 Comparison of IRI–$PI_{0.0}$ relationships for different filter types and settings 185
74 Illustration of predicted vs. actual CRS both before calibration and after calibration with new data 190
75 Flow chart for developing pavement distress models for rigid pavements 197

LIST OF TABLES

Table No.

1 Summary of recently developed distress indicator models considered relevant to the PRS methodology 9
2 Summary of required data elements included in the short list of best-available JPCP transverse joint faulting models 12
3 Summary of required data elements included in the short list of best-available JPCP transverse fatigue cracking models 13
4 Summary of required data elements included in the short list of best-available JPCP transverse joint spalling models 14
5 Summary of required data elements included in the short list of best-available JPCP IRI models 15
6 Availability of data required by the short-listed JPCP transverse joint faulting models 22
7 Availability of data required by short-listed JPCP transverse cracking models 23
8 Availability of data required by the short-listed JPCP transverse joint spalling models 24
9 Availability of data required by the short-listed JPCP IRI models 25
10 Assessment of best-available JPCP transverse joint faulting models 26
11 Assessment of best-available JPCP transverse cracking models 27
12 Assessment of best-available JPCP transverse joint spalling models 27
13 Assessment of best-available JPCP IRI models 28
14 Specific databases that will be used to validate/improve chosen best available distress indicator models 30
15 Example of paired t-test analysis results (from an investigation of the AASHTO rigid pavement design model using LTPP data) 35
16 Results of the components of variance example 36
17 Summary of JPCP data used in the initial validation of the current transverse joint faulting model 42
18 Summary of variables found to significantly affect JPCP transverse joint faulting 52
19 PIARC recommendations for erosion potential of base/subbase materials (based on base type and base cement and asphalt content) 54
20 Supplemental recommendations for erosion potential of CTB (based on long-term compressive strength) 54
21 Recommendations for assigning of erodibility factor based on PIARC erodibility class 55
22 Range of values of data used in the sensitivity analysis for the final validated JPCP transverse joint faulting model 61
23 Average daytime thermal gradients (based on slab thickness and climatic zone), °F/in 73

LIST OF TABLES (continued)

24 JPCP data used in the initial validation of the current transverse slab cracking model 74
25 Temperature shift factor coefficients by climatic zone 86
26 Frequency distributions of temperature gradients for the wet-freeze region (based on rounded effective thickness) 97
27 Frequency distributions of temperature gradients for the wet-nonfreeze region (based on rounded effective thickness) 99
28 Frequency distributions of temperature gradients for the dry-freeze region (based on rounded effective thickness) 101
29 Frequency distributions of temperature gradients for the dry-nonfreeze region (based on rounded effective thickness) 103
30 Summary of LTPP data used in the initial validation of the PaveSpec 2.0 JPCP transverse joint spalling model 119
31 Summary of variables found to significantly affect JPCP transverse joint spalling 128
32 Summary of GPS-3 JPCP data and CTL laboratory data used in model development and calibration 129
33 Range of values of data used in sensitivity analysis 132
34 Summary of JPCP LTPP data used in the initial validation of the current IRI model 140
35 Summary of distresses and variables identified in previous research as significantly affecting JPCP IRI 146
36 Summary of t-test results for the comparison of measured and backcasted initial IRI for JPCP 151
37 Summary of GPS-3 JPCP data considered in the IRI model development and calibration procedures 153
38 Diagnostic statistics for JPCP IRI model 155
39 Summary of documented IRI–PI relationships 174
40 Summary of JPCP test sections included in LTPP correlation analysis 177
41 Summary of IRI–PI relationships based on different filter types and settings 184
42 Effects of alternative filter types and settings on IRI–PI relationships 186
43 Format for a calibration data set 191
44 Example calibration data set table with predicted values included 191

LIST OF ACRONYMS AND ABBREVIATIONS

AASHTO	American Association of State Highway and Transportation Officials
AC	Asphalt concrete
AC-AD RATIO	As-constructed to as-designed CTL spalling ratio
ACPA	American Concrete Pavement Association
ANOVA	Analysis of variance
AQC	Acceptance quality characteristic
ATB	Asphalt treated base
BPR	Bureau of Public Roads
COPES	Concrete Pavement Evaluation System (NCHRP Project 1-19)
CRCP	Continuously reinforced concrete pavement
CRS	Condition rating survey
CTB	Cement treated base
CTL	Construction Technology Laboratories, Inc.
DMI	Distance measuring instrument
DOT	Department of transportation
EP	Expected pay
ERD	Engineering Research Division
ESAL	Equivalent single axle-load
FHWA	Federal Highway Administration
FWD	Falling-weight deflectometer
GPS	LTPP general pavement studies
HPMS	Highway Performance Monitoring System
ICC	International Cybernetics Corporation
ICM	Integrated Climate and Materials
IMS	LTPP Information Management System
IRI	International Roughness Index
JPCP	Jointed plain concrete pavement
JRCP	Jointed reinforced concrete pavement
LCB	Lean concrete base
LCC	Life-cycle cost
LTPP	Long Term Pavement Performance
M&R	Maintenance and rehabilitation
Mn/ROAD	Minnesota Test Road
MRN	Mays ride number
NAPCOM	Nationwide Pavement Cost Model (FHWA project)
NCHRP	National Cooperative Highway Research Program

LIST OF ACRONYMS AND ABBREVIATIONS (continued)

NCRCO	LTPP North Central Regional Contracting Office
NLIN	SAS nonlinear procedure
NOAA	National Oceanic and Atmospheric Administration
PCA	Portland Cement Association
PCC	Portland cement concrete
PI	Profile index
PIARC	Permanent International Association of Road Congresses
PMS	Pavement management system
PRS	Performance-related specifications
PSR	Present serviceability rating
PTI	Pennsylvania Transportation Institute
PW	Present worth
PW$	Present worth dollars
R^2	Coefficient of determination
RMSVA	Root Mean Square Vertical Acceleration
RPPR	FHWA Rigid Pavement Performance and Rehabilitation study
SEE	Standard error of the estimate
SHA	State highway agency
SHRP	Strategic Highway Research Program
SPS	Specific pavement studies
TTI	Texas Transportation Institute
UMTRI	University of Michigan Transportation Research Institute

CHAPTER 1: INTRODUCTION

Over the past decade, significant progress has been made in the development of performance-related specifications (PRS) for the acceptance of newly constructed jointed plain concrete pavements (JPCP). A PRS is a construction specification that describes the desired levels of key materials and construction acceptance quality characteristics (AQC's) that have been found to correlate with fundamental engineering properties that predict performance. These AQC's (e.g., smoothness, thickness, strength, air content, and percent consolidation around dowels) are amenable to acceptance testing at the time of construction. A true PRS not only describes the desired levels of the selected AQC's, but also employs the quantified relationships to predict subsequent pavement performance and associated life-cycle costs (LCC's) for a given project. This ability to relate AQC's (measured during construction) to the level of expected performance and future LCC provides the basis for rational acceptance and price adjustment decisions.[1]

Because price adjustments are directly dependent on the future pavement performance predicted through selected mathematical distress indicator prediction models (e.g., transverse joint faulting and spalling, transverse fatigue cracking, International Roughness Index [IRI]), it is important to have confidence in the validity or accuracy of these models. In recent years, State highway agencies (SHA's) have expressed concern over whether the distress indicator prediction models used in the current PRS approach would accurately predict the pavement performance associated with their agency's specific designs, materials, subgrades, traffic, and climatic conditions. This important question must be adequately addressed, or it will inhibit the implementation of the PRS in many States. Therefore, the focus of this study was to validate or improve the default performance models used in the current PRS approach (included in the PaveSpec 2.0 software) and to provide guidelines for SHA's that allow them to calibrate the default models, or develop new models that reflect their local conditions.

RECENT PROGRESS IN PRS DEVELOPMENT

The advancement of PRS research has been a high-priority research area within the Federal Highway Administration (FHWA) since 1987. Some of the more notable early efforts include the pioneering PRS work done in New Jersey by Weed, a National Cooperative Highway Research Program (NCHRP)-sponsored study on PRS for asphalt concrete (AC) pavements, and the initial FHWA study on developing PRS for portland cement concrete (PCC) pavements.[2,3,4]

Based on the promising results of these early projects, FHWA sponsored additional research in the early 1990's that focused on the development of a more practical (and easily implementable) prototype PRS for PCC pavements. The first of these studies

considerably advanced the PCC PRS research by developing a prototype PRS approach driven by LCC's.[5,6,7] Using this approach, the estimated total future (after initial construction) LCC of a pavement lot is directly related to the AQC quality (means and standard deviations) and is used as the overall measure of quality for the lot.

The approach requires the agency to define the desired as-designed AQC quality *target* values (means and standard deviations) for a pavement lot. The quality of the as-constructed pavement is determined by taking samples directly from the constructed pavement lot. A difference in AQC quality between the as-designed and as-constructed lots, therefore, results in a difference in predicted future LCC's. The lot pay factor is determined, as a function of these two estimated LCC's, using the following equation:

$$PF_{LOT} = 100 * (BID + [LCC_{DES} - LCC_{CON}]) / BID \quad (1)$$

where:

PF_{LOT} = Pay factor, percentage of original bid price.

BID = Contractor's unit bid price for the lot, present worth dollars per km (PW$/km).

LCC_{DES} = As-designed life-cycle unit cost for the lot (computed using target AQC's), PW$/km.

LCC_{CON} = As-constructed life-cycle unit cost for the lot (computed using AQC test results from the as-constructed lot), PW$/km.

As can be seen from this equation, both positive and negative pay adjustments are possible. The approach is in accordance with the legal principle of liquidated damages, which are computed at the time of construction on the basis of the projected increase or decrease in estimated future costs.

The first version of the PRS demonstration software, PaveSpec, was developed under this 1990–1993 FHWA research study and was used to simulate the construction of the lot, predict future performance and costs, and generate pay adjustments for a given project.

Also as part of this 1990–1993 FHWA research study, an extensive laboratory testing program was conducted to fill several gaps in the materials area. Among the major laboratory studies that were conducted were:

- An evaluation of the factors that affect concrete strength and modulus of elasticity (many PCC mixes were evaluated over a range of materials).
- An investigation into inter-strength (e.g., flexural to compressive) relationships.
- A comparison of the compressive strengths of cores to the compressive strengths of cylinders having the same maturity.

- A demonstration of the use of maturity and pulse velocity for monitoring the in-situ slab strength for potential use in determining early strength.

- An investigation of the effect of air void system parameters on joint spalling.

A final part of the FHWA research study was the development of test plans for the evaluation of various construction variables. These studies were needed so that the effect of other AQC's that are under the control of the contractor could be quantified and eventually included in the PRS.

A second FHWA research study was therefore conducted, from 1994 to 1998, involving field and laboratory investigations of several performance-related PCC pavement construction variables.[8,9,10,11] Under this study, the researchers:

- Determined typical variability of key AQC's (air voids, slab thickness, initial smoothness, concrete strength, and others) and provided recommendations for default variabilities of each AQC.

- Revised the prototype PRS developed under the first contract by adding new and improved construction AQC's (consolidation near dowels, air void validations) and by defining three levels of PRS implementation.

- Fully developed the first level of PRS implementation, which is practical and immediately implementable by SHA's (with the exception of verified performance prediction models).

- Developed version 2.0 of the PaveSpec computer program to give it many additional PRS capabilities, including the ability to automatically simulate and generate pay factors based on user-defined inputs for a given highway construction project and the ability to input testing results directly from a lot to compute the corresponding pay factors.

- Replaced most of the existing performance prediction models with improved models from recent FHWA and Long Term Pavement Performance (LTPP) studies.

- Conducted several field trials of the prototype PRS and used the findings to improve the prototype PRS.

It is clear that these studies on the development of PRS for PCC pavements made significant advancements in several areas:

- Extension of the underlying theory governing PRS.

- Development of a first level (Level 1) implementable PRS.

- Laboratory demonstrations of the development of concrete strength / stiffness relationships, the application of nondestructive testing, the effect of concrete durability on spalling / scaling, and cylinder versus core strength.

- The consideration of several key AQC's (concrete strength, slab thickness, initial smoothness, PCC air content, percent consolidation around dowels) and the variability of these characteristics.

- Several successful field trials of PRS implementation.

PROJECT OBJECTIVES AND SCOPE

The focus of this study was to conduct research that will continue the advancement toward the development of a fully practical and implementable PRS for JPCP construction. Specifically, the contract objectives were to:

1. Validate and, where appropriate, make improvements or adjustments to the distress indicator prediction models currently used in the prototype PRS (and PaveSpec 2.0) for JPCP paving.

2. Develop guidelines to assist those SHA's that may want to 1) calibrate national distress-prediction models to reflect local conditions or 2) develop new distress indicator models using a separate data set.

3. Conduct a study to investigate relationships between different methods of measuring initial smoothness (e.g., IRI versus profile index [PI] using different blanking bands) so that smoothness could be more adequately predicted over time.

4. Update the PaveSpec 2.0 software.

RESEARCH APPROACH

The research team began by evaluating the distress indicator models used in the current prototype PRS (those used in PaveSpec 2.0). Specifically, the distress indicator models considered were limited to the following:

- Transverse joint faulting.
- Transverse fatigue cracking.
- Transverse joint spalling.
- IRI.

The research team assessed the practicality, completeness, and accuracy of each of the models and compiled a plan to validate or improve each model independently.

Next, data sources that could potentially be used to validate/improve the models were identified and evaluated for content and accuracy. Specifically, each potential database was assessed by evaluating the following types of data:

- Time-series distress indicators.
- Design feature characteristics.
- Traffic.
- Construction AQC's.
- Climatic variables.

Those data sources that were found to be adequate were compiled into a national PRS database.

Each distress indicator model was then validated or improved using a series of statistical methods. The sensitivity of each of the validated/improved models was assessed. Improvements were made to the models until they were considered adequate for use in the current PRS methodology.

During the evaluation of the IRI model, it was determined that more guidance was needed in the area of initial smoothness relationships. The PRS approach allows the user to predict smoothness over time in terms of IRI; however, an initial IRI value is not typically measured directly by a SHA. While a few SHA's are now starting to measure initial IRI with a lightweight profiler, the majority of SHA's continue to assess the initial smoothness of a new pavement by measuring a PI using a California profilograph. Because of this situation, a study was conducted to determine the best relationships between the initially measured PI values (using different blanking bands) and the initial IRI values required by the smoothness-over-time models.

In addition to the model validation and improvement procedures, the research team also compiled a set of model calibration guidelines. The model calibration procedure allows a SHA to calibrate any of the national distress indicator models with a data set that better reflects the local conditions of a project. If the SHA would rather develop new or additional distress indicator models for use in a PRS, some general model development guidelines are also provided.

The previous version of the PRS demonstration software (PaveSpec 2.0) was also greatly improved under the current contract. Specific improvements included in PaveSpec 3.0 include:

- Incorporation of validated or improved distress indicator models.

- The capability to calibrate or modify a national distress indicator model to better reflect a project's local conditions.

- Inclusion of sensitivity analysis capabilities.

- The ability to assess risks to both the contractor and agency through the development of project-specific expected pay (EP) charts.

- An online user's guide.

SEQUENCE OF REPORT

This volume summarizes the results of this research. Specifically, the chapters of this report discuss the following:

- Chapter 2 describes the preliminary work conducted by the research team during the development of the PRS national database (required for model validation/improvement). This preliminary work consisted of a simultaneous evaluation of existing distress indicator models and potential data sources.

- Chapter 3 outlines the different evaluation methods and tools used in the procedures followed to validate or improve the distress indicator models.

- Chapters 4 through 7 present the validated/improved models for JPCP transverse joint faulting, transverse fatigue cracking, transverse joint spalling, and IRI.

- Chapter 8 summarizes the approach and results of the study conducted to identify best-available initial smoothness relationships.

- Chapter 9 provides guidelines that a SHA can use to calibrate an existing national distress indicator model to reflect local conditions. A basic procedure for developing new distress indicator models is also included as part of this chapter.

- Chapter 10 provides a summary of the research conducted under this study, as well as recommendations for future research.

Appendix A contains the complete user's guide for the PaveSpec 3.0 computer software.

As a result of this work, a complete PRS for JPCP is now available for implementation. A user-friendly software package, PaveSpec 3.0, is available to demonstrate the PRS approach and assist in the implementation procedures.

CHAPTER 2: EVALUATION OF DISTRESS INDICATOR MODELS AND POTENTIAL DATA SOURCES

INTRODUCTION

One of the most important components of the current PRS approach is the set of pavement distress indicator models used to predict pavement performance. Such models predict the development of joint spalling and faulting, slab cracking, and pavement smoothness over time, and are based on carefully controlled and well-documented pavement research studies conducted at the *national* level. Although these national models are of generally high merit, many SHA's are concerned about the models' abilities to adequately predict performance representative of their specific designs, materials, subgrades, traffic, and climatic conditions. Given that the data supporting each model fall well short of covering the limitless combinations of these factors, this concern is a legitimate one. If not properly addressed, this issue could inhibit the advancement toward implementation of PRS in many States.

This project addressed the validation or improvement of the distress indicator models included as part of the current PRS approach. These validations/improvements were based on the best available data that represented as many different North American site conditions as possible. As a result of completing the following steps, a new nationwide PRS database was compiled to serve as the basis for validating/improving a chosen set of best-available models:

1. Identification of available JPCP distress indicator models—The most recently published JPCP distress indicator models of the same types as those included in the current PRS methodology were identified and evaluated. Only those models deemed applicable to the current PRS methodology are discussed in this report.

2. Identification and evaluation of potential data sources—All data sources believed to be potentially useful in the validation/improvement of JPCP-related distress indicator models were identified and evaluated.

3. Selection of *best-available* distress indicator models—Based on a comparative analysis of the available distress indicator models (identified in step 1) and the data sources deemed relevant to the model validation/improvement process (identified under step 2), a set of best-available models was selected for validation/improvement under this study.

4. Identification of specific data sources to be included in the nationwide PRS database—The initial list of potential data sources (identified in step 2) was refined to include only those data sources that were directly applicable to the validation/improvement of the chosen best-available distress indicator models. Useful data from all applicable sources were compiled into a nationwide PRS

database, representative of as many North American geographical locations as possible.

The details of each step in this database compilation process are discussed separately in the sections below.

STEP 1—IDENTIFICATION OF AVAILABLE JPCP DISTRESS INDICATOR MODELS

The distress indicator models included in the 1993 original prototype PRS (PaveSpec 1.0) were largely empirical, and thus related the material test result (or construction process test) to a distress through correlation, not necessarily causation. The models incorporated into PaveSpec 2.0 in 1998 were considered to be significant improvements over the original PaveSpec models, but were still lacking in many ways.

The ideal distress prediction models for PRS are those that explain the cause and effect mechanism involved. Hence, they relate the material test value to the resulting development of distress through the mechanisms that occur between the pavement/subgrade structure, traffic loadings, and climate. Such models are referred to as *mechanistic-empirical* models, and they incorporate fundamental engineering properties and relationships.

Since 1993, many studies have been conducted that have produced improved distress indicator models for JPCP. The initial list of distress indicator models investigated in this project was limited to mechanistic-empirical models that meet all of the following criteria:

- *Model type*—Only prediction models for transverse joint faulting, transverse fatigue cracking, transverse joint spalling, and IRI were chosen for investigation under this project.

- *Recently developed models*—The initial list of models was limited to those included in research reports published in 1993 or after.

- *Functions of PRS-related AQC's*—Only existing models that were functions of one or more of the currently identified PRS-related AQC's (concrete strength, slab thickness, air content, initial smoothness, or percent consolidation around dowels) were included in the initial list of distress indicator models to be investigated.

The initial models and the associated research studies that were identified for consideration are summarized in table 1.

Table 1. Summary of recently developed distress indicator models considered relevant to the PRS methodology.

Distress Indicator Model	Pavement Type	Model Source (see list below)	Used in PaveSpec 2.0*
Transverse joint faulting	Doweled JPCP	Simpson et al., 1994	
		Yu et al., 1997	
	Non-doweled JPCP	Simpson et al., 1994	
		Yu et al., 1997	
	Doweled and Non-doweled JPCP	Owusu-Antwi et al., 1997	
		Titus-Glover et al., 1999	
		Yu et al., 1998	√
Transverse fatigue cracking	Doweled and Non-doweled JPCP	Simpson et al., 1994	
		Owusu-Antwi et al., 1997	
		Titus-Glover et al., 1999	
		Yu et al., 1997	
Transverse joint spalling	Doweled and Non-doweled JPCP	Simpson et al., 1994	
		Titus-Glover et al., 1999	
		Yu et al., 1997	√
IRI	Doweled and Non-doweled JPCP	Byrum et al., 1997	
		Titus-Glover et al., 1999	
		Yu et al., 1997	
		Hoerner et al., 1999	√
	Doweled JPCP	Simpson et al., 1994	
	Non-doweled JPCP	Simpson et al., 1994	

* The transverse cracking model used in PaveSpec 2.0 was a modified version of the 1990 transverse cracking model by Smith et al.[18]

Model Source Reference List

Byrum et al., 1997. *The Effect of PCC Strength and Other Parameters on the Performance of PCC Pavements.*[12]
Hoerner et al., 1999. *Guide to Developing Performance-Related Specifications for PCC Pavements, Volume III: Appendixes C Through F.*[10]
Owusu-Antwi et al., 1997. *Development and Calibration of Mechanistic-Empirical Distress Models for Cost Allocation.*[13]
Simpson et al., 1994. *Early Analysis of LTPP General Pavement Studies Data, Volume III: Sensitivity Analyses for Selected Pavement Distresses.*[14]
Titus-Glover et al., 1999. *Design and Construction of PCC Pavements, Volume III: Improved PCC Performance.*[15]
Yu et al., 1997. *Performance of Concrete Pavements, Volume III: Improving Concrete Pavement Performance.*[16]
Yu et al., 1998. Final Report, NCHRP Project 1-34—*Guidelines for Subsurface Drainage.*[17]

STEP 2—IDENTIFICATION AND EVALUATION OF POTENTIAL DATA SOURCES

This section contains a complete summary of the procedures used to identify and evaluate the potential data sources included in the national PRS model validation/improvement database. The evaluation includes an assessment of the accuracy, applicability, advantages, and limitations of the data included in each data source.

Identification of Required Data Types for Inclusion in the National PRS Database

To successfully validate/improve the distress indicator models, it was imperative that the national PRS database be as comprehensive and complete as possible. To be included in the database, pavement sections were required to have some form of each of the following five data types:

- *Traffic data*—Most of the existing PRS distress indicator models require cumulative or annual 80-kN (18-kip) equivalent single-axle loads (ESAL's) as an input. (Note: the only model exceptions to this traffic requirement are some transverse joint spalling and pavement smoothness-related models, which are a function of age rather than traffic.) Because of this large dependency on traffic information, only data sources with adequate time-series traffic data were targeted for inclusion in the national database. Although the American Association of State Highway Transportation Officials (AASHTO)-based load equivalency factors have certain limitations, the limited resources of this project did not allow for a more thorough consideration of traffic loads.

- *Design feature characteristic data*—Each useful data source must contain adequate pavement design feature data to relate design characteristics to the measured performance (time-series distress data). For clarification, design features can be divided into materials-, PCC slab support-, drainage-, and joint-related variables. Examples of variables included in each of these design-related categories include the following:

    - Materials—PCC strength and coefficient of thermal expansion, joint sealant type, and base material strength.

    - PCC slab support—base type, modulus of subgrade reaction (k-value), subgrade type, and shoulder type.

    - Drainage—AASHTO drainage coefficient (C_d), base permeability, presence of longitudinal edge drains, and subgrade soil type.

    - Joints—presence of dowel bars, dowel bar diameter, and transverse joint spacing.

The usefulness of each potential database was assessed by comparing the types of design inputs available in a given database to those design inputs specifically required by the available models.

- *Climatic data*—It was desired that each data source chosen for inclusion in the PRS database have climatic data characterizing the included sections. Examples of climate-related variables include average annual total precipitation, average annual number of wet days, mean freezing index, and number of days above 32 °C (90 °F). Such climatic information was very important to this study, since a major focus of the model validation/improvement process was to develop models that more accurately represent the local geographical conditions of a project.

- *AQC construction data*—The current PRS methodology is driven by the comparison of the as-designed AQC values with as-constructed AQC values measured in the field. The AQC values are used in the distress indicator models to predict the expected performance and corresponding LCC's of both the as-designed and as-constructed pavements. It was therefore critical that each useful data source included in the national PRS database have construction data directly or indirectly representing at least one of the five AQC's available in the current PRS approach (i.e., concrete strength, slab thickness, air content, initial smoothness, and percent consolidation around dowels).

- *Time-series distress indicator data*—Adequate time-series distress data were required to quantify the long-term performance of JPCP sections. Data sources containing time-series data for transverse joint faulting, transverse cracking, transverse joint spalling, and IRI were targeted. The performance data within each data source were evaluated based on many different characteristics, including the number of independent sections, the number of years of time-series data, and the measurement units used to define each distress type.

Specific Data Elements Required by the Available Distress Indicator Models

In preparation for the search for potential data sources, it was important to summarize all of the specific data elements required by the short list of best-available distress indicator models identified under step 1. Tables 2 through 5 summarize the data elements (cross-referenced by model type and source) required by the best available JPCP transverse joint faulting, transverse fatigue cracking, transverse joint spalling, and IRI models. This model information was used to identify specific data sources that could be included in the national PRS database.

Identification and Evaluation of Potential Data Sources

Since the overall objective of the study was to validate or improve the best available existing models, it was important that some or all of the required model inputs and outputs be compatible with the data available from the data sources. Based on the

Table 2. Summary of required data elements included in the short list of best-available JPCP transverse joint faulting models.

Pavement Type	Model Source	Used in PaveSpec 2.0	Model Inputs (in English units)																							Model Output (in English units)
			Cumulative ESAL's	Age, years	Avg. Joint Spacing/Slab Length, ft	Presence of Dowel Bars	Dowel Bar Diameter, in	PCC Modulus of Elasticity, psi	Avg. Annual Freezing Index, °F-days	Avg. Annual Precipitation, in	Avg. Annual Number of Wet Days	Avg. Annual No. of Days Above 90 °F	Avg. Temperature Range, °F	Base Type	Erodibility of Base (erodible vs. non-erodible)	Presence of Lean Concrete Base	Mod. of Subgrade Reaction (k-value), psi/in	Presence of Widened Lane	Widened Lane Amount, in	Shoulder Type/Edge Support	AASHTO Drainage Coefficient, Cd	Base Permeability	Presence of Long. Edge Drains	PCC Slab Thickness, in	Percent Consolidation Around Dowels, %	
Doweled	Simpson et al., 1994.[14]		√	√	√		√										√			√						Avg. faulting per joint, in
	Yu et al., 1997.[16]		√	√	√		√	√	√	√			√	√			√	√			√			√		
Non-doweled	Simpson et al., 1994.[14]		√	√					√	√													√			
	Yu et al., 1997.[16]		√		√				√	√		√		√				√			√			√		
Doweled and Non-doweled	Owusu-Antwi et al., 1997.[13]		√		√		√	√	√						√		√		√		√			√		
	Titus-Glover et al., 1999.[15]		√		√		√	√			√				√		√		√		√			√		
	Yu et al., 1998.[17]		√		√	√	√	√			√	√		√		√	√		√			√		√		
	Hoerner et al., 1999.[10]	√*	√		√	√	√	√			√	√		√		√	√		√			√		√	√	

* The transverse joint faulting model used in PaveSpec 2.0 is a modified version of the 1998 faulting model by Yu et al.

Table 3. Summary of required data elements included in the short list of best-available JPCP transverse fatigue cracking models.

Model Source	Used in PaveSpec 2.0*	Model Inputs (in English units)																	Model Output
		Cumulative ESAL's	Age, years	Avg. Joint Spacing/Slab Length, ft	PCC Coefficient of Thermal Expansion	PCC Modulus of Elasticity, psi	Avg. Annual Number of Wet Days	Avg. Annual Freeze-Thaw Cycles (air)	Avg. Annual No. of Days Above 90 °F	Thermal Gradient in Slab	Base Type (stabilized/non-stabilized)	Base Thickness, in.	Base Modulus of Elasticity, psi	Mod. of Subgrade Reaction (k-value), psi/in	Presence of Widened Lane	Presence of Tied PCC Shoulder	PCC 28-day Flexural Strength, psi	PCC Slab Thickness, in	
Owusu-Antwi et al., 1997.[13]		√		√	√	√				√	√			√		√	√	√	% Slabs Cracked (all severities)
Titus-Glover et al., 1999.[15]		√	√			√	√	√	√									√	
Yu et al., 1997.[16]		√		√	√	√				√	√	√	√	√	√	√	√	√	

* The transverse cracking model used in PaveSpec 2.0 is a modified version of the 1990 model by Smith et al.[18]

Table 4. Summary of required data elements included in the short list of best-available JPCP transverse joint spalling models.

Model Source	Used in PaveSpec 2.0	Model Inputs (in English units)																							Model Output
		Cumulative ESAL's	Age, years	Avg. Joint Spacing/Slab Length, ft	PCC Coefficient of Thermal Expansion	PCC Modulus of Elasticity, psi	Average Daily Temperature Range, °F	Avg. Annual Freezing Index, °F-days	Avg. Annual Freeze-Thaw Cycles (air)	Avg. Ann. Freeze-Thaw Cycles (in-pavement)	Avg. Annual No. of Days Above 90 °F	Thermal Gradient in Slab	Avg. Daily Range of Relative Humidity During the Month of Construction	Presence of Salt	Subbase Friction Factor	Joint Sealant Type	Joint Sealant Modulus, psi/in	Joint Sealant Depth, in	Mod. of Subgrade Reaction (k-value), psi/in	Presence of Dowel Bar Corrosion	PCC Slab Thickness, in	Indirect Tensile Strength, psi	28-day Compressive Strength, psi	PCC Air Content, %	
Simpson et al., 1994.[14]			√						√																% of spalled joints (all severities)
Titus-Glover et al., 1999.[15]		√	√	√	√	√	√		√			√	√		√		√	√	√		√	√			
Yu et al., 1997.[16]			√	√				√			√					√				√					% of spalled joints (medium and high severities)
Hoerner et al., 1999.[10]	√		√	√				√		√	√			√		√				√			√	√	

Table 5. Summary of required data elements included in the short list of best-available JPCP IRI models.

Pavement Type	Model Source	Used in PaveSpec 2.0	Model Inputs (in English units)																															Model Output (in English units)
			Cumulative ESAL's	Annual ESAL's	Age, years	Avg. Joint Spacing/Slab Length, ft	Avg. Annual Freezing Index, °F-days	Avg. Annual Precipitation, in.	LTPP Climatic Zone (freeze/non-freeze)	Avg. Annual Number of Wet Days	Avg. Annual Freeze-Thaw Cycles (air)	Avg. Annual No. of Days Below 32 °F	Base Type (stabilized/non-stabilized)	Mod. of Subgrade Reaction (k-value), psi/in	Subgrade AASHTO Soil Classification	Subgrade Type (fine/coarse)	Subgrade Percent Passing #200	Subgrade Moisture Content, %	Subgrade Overburden Pressure, psf	Presence of Tied PCC Shoulder	Dowel Diameter, in.	PCC Modulus of Elasticity, psi	PCC Split-Tensile Strength, psi	PCC Water/Cement (w/c) Ratio	PCC Slab Thickness, in	Initial IRI	Initial PSR	Total Trans. Joint Faulting Per Mile, in/mile	Avg. Trans. Faulting Per Joint, in	Percentage of Spalled Joints, %	Total No. of Transverse Cracks, #/mi	Percentage of Cracked Slabs, %	Total Length of Long. Cracking, ft/mi	
Doweled	Simpson et al., 1994.[14]				√	√								√						√					√										IRI, in / mi
Non-doweled	Simpson et al., 1994.[14]		√					√			√		√		√																			
Doweled and Non-doweled	Byrum et al., 1997.[12]			√	√	√	√			√		√					√	√	√			√	√	√	√									
	Titus-Glover et al., 1999.[15]		√		√		√		√	√						√					√	√												
	Yu et al., 1997.[16]																											√		√	√			
	Hoerner et al., 1999.[10]	√			√																					√			√	√		√		

identification of available distress indicator models and their required data elements, the following initial list of five data sources identified for potential inclusion in the national PRS database was created:

- FHWA Rigid Pavement Performance and Rehabilitation (RPPR) database.[16,18]
- Strategic Highway Research Program (SHRP)/FHWA LTPP program database—includes Ohio Test Road sections.
- NCHRP Project 1-19 database—includes sections from six States plus the extended AASHTO Road Test.[19]
- NCHRP Project 1-34 database.[17]
- Minnesota Test Road (Mn/ROAD) database.

To determine if the data included in each of these five data sources were suitable for use in the model validation/development task of this study, each database was evaluated in terms of the applicability, completeness, advantages, and limitations of the data. Some examples of specific data source characteristics that were assessed include the following:

- Number of independent sections.
- Geographic coverage (national, regional, State, other).
- Availability of time-series distress data (types of distress data, number of years of data, units of measured distress data).
- Availability of site condition data (traffic, climate, subgrade type).
- Availability of design feature data (design slab thickness, joint spacing, joint load transfer, subdrainage, shoulders, widened slab, base-related variables).
- Availability of construction AQC data (concrete strength, slab thickness, air content, initial smoothness, and percent consolidation around dowels).
- Assessments of the consistency and accuracy of the data.

The results of each evaluation are summarized in the following sections.

FHWA RPPR[16,18]

The FHWA RPPR database contains data on 303 concrete pavement sections located throughout 15 U.S. States and 1 Canadian Province. Of these 303 sections, 161 are JPCP with or without dowels. The JPCP sections cover all 16 States/Provinces and all 4

SHRP climatic zones. Of the 161 JPCP sections, 53 were evaluated for field performance (i.e., distresses, roughness) during two separate years: 1987 and 1992. The remaining 108 sections were evaluated only in 1992. Hence, initial performance data (actual or assumed) aside, true time-series performance data (i.e., 2 or more performance data points over time following an immediate post-construction testing period) are available for 53 sections.

In general, the RPPR database was found to be fairly complete with regard to site condition data (e.g., traffic, climate, subgrade) and design feature data (e.g., PCC thickness, joint spacing, base, drainage, load transfer, shoulder). Traffic loading values are estimated values based on traffic data provided by participating highway agencies, and many climatic variables are available and complete. AQC data include PCC core thickness values for approximately one-third of the sections and PCC core modulus of rupture (MR) values (converted from split-tensile strength tests) for approximately one-fourth of the sections (falling-weight deflectometer [FWD] backcalculated slab modulus of elasticity values are available for all sections). Initial smoothness measurements and PCC air content measurements are not available for any sections.

The RPPR performance data of primary interest in this study included transverse joint edge faulting (average faulting expressed in inches per joint), transverse fatigue cracking (percent cracked slabs), transverse joint spalling (percent spalled joints), and surface smoothness (present serviceability rating [PSR], expressed as a rating between 0 and 5; IRI, expressed in inches/mile; and Mays ride number [MRN], expressed in inches/mile). Faulting, cracking, spalling, and PSR values were obtained through the on-site surveys in 1987 and 1992. IRI values were obtained in the 1992 surveys through profile measurements using a South Dakota-type inertial profiler. MRN values were obtained in the 1987 surveys through Mays Ride Meter testing. It is important to note that the LTPP distress identification definitions were used in all field surveys.

SHRP/FHWA Long Term Pavement Performance Program

The SHRP/FHWA LTPP program database was the most comprehensive and detailed database considered in this study. It contains information on 916 general pavement studies (GPS) sections and approximately 2,500 specific pavement studies (SPS) sections located throughout 50 U.S. States, 10 Canadian Provinces, the District of Columbia, and Puerto Rico. Of the 916 GPS sections, 134 are designated as GPS-3 sections, which are doweled or non-doweled JPCP. The GPS-3 sections cover 33 States, 3 Canadian Provinces, and Puerto Rico, and all 4 SHRP climatic zones.

The latest official release of the LTPP database was made in 1999 through the release of DataPave 2.0. This software facilitates the exploration and retrieval of all available GPS and SPS pavement section data (inventory, material testing, monitoring, climatic, traffic, maintenance, rehabilitation, and seasonal testing) collected and reviewed to the highest quality assurance level (level E). In general, the current LTPP

database is fairly complete with regard to site condition and design feature data for GPS-3 sections. Traffic loading data, based on traffic counts and weigh-in-motion devices, are available for nearly all sections; however, for several sections, the data only represent 1 or 2 years or are not very recent (i.e., before 1995). Climate and subgrade data are largely complete, as are pavement design data, such as PCC thickness, joint spacing, load transfer, and shoulder data.

AQC data available in the LTPP database include PCC thickness, concrete strength (various strength types and PCC elastic modulus), air content, and historical smoothness data (which can be used to backcast the initial smoothness). Though average PCC thickness values are largely available from the construction records (i.e., inventory data) kept by participating highway agencies, most sections include multiple thickness measurements made on cores extracted under the LTPP testing program. Although the database includes PCC strength (flexural, compressive, split-tensile) and modulus data (based on different test methods and core/beam specimen ages) derived from highway agency construction testing records, those data are often not complete and typically include only average values. Strength and modulus data on cores extracted under the LTPP testing program are also available and are quite complete; however, these data represent long-term measurements rather than initial construction measurements. Initial smoothness data, in the form of profilograph PI values and K.J. Law Profilometer IRI values, are available for several SPS-2 (PCC pavement) sections. Lastly, inventory PCC air content values are available for a limited number of sections.

LTPP performance data are fairly abundant and generally span 3 to 5 years from the year of the first field survey. Both automated and manual distress survey data are available, with the manual survey data believed to be more reliable. Though many forms of performance data exist within the LTPP database, those of primary interest in this study were largely complete and available for use. They included transverse joint edge faulting (average joint faulting in millimeters), transverse fatigue cracking (number of cracked slabs), transverse joint spalling (number of medium and high severity spalled joints), and surface smoothness (expressed in various forms, including average IRI).

NCHRP Project 1-19[19]

The NCHRP 1-19 Concrete Pavement Evaluation System (COPES) database contains data on 425 JPCP and jointed reinforced concrete pavement (JRCP) sections located throughout 8 U.S. States. Of these 425 sections, 152 are JPCP with and without dowel bars. The JPCP sections represent five States and all four SHRP climatic zones. For some sections, time-series performance data are available. However, the long-term performance measurements of most sections are depicted by one point in time.

In general, site condition data in the COPES database were found to be available and complete. Subgrade reaction moduli reflect estimated values based on the AASHTO

soil classification. Traffic loading data are derived from traffic counts provided by participating agencies.

AQC data are essentially not available. Thickness measurements contained in the database represent the design thickness. Moreover, although flexural strength values (based on beam tests) are available, only the average value for each section is listed and different test methods and test ages were used. Data for PCC air content, initial surface smoothness, and percent consolidation around dowels were not available.

The following types of long-term performance data are available on the COPES evaluation sections:

- Average transverse joint edge faulting.
- Percentage of spalled transverse joints.
- Length of transverse fatigue cracking.
- Length of longitudinal cracking.
- PSR.

For each of these performance variables, no more than one-third of the JPCP sections have true time-series performance data available. The definitions of these distresses are generally similar to the LTPP definitions.

NCHRP Project 1-34[17]

The NCHRP Project 1-34 database consists of pavement sections from three recent pavement research studies: FHWA RPPR, SHRP/FHWA LTPP, and the NCHRP Project 1-34 drainage surveys. It contains data on 483 flexible, rigid, and composite pavement sections located throughout the United States and Canada. The 1-34 database was developed with the specific objectives of quantifying the benefits of subsurface drainage and identifying criteria and conditions for which subsurface drainage is appropriate.

The FHWA RPPR and LTPP databases were discussed earlier. The NCHRP 1-34 drainage survey contains a total of 26 doweled or non-doweled JPCP sections. These sections are located in five U.S. States and one Canadian Province, and they represent the wet-freeze and wet-nonfreeze SHRP climatic zones. The sections were constructed between 1980 and 1990, and each section was manually surveyed once in the fall of 1996. Hence, true time-series performance data are not available for any of the 26 JPCP sections.

With the exception of modulus of subgrade reaction (k-value) data, the 1-34 drainage database was found to be quite complete with respect to site condition data. Estimated cumulative ESAL's at the time of field surveys are available for each section, as are several key climatic variables and subgrade soil classifications. Since FWD testing was not part of the drainage surveys, backcalculated subgrade k-values and PCC elastic modulus values are not available. It should be noted that in the

development of the NCHRP 1-34 JPCP faulting model, k-values for these sections were estimated based on AASHTO soil classification. Design feature data, such as layer types and thicknesses, joint and load transfer information, and drainage system data, are available and complete.

AQC data on the 1-34 drainage survey sections are nonexistent. PCC thickness values contained in the database represent the design thickness, not as-constructed thickness. There are no PCC strength, air content, percent consolidation around dowels, or initial smoothness measurements available.

Though the performance data contained in the database represent only one point in time, they are complete. Each JPCP section has measured values of transverse joint faulting (average joint edge faulting), transverse fatigue cracking (percent cracked slabs), transverse joint spalling (percent spalled joints), and surface smoothness (PSR).

Mn/ROAD Test Sections

The Mn/ROAD database contains comprehensive information on 40 pavement sections constructed in the early 1990s along I-94 near Otsego, Minnesota. The sections, which are denoted as test cells, include 23 flexible and rigid pavement designs that are part of the I-94 mainline roadway and 17 flexible and rigid designs that are part of a low-volume, controlled traffic test loop lying parallel to I-94.

The Mn/ROAD test sections represent only one State (Minnesota) and one SHRP climatic zone (wet-freeze). There are nine doweled JPCP sections on the I-94 mainline and five doweled and non-doweled JPCP sections on the low-volume test loop.

Climatic, traffic, and subgrade data in the Mn/ROAD database were found to be comprehensive and complete. Climatic data are available for various time frames (i.e., hourly, daily, monthly), and accurate traffic loading data have been produced from weigh-in-motion devices. Subgrade reaction moduli and layer elastic moduli are available as a result of FWD testing and analysis. Design feature data are also comprehensive and complete.

True time-series performance data are available for all 14 JPCP sections. Key pavement distress data, such as transverse joint spalling (percent joints spalled), transverse fatigue cracking (number of cracked slabs), and longitudinal cracking (length of cracking) have been measured manually every year since about 1994. IRI measurements made with a PaveTech inertial profiler are available on a quarterly basis for the years 1994 through 1996, and average transverse joint faulting data using the Georgia fault meter are available on a quarterly basis for the years 1994 through 1998.

Availability of Required Data Elements in the Identified Potential Data Sources

As a first step in assessing the usefulness of the identified potential data sources to the validation or improvement of the available distress indicator models, the data inputs required by the short-listed best-available models (those variables shown in tables 2 through 5) were cross referenced with each of the five potential databases. Tables 6 through 9 contain model-type specific tables that illustrate the availability of specific data elements required by the transverse joint faulting, transverse slab cracking, transverse joint spalling, and IRI models.

STEP 3—SELECTION OF BEST-AVAILABLE DISTRESS INDICATOR MODELS

After completing an initial review of both the available distress indicator models and potential data sources, the most suitable models of each type were selected for use within the PRS methodology. This model selection procedure consisted of a multi-part process that assessed the general quality of each model, evaluated each model's applicability for use within the current PRS methodology, and finally reviewed the availability of data required to validate/improve each model. For this comparative study, the following characteristics were appraised for each model:

- *Mechanistic/empirical*—Is the model based on mechanistic or empirical concepts?
- *Development database*—What data sources were used in the development of the model?
- *Data quality*—What is the quality of the data used in the model development process?
- *AQC's included in model*—What PRS AQC's are included as inputs to the model?
- *Model statistics*—What are the model statistics (i.e., number of data points, coefficient of determination [R^2], standard error estimate [SEE]) associated with each model?
- *Availability of required model inputs*—Are there sufficient data available (in the collective potential data sources) to sufficiently validate or improve the model? If specific data elements are not available, can values for these required data elements be estimated or interpreted from other data in the data sources (e.g., flexural strength estimated from compressive strength)?

Based on significant past experience in developing distress indicator models for JPCP, the most suitable models for the validation/improvement portion of the study were selected. Tables 10 through 13 summarize the evaluations of each model's characteristics as they relate to the questions outlined above. Brief discussions of the processes used to select the best available model for each model type are presented in the following sections.

Table 6. Availability of data required by the short-listed JPCP transverse joint faulting models.

Data Element	Database				
	RPPR	LTPP	NCHRP 1-19	NCHRP 1-34	Mn/ROAD
Traffic loads (ESAL's)	Estimated ESAL's	Estimated ESAL's and WIM data	Estimated ESAL's	Estimated ESAL's	WIM data
Pavement age	Yes	Yes	Yes	Yes	Yes
Avg. transverse joint spacing	Yes	Yes	Yes	Yes	Yes
Presence of dowel bars	Yes	Yes	Yes	Yes	Yes
Dowel bar diameter	Yes	Yes	Yes	Yes	Yes
PCC modulus of elasticity	Backcalculated	Field testing data (cores and cylinders)	No	No	Field testing data (cores)
Avg. annual freezing index	Yes	Yes	Yes	Yes	Yes
Avg. annual precipitation	Yes	Yes	Yes	Yes	Yes
Avg. annual no. of wet days	Yes	Yes	No	Yes	Yes
Avg. annual no. of hot days	Yes	Yes	No	No	Yes
Avg. temperature range	Yes	Yes	Yes	Yes	Yes
Base type information	Yes	Yes	Yes	Yes	Yes
Modulus of subgrade reaction (k-value)	Backcalculated from deflection data	Backcalculated from deflection data	Estimated	Estimated	Yes
Widened lane information	Yes	Yes	No	Yes	Yes
Shoulder type	Yes	Yes	Yes	Yes	Yes
AASHTO drainage coefficient, C_d	Yes	No	No	No	No
Base permeability (yes/no)	Yes	Yes	No	Yes	Yes
Drainage type	Yes	Yes	Yes	Yes	Yes
PCC slab thickness	Design and from cores	Design and from cores	Yes (design)	Yes (design)	Yes (design/cores)
Percent consolidation around dowels	No	No	No	No	No
Transverse joint edge faulting time-series data	Yes	Yes	Yes	No	Yes

Table 7. Availability of data required by short-listed JPCP transverse cracking models.

Data Element	Database				
	RPPR	**LTPP**	**NCHRP 1-19**	**NCHRP 1-34**	**Mn/ROAD**
Traffic loads (ESAL's)	Estimated ESAL's	Estimated ESAL's and WIM data	Estimated ESAL's	Estimated ESAL's	WIM data
Pavement age	Yes	Yes	Yes	Yes	Yes
Avg. transverse joint spacing	Yes	Yes	Yes	Yes	Yes
PCC coefficient of thermal expansion	No	Yes	No	No	No
PCC modulus of elasticity	Backcalculated from deflection data	Field testing data (cores and cylinders)	No	No	Field testing data (cores)
Avg. annual no. of wet days	Yes	Yes	No	Yes	Yes
Avg. annual freeze-thaw cycles (air)	Yes	Yes	No	Yes	Yes
Avg. annual no. of hot days	Yes	Yes	No	No	Yes
Temperature gradient in slab	Estimated	Measured for some sections	No	No	Yes
Base type information	Yes	Yes	Yes	Yes	Yes
Base thickness	Design and from cores	Yes	Yes	Yes	Yes
Base modulus of elasticity	No	From cores and cylinders	No	No	Yes
Modulus of subgrade reaction (k-value)	Backcalculated from deflection data	Backcalculated from deflection data	Estimated	Estimated	Yes
Widened lane information	Yes	Yes	No	Yes	Yes
Shoulder type	Yes	Yes	Yes	Yes	Yes
PCC flexural strength	Estimated from elastic modulus and cores	Yes	Yes	No	Yes
PCC thickness	Design and from cores	Design and from cores	Yes (design)	Yes (design)	Yes (design / cores)
Transverse fatigue cracking time-series data	Yes	Yes	Yes	No	Yes

Table 8. Availability of data required by the short-listed JPCP transverse joint spalling models.

Data Element	Database				
	RPPR	**LTPP**	**NCHRP 1-19**	**NCHRP 1-34**	**Mn/ROAD**
Traffic loads (ESAL's)	Estimated ESAL's	Estimated ESAL's and WIM data	Estimated ESAL's	Estimated ESAL's	WIM data
Pavement age	Yes	Yes	Yes	Yes	Yes
Avg. transverse joint spacing	Yes	Yes	Yes	Yes	Yes
PCC coefficient of thermal expansion	No	Yes	No	No	No
PCC modulus of elasticity	Backcalculated from deflection data	Field testing data (cores and cylinders)	No	No	Yes (cores)
Average daily temperature range	Yes	Yes	Yes	Yes	Yes
Avg. annual freezing index	Yes	Yes	Yes	Yes	Yes
Avg. annual freeze-thaw cycles (air)	Yes	Yes	No	Yes	Yes
Avg. annual freeze-thaw cycles (in-pavement)	No	No	No	No	No
Avg. annual no. of hot days	Yes	Yes	No	No	Yes
Thermal gradient in slab	Estimated	Measured for some sections	No	No	Yes
Average daily range of relative humidity during the month of construction	No	Yes	No	No	Yes
Presence of salt	No	No	No	No	Yes
Subbase friction factor	No	No	No	No	No
Joint sealant type	Yes	Yes	Yes	No	Yes
Joint sealant modulus	No	No	No	No	No
Joint sealant depth	No	No	No	No	Yes
Modulus of subgrade reaction (k-value)	Backcalculated from deflection data	Backcalculated from deflection data	Estimated	Estimated	Yes
Presence of dowel bars	Yes	Yes	Yes	Yes	Yes
Presence of dowel bar corrosion	No	No	No	No	No
PCC slab thickness	Design and from cores	Design and from cores	Yes (design)	Yes (design)	Yes (design/cores)
PCC indirect tensile strength	Estimated	Lab and field testing data	No	No	Yes
PCC Compressive strength	Estimated	Lab and field testing data	No	No	Yes
PCC air content	No	Some design, fresh, and hardened air data	No	No	Yes
Transverse joint spalling time-series data	Yes	Yes	Yes	No	Yes

Table 9. Availability of data required by the short-listed JPCP IRI models.

Data Element	Database				
	RPPR	**LTPP**	**NCHRP 1-19**	**NCHRP 1-34**	**Mn/ROAD**
Traffic loads (ESAL's)	Estimated ESAL's	Estimated ESAL's and WIM data	Estimated ESAL's	Estimated ESAL's	WIM data
Pavement age	Yes	Yes	Yes	Yes	Yes
Avg. transverse joint spacing	Yes	Yes	Yes	Yes	Yes
Avg. annual freezing index	Yes	Yes	Yes	Yes	Yes
Avg. annual precipitation	Yes	Yes	Yes	Yes	Yes
LTPP climatic zone	Yes	Yes	Yes	Yes	Yes
Avg. annual no. of wet days	Yes	Yes	No	Yes	Yes
Avg. annual freeze-thaw cycles (air)	Yes	Yes	No	Yes	Yes
Avg. annual no. of freezing days	Yes	Yes	No	No	Yes
Base type information	Yes	Yes	Yes	Yes	Yes
Modulus of subgrade reaction (k-value)	Backcalculated from deflection data	Backcalculated from deflection data	Estimated	Estimated	Yes
Subgrade AASHTO soil classification	Yes	Yes	No	No	Yes
Subgrade type	Yes	Yes	Yes	Yes	Yes
Subgrade % passing 200	No	Yes	Yes	No	Yes
Subgrade moisture content	No	Yes	No	No	No
Subgrade overburden pressure	No	No	No	No	No
Shoulder type	Yes	Yes	Yes	Yes	Yes
Dowel bar diameter	Yes	Yes	Yes	Yes	Yes
PCC modulus of elasticity	Backcalculated from deflection data	Field testing data (cores and cylinders)	No	No	Field testing data (cores)
PCC tensile strength	Estimated	Lab and field testing data	No	No	Yes
PCC water/cement (w/c) ratio	No	Yes	No	No	Yes
PCC slab thickness	Design and from cores	Design and from cores	Yes (design)	Yes (design)	Yes (design/cores)
Initial IRI	No	Estimated from time-series data	No	No	Yes
Transverse joint edge faulting time-series data	Yes	Yes	Yes	No	Yes
Transverse joint spalling time-series data	Yes	Yes	Yes	No	Yes
Transverse fatigue cracking time-series data	Yes	Yes	Yes	No	Yes
IRI time-series data	Yes	Yes	No	No	Yes

Table 10. Assessment of best-available JPCP transverse joint faulting models.

Pavement Type	Model Source	Model Type	Development Database	Quality of Data Used in Model Development	Current PRS AQC's Included in Model	Model Statistics	Availability of Required Model Inputs
Doweled JPCP	Simpson et al., 1994.[14]	Empirical	LTPP	Good	None	N=59 sections R^2=0.53 SEE=0.028 in	All 6 inputs are available in all potential databases.
	Yu et al., 1997.[16]	Mechanistic-Empirical	RPPR	Good	Thickness	N= 146 sections R^2=0.60 SEE=0.022 in	Sufficient data available for 12 of 13 inputs. Limited data for AASHTO drainage coefficient.
Non-doweled JPCP	Simpson et al., 1994.[14]	Empirical	LTPP	Good	None	N=25 sections R^2=0.55 SEE=0.047 in	All 5 inputs are available in all potential databases.
	Yu et al., 1997.[16]	Mechanistic-Empirical	RPPR	Good	Thickness	N= 131 sections R^2=0.45 SEE=0.034 in	Sufficient data available for 8 of 9 inputs. Limited data for AASHTO drainage coefficient.
Doweled and Non-doweled JPCP	Owusu-Antwi et al., 1997.[13]	Mechanistic-Empirical	RPPR	Good	Thickness	N=101 sections R^2=0.52 SEE=0.03 in	Sufficient data available for 9 of 10 inputs. Limited data for AASHTO drainage coefficient.
	Titus-Glover et al., 1999.[15]	Mechanistic-Empirical	LTPP	Good	Thickness	N=120 sections R^2=0.56 SEE=0.03 in	Sufficient data available for 9 of 10 inputs. Limited data for AASHTO drainage coefficient.
	Yu et al., 1998.[17]	Mechanistic-Empirical	RPPR LTPP	Good	Thickness	N= 351 sections R^2=0.50 SEE=0.035 in	Sufficient data available for all 13 inputs.
	Hoerner et al., 1999.[10]	Mechanistic-Empirical	RPPR LTPP	Good	Thickness % Consolidation[1]	N= 351 sections R^2=0.50 SEE=0.035 in	Sufficient data available for 13 of 14 inputs. No data available for percent consolidation around dowels.

[1] The faulting model used in PaveSpec 2.0 is the 1998 faulting model (developed by Yu) modified to include percent consolidation around dowels.

Table 11. Assessment of best-available JPCP transverse cracking models.

Model Source	Model Type	Development Database	Quality of Data Used in Model Development	Current PRS AQC's Included in Model	Model Statistics	Availability of Required Model Inputs
Owusu-Antwi et al., 1997.(13)	Mechanistic-Empirical	RPPR	Good	Strength Thickness	N= 302 sections R^2=0.88 SEE=9.8% cracked slabs	Sufficient data available for 9 of 10 inputs. Limited data for PCC coefficient of thermal expansion.
Titus-Glover et al., 1999.(15)	Mechanistic-Empirical	LTPP	Good	Thickness	N=92 sections R^2=0.64 d = 1.816 VIF=0 to 2.32	Sufficient data available for all 7 inputs.
Yu et al., 1997.(16)	Mechanistic-Empirical	RPPR	Good	Strength Thickness	N=465 sections R^2=0.91 SEE=6.8% cracked slabs	Sufficient data available for 12 of 13 inputs. Limited data for PCC coefficient of thermal expansion.

Table 12. Assessment of best-available JPCP transverse joint spalling models.

Model Source	Model Type	Development Database	Quality of Data Used in Model Development	Current PRS AQC's Included in Model	Model Statistics	Availability of Required Model Inputs
Simpson et al., 1994.(14)	Empirical	LTPP	Good	None	N= 56 sections R^2=0.36 SEE=11.05% spalled joints	Sufficient data available for both inputs.
Titus-Glover et al., 1999.(15)	Mechanistic-Empirical	LTPP	Good	Thickness Strength	N=52 sections R^2=0.61 SEE=12.0% spalled joints	Sufficient data available for 11 of 15 inputs. Limited data for PCC coefficient of thermal expansion, and no data for subbase friction factor, joint sealant modulus, and joint sealant depth.
Yu et al., 1997.(16)	Mechanistic-Empirical	RPPR	Good	None	N= 164 sections R^2=0.76 SEE=5.4% spalled joints	Sufficient data available for 5 of 6 inputs. No data for presence of dowel bar corrosion.
Hoerner et al., 1999.(10)	Mechanistic-Empirical	RPPR	Good	Strength Air Content[1]	N= 164 sections R^2=0.76 SEE=5.4% spalled joints	Sufficient data available for 6 of 10 inputs. Limited data for PCC air content and presence of salt, and no data for average annual in pavement freeze-thaw cycles and presence of dowel bar corrosion.

[1] The spalling model used in PaveSpec 2.0 is the 1997 joint spalling model (developed by Yu) modified to include PCC 28-day compressive strength and air content.

Table 13. Assessment of best-available JPCP IRI models.

Pavement Type	Model Source	Model Type	Development Database	Quality of Data Used in Model Development	Current PRS AQC's Included in Model	Model Statistics	Availability of Required Model Inputs
Doweled JPCP	Simpson et al., 1994.[14]	Empirical	LTPP	Good	Thickness	N=21 sections R^2=0.55 SEE=19.06 in/mi	All 5 inputs are available in all potential databases.
Non-doweled JPCP	Simpson et al., 1994.[14]	Empirical	LTPP	Good	None	N=28 sections R^2=0.644 SEE=31.29 in/mi	Sufficient data available for all 5 inputs.
Doweled and Non-doweled JPCP	Byrum et al., 1997.[12]	Mechanistic-Empirical	LTPP	Good	Strength Thickness	N=104 sections R^2=0.79 SEE=21.8 in/mi	Sufficient data available for 10 of 13 inputs. Limited data for subgrade moisture content and PCC water/cement ratio, and no data for subgrade overburden pressure.
	Titus-Glover et al., 1999.[15]	Empirical	LTPP	Good	Function of other distresses	N=155 sections R^2=0.50 SEE=22.0 in/mi	Sufficient data available for all 8 inputs.
	Yu et al., 1997.[16]	Empirical	RPPR	Good	Function of other distresses	N=144 sections R^2=0.61 SEE=64.11 in/mi	Sufficient data available for all 3 inputs.
	Hoerner et al., 1999.[10]	Empirical	LTPP	Good	Function of initial IRI and other distresses	N=122 sections R^2=0.51 SEE=28.35 in/mi	Sufficient data available for 4 of 5 inputs. Limited data for initial IRI.

Transverse Joint Faulting Model

The faulting model developed by Yu et al. in 1998 (under the NCHRP 1-34 project) and modified by Hoerner et al. in 1999 was identified as the most suitable for inclusion in the current PRS methodology.[10,17] The original model was developed using 351 data points from two reliable databases (RPPR and LTPP) and included one PRS AQC (slab thickness) as an input. In 1999, this NCHRP 1-34 faulting model was modified to include percent consolidation around dowels as an input.[10] This modified version of the model was used in the PaveSpec 2.0 software. Based on its many merits, including a strong basis on mechanistic principles, the modified NCHRP 1-34 faulting model was chosen as the most appropriate faulting model for validation/improvement under this project.

Transverse Fatigue Cracking Model

A comparison of the three short-listed transverse cracking models resulted in the identification of the model developed by Yu et al. in 1997 (under the RPPR project) as the most suitable for this project.[16] The 1997 model by Yu is a largely mechanistic transverse cracking model that includes two PRS AQC's as inputs (thickness and strength). A significant number of reliable data points (465 from the RPPR database) were used to develop the original model, with very good associated model statistics (R^2=0.91, SEE=6.8% cracked slabs). This model was selected because of its strong mechanistic characteristics and the extensive data used for calibration.

Transverse Joint Spalling Model

The transverse joint spalling model developed by Yu et al. in 1997 (under the RPPR project) and modified by Hoerner et al. in 1999 was identified as the most suitable for inclusion in the current PRS methodology.[10,16] The original model was developed using 164 data points from the reliable 1997 RPPR database, with very good associated model statistics (R^2=0.76, SEE=5.4% spalled joints). One drawback of Yu's original model, from a PRS standpoint, is that it is not a direct function of any PRS AQC's. In an attempt to remedy this problem, Hoerner et. al. used Yu's 1997 model in a modified procedure that incorporated concrete strength and PCC air content (based on a major laboratory study of PCC freeze-thaw).[7,10] This modified version of the 1997 Yu spalling model was used in the PaveSpec 2.0 software.

IRI Model

The original list of six IRI models was first reduced to the three models in which IRI is a function of other predicted distresses—those developed by Titus-Glover et al. (1999), Yu et al. (1997), and Hoerner et al. (1999).[10,15,16] An IRI model directly based on other distress is a very desirable characteristic for the model chosen for use in the PRS procedure, since the other distresses directly identify predicted performance. Of the three IRI models identified, the model developed by Hoerner et al. in 1999 was chosen

as the most appropriate for use in the PRS methodology because of its inclusion of initial IRI, key distresses, and a good model development database (i.e., LTPP).[10]

STEP 4—IDENTIFICATION OF SPECIFIC DATA SOURCES TO BE INCLUDED IN THE NATIONAL PRS DATABASE

After identifying the most suitable distress indicator models for use within this study, the five identified potential data sources were investigated for their applicability to the validation/improvement of each specific model. Table 14 summarizes the specific databases deemed useful to the validation/improvement of each model. Data from these data sources were imported into Microsoft® Access (database software) and organized into a national PRS database in preparation for the validation/improvement portion of this study.

Table 14. Specific databases that will be used to validate/improve chosen best-available distress indicator models.

Distress Indicator Model Type	Source of Chosen Best-Available Model	Databases Deemed Appropriate for Use in the Validation/Improvement Effort
Transverse joint faulting	Yu et al., 1998 (modified by Hoerner et al. in 1999).[10,17]	RPPR LTPP (including Mn/ROAD data) NCHRP 1-19
Transverse fatigue cracking	Yu et al., 1997.[16]	RPPR LTPP (including Mn/ROAD data)
Transverse joint spalling	Yu et al., 1997 (modified by Hoerner et al. in 1999).[10,16]	LTPP (including Mn/ROAD data)
IRI	Hoerner et al., 1999.[10]	LTPP (including Mn/ROAD data)

CHAPTER 3: PROCEDURES USED TO VALIDATE/IMPROVE DISTRESS INDICATOR MODELS

INTRODUCTION

After choosing the models that were most promising for use within the current PRS methodology, the next step was to determine how to validate the models and, if necessary, improve them. First, a more detailed evaluation of each model was conducted to determine which models (if any) could simply be validated (confirmed) using the compiled national PRS database. If a given model could be adequately validated with the new data set, then no model improvement efforts would be attempted. If it was determined that a model needed to be improved (i.e., re-regressed with the possible addition or removal of variables), then a number of statistical tools were identified that could be used to achieve that goal.

This chapter includes discussions of the following:

- Compilation of the national PRS database and specific model type data sets.
- The techniques used in the model validation/improvement process (engineering assessment, statistical analyses, and sensitivity analyses).
- The criteria used to determine when a model was acceptable for use within the PRS methodology.

PREPARATION OF MODEL TYPE-SPECIFIC DATA SETS

In preparation for the initial model evaluation procedures, the data compiled in the national database were organized into subsets associated with each distress indicator model. Each of these model-specific data sets contained all potential data elements (design, climatic, traffic, time-series distress, AQC quality) associated with the particular distress model being validated/improved. Specific data sets were organized using Microsoft® Access and exported to Microsoft® Excel or the SAS statistical software for further data manipulation and analysis.

TECHNIQUES OF THE MODEL VALIDATION/IMPROVEMENT PROCESS

After the specific data sets were organized, each distress indicator model was evaluated in more detail to assess its adequacy and sensitivity to key variables. The evaluations were not only based on an engineering assessment of the models (documenting observed model capabilities and limitations), but the results of statistical and sensitivity analyses as well. Each of the methods used in the model evaluation methods is discussed briefly in the following sections.

Engineering Assessment

The capabilities and limitations of each distress indicator model were identified and documented as a first step in the evaluation process. Under this general assessment, the models were evaluated on the basis of such items as:

- Specific variables (inputs) included in the model (especially the inclusion of the PRS AQC's).
- Specific variables obviously missing from the model.
- Applicable ranges for input variables.
- Ability of a SHA to estimate the model inputs.
- Errors associated with estimating model inputs (especially the sampling and testing of AQC's).
- Consideration of materials- or mix-related problems.
- Appropriateness of the model output units.
- Geographic scope—inference space of the development database.
- Relative effects (reasonableness) of each input variable.

Much of this general assessment work was completed during the initial model review presented in chapter 2.

Statistical Analyses

Many different statistical analysis tools were used to evaluate the initial model and assess the quality of the model after any validation or improvements were made. All of the utilized statistical analysis tools focused on a comparison of predicted and actual distress indicator data. The actual distress indicator data are represented by those time-series distress data collected for each pavement section. The predictive distress indicator models are used to generate the predicted values. Each predicted value is based on a specific cumulative traffic (ESAL) value or age, as well as project-specific site and design-related inputs extracted from the national PRS database. Note that comparisons between predicted and actual values (for a pavement section) are only valid if the predicted value is calculated using the same cumulative ESAL's (or age for spalling models) as observed for the actual value. The four different statistical analysis procedures used in this study are described separately below.

Plots of Predicted versus Actual Data

Plots of predicted versus actual data provide visual evidence of how well a model predicts, by comparing the general location of the data points to a one-to-one line (representing predicted = actual). A general understanding of the *bias* in a prediction model is determined by how well the plotted data are centered around this one-to-one line. A model is said to have an overprediction bias if most of the data points lie above this line; conversely, an underprediction bias is said to be observed when most of the data points lie below the line. A general understanding of the *precision* of a model is determined by the amount of scatter of the data points around the one-to-one line. Figure 1 shows an example of such a plot from a former evaluation of the NCHRP 1-19 JPCP faulting model as it is applied to the data in the wet-freeze climatic region only.[19] Figure 2 shows a more conceptual diagram that illustrates the difference between bias and precision in a model.[20]

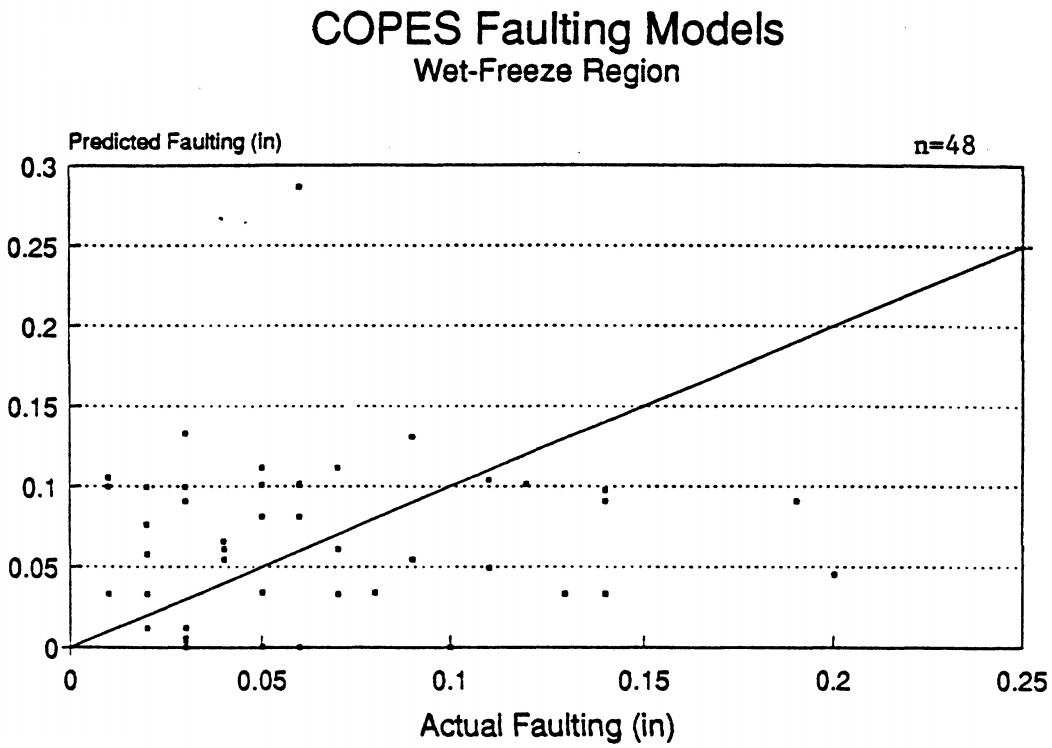

Figure 1. Example of a plot of predicted versus actual data.[19]

Plots of Residuals versus Actual Data

A residual is defined as the difference between the predicted and actual data values (predicted – actual) for a given pavement section. A plot of residuals versus predicted data is used to examine how well a model predicts over the range of the predicted data. If a trend is observed in the plot, it generally means that one or more significant variables are missing from the model. Under this project, plots of residuals versus predicted data were used to provide insight into the type, trend, and possibly the source of any observed bias.

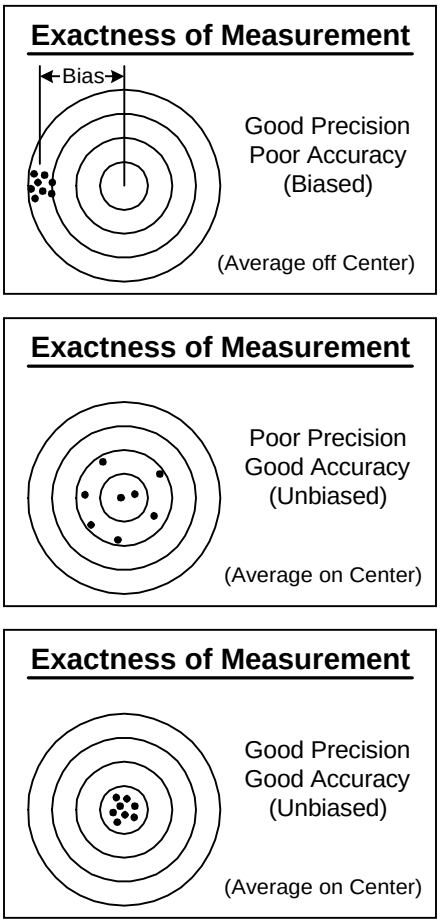

Figure 2. Conceptual illustration of the difference between bias and precision.[20]

Paired t-tests

Although the plots of predicted versus actual data provide visual feedback into the bias of a model, a statistical test is required to *quantify* the amount of bias and determine its significance. The research team used a two-tailed t-test (or other appropriate test) to investigate the bias of each model. Specifically, the t-test was used to determine if the mean difference between the sets of predicted and actual values is significantly different from zero. The following demonstrates this statistical method.

A recent study by Hoerner et al. evaluated the 1986 AASHTO rigid pavement design model by comparing the predicted ESAL's with the actual ESAL's (to a given level of roughness) using LTPP data.[21] Table 15 contains results of the paired t-test analysis conducted on the JPCP section data.

The paired t-test was used to evaluate these results for bias. The null hypothesis is that the mean difference between predicted log ESAL and actual log ESAL is equal to zero, and the alternate hypothesis is that it is not equal to zero (the model could over- or underpredict log ESAL). The results show that the absolute value of the computed *t*

Table 15. Example of paired t-test analysis results (from an investigation of the AASHTO rigid pavement design model using LTPP data).[21]

Pavement Type	No. of Sections	Pred. Log ESAL's	Actual Log ESAL's	t-calc	t-crit (0.05 level)	Reject Null Hypoth.?	Ratio of Pred. to Actual ESAL's	Standard Error of the Estimate*
JPCP	94	6.80	6.45	-5.19	1.99	Yes	2.25	0.66

* Standard deviation of the differences between predicted and actual log ESAL's.

(5.19) is greater than the critical *t* (1.99) at the 0.05 level of significance; therefore, the null hypothesis is rejected at the 0.05 level of significance. Thus, in engineering terms, the mean difference between predicted log ESAL and actual log ESAL values for JPCP sections is not zero for these conditions. The mean actual and predicted ESAL values are 2.8 million and 6.3 million, respectively, showing that the model overpredicts ESAL's by a ratio of 2.25 (on average) for JPCP. Similar analyses were conducted on the predicted versus actual data sets compiled under this project.

Investigation of Components of Variability

The final statistical investigation evaluated the magnitude of variation in predicting the distress indicator values for individual sections. This investigation attempted to explain, and quantify, the overall scatter of points about the one-to-one line between the predicted and actual data.

This procedure is also best illustrated by an example. Under a recent study by Hall et al., many plots of predicted log ESAL's versus actual log ESAL's were used to evaluate an improved AASHTO rigid pavement design model.[22] In an attempt to explain the scatter of the plotted data points, an investigation of the components of variation was conducted. It was first determined that there were four primary components of variation adding to the scatter observed on these plots:

- Errors associated with the estimation of actual traffic (V_T).
- Errors associated with estimating each design input for each LTPP section (V_I).
- Random or normal variation between the performance of supposedly identical replicate sections (similar to the variation of strength between two replicate concrete specimens) (V_R).
- Inability of the model to predict actual pavement performance (serviceability, in this case) due to deficiencies in the model (V_M). This is the real model associated error in prediction. The relatively simple function form of the model does not, of course, completely represent the real pavement behavior under load and climate.

These components of variance were mathematically expressed as follows (base 10 logs):

$$\text{Prediction Error} = \text{Log[Actual ESAL's]} - \text{Log[Predicted ESAL's]} \quad (2)$$

$$\text{Variance [Prediction Error]} = \text{Variance Log[Actual ESAL's]} + \text{Variance Log[Predicted ESAL's]} - \text{Covariance [Log(Actual ESAL's), Log(Predicted ESAL's)]} \quad (3)$$

Thus, the total scatter of data in any of the actual versus predicted ESAL plots consisted of several components of variation, including:

- Estimation of the historical ESAL's (horizontal axis).
- Estimation of true inputs to the model for each section (vertical axis).
- Random differences in performance between sections due to unknown replication error (vertical axis).
- True lack of ability of the model to represent pavement performance (vertical axis).

These components of variance were divided into percentages of the total variation (V_E), as shown in table 16. Similar analyses were conducted on the predicted versus actual data sets compiled under this project. However, the analyses are in terms of distress rather than traffic.

Table 16. Results of the components of variance example.[22]

Variance Component	Estimated Variance	Percent of Total
ESAL Estimation, V_T	0.09	28
Input Estimation, V_I	0.07	22
Random Variation, V_R	0.06	19
Model Error, V_M	0.10	31
Total, V_E	0.32	100

Sensitivity Analyses

The sensitivity of each model output (distress) to its corresponding inputs was investigated as part of the model validation/improvement process. Such an analysis will quantify the significance of each input relative to changes in output. Plots showing the sensitivity of the individual inputs are included. A reasonable sensitivity of each input variable is critical to a successful prediction model. Figure 3 contains an example of such a plot showing the sensitivity of JPCP cracking with respect to slab thickness and cumulative ESAL's. Under this project, similar two-dimensional plots were developed to illustrate the sensitivity of the distress indicator models to specific inputs.

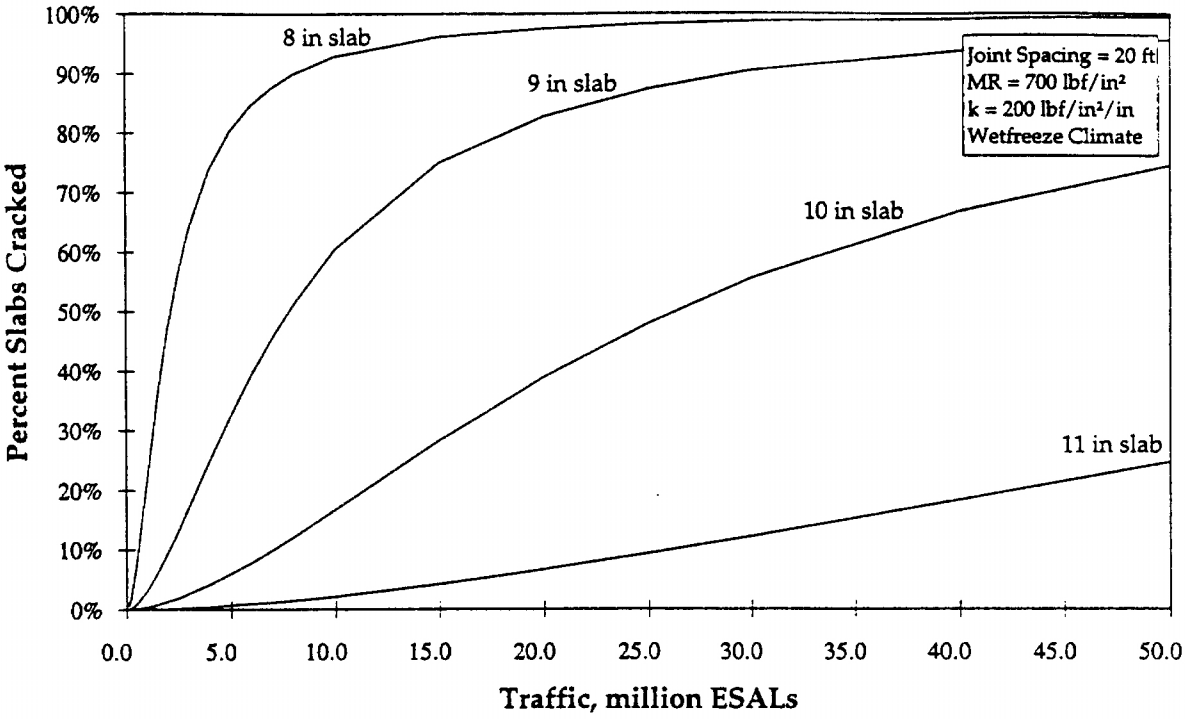

Figure 3. Example of the sensitivity of a JPCP cracking model to slab thickness.[16]

ACCEPTABILITY OF MODELS

The acceptability of each validated / improved model was judged based on the results of the engineering assessment, statistical analysis, and sensitivity analysis. Specifically, the validation / improvement process focused on achieving the following for each model:

- *Eliminating model bias (improving accuracy)*—The research team attempted to remove (or minimize) any observed bias in the plot of predicted versus actual data points.

- *Improving model precision (reducing scatter)*—Model improvements (variable changes, model form changes, or model re-regressions) were conducted to improve accuracy. The accuracy of the model can be assessed by observing how close the data points fall to the one-to-one line in the predicted versus actual plot. The closer the data points are to the line, the more precise the model.

- *Including PRS-related AQC's as inputs*—An acceptable model under this study must be a function of one or more PRS-related AQC's.

- *Obtaining reasonable model sensitivity*—The output sensitivity of the prediction model to changes in model inputs was assessed for each model. Engineering

judgment based on extensive previous experience was used to determine if the created sensitivity plots were reasonable.

- *Expanding the inference space of the model*—The focus of this study was to base all validation/improvement efforts on a much more comprehensive database (the national PRS database). The intention is to make each validated/improved model much more applicable and accurate over a larger range of geographical and site conditions.

Using these criteria as a guide, each best-available model (identified in chapter 2) was investigated separately to determine if it could be simply validated, or if it needed to be improved. The specific procedures used in the validation/improvement of the transverse joint faulting, transverse fatigue cracking, transverse joint spalling, and IRI models are presented in chapters 4 through 7.

CHAPTER 4: TRANSVERSE JOINT FAULTING MODEL

INTRODUCTION

Transverse joint faulting is defined as the difference in elevation between adjacent joints at a transverse joint. The development of faulting is often attributed to a combination of repeated heavy axle loads, insufficient load transfer between the adjacent slabs, free moisture in the pavement structure, and erodible base or subgrade material.[17] When excess moisture exists in a pavement with an erodible base or underlying fine-grained subgrade material, repeated vehicle loadings typically cause the mixture of water and fine material (fines) to be removed from beneath the leave slab corner and ejected to the surface through the transverse joint or along the shoulder. This process, commonly referred to as *pumping*, will eventually result in a void below the leave slab corner. In addition, some of the fines that are not ejected will be deposited under the approach slab corner, causing the approach slab to rise. This combination of a buildup of material beneath the approach corner and the loss of support resulting from a void under the leave corner can lead to significant faulting at the joint (especially for JPCP without dowels). Significant joint faulting has a major impact on the LCC of the pavement in terms of early rehabilitation and vehicle operating costs.[17]

This chapter describes the attempted validation of the chosen best-available JPCP transverse joint faulting model (that used in PaveSpec 2.0) and the subsequent development of a new, improved faulting model for use in PaveSpec 3.0.

CURRENT PRS JPCP TRANSVERSE JOINT FAULTING MODEL

The selected best-available transverse joint faulting model was that incorporated into the PaveSpec 2.0 software by Hoerner et al. in 1999.[10] The procedure is based on the faulting model developed in 1998 by Yu et al. [17] In 1999, this model was adjusted (specifically for use in PaveSpec 2.0) to incorporate the effects of percent consolidation of PCC around dowel bars.

Within the PaveSpec 2.0 software, two different procedures were used to estimate transverse joint faulting, depending on whether percent consolidation around dowels is considered. Regardless of the procedure chosen, the baseline transverse joint faulting model is that developed by Yu et al. in 1998.[17] If percent consolidation around dowels (percent of consolidation at other locations away from joint) is not considered, transverse joint faulting is predicted directly using the baseline model. If percent consolidation around dowels is considered, the transverse joint faulting values (predicted using the baseline model) are then altered by adjusting the non-dimensional aggregate interlock stiffness (AGG*) term of the model. The procedures making up both situations are summarized in the following sections. (Note: The model outputs and inputs are presented in English units.)

JPCP Transverse Joint Faulting (Not Including Percent Consolidation Around Dowels)

When percent consolidation around dowels is not considered, transverse joint faulting is computed using the following (baseline) equation:[17]

$$FAULT = DAMAGE^{0.2475} * [0.2405 - 0.00118 * DAYS90 + 0.001216 * WETDAYS - 0.04336 * BASETYPE - (0.004336 + 0.007059 * (1 - DOWEL)) * LCB] \quad (4)$$

where:

FAULT = Average transverse joint faulting per joint, in.
BASETYPE = Base type (0 if nonstabilized; 1 if asphalt stabilized [ATB], cement stabilized [CTB], or lean concrete base [LCB]).
LCB = Presence of lean concrete base (1 if LCB is present, 0 if LCB is not present).
WETDAYS = Average number of wet days per year.
DAYS90 = Number of days per year with the maximum temperature greater than 32 °C (90 °F).
DOWEL = Presence of dowels (1 if dowels are present, 0 if dowels are not present).
DAMAGE = n / N.
n = *Actual* number of applied cumulative ESAL's.
N = *Allowable* number of applied cumulative ESAL's.

Statistics:
N = 391.
R^2 = 0.50.
SEE = 0.035 in (0.89 mm).

Equation 5 is used to compute allowable ESAL's (N):

$$Log(N) = 0.785983 - 0.92991 * (1 + 0.40 * PERM * (1 - DOWEL)) * Log (DE) \quad (5)$$

where:

PERM = Base permeability (0 = not permeable, 1 = permeable).
DE = Differential energy density at a corner.

The DE at a corner is defined as the energy difference in the elastic subgrade deformation under the loaded slab (leave) and the unloaded slab (approach). The computation of DE involves completing a multi-step process in which maximum corner

deflections are computed for loaded and unloaded conditions. The details of this calculation are presented later in this chapter (in the section describing the final joint faulting model developed under this study).

One important equation used in the computation of DE concerns the non-dimensional aggregate interlock stiffness (AGG*) factor. When percent consolidation around dowels is not considered, AGG* is computed using equation 6.

$$\begin{aligned} AGG^* &= (AGG / kL) \\ &= 2.3\ \mathrm{Exp}(1 - 1.987 * JTSPACE\ /\ L + 3.48 * DOWELDIA^{3.56}) \end{aligned} \tag{6}$$

where:

AGG* = Nondimensional aggregate interlock stiffness.
AGG = Aggregate load transfer stiffness, psi.
k = Dynamic modulus of subgrade reaction (dynamic k-value), psi/in.
L = Slab's radius of relative stiffness, in.
= $[(E_{PCC} * h_{PCC}^3)\ /\ (12 * (1 - \mu^2) * k)]^{0.25}$
E_{PCC} = PCC modulus of elasticity, psi.
h_{PCC} = Slab thickness, in.
μ = PCC Poisson's ratio (assumed to be equal to 0.15).
JTSPACE = Slab length (joint spacing), ft.
DOWELDIA = Dowel diameter, in.

JPCP Transverse Joint Faulting (Including Percent Consolidation Around Dowels)

The only difference between computing transverse joint faulting with or without considering percent consolidation around dowels (percent of consolidation at other locations away from joint) is a change in the equation used to compute AGG*. When percent consolidation is considered, the AGG* (computed using equation 6) is adjusted to incorporate the effects of percent consolidation. This adjusted AGG* is termed AGG^*_{NEW} and is computed using the following equation:

$$AGG^*_{NEW} = 10^{[\mathrm{Log}(AGG^*) + 0.27 * (\%CON - 100)]} \tag{7}$$

where:

AGG^*_{NEW} = Nondimensional aggregate interlock stiffness (adjusted to incorporate the effects of percent consolidation around dowels).
AGG* = Nondimensional aggregate interlock stiffness computed using equation 6.
%CON = Percent consolidation around dowels.

The DE is then computed by substituting AGG^*_{NEW} for AGG* in the equations making up the multi-step DE procedure.

LIMITATIONS OF THE CURRENT PRS TRANSVERSE JOINT FAULTING MODEL

The first step in the process of validating/improving the current PRS transverse joint faulting model involved identifying any weaknesses in the model. Specifically, weaknesses were first identified by:

- Reviewing plots of predicted versus measured faulting.
- Reviewing plots of residuals versus predicted faulting.
- Analyzing diagnostic statistics such as the R^2 and SEE to determine the goodness-of-fit of the models when used with independent data.

In addition, the models were checked to determine whether they made engineering sense and agreed with trends and observations from previous research.

The independent data used in the initial model validation process consisted of JPCP data from the RPPR, LTPP (GPS-3 data only), and NCHRP-19 (COPES) databases.[16,18,19] The final validation data set consisted of 338 pavement test sections located in 34 States and Provinces. A summary of the validation data is presented in table 17.

Table 17. Summary of JPCP data used in the initial validation of the current transverse joint faulting model.

Variable	Range		Mean	Standard Deviation
	Min.	Max.		
Cumulative ESAL's, millions	0.15	56.0	6.5	6.4
Joint spacing, ft	7.0	30.0	17.4	4.8
Presence of dowel bars	150 data points used dowels and 361 aggregate interlock as the load transfer mechanism			
Dowel bar diameter, in	1.0	1.5	1.2	0.2
PCC modulus of elasticity, psi	3,050,000	14,492,739	5,948,588	1,880,322
Avg. annual number of wet days	34.0	180.0	92.2	40.7
Avg. total precipitation, in	4.9	60.7	30.6	15.5
Number of hot days (days with temperature above 32 °C (90 °F)	0.2	150.0	40.9	32.2
Base type	79 data points had ATB, 201 had CTB, 46 had LCB, 166 had granular bases, and 19 had no base			
Dynamic modulus of subgrade reaction (k-value), psi [backcalculated from FWD data]	45	1,800	468	384
Base permeability	43 data points had permeable bases while 470 did not			
PCC slab thickness, in	7.0	15.0	9.4	1.3
Percent consolidation around dowels, %	No data were available			

ATB = asphalt treated base; CTB = cement treated base; LCB = lean concrete base.

Unfortunately, no percent consolidation around dowel data were available for the validation process. Therefore, a validation attempt could only be made on the baseline model, which does not consider consolidation.

The validation data set was used in the current transverse joint faulting model to obtain predicted faulting values for each section. Associated measured faulting values were obtained directly from the selected databases. Figures 4 and 5 show plots of predicted versus measured faulting, and residuals versus predicted faulting, respectively. The diagnostic statistics and both plots indicate that the predicted transverse joint faulting has a reasonable correlation with the measured transverse joint faulting. However, additional calibration of the existing model may significantly improve the model's prediction ability.

The key model limitations identified in the initial validation process were:

- The model significantly overestimates load transfer efficiency of transverse joints (an average estimate of LTE was 69 percent for non-doweled pavements and 99 percent for doweled pavements).
- The base layer erodibility potential needs to be incorporated in a more rational manner.
- The empirical portion in equation 4 is a function of climate and design-related variables (i.e., DAYS 90, Wet days, base type, presence of lean concrete base, and presence of dowels), but it is more desirable for this factor to be dependent on site condition factors only.

Based on the results of this initial validation process, it was decided to recalibrate the existing faulting model using the data available in the newly compiled PRS national database. The recalibration effort focused on addressing the identified limitations of the model and improving its overall predictability.

EXISTING JPCP TRANSVERSE JOINT FAULTING MODELS

In preparation for the development of a new JPCP transverse joint faulting model, many of the faulting models developed under previous research were reviewed. During the review process, specific attention was paid to the variables chosen for inclusion in the models. The details of each of the faulting models reviewed under this study are described separately in the following sections.

SHRP P-020 JPCP Transverse Joint Faulting Model[14]

In a SHRP study conducted by Simpson et al. in 1994, titled *Early Analysis of LTPP General Pavement Studies Data*, separate JPCP faulting models were developed for doweled and non-doweled JPCP.[14] Each of these models are presented as follows:

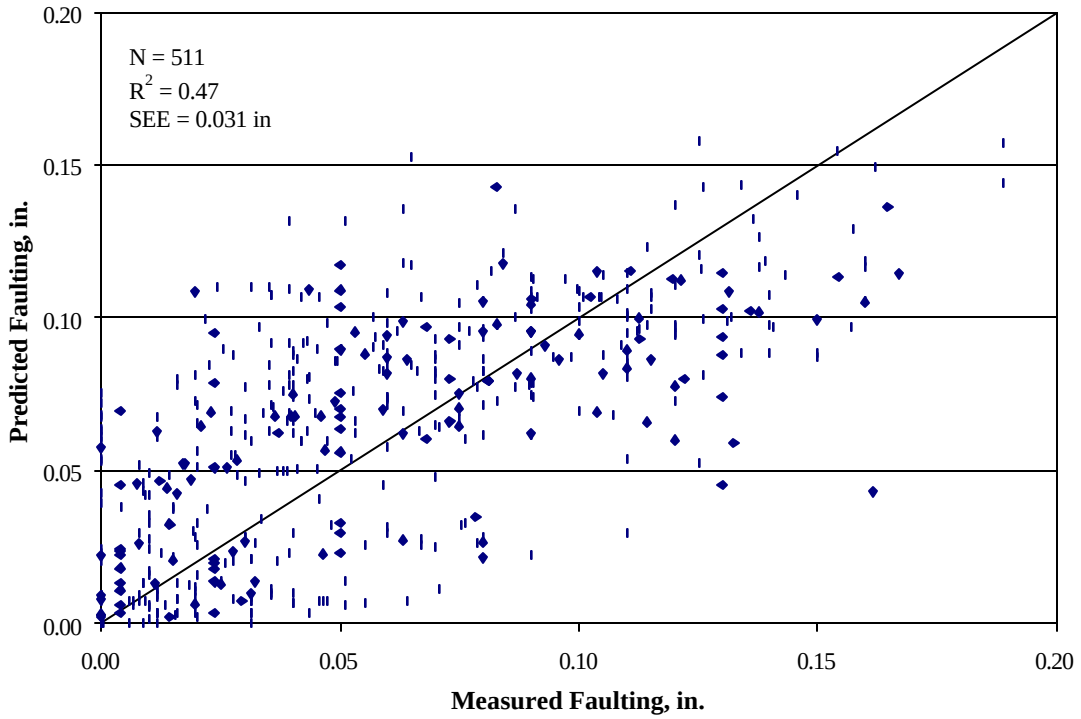

Figure 4. Predicted versus measured transverse joint faulting (using the compiled validation data set).

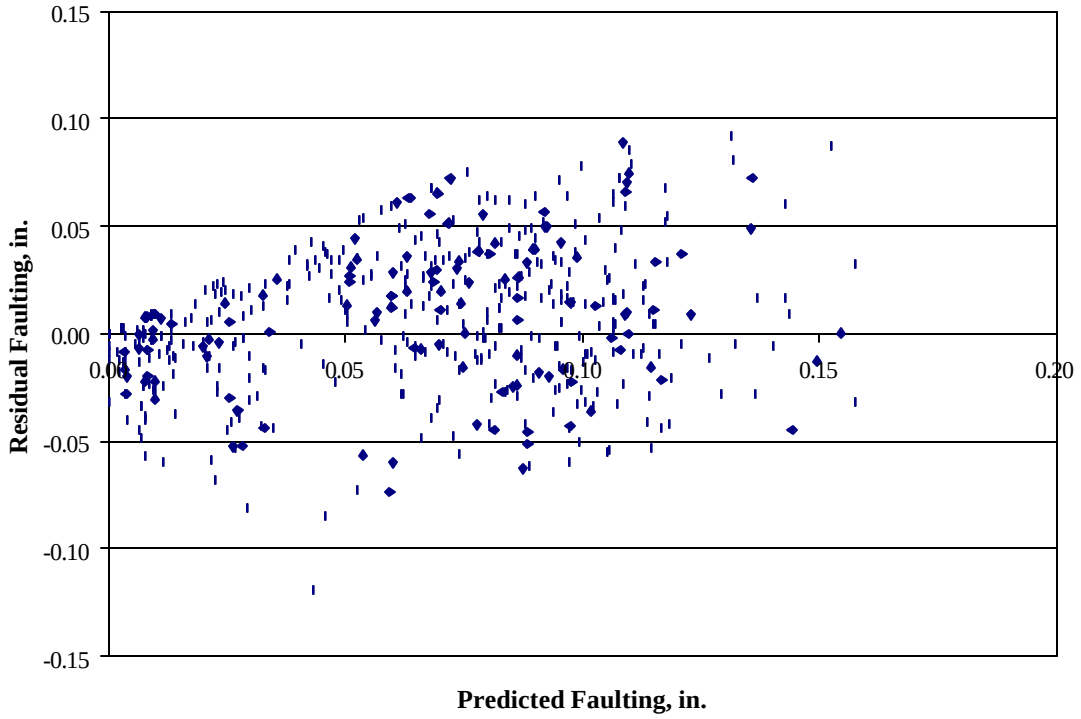

Figure 5. Residual versus predicted transverse joint faulting (using the compiled validation data set).

SHRP P-020 Faulting Model for JPCP With Dowels

$$FAULTD = CESAL^{0.25} * [0.0238 + 0.0006 * \left(\frac{JTSPACE}{10}\right)^2 + 0.0037 * \left(\frac{100}{KSTATIC}\right)^2 + 0.0039 * \left(\frac{AGE}{10}\right)^2 - 0.0037 * EDGESUP - 0.0218 * DOWELDIA] \quad (8)$$

where:

FAULTD = Mean transverse doweled joint faulting, in.
CESAL = Cumulative 80-kN (18-kip) ESAL's in traffic lane, millions.
JTSPACE = Mean transverse joint spacing, ft.
KSTATIC = Mean backcalculated static k-value, psi/in.
AGE = Age since construction, years.
EDGESUP = Edge support (1=tied PCC shoulder, 0=any other shoulder type).
DOWELDIA = Diameter of dowels in transverse joints, in.

Statistics:
N = 59.
R^2 = 0.534.
SEE = 0.028 in (0.7 mm).

SHRP P-020 Faulting Model for JPCP Without Dowels

The faulting model developed for non-doweled JPCP was the following:

$$FAULTND = CESAL^{0.25} * [-0.07575 + 0.0251 * \sqrt{AGE} + 0.0013 * \left(\frac{PRECIP}{10}\right)^2 + 0.0012 * \left(FI * \frac{PRECIP}{1000}\right) - 0.0378 * DRAIN] \quad (9)$$

where:

FAULTND = Mean transverse non-doweled joint faulting, in.
CESAL = Cumulative 80-kN (18-kip) ESAL's in traffic lane, millions.
PRECIP = Mean annual precipitation, in.
FI = Mean freezing index, °F-days.
AGE = Age since construction, years.
DRAIN = Drainage type (1=longitudinal subdrainage, 0=otherwise).

Statistics:

$N = 25.$
$R^2 = 0.550.$
$SEE = 0.047$ in (1.2 mm).

Both of these models predict faulting as a function of traffic, age, and various site conditions and pavement design features. A review of the output of these models indicates a trend that non-doweled pavements develop more faulting than doweled pavements. In addition, for doweled pavements, faulting decreases as dowel diameter increases. As expected, both models were positively correlated with cumulative ESAL's (i.e., faulting increases with an increase in cumulative ESAL's). Pavement design features that were found to be significant in the models included drainage type, joint spacing, base type, and presence of a tied PCC shoulder. Two climatic variables (precipitation and freezing index) were found to significantly affect the development of faulting for non-doweled pavements; however, it is interesting to note that no climate-related variables were included in the model for doweled JPCP.

In the final SHRP P-020 report, the research team that developed these models acknowledged that both models were developed with limited data, which most likely led to relatively low coefficients of correlation and fairly high SEE. Because of these model statistics, the research team stated that improvements could most likely be made to both models.

FHWA RPPR 1997 JPCP Transverse Joint Faulting Model[16]

In 1997, Yu et al. also developed separate JPCP faulting models for doweled and non-doweled pavements as part of the FHWA RPPR project.[16] The development of these models identified several pavement design features and site conditions that significantly affect transverse joint faulting. Each of these models is discussed separately below:

<u>RPPR Faulting Model for JPCP With Dowels</u>

$$\begin{aligned} FAULTD = {} & CESAL^{0.25} * [0.0628 - 0.0628 * C_d + 0.3673*10^{-8} * BSTRESS^2 \\ & + 0.4116 * 10^{-5} * JTSPACE^2 + 0.7466 * 10^{-9} * FI^2 * PRECIP^{0.5} \\ & - 0.009503 * BASE - 0.01917 *WIDENLANE + 0.0009217 * AGE] \end{aligned} \quad (10)$$

where:

FAULTD = Mean transverse doweled joint faulting, in.
CESAL = Cumulative 80-kN (18-kip) ESAL's in traffic lane, millions.
C_d = Modified AASHTO drainage coefficient, calculated from database information.
BSTRESS = Maximum dowel/concrete bearing stress, psi.

JTSPACE = Mean transverse joint spacing, ft.
FI = Mean freezing index, °F-days.
PRECIP = Mean annual precipitation, in.
BASE = Base type (0 = nonstabilized base; 1 = stabilized base).
WIDENLANE = Widened lane (0 = not widened, 1 = widened).
AGE = Age since construction, years.

Statistics:
N = 146.
R^2 = 0.60.
SEE = 0.022 in (0.56 mm).

RPPR Faulting Model for JPCP Without Dowels

$$FAULTND = CESAL^{0.25} * [0.2347 - 0.1516*C_d - 0.000250 * Hpcc^2 / JTSPACE^{0.25} - 0.0115 * BASE + 0.7784 * 10^{-7} * FI^{1.5} * PRECIP^{0.25} - 0.002478 * DAYS90^{0.5} - 0.0415 * WIDENLANE] \quad (11)$$

where:

FAULTND = Mean transverse non-doweled joint faulting, in.
CESAL = Cumulative 80-kN (18-kip) ESAL's in traffic lane, millions.
C_d = Modified AASHTO drainage coefficient, calculated from database information.
h_{PCC} = PCC slab thickness, in.
JTSPACE = Mean transverse joint spacing, ft.
BASE = Base type (0 = nonstabilized base; 1 = stabilized base).
FI = Mean freezing index, °F-days.
PRECIP = Mean annual precipitation, in.
DAYS90 = Mean annual number of hot days (days with maximum temperature greater than 32 °C [90°F]).
WIDENLANE = Widened lane (0 = not widened, 1 = widened).

Statistics:
N = 131.
R^2 = 0.45.
SEE = 0.034 in (0.86 mm).

The results of these models were found to generally agree with the results from the models developed under the LTPP Early Analysis (SHRP P-020) study.[14,16] One important characteristic of both RPPR models that was not addressed in the SHRP P-020 models is the inclusion of *presence of a widened traffic lane* as an independent variable. The presence of a widened traffic lane was found to be negatively correlated with faulting in both RPPR models (i.e., predicted faulting for pavements with a

widened lane will be less than that predicted for a similar pavement without a widened lane).

ACPA JPCP Transverse Joint Faulting Model[23]

In 1994, Wu et al. developed separate mechanistic-empirical JPCP faulting models for doweled and non-doweled pavements for the American Concrete Paving Association (ACPA).[23] These models were extensions of faulting models originally developed for the Portland Cement Association (PCA) in 1977.[24] These models are unique in that they include *erodibility of the base/subgrade material* as the main factor influencing faulting. Using the concept of Miner s linear damage, the percent of erosion damage occurring at the slab corner was computed using the following equation:[23]

$$\text{EROSION} = 100 \sum_i n_i * \frac{C_2}{N_i} \tag{12}$$

where:

EROSION = Percent erosion damage.
n_i = Expected number of axle load repetitions for each axle group i.
N_i = Allowable number of repetitions for axle group i.
C_2 = 0.06 for pavements without a tied PCC shoulder and 0.94 for pavements with a tied PCC shoulder.

Next, the allowable number of load applications (N) was computed as a function of the power, or rate of work, of each axle pass at the corner of the slab. This equation is shown as the following:[23]

$$\log N = 14.524 - 6.777 * (C_1 * P - 9.0)^{0.103} \tag{13}$$

where:

N = Allowable load repetitions to end of design period.
P = Power (rate of work) of each axle pass at the corner of the slab.
C_1 = $1 - (\text{KSTATIC} / 2000 * [4 / \text{Hpcc}])^2$.
KSTATIC = Modulus of subgrade reaction, psi/in.
h_{PCC} = Slab thickness, in.

The power of each axle pass at the corner of the slab is computed using equation 14:[23]

$$P = 268.7 * p^2 / h_{PCC} / \text{KSTATIC}^{0.73} \tag{14}$$

where:

P = Power (rate of work) of each axle pass at the corner of the slab.
p = Pressure at slab-foundation interface, psi.

The final JPCP faulting models developed under this ACPA study are included as equations 15 and 16, respectively.[23]

$$FAULTD = EROSION^{0.25} * [0.0038332 * (PRECIP / 10)^{1.84121} + 0.0057763 * JTSPACE^{0.38274}] \quad (15)$$

$$FAULTND = EROSION^{0.25} * [9.75873 * 10^{-4} * (PRECIP)^{0.91907} + 0.0060291 * JTSPACE^{0.54428} - 0.016799 * DRAIN] \quad (16)$$

where:

FAULTD = Mean transverse doweled joint faulting, in.
FAULTND = Mean transverse non-doweled joint faulting, in.
EROSION = Calculated accumulated erosion (using equation 12).
PRECIP = Annual precipitation, in.
JTSPACE = Transverse joint spacing, ft.
DRAIN = Dummy variable for the presence of edge drains (1 = edge drains are present, 0 = edge drains are not present).

An evaluation of these models by Yu et al. in 1998 found that they generally agreed with the JPCP faulting models developed under the RPPR and SHRP P-020 studies.[17] In addition, it was noted that PCC slab thickness was found to be a significant parameter that is negatively correlated with faulting (i.e., an increase in slab thickness results in a decrease in transverse joint faulting).[23] It is also important to note that the presence of edge drains was included in the non-doweled faulting model, whereas no drainage-related variables were used in the doweled model.

FHWA NAPCOM JPCP Transverse Joint Faulting Model[13]

Under the FHWA Nationwide Pavement Cost Model (NAPCOM) study completed in 1997, Owusu-Antwi et al. developed the following mechanistic-empirical faulting model for doweled and non-doweled JPCP:[13]

$$FAULT = DAMAGE^{0.23} * (0.35 - 0.0277 * BASE - 0.25 * C_d + 2.17 * 10^{-5} * FI) \quad (17)$$

where:

FAULT = Mean transverse joint faulting, in.
DAMAGE = n / N.

n = Cumulative number of actual axle load applications, in thousands.
N = Number of allowable axle load applications, in thousands.
C_d = AASHTO drainage coefficient.
BASE = Base type (0 = erodible base; 1 = nonerodible base).
FI = Freezing index, °F-days.

Statistics:
N = 101.
R^2 = 0.52.
SEE = 0.03 in (0.8 mm).

The allowable number of load applications (N) is defined as follows:

$$\text{Log}(N) = 4.27 - 1.6 * \text{Log}(DE - 0.002) \quad (18)$$

where:

N = Number of allowable axle load applications, in thousands.
DE = Differential of subgrade elastic energy density.

The NAPCOM model (equation 17) illustrates that the presence of dowels significantly reduces faulting by reducing the differential of subgrade elastic energy density. In addition, the output of the model illustrates trends showing that a stabilized base, stiff subgrade, and improved drainage are negatively correlated with faulting.[13]

LTPP Data Analysis Study JPCP Transverse Joint Faulting Model[15]

In 1999, Titus-Glover et al. recalibrated the 1997 NAPCOM JPCP transverse joint faulting model under a FHWA LTPP data analysis contract.[15] This model, recalibrated using LTPP data only, is as follows:

$$FAULT = DAMAGE^{0.3} * [0.05 + 0.00004 * WETDAYS - 0.0024 * DOWDIA - 0.025 * C_d * (0.5 + BASE)] \quad (19)$$

where:

FAULT = Mean transverse joint faulting, in.
DAMAGE = n / N.
n = Cumulative number of actual 90-kN (18-kip) ESAL applications, in thousands.
N = Number of allowable 90-kN (18-kip) ESAL applications, in thousands.
WETDAYS = Annual average number of wet days.
DOWDIA = Dowel diameter, in.
C_d = AASHTO drainage coefficient.
BASE = Base or subbase type (0 = erodible base; 1 = nonerodible base).

Statistics:
N = 120.

R^2 = 0.56.
SEE = 0.03 in (0.8 mm).

The main difference between the recalibrated model and the original NAPCOM model is that the recalibrated model expresses traffic in terms of ESAL's, whereas the original NAPCOM model uses actual axle loads. In addition, the effects of climate are characterized with different variables in the two models. In the original NAPCOM model, the influence of climate is considered by freezing index, whereas the average annual number of wet days was used as the important climatic parameter in the calibrated LTPP model.[13]

Overview of Existing JPCP Transverse Joint Faulting Models

A review of recently developed JPCP faulting models identified a number of distinct relationships between faulting and traffic, age, and various climatic, site, and pavement design variables. All of the models showed trends of faulting increasing rapidly and then slowly leveling off over time. Several of the models indicate that shoulder type has a significant effect on faulting. While the SHRP P-020 doweled faulting model calculates less faulting if a tied PCC shoulder is used, the more recent RPPR study showed that tied PCC shoulders do not have a significant effect in reducing faulting.[14,16] This finding is attributed to the observation that the sections included in the RPPR database did not supply significant load transfer efficiency at the slab corner to reduce deflections and affect faulting. The RPPR study did, however, find that the presence of a widened lane significantly reduced faulting.[16]

Most of the models discussed in this section indicate that an improved pavement drainage system will generally reduce the potential of faulting, particularly for non-doweled joints. In the RPPR, LTPP, and NAPCOM models, drainage quality was characterized by using the modified AASHTO drainage coefficient, C_d. This coefficient is based on several parameters, such as presence of a permeable base and edgedrains, precipitation level, and subgrade type. Although this coefficient provides a reasonable estimate of the pavement's ability to drain excessive moisture from the structure, it can confound the effect of different design features and site conditions on faulting.[17]

The review of the recently developed transverse joint faulting models identified a number of variables that have been consistently found to significantly influence faulting. A summary of the significant variables used in past model development (for those models reviewed in this section) is summarized in table 18. This collective list of variables (or variables related to these) will be considered in the transverse faulting model validation/development procedures conducted under this project.

RECALIBRATION OF THE CURRENT JPCP TRANSVERSE JOINT FAULTING MODEL

An analysis of the data parameters included in table 18 shows that the current PRS JPCP transverse joint faulting model (that used in PaveSpec 2.0) accounts for the most significant design parameters and site conditions. As was stated earlier, the

Table 18. Summary of variables found to significantly affect JPCP transverse joint faulting.

Variable	SHRP P-020 (1984)[14]	RPPR (1997)[16]	ACPA (1994)[23]	NAPCOM (1997)[13]	LTPP Data Analysis (1997)[15]	PaveSpec 2.0[10]
Age	✓	✓				
80-kN (18-kip) ESAL's	✓	✓			✓	✓
Axle load repetitions			✓	✓		
Annual temperature range		✓				
Average annual number of wet days					✓	✓
Freezing index	✓	✓		✓		
Mean annual precipitation	✓	✓	✓			
Average annual number of days with maximum temperature > 32°C (90 °F)		✓				
Drainage type	✓		✓			✓[1]
AASHTO drainage coefficient, C_d		✓		✓	✓	
PCC slab thickness		✓	✓	✓	✓	✓
PCC modulus of elasticity		✓		✓	✓	✓
Modulus of subgrade reaction (k-value)	✓	✓	✓	✓	✓	✓
Base type		✓		✓	✓	✓
Shoulder type	✓	✓		✓[2]	✓[2]	✓[2]
Transverse joint spacing	✓	✓	✓	✓	✓	✓
Dowel diameter	✓	✓			✓	✓

Notes:

1 Includes the effects of base permeability.
2 Includes the effects of presence of widened lane.

model was found to predict faulting with reasonable accuracy. Nevertheless, it was believed that the current model could be greatly improved under this study by:

1. Accounting for base erodibility potential in a more rational manner.

2. Estimating load transfer efficiency of transverse joints using a more realistic procedure.

3. Incorporating all design variables into the *damage* calculation portion of the model, making the empirical adjustment factor portion of the model a function of site condition variables only.

The recalibration procedures used to address these limitations are described in detail below.

Data Preparation

In preparation for the recalibration of the PaveSpec 2.0 faulting model, all pertinent data from the database used for verification of the current faulting model (see table 17) was compiled into a faulting model development database. As mentioned previously, the independent data used in the initial model validation process consisted of JPCP data from the RPPR, LTPP (GPS-3 data only), and NCHRP-19 (COPES) databases. The final validation data set consisted of 338 pavement test sections located in 34 States and Provinces. This database not only consisted of all variables used in the validation process, but contained additional climate- and design-related variables as well.

One of the key variables added to the database is a base erodibility factor. This factor is a subjective classification that characterizes the potential for base erosion beneath the PCC slab. Accounting for erodibility is important because it was shown in several previous studies that JPCP constructed over base/subbase materials with a high potential for erosion generally experience significantly higher levels of pumping and faulting.[16,17,19]

Several field and laboratory analyses have been performed to determine the most suitable procedure for characterizing paving materials erodibility. The most rational and widely accepted procedure is that developed by the Permanent International Association of Road Congresses (PIARC). This procedure was developed using data collected from more than 100 concrete pavement sections in an international survey of 26 countries, including the United States.[25,26,27,28] The PIARC recommendations (modified to include a permeable drainage base layer) for the erosion potential of base/subbase materials (based on base type and material characteristics) are presented in table 19. Moving from A to E, each class has approximately 10 times as much erodibility potential as the class before it (e.g., class C material is approximately 10 times as erodible as class B material). These guidelines have been used extensively in Europe with success.

Table 19. PIARC recommendations for erosion potential of base / subbase materials (based on base type and base cement and asphalt content).[25]

Erodibility Class	Material Description
A	Lean concrete with 8 percent cement; bituminous concrete with 6 percent asphalt cement, or a permeable drainage layer.
B	Cement treated granular material with 5 percent cement manufactured in plant; bitumen treated granular material with 4 percent asphalt cement.
C	Cement-treated granular material with 3.5 percent cement manufactured in plant; bitumen treated granular material with 3 percent asphalt cement.
D	Granular material treated in place with 2.5 percent cement, treated soils.
E	Untreated granular material.

While the PIARC recommendations are based on the stabilizer content (asphalt or portland cement) of the base / subbase materials, this information was not available or reliable for many pavement sections in the compiled PRS database. However, recent research conducted in Germany demonstrated that the long-term compressive strength (strength measured at a time much later than 28 days) of cement treated bases is another reliable indicator of their erodibility.[29] Since compressive strength information was available for the majority of the pavement sections with CTB in the model development database, PIARC classifications were estimated based on ranges of cement stabilized base long term compressive strength. The chosen correlations are shown in table 20. (Note: the development of table 20 was based on general relationships observed in the LTPP database.) Long-term compressive strength was used to estimate base erodibility class for those sections in which cement content information was not available.

Table 20. Supplemental recommendations for erosion potential of CTB (based on long-term compressive strength).

Base Erodibility Class	Material Description
A	Cement treated granular material with long-term compressive strength > 2,500 psi.
B	Cement treated granular material with long-term compressive strength <= 2,500 and > 2,000 psi.
C	Cement treated granular material with long-term compressive strength <= 2,000 and > 1000 psi.
D	Cement treated granular material with long-term compressive strength <= 1000 psi.

Based on these recommendations, an erodibility class was estimated for each section. This erodibility class was then converted into a numerical base erodibility factor, EROD. It was assumed that if two sections have the same design parameters and site conditions except different erodibility of base layers, then to exhibit the same level of faulting they have to receive an amount of traffic in reverse proportion of their base erodibility factors, i.e.

$$\frac{n_1}{n_2} = \frac{EROD_2}{EROD_1} \tag{20}$$

where:

n_1, n_2 = Number of applied cumulative ESAL's to achieve a certain level of faulting for sections 1 and 2, respectively.

$EROD_1$,$EROD_2$ = Base erodibility factors for sections 1 and 2, respectively.

Table 21 presents the final base erodibility factors associated with each PIARC erodibility class.

Table 21. Recommendations for assigning erodibility factor based on PIARC erodibility class.

PIARC Erodibility Class	Recommended Ranges for Base Erodibility Factor
A	0.5–1.5
B	1.5–2.5
C	2.5–3.5
D	3.5–4.5
E	4.5–5.5
No base	5.5–7.5

The entire model development database was thoroughly evaluated to identify any missing data elements and possible problem spots in the database (e.g., time series data with a significant decrease in faulting over time). Attempts were made to obtain replacements for missing data where possible. The data set was also checked and cleaned for anomalies and gross data error.

Statistical Tools for Regression and Optimization

The SAS nonlinear procedure (NLIN) was selected as the appropriate nonlinear regression tool to be used in model development and calibration.[30] Other SAS procedures, such as STEPWISE, REG, RSQUARE, and RSREG, were used in selecting the most suitable variables for incorporation into the model.

Final JPCP Transverse Joint Faulting Model

The final recalibration procedure consisted of solving for the various constants in the conceptual faulting model using the nonlinear regression approach. Optimization

techniques and regression analysis were used to determine regression coefficients that minimized the error between the predicted and measured faulting values. The specific procedure used is the following:

1. Assign initial values to the variables and parameters in the conceptual model.

2. For those assigned values, perform nonlinear regression analysis to find the values of the faulting prediction model parameters that minimize the error vector, ,.

3. Repeat step 2 for different values of $ until the error vector is minimized and the conversion criteria are met (i.e., error is within acceptable limits).

Based on the successful completion of the iterative optimization process, the final models making up the final JPCP transverse joint faulting procedure were determined.

As with the faulting procedure used in PaveSpec 2.0, two different processes are used to estimate transverse joint faulting, depending on whether percent consolidation around dowels is considered. The specific multi-step procedures used to compute transverse joint faulting for both situations are summarized in the following sections. (Note: The model outputs and inputs are presented in English units.)

<u>JPCP Transverse Joint Faulting (Not Including Percent Consolidation Around Dowels)</u>

$$FAULT = DAMAGE^{0.275} * [0.1741 - 0.0009911 * DAYS90 + 0.001082 * PRECIP] \quad (21)$$

where:

FAULT = Average transverse joint faulting per joint, in.
DAMAGE = n / N.
n = *Actual* number of applied cumulative ESAL's.
N = *Allowable* number of applied cumulative ESAL's.
DAYS90 = Number of days per year with the maximum temperature greater than 32 °C (90 °F).
PRECIP = Average annual precipitation, in.

Statistics:
No. of data = 511.
R^2 = 56 percent.
SEE = 0.029 in (0.74 mm).

Equation 22 is used to compute allowable ESAL's (N):

$$\text{Log}(N) = 0.785983 - \text{Log}(\text{EROD}) - 0.92991 * (1 + 0.40 * \text{PERM} * (1 - \text{DOWEL})) * \text{Log}\,(\text{DE}*(1 - 1.432*\text{DOWELDIA} + 0.513*\text{DOWELDIA}^{2.})) \quad (22)$$

where:

N = *Allowable* number of applied cumulative million ESAL's.
EROD = Base erodibility factor for the base (value between 0.5 and 7.5).
PERM = Base permeability (0 = not permeable, 1 = permeable).
DOWEL = Presence of dowels (1 if dowels are present, 0 if dowels are not present).
DOWELDIA = Dowel diameter, in. (maximum allowed is 1.50 in)
DE = Differential energy density at a corner.

As stated previously in this chapter, the DE at a corner is defined as the energy difference in the elastic base/subgrade deformation under the loaded slab (leave) and the unloaded slab (approach). One important equation used in the computation of DE is that for the nondimensional aggregate interlock stiffness (AGG*) factor. When percent consolidation around dowels is not considered, AGG* is computed using equation 23.

$$\text{AGG}^* = (\text{AGG}/\text{kL}) = 2.3 * \text{Exp}(-1.987 * \text{JTSPACE} / \text{L} + \text{DOWELDIA}^{2.2}) \quad (23)$$

where:

AGG* = Nondimensional aggregate interlock stiffness.
AGG = Aggregate load transfer stiffness, psi.
k = Dynamic modulus of subgrade reaction (dynamic k-value), psi/in.
L = Slab's radius of relative stiffness, in.
= $[(E_{PCC} * h_{PCC}^3) / (12 * (1 - \mu^2) * k)]^{0.25}$
E_{PCC} = PCC modulus of elasticity, psi.
h_{PCC} = Slab thickness, in.
μ = PCC Poisson's ratio (assumed to be equal to 0.15).
JTSPACE = Slab length (joint spacing), ft.
DOWELDIA = Dowel diameter, in. (maximum allowed is 1.50 in)

The computation of DE involves completing a multi-step process in which maximum corner deflections are computed for loaded and unloaded conditions. The detailed step-by-step procedure used to compute DE is described below.

1. Calculate the radius of relative stiffness (L) using equation 24.

$$L = [(E_{PCC} * h_{PCC}^3) / (12 * (1 - \mu^2) * k)]^{0.25} \quad (24)$$

2. Calculate AGG* using equation 23.

3. Calculate the maximum corner deflections of the loaded and unloaded slabs assuming that the 80-kN ESAL is located 305 mm from the corner (914 mm from the corner if widened slab is used). The following steps are used:

   a. Use equation 25 to calculate the free-edge corner deflection (no load transfer to the adjacent slab) assuming that the load is placed at the slab corner.

$$w_{fe,0} = (0.0000864 * L^2 + 0.002824 * L + 0.2953) * 18000 / kL^2 \quad (25)$$

   b. Use equation 26 to calculate the free-edge corner deflection (no load transfer to the adjacent slab) assuming that the load is placed at the transverse joint 914 mm away from the slab corner.

$$w_{fe,914} = (0.0000648 * L^2 + 0.003934 * L - 0.02548) * 18000 / kL^2 \quad (26)$$

   c. Use equation 27 to calculate the corresponding load transfer efficiency (LTE) for a load placed at the slab corner.

$$LTE_{x=0}(\%) = 1 / [0.01 + 0.012 * (AGG^*)^{-0.849}] \quad (27)$$

   d. Use equation 28 to calculate the corresponding LTE at the slab corner for a load placed 914 mm away from the slab corner.

$$LTE_{x=914}(\%) = 1 / [0.01 + 0.003483 * (AGG^*)^{-1.13677}] \quad (28)$$

   e. Calculate the corner deflection of the unloaded slab for a load placed at 0 and 914 mm from the slab corner using equations 29 and 30, respectively.

$$w_{UL,0} = w_{fe,0} * (LTE_{x=0}) / (1 + LTE_{x=0}) \quad (29)$$

$$w_{UL,91.4} = w_{fe,91.4} * (LTE_{x=91.4}) / (1 + LTE_{x=91.4}) \quad (30)$$

   f. Use equation 31 to calculate the corner deflection of the unloaded slab for an axle load located at a transverse joint in the wheelpath (305 mm from the slab corner for a non-widened slab).

$$w_{UL} = w_{UL,0} + (w_{UL,914} - w_{UL,0}) * x / 914 \quad (31)$$

   This equation interpolates between the unloaded slab deflections at x = 0 and 914 mm, where "x" is the distance from the wheelpath to the slab corner. The variable “x” is calculated as the additional width provided by the widened

lane plus 305 mm (this sum is limited to 914 mm). For example, if the chosen widened lane width is 4.3 m, and the regular lane width is 3.7 m, the added width is 609 mm. The variable "x" is then calculated as 609 mm + 305 mm, or 914 mm.

g. Use equation 32 to calculate the LTE at the slab corner for an axle load located at the transverse joint in the wheelpath (305 mm from the slab corner for a non-widened slab).

$$LTE = LTE_0 + (LTE_{914} - LTE_0) * x / 914 \quad (32)$$

This equation interpolates between the LTE's computed for x = 0 and 914 mm.

h. Use equation 33 to calculate the loaded corner deflection for the load located in the wheelpath.

$$w_L = w_{UL} / LTE \quad (33)$$

i. Use equation 34 to calculate the differential energy density, DE.

$$DE = 0.5 * k * (w_L^2 - w_{UL}^2) \quad (34)$$

4. Calculate the allowable number of ESAL applications (N) using equation 22.

5. Calculate predicted faulting using equation 21.

<u>JPCP Transverse Joint Faulting (Including Percent Consolidation Around Dowels)</u>

The only difference between computing transverse joint faulting with or without considering percent consolidation around dowels is a change in the equation used to compute AGG*. When percent consolidation is considered, AGG* (computed using equation 23) is adjusted to incorporate the effects of percent consolidation. This adjusted AGG* is termed AGG^*_{NEW} and is computed using the following equation:

$$AGG^*_{NEW} = 10^{[Log(AGG^*) + 0.27 * (\%CON - 100)]} \quad (35)$$

where

AGG^*_{NEW} = Nondimensional aggregate interlock stiffness (adjusted to incorporate the effects of percent consolidation around dowels).
AGG* = Nondimensional aggregate interlock stiffness computed using equation 23.
%CON = Percent consolidation around dowels.

The DE is then computed by substituting AGG^*_{NEW} for AGG* in the equations making up the multi-step DE procedure.

Final Faulting Model Summary

Plots of the predicted versus measured faulting, and residuals versus predicted faulting, are shown in figures 6 and 7, respectively. The diagnostic statistics and both plots verify that the model is effective for predicting transverse joint faulting. The R^2 of 56 percent and SEE of 0.7 mm (0.029 in) are very reasonable given the large number of data points (N = 511) used in model development.

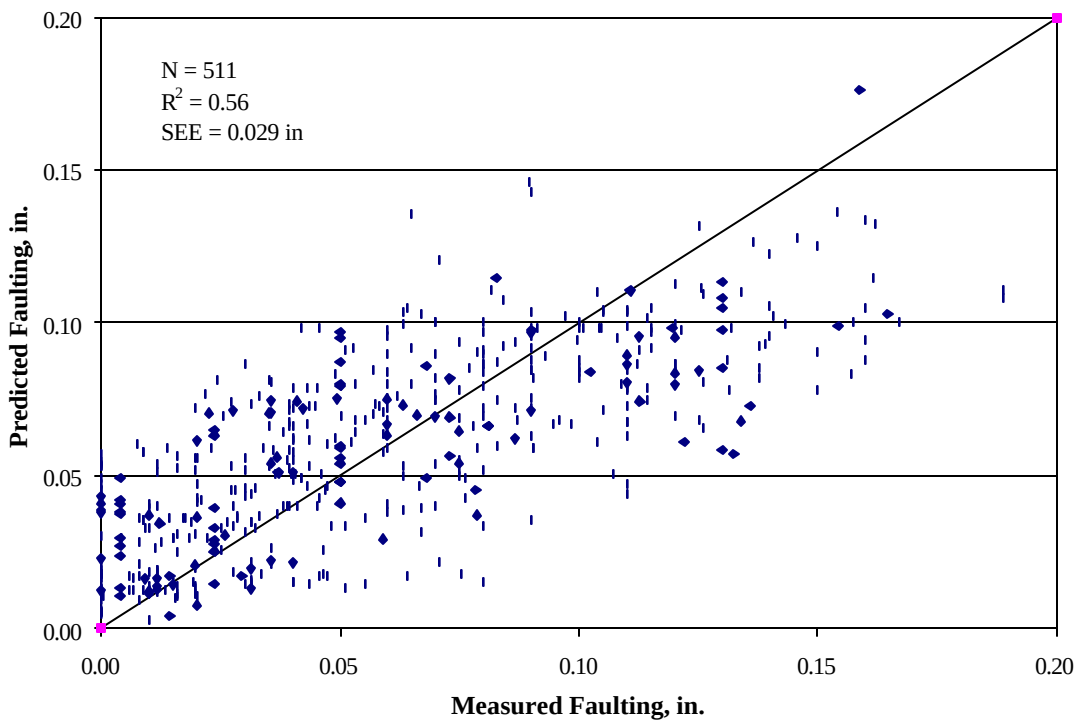

Figure 6. Predicted versus measured faulting for the validated JPCP faulting model.

MODEL VERIFICATION (SENSITIVITY ANALYSIS)

A sensitivity analysis was conducted on the final faulting model to determine its reliability for predicting faulting within and outside of the inference space of the development database. This was accomplished by studying the effects of the various input parameters on the output generated by the faulting model. The ranges of the input values used in the sensitivity analysis are presented in table 22. Note that the sensitivity analyses were accomplished by investigating the effects of changing one variable at a time, while holding all other variables at their mean values.

Effect of Material- and Design-Related Factors

Various material-, site-, and pavement design-related variables were included in the final validated faulting model. These variables consist of dowel diameter, transverse joint spacing, base erodibility factor, dynamic modulus of subgrade reaction,

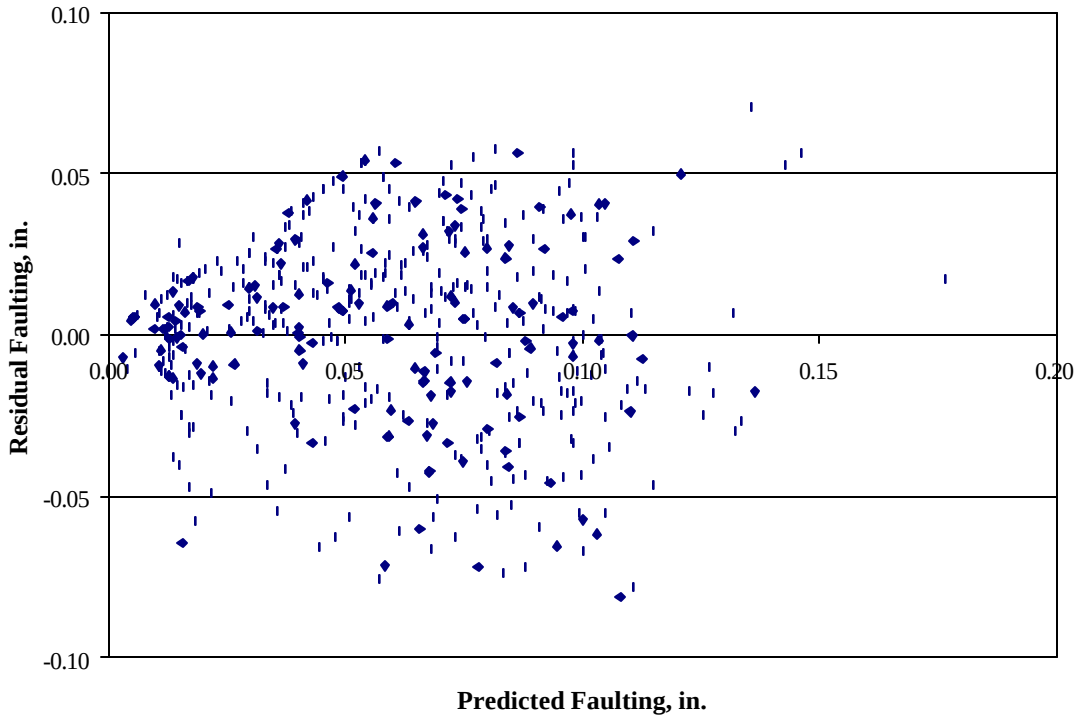

Figure 7. Residual versus predicted faulting for the validated JPCP faulting model.

Table 22. Range of values of data used in the sensitivity analysis for the final validated JPCP transverse joint faulting model.

Variable	Range		Default
	Min.	Max.	
Cumulative ESAL's	0	20,000,000	
Presence of dowels	1 = dowels are present, 0 = dowels are not present		
Dowel diameter, in	1.0	1.5	-
Transverse joint spacing, ft	13	30	15
Average annual hot days (number of days with maximum temperature > 32 °C (90 °F)	10	90	30
Average annual precipitation, in	5.0	60.0	30.0
Erodibility factor, EROD	1.0	5.0	4.0
Dynamic modulus of subgrade reaction (dynamic k-value), psi/in [backcalculated from FWD data]	100	500	200
Base permeability	1 = permeable, 0 = not permeable		
PCC modulus of elasticity, psi	3,000,000	8,000,000	4,000,000
PCC slab thickness, in	8.0	12.0	9.0

Percent consolidation around dowels, %	90	102	100

permeability of the base, PCC modulus of elasticity, PCC slab thickness, and percent consolidation around dowels. The sensitivity of the final faulting model to each of these variables is discussed separately in the following sections.

Dowel Diameter

Figure 8 provides a sensitivity plot of the joint faulting with ESAL and dowel diameter. It is clearly shown that dowels decrease faulting and that faulting decreases with an increase in dowel diameter.

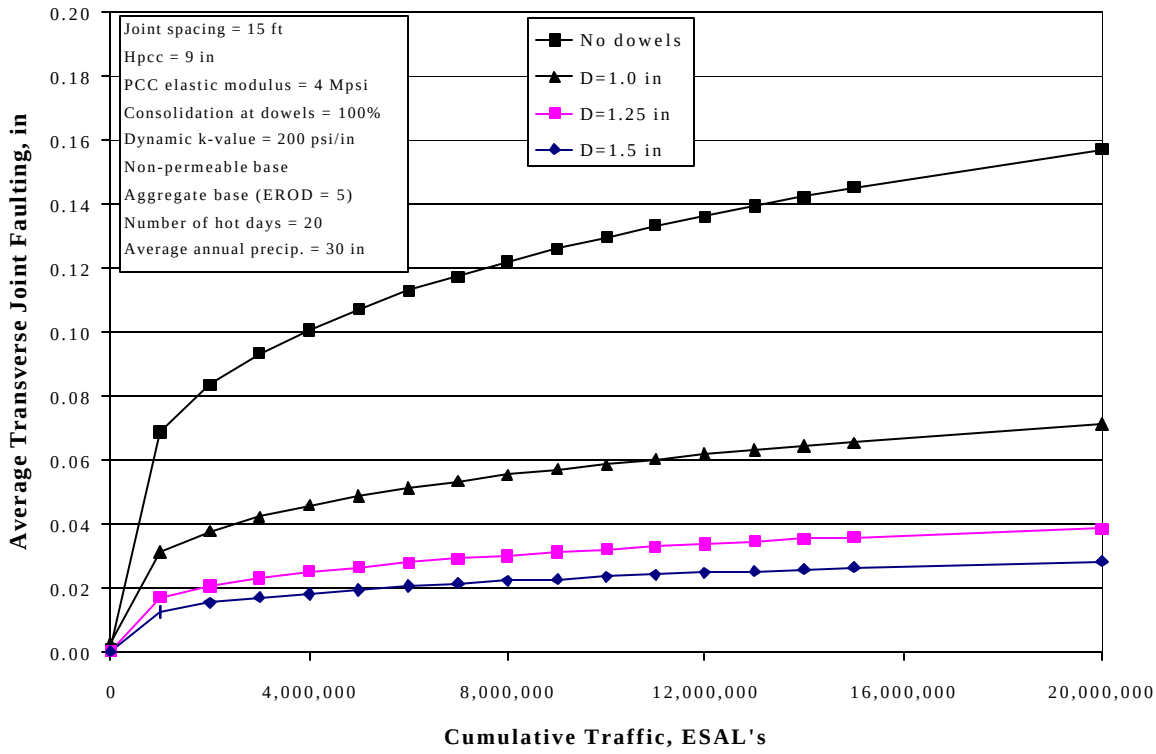

Figure 8. Sensitivity of the final JPCP transverse joint faulting model to changes in dowel diameter.

Transverse Joint Spacing

Figure 9 demonstrates that the model predicts higher faulting for pavements with longer PCC slabs. This is reasonable since an increase in joint spacing increases slab movements due to temperature contraction, which increases joint opening and reduces load transfer efficiency at the joint. The latter causes higher corner and differential deflections and, therefore, higher faulting.

Base Erodibility Factor

Figure 10 shows that the model predicts a significant reduction in faulting level if a less erodible base layer is used (for example, changing from an unbound granular base where EROD = 5.0 to a high quality lean concrete or hot-mixed asphalt treated base where EROD = 1.0). This agrees with the findings of the previous studies that pavements with stabilized bases exhibit less faulting than pavements with granular bases. Pavements with lean concrete bases (with higher cement content and

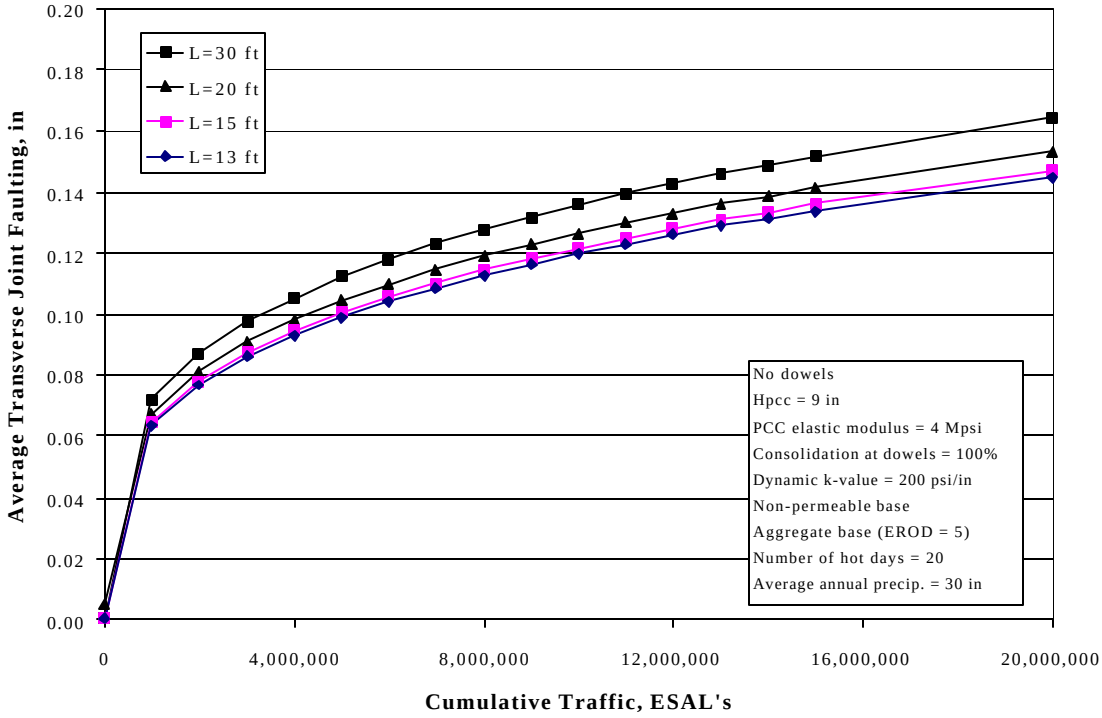

Figure 9. Sensitivity of the final JPCP transverse joint faulting model to changes in transverse joint spacing.

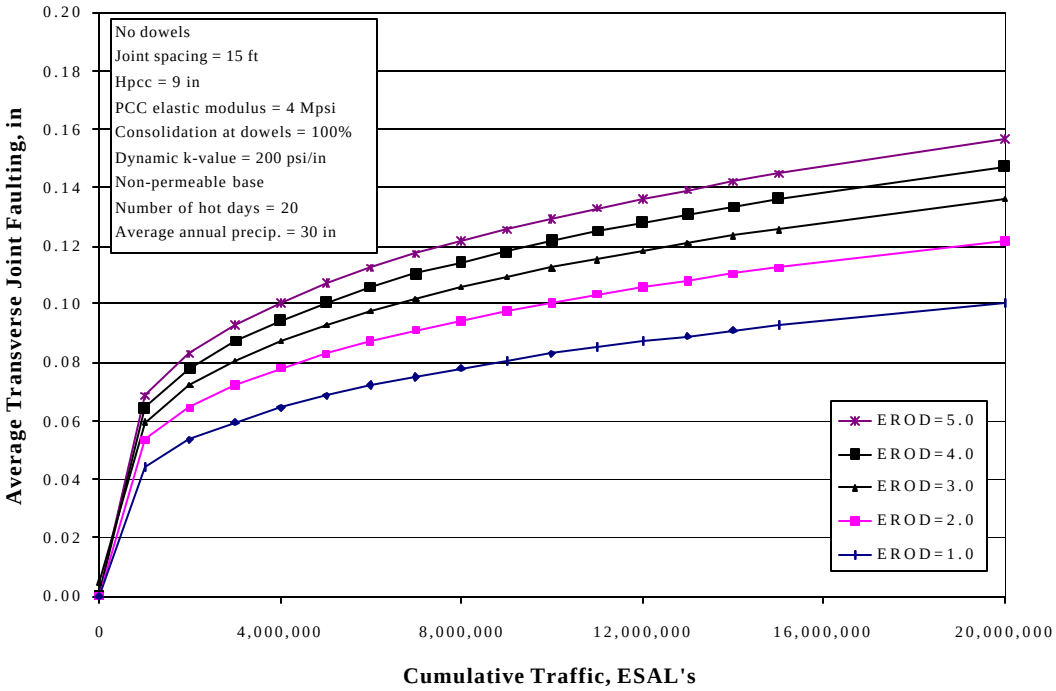

Figure 10. Sensitivity of the final JPCP transverse joint faulting model to changes in base erodibility factor.

compressive strength) exhibited less faulting than pavements with lower strength stabilized bases (assuming all other factors remain the same).

Dynamic Modulus of Subgrade Reaction (dynamic k-value)

Figure 11 shows that pavements built on softer subgrades (with lower k-values) are more likely to develop higher faulting than pavements built on a stronger subgrade (with higher k-values), assuming that all other parameters are the same. This highlights the importance of using positive design features (dowels and / or less erodible bases) for pavements built on softer subgrade.

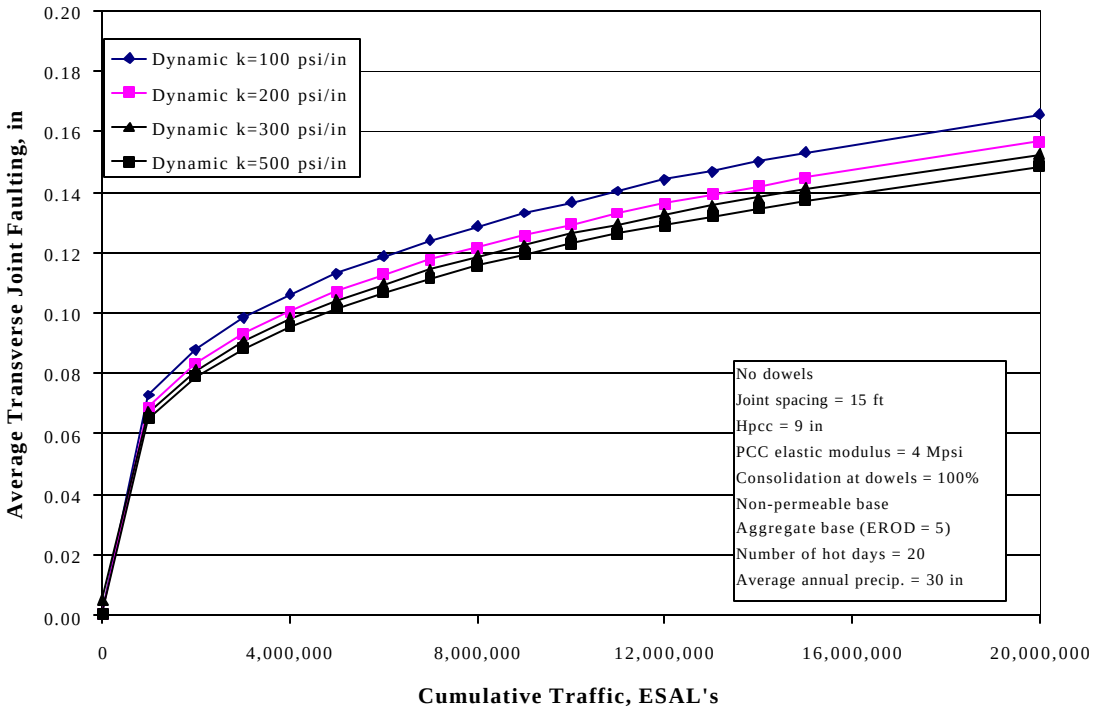

Figure 11. Sensitivity of the final JPCP transverse joint faulting model to changes in dynamic modulus of subgrade reaction.

Base Permeability

Figure 12 demonstrates that a permeable base significantly reduces faulting of non-doweled pavements. However, this reduction is less than what could be achieved if dowels were installed.

PCC Thickness and Modulus of Elasticity

Figures 13 and 14 show an increase in PCC thickness and elastic modulus reduces faulting. This is reasonable since more rigid PCC slabs experience lower deflections that reduce faulting potential.

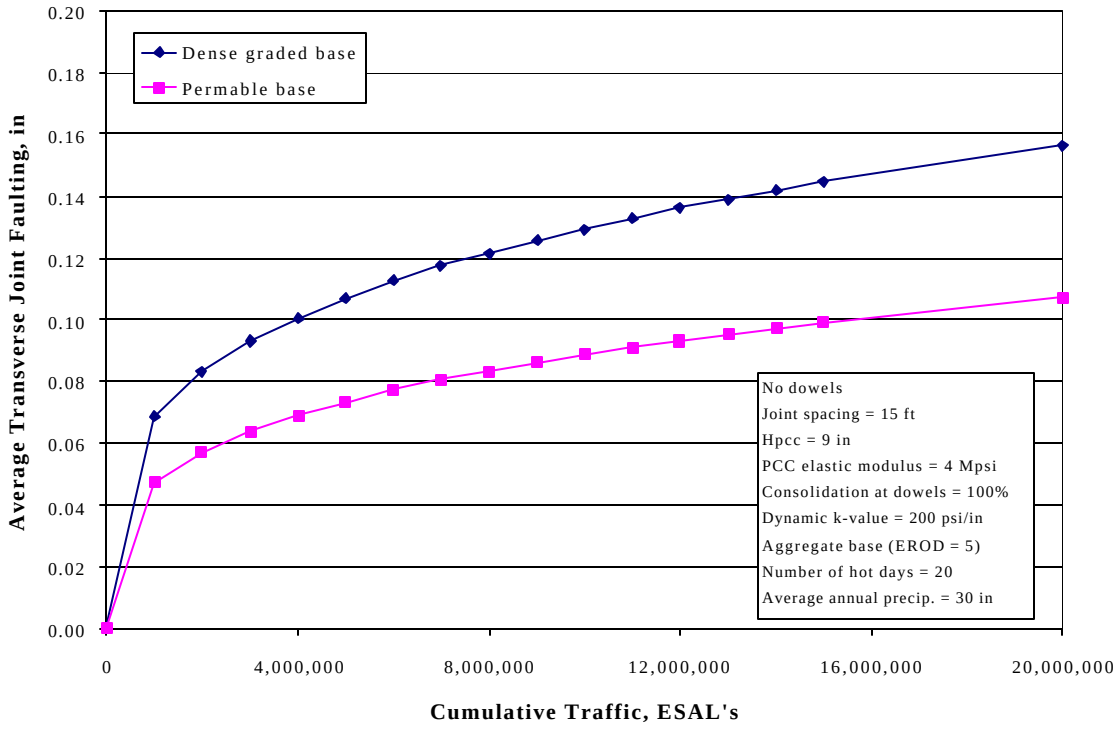

Figure 12. Sensitivity of final validated JPCP joint faulting model to changes in base permeability.

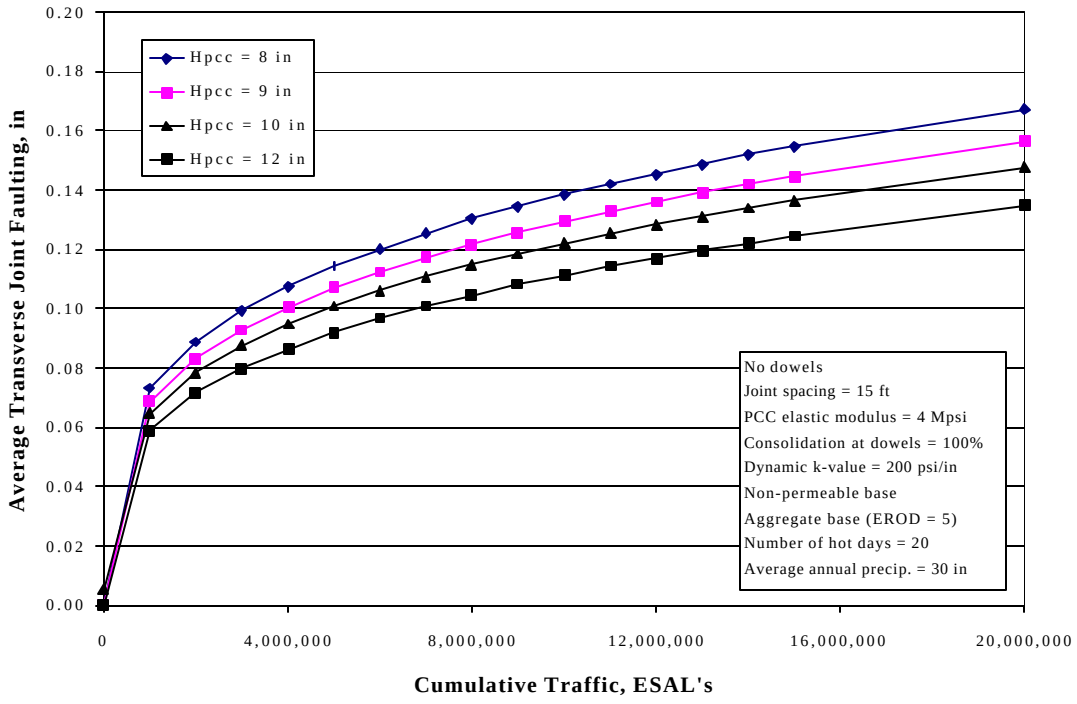

Figure 13. Sensitivity of the final JPCP transverse joint faulting model to changes in PCC slab thickness.

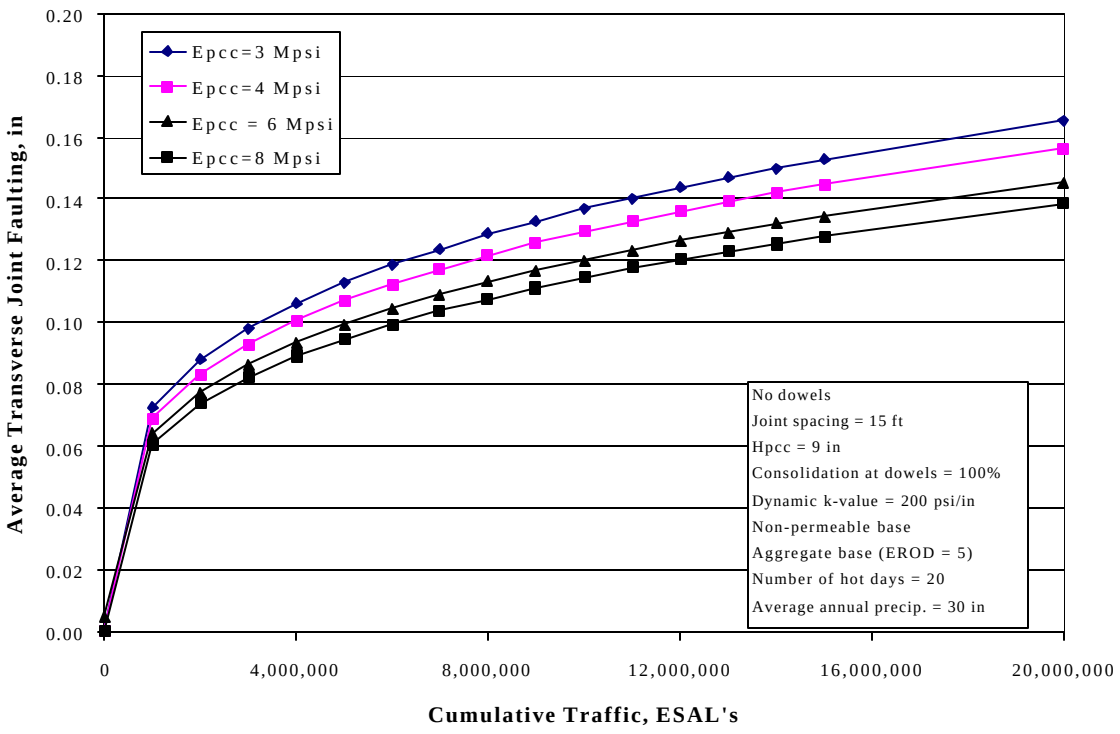

Figure 14. Sensitivity of the final JPCP transverse joint faulting model to changes in PCC modulus of elasticity.

Percent Consolidation of PCC Around Dowels

Figures 15 and 16 show the importance of proper consolidation of PCC around 25.4- and 38.1-mm (1- and 1.5-in) dowels. Poor consolidation may significantly reduce the effectiveness of dowels. Note that the trend in figure 15 demonstrates that 90 percent consolidation around a 25.4-mm (1-in) dowel reduces its effectiveness almost to the level of a non-doweled joint.

Effect of Climatic Variables

Two climatic variables were included in the final validated JPCP transverse joint faulting model—average annual precipitation and average annual number of hot days (days above 32 °C [90 °F]). The sensitivity of the final faulting model to each of these climatic variables is discussed below.

Average Annual Precipitation

Figure 17 shows that transverse joint faulting is positively correlated with average annual precipitation (i.e., an increase in precipitation causes an increase in faulting while holding all other variables constant). This trend is explained by the fact that JPCP

subjected to greater total precipitation (or days with precipitation) will have more free water beneath the slab to cause erosion (all other design features being equal).

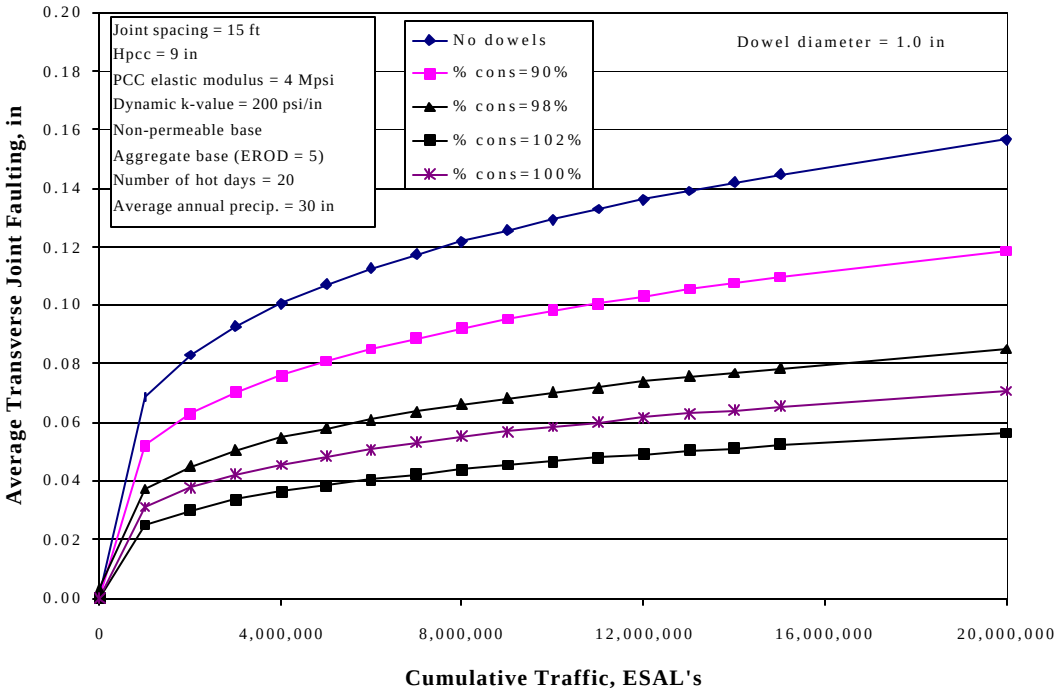

Figure 15. Sensitivity of the final JPCP transverse joint faulting model to changes in percent consolidation of PCC around 25.4-mm (1-in) dowels.

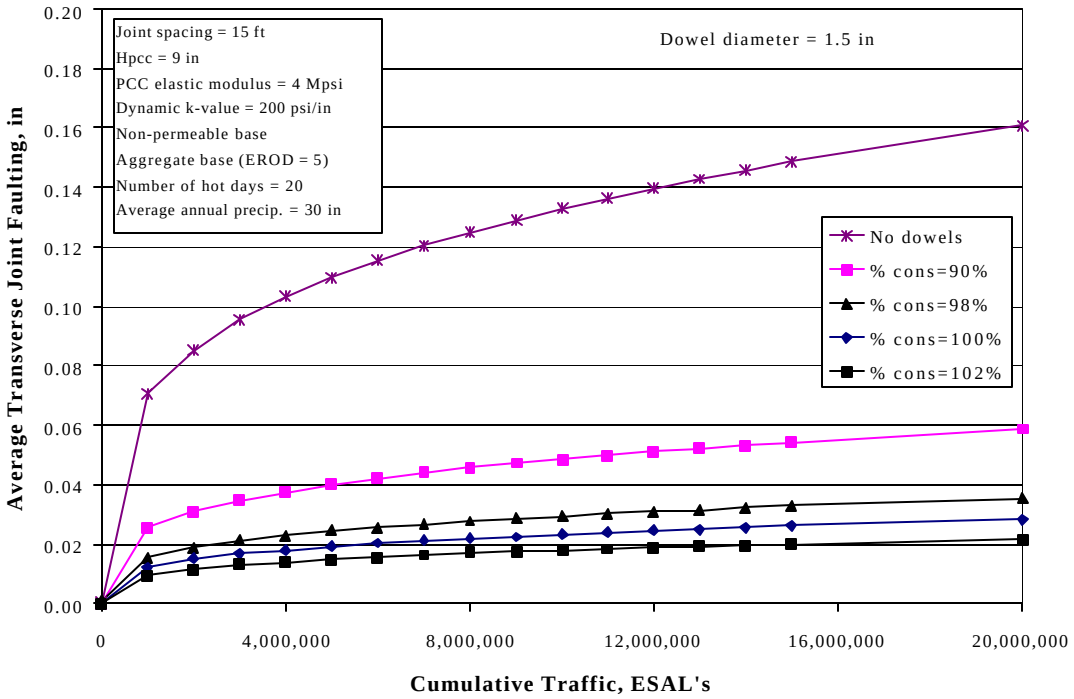

Figure 16. Sensitivity of the final JPCP transverse joint faulting model to changes in percent consolidation of PCC around 38.1-mm (1.5-in) dowels.

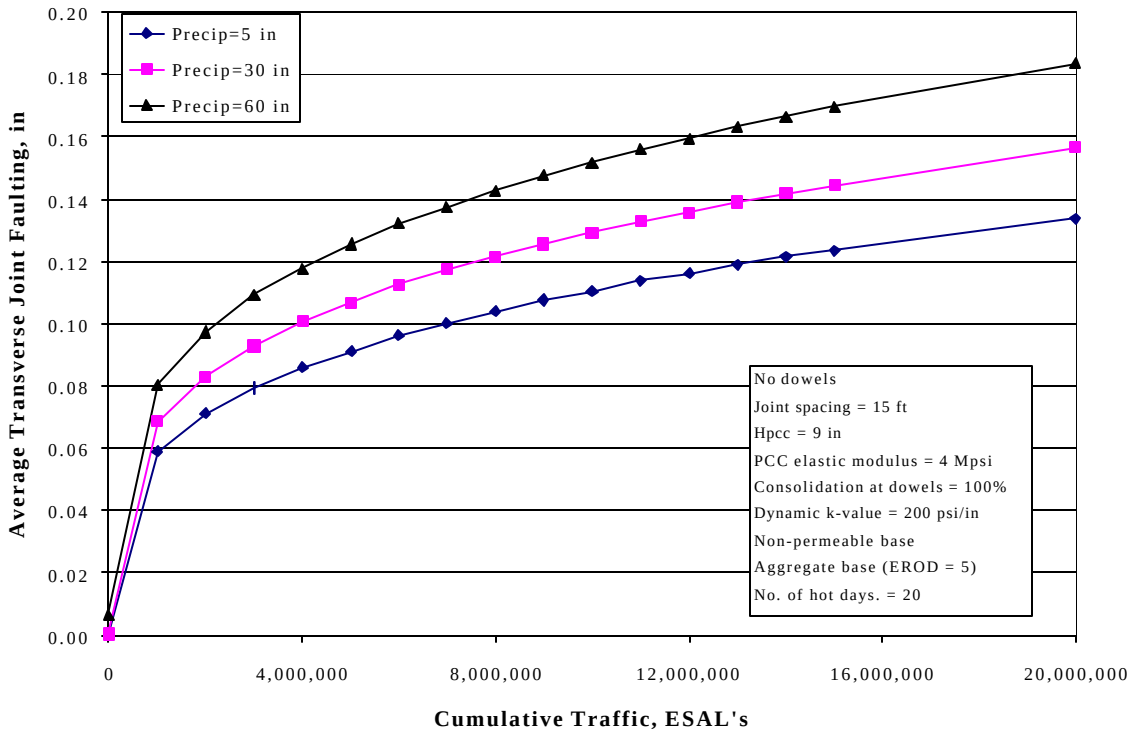

Figure 17. Sensitivity of the final JPCP transverse joint faulting model to changes in precipitation.

Average Annual Number of Hot Days

Figure 18 demonstrates the importance of air temperature on the development of transverse joint faulting. The observed trends show that faulting typically decreases as the number of hot days increases. This trend is due to the fact that pavements in warmer climates experience less damage associated with the spring thawing period. Another possible explanation of this effect is that greater use of deicing salts and increased moisture level accelerate corrosion of the dowel bars.

SUMMARY

The previous PRS faulting model was improved under this study by validating the model with a larger, more comprehensive data set, and also by directly considering the effect of base erosion. This validated model is deemed suitable for use with the current PRS procedure because it incorporates PRS-related AQC's (slab thickness and percent consolidation around dowel bars) as well as other site-, design-, material-, and climate-related variables that significantly influence faulting. Base erosion was considered in a realistic way in the calibrated model and proved to be highly significant. The final

calibrated model has a reasonable correlation ($R^2 = 0.56$) and a low SEE (0.029 in per joint) for a large number of data points (N = 511).

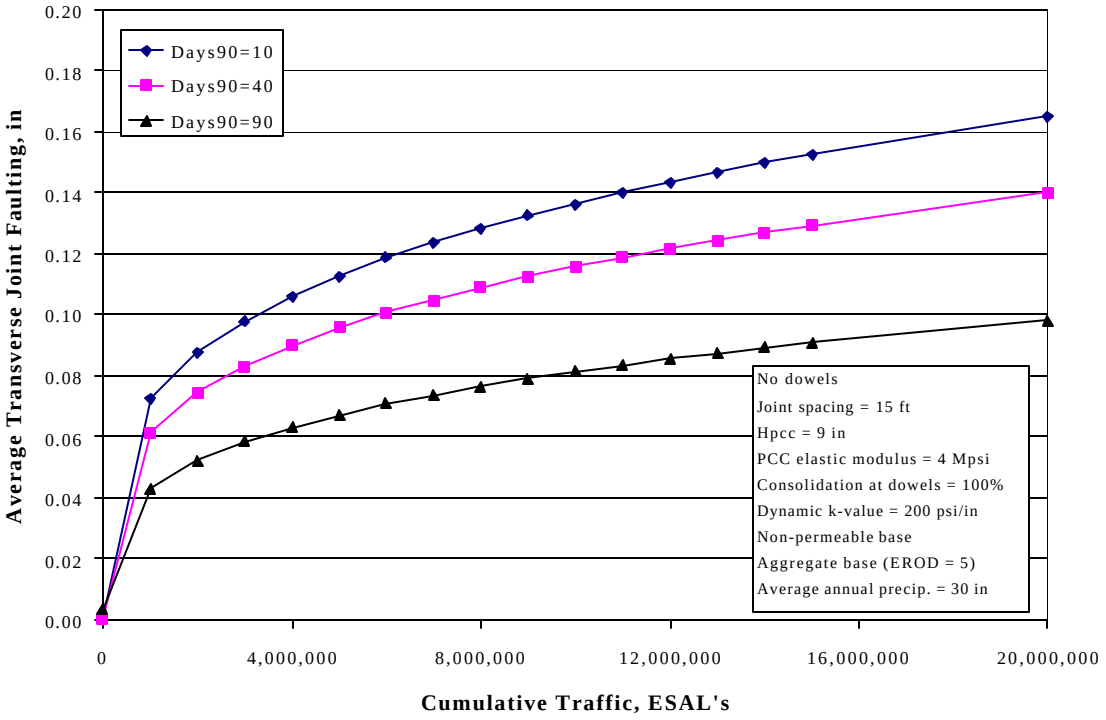

Figure 18. Sensitivity of the final JPCP transverse joint faulting model to changes in number of hot days.

CHAPTER 5: JPCP TRANSVERSE FATIGUE CRACKING MODEL

INTRODUCTION

Fatigue cracking is a key measure of concrete pavement performance for JPCP. The deterioration of a transverse crack in JPCP often leads to roughness and additional cracks in the slab, eventually becoming a shattered slab that requires replacement. Slab replacement is costly and can lead to early rehabilitation of the pavement as more and more cracking occurs. Fatigue cracking is caused by the repeated application of traffic and environmental loading at stress levels less than ultimate. As the loadings are repeated over time, cracking can occur in the slab. The keys to accurately predicting the development of such cracking include:

- The accurate determination of stresses in the slab (both traffic and environmentally induced stresses).
- The identification of the critical location in the slab where both traffic and environmentally induced stresses are greatest.
- The accurate prediction of fatigue damage using a reliable fatigue damage algorithm.

Previously developed transverse cracking models have typically only considered bottom-up cracking since the critical bending stress considered is at the bottom of the slab along the longitudinal edge. Recently, the phenomenon of top-down cracking (consisting of transverse, longitudinal, and corner cracking) has been observed on several in-service JPCP projects. These projects were constructed during hot sunny days and thus had significant built-in construction curling. These construction conditions result in a slab that is concave upward when the temperature gradient is zero through the slab. Drying shrinkage of the slab surface also significantly contributes to an upward curling of a slab. Slabs that are built with built-in curl plus significant drying shrinkage of the surface have an increased probability of experiencing top-down cracking when the load is near the joint, and a decreased probability of bottom-up cracking at the longitudinal edge. Although procedures for predicting top-down cracking are under development at this time, they are out of the scope of this PRS study and will not be included in the PRS model development procedures discussed in this chapter. The full consideration of top-down cracking would be a very beneficial addition to PRS as it would add an appropriate AQC representing the curling process.

This chapter describes the attempted validation of the chosen best-available transverse fatigue cracking model (that used in PaveSpec 2.0), as well as the development of a new, improved fatigue cracking model for use in PaveSpec 3.0.

CURRENT PRS JPCP TRANSVERSE SLAB CRACKING MODEL

The current PRS 2.0 transverse slab cracking model is based on a fatigue cracking model developed by Smith et al. in 1990.[18] Specifically, the model is based on a fatigue-consumption approach that assumes a concrete pavement has a finite life and can only withstand a maximum allowable number of 80-kN (18-kip) ESAL repetitions.

The transverse slab cracking model included in PaveSpec 2.0 consists of a multi-step procedure that gives the expected amount of slab cracking as a function of the accumulated fatigue damage at the critical point in the slab. The accumulated fatigue damage is determined considering load stress, slab curling from thermal gradients, and lateral distribution of traffic. The details of this transverse slab cracking model are presented in this section as they were presented in a 1999 report by Hoerner et al.[10] Note that the model was developed using English units.

$$\%CRACKED = 1 / [0.01 + 0.03 * (20^{-\log(n/N)})] \quad (36)$$

where:

%CRACKED = Slabs cracked (transverse cracking), %.

n = Actual number of 80-kN (18-kip) ESAL applications at slab edge.
= (0.05 * *TotESAL's*) for pavements without widened slabs.
= (0.001 * *TotESAL's*) for pavements with widened slabs.

TotESAL's = Cumulative total number of measured 80-kN (18-kip) ESAL applications.

N = Allowable 80-kN (18-kip) ESAL applications.

$$= 10^{[2.13*(1/Ratio)\wedge 1.2]} \quad (37)$$

Ratio = The ratio of computed edge stress (σ_{EDGE}) to 28-day modulus of rupture (MR_{28}).

σ_{EDGE} = Total resultant stress in the longitudinal direction at the bottom of the PCC slab edge when the wheel load is located at the slab edge, psi.

$$= \sigma_{TRAFFIC} + (R) * \sigma_{CURLING} \quad (38)$$

$\sigma_{TRAFFIC}$ = Stress at bottom of PCC slab edge when load is located at slab edge (no thermal curling stress), psi.

$$= [P / 18.0 * h^2] * [17.35783 + (0.07801 * ES) - (0.05388 * h^3 / k) + 7.41722 * \log_{10}(h^3 / k)] \quad (39)$$

$\sigma_{CURLING}$ = Stress at bottom of PCC slab edge caused by curling of slab due to thermal gradient (no traffic load), psi.

$$= [(G * ET) / (5 \times 10^{-6})] * [(0.06712 * k) + (79.07391 * \log_{10}(k)) + (11.72690 * L) - (0.00720 * k * L) - (3.22139 * L * \log_{10}(k)) - (0.06883 * L * ES) - (0.59539 * ES * \log_{10}(k)) - (204.39477 * h / k) - (38.08854 * L / h) - (8.36842 * h * \log_{10}(k)) + (0.07151 * ES * h) + (0.05691 * L * ES * \log_{10}(k)) + (0.20845 * L * h * \log_{10}(k)) + (0.00058 * L * h * k) - (0.00201 * L * ES * \log_{10}(k))] \quad (40)$$

R = Adjustment factor for $\sigma_{CURLING}$ so that it can be combined with $\sigma_{TRAFFIC}$ to give correct σ_{EDGE}.

$$= 0.48039 + (0.01401 * h) - (0.00427 * ES) - (0.27278 * G) - (0.00403 * L) + (0.19508 * \log_{10}(k)) + (0.45187 * G * \log_{10}(h)) - (0.00532 * G^2) + (0.01246 * G * L) - (0.00622 * G * L * \log_{10}(k)) + (8.7872 * \log_{10}(h^3 / k) / h^2) + (0.00104 * G * ES) - (0.11846 * G * \log_{10}(h^3 / k)) + (0.07001 * \log_{10}(ES + 1.0)) - (0.01331 * G * \log_{10}(ES + 1.0)) \quad (41)$$

P = Total applied load, lb (assumed to be 9,000 lb).

h_{PCC} = Slab thickness, in.

ES = Erodibility of support along slab edge, in (assumed to be zero).

k = Modulus of subgrade reaction, psi/in.

ET = PCC coefficient of thermal expansion (assumed to be 0.0000055).

L = Slab length (joint spacing), ft.

MR_{28} = 28-day modulus of rupture (third-point loading flexural strength), psi.

G = Thermal gradient through slab (estimated from table 23), °F/in.

Table 23. Average daytime thermal gradients (based on slab thickness and climatic zone), °F/in.[18]

Slab Thickness, mm	Wet-Nonfreeze Climatic Zone	Dry/Wet-Freeze Climatic Zones	Dry-Nonfreeze Climatic Zone
203	1.40	1.13	1.41
229	1.30	1.05	1.31
254	1.21	0.96	1.21
279	1.11	0.87	1.10
305	1.01	0.79	1.00

ATTEMPTED VALIDATION OF THE CURRENT PRS TRANSVERSE SLAB CRACKING MODEL

Before any new model development or calibration techniques were pursued, the research team attempted to validate the current PRS JPCP transverse fatigue cracking model with an expanded data set. The validity of the current cracking model was assessed by:

- Reviewing plots of predicted (equation 36) versus measured cracking.
- Reviewing plots of residuals versus predicted (equation 36) cracking.
- Analyzing diagnostic statistics such as R^2 and SEE to determine the goodness-of-fit of the model when the expanded data set is used.
- Identifying any general observed weaknesses in the model.

The data used in the initial model validation process consisted of JPCP data from the RPPR and LTPP (GPS-3) experiment databases. The final data set consisted of a total of 815 observations for pavement test sections located in 28 States and 3 Canadian Provinces. A summary of the validation data is presented in table 24.

Table 24. JPCP data used in the initial validation of the current transverse slab cracking model.

Variable	Range		Mean	Standard Deviation
	Min.	Max.		
Cumulative ESAL's, millions	0.003	56.0	5.6	7.0
PCC thickness, in	7.0	15.0	9.3	1.2
Joint spacing, ft	3.0	30.0	17.0	3.9
PCC modulus of elasticity, ksi	3,050	12,200	5,750	1,540
Dynamic modulus of subgrade reaction (k-value), psi/in	35	1,298	258	147
PCC modulus of rupture, psi	621	1,018	739	67
Base thickness, in	0.0	23.2	4.9	2.2
Base modulus of elasticity, ksi	0	3,386	440	478
Shoulder type	337 data points with AC shoulder 331 data points with tied PCC shoulder 147 data points with widened lane			
Climate	346 data points in wet-freeze region 170 data points in wet-nonfreeze region 111 data points in dry-freeze region 188 data points in dry-nonfreeze region			

The validation data set was used in the current transverse slab cracking model to obtain predicted percentages of cracked slabs for each section. The actual measured percentages of cracked slabs were obtained directly from the database. A comparison of the measured and predicted slab cracking (using the expanded database) showed a low R^2 value of 0.18 percent and an SEE of 35.8 percent.

Figures 19 and 20 show plots of predicted versus measured slab cracking, and residuals versus predicted slab cracking, respectively. The diagnostic statistics and both plots indicate that the predicted transverse slab cracking is much higher than measured cracking. The most likely explanation of this phenomenon is that the current PRS model does not adequately address the effect of base layer properties or the effects of PCC shrinkage, construction curling, and moisture warping. Recent research has indicated that accounting for these effects is imperative to accurately predic the development of transverse cracking.[16]

Because of the limitations of the cracking model currently included in PaveSpec 2.0, it was decided that the current model could not be simply validated. Instead, a new transverse cracking model was developed under this study using the compiled validation data set. The details of this model development procedure are discussed in the remaining sections of this chapter.

EXISTING JPCP TRANSVERSE SLAB CRACKING MODELS

In preparation for the development of a new JPCP transverse cracking model, many of the cracking models developed under previous research were reviewed. A review of previous models not only provided guidance as to what variables should be considered for inclusion in the new model, but also added expert knowledge into the model development process at an early stage. During the review process, specific attention was paid to the engineering significance of the variables.

JPCP transverse cracking has been the focus of numerous field and laboratory investigations over the past 25 years. The FHWA-sponsored *Design of Zero-Maintenance Plain Jointed Concrete Pavement* study was the first mechanistic-based study to show a direct correlation between fatigue damage accumulation and measured transverse cracking in the field.[31] This approach was later expanded under the FHWA-sponsored *Rigid Pavement Performance Study* (RPPR) and the NCHRP Project 1-26 study.[16,18,32,33] A summary of some of the past JPCP cracking models, other than the 1990 model by Smith et al. (presented above), are summarized in the following sections.

NCHRP Project 1-26 JPCP Transverse Cracking Model[32,33]

Under the NCHRP 1-26 study, the following JPCP transverse cracking model was developed:

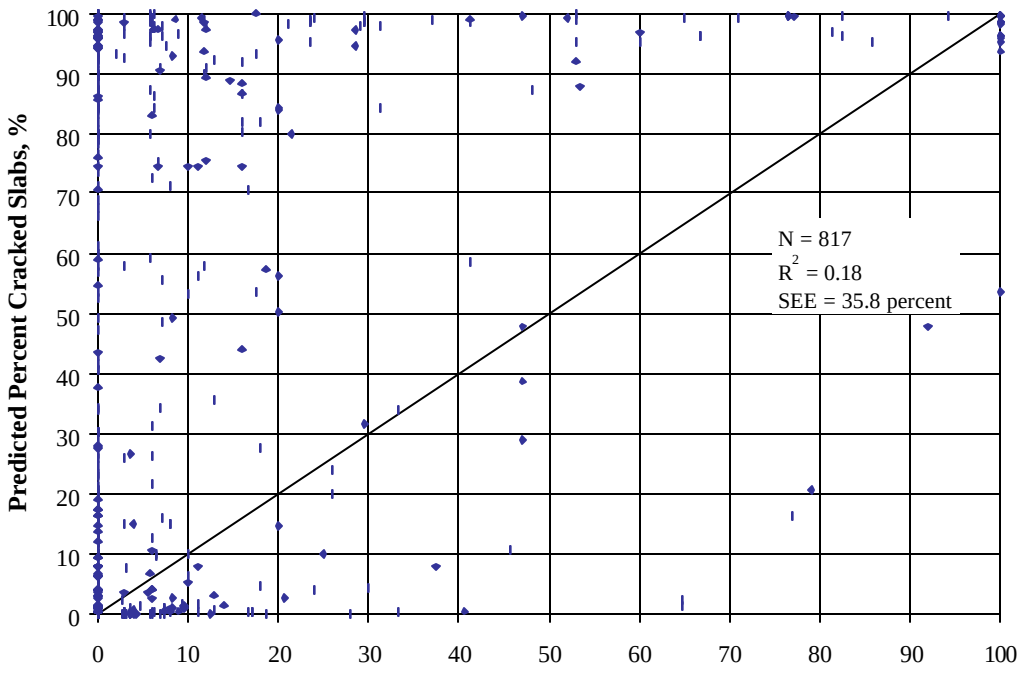

Figure 19. Predicted (equation 36) versus measured JPCP transverse slab cracking (using the compiled validation data set).

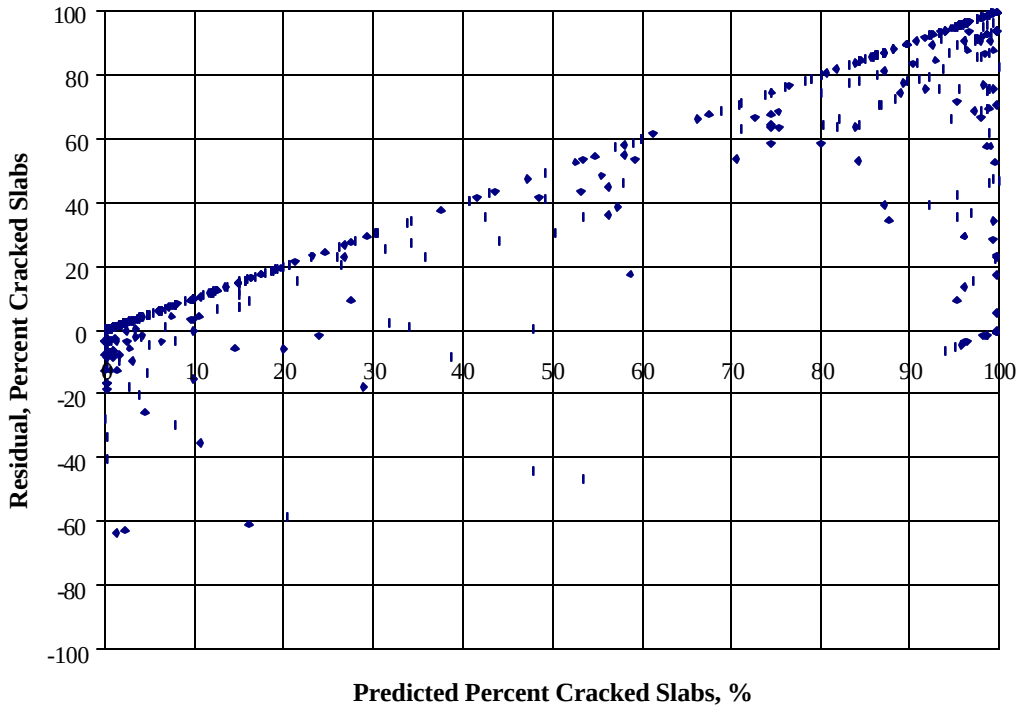

Figure 20. Residual versus predicted (equation 36) transverse JPCP slab cracking (using the compiled validation data set).

$$\%CRACKED = \frac{1}{0.01 + 0.0713 * \left(2.5949^{-\log FD}\right)} \tag{42}$$

where:

%CRACKED = Slabs cracked (transverse cracking), %.

FD = Total accumulated fatigue damage occurring at the critical fatigue location in the slab, defined as follows:

$$= \sum_{k=1}^{p} \sum_{j=1}^{2} \sum_{i=1}^{m} \frac{n_{ijk}}{N_{ijk}}$$

n_{ijk} = Number of edge stress repetitions of the i-th magnitude over day or night for the k-th month.

N_{ijk} = Number of edge stress repetitions of i-th magnitude over day or night for the k-th month.

i = Counter for the magnitude of the axle load.

j = Counter for day or night.

k = Counter for months over the design period.

m = Total number of axle load groups.

p = Total number of months in the design period.

The allowable number of 80-kN (18-kip) ESAL applications (N) is defined from the following equations:

$$N = 10^{\left(\frac{-\left(\frac{\sigma_{EDGE}}{MR_{28}}\right)^{-5.367} \log(1-P)}{0.0032}\right)^{\frac{1}{4.394}}} \tag{43}$$

where:

σ_{EDGE} = Total resultant stress in the longitudinal direction at the bottom of the PCC slab edge when the wheel load is located at the slab edge, psi.

MR_{28} = PCC modulus of rupture at 28-days, psi.

P = Probability level.

The equation for total resultant stress in the longitudinal direction is defined as follows:

$$\sigma_{EDGE} = \sigma_{TRAFFIC} + R * \sigma_{CURLING} \tag{44}$$

where:

$\sigma_{TRAFFIC}$ = Edge stress due to traffic load, psi.

$\sigma_{CURLING}$ = Curling stress due to temperature gradient, psi.
R = Curling stress reduction factor.

The traffic load edge stresses are obtained using Westergaard's equation for an infinite slab under a circular load with a free edge loading condition. The computed Westergaard free edge stress (σ_{FE}) is then corrected for slab size, presence of stabilized base, and edge support. (Note: the correction factors were applied in an attempt to reproduce the results obtained from the ILLI-SLAB finite element program.) The final equation used to compute the corrected traffic load edge stress is the following:

$$\sigma_{TRAFFIC} = f_{LTE} f_{SLAB} f_{BASE} \sigma_{FE} \tag{45}$$

where f_{LTE}, f_{SLAB}, and f_{BASE} are edge support, slab size, and base correction factors, and the equation for Westergaard's free edge stress is defined as:

$$\sigma_{FE} = \frac{3(1+\mu_{PCC})\frac{P}{2}}{\pi(3+\mu_{PCC})h_{PCC}^2}\left[Ln\left(\frac{E_{PCC}h_{PCC}^3}{100ka_e^4}\right)+184-0.75\mu_{PCC}+\frac{1-\mu_{PCC}}{2}+1.18*(1+2\mu_{PCC})*\frac{a_e}{\ell}\right] \tag{46}$$

where:

P = Total axle load, lb.
h_{PCC} = PCC slab thickness, in.
E_{PCC} = PCC modulus of elasticity, psi.
$:_{PCC}$ = Poisson's ratio.
k = Coefficient of subgrade reaction, psi/in.
a_{eq} = Equivalent radius, in. (An equivalent radius [a_{eq}] of a multiple-wheel assembly is used as the load radius of the Westergaard equation, resulting in the same stress as the one obtained from finite element method with the real wheel configuration.)
l = Radius of relative stiffness, in.

$$= \sqrt[4]{\frac{E_{PCC}h_{PCC}^3}{12(1-\mu_{PCC}^2)k}} \tag{47}$$

The stress caused by the temperature differential only is defined using the following Westergaard's expression:

$$\sigma_{CURLING} = \frac{CE_{PCC}ET\ \Delta T}{2} \tag{48}$$

where:

$\sigma_{CURLING}$ = Curling stress due to temperature differential in slab, psi.
C = Coefficient that depends on the ratio of the slab length to the radius of relative stiffness.
E_{PCC} = PCC modulus of elasticity, psi.
ET = PCC coefficient of thermal expansion.
ΔT = Temperature differential throughout the slab thickness, °F (defined as the difference between the temperature at the top and that at the bottom of the slab). It was recommended to predict distribution of temperature differentials using a calibrated model like the Integrated Climate and Materials (ICM) model.[34]

FHWA RPPR 1997 JPCP Transverse Cracking Model[16]

In 1997, Yu et al. developed another JPCP transverse cracking model under a second RPPR contract.[16] Although this model uses the same approach as the RPPR 1990 and the NCHRP Project 1-26 models, it included a number of improvements, such as:[18,32,33]

- The model was calibrated with a more widespread database.
- The effect of construction curling and differential shrinkage was incorporated.
- A more rigorous procedure for traffic wander was introduced.
- The critical stress calculation procedure was corrected.

The RPPR 1997 model used the following relationship between cumulative fatigue damage (FD) and percentage of cracked slabs (%CRACKED):

$$\%CRACKED = \frac{100}{1 + 4.15 * FD^{-1.52}} \tag{49}$$

Statistics:
N = 465.
R^2 = 0.91.
SEE = 7.1.

Under this study, accumulated fatigue damage is defined as follows:

$$FD = \sum_i \frac{pc(\sigma_{EDGE})\, n(\Delta T_i)}{N(\Delta T_i)} \tag{50}$$

where:

FD = Fatigue damage.
$n(\Delta T)$ = Actual number of 80-kN (18-kip) ESAL applications acting together with the temperature gradient ΔT.

σ_{EDGE} = Total resultant stress in the longitudinal direction at the bottom of the PCC slab edge when the wheel load is located at the slab edge, psi.

pc = Pass-to-coverage ratio (based on σ_{edge}).

N = Allowable number of 80-kN (18-kip) ESAL applications.

$$= 10^{2.13*\left(\frac{s_{EDGE}}{MR}\right)^{1.2}} \tag{51}$$

MR = PCC modulus of rupture

The total resultant stress in the longitudinal direction is defined using the same equation as the NCHRP Project 1-26 model (equation 44). In the NCHRP Project 1-26 procedure, the stress due to traffic loading is determined by applying various adjustment factors to the free edge stress calculated using Westergaard's equation (equation 45).[32,33] However, in the RPPR 1997, model the adjustment factor for the slab size effect was not used because the ILLI-SLAB analysis performed to validate the stress calculation procedure showed that the use of this factor could result in overcompensation for the slab size effect. The analysis showed that the response of a multiple slab system, with even a moderate load transfer efficiency at the transverse joints, closely approximates that of an infinitely long slab.

One of the main differences between the RPPR 1997 and NCHRP Project 1-26 models is the method used to calculate curling stress. Although the same Westergaard's equation is applied (equation 48), the actual ΔT is reduced by a determined shift factor (T_S), as follows:

$$\sigma_{CURLING} = \frac{CE_{PCC}ET\ (\Delta T - T_S)}{2} \tag{52}$$

where:

$\sigma_{CURLING}$ = Curling stress due to temperature differential in slab, psi.

C = Coefficient that depends on the ratio of the slab length to the radius of relative stiffness.

E_{PCC} = PCC modulus of elasticity, psi.

ET = PCC coefficient of thermal expansion.

ΔT = Temperature differential throughout the slab thickness, °F (defined as the difference between the temperature at the top and that at the bottom of the slab).

T_S = Temperature shift factor, °F (defined as the effective temperature gradient that would produce the total built-in construction curling in a pavement).

The total built-in construction curling present in a pavement is caused by a number of factors, including the following:

- *Moisture gradient*—The top of the slab is usually drier than the bottom throughout most of the year; therefore, moisture gradients generally tend to cause lifting of the slab corners. The moisture gradients could be treated as equivalent negative temperature gradients, but insufficient information is available to adequately quantify this effect.

- *Differential drying shrinkage*—Field moisture measurements have shown that surface shrinkage of PCC occurs only to a depth of about 51 mm (2 in).[35] The net effect of this phenomenon is an equivalent temperature gradient (temperature difference between top and bottom) of about –1.4 °C (–2.5 °F) for a 250-mm- (10-in-) thick slab.

- *Built-in temperature gradient (residual temperature gradient)*—At the time when an as-constructed slab hardens, the temperature difference between the top and bottom of the slab (temperature differential) will greatly influence the amount of curling that develops in the slab. When a positive temperature differential (temperature at the top > temperature at bottom) is present at the time of hardening, the hardened slab will permanently experience what appears to be a *negative* built-in temperature gradient. This built-in negative gradient is explained by realizing that the slab was flat when it hardened with a positive temperature differential. Therefore, when this temperature differential becomes zero (i.e., temperature at top = temperature at bottom) the slab will be curled upward (due to the combination of contraction of the upper portion and expansion of the lower portion of the slab). A slab hardened under such a condition will only become flat when it is subjected to a positive temperature gradient of the same magnitude that was present at the time of hardening.

  Daytime construction with sunshine generally causes positive temperature gradients through the PCC at hardening, resulting in built-in negative temperature gradients in the slabs. Since pavement slabs are exposed to daily cycling of temperature gradients (from large positive gradient at midday to negative gradients at night), any relaxing of the residual gradients through creep effects are not likely. Studies have shown that the magnitude of this residual temperature gradient in some highway pavements is –0.055 °C / mm (–2.5 °F / in) or more, which translates to a –14 °C (–25 °F) gradient in a 250-mm- (10-in-) thick slab.[36]

Moisture gradients, differential drying shrinkage, and built-in temperature gradients all cause upward curling of the pavement slabs, and the effects of the last two are permanent. According to these factors, the magnitude of negative residual temperature gradient could be very significant in many pavement sections. The combined net effects of all factors that cause curling or warping of pavement slabs can be expressed in terms of an effective temperature gradient. The magnitude of curling stress depends on the net result of all factors at work. Hence, the initial upward curling

has the effect of shifting the actual temperature gradients in the negative direction by the amount corresponding to the degree of initial curling. The initial upward curling, therefore, reduces the combined stress at the longitudinal edge but increases the critical tensile stresses at the surface under corner loading conditions.

In the RPPR 1997 model calibration, the cumulative effects of curling (or warping) caused by all factors other than temperature gradients were addressed by shifting the temperature gradients determined for each pavement section individually. The actual magnitude of the effective residual curling is unknown; however, the consistency within the data set was used as the guide to make relative adjustments. Random joint sections typically included a wide range of slab sizes (e.g., 3.7 to 5.8 m [12 to 19 ft]). Since the edge stress is very sensitive to temperature gradient and slab length, any changes in the temperature gradient had a significant effect on fatigue damage. Since the temperature gradient was required to be assigned consistently to slabs of different sizes within a given pavement section, the calculated fatigue damage had to be reasonable for all slab sizes in order for the assignment to be made.

Overview of Existing JPCP Transverse Cracking Models

The review of past JPCP transverse fatigue cracking model development efforts indicates that significant progress has been achieved in the past 20 years. Of those models reviewed, that developed by Yu et al. under the 1997 FHWA RPPR study was selected as the best-available JPCP transverse cracking model for the following reasons:[16]

- The model development utilized experience gained in the development of models developed under previous research (i.e., the Zero-Maintenance, NCHRP Project 1-26, and RPPR 1990 models).[18,31,32,33]

- The model has the most advanced stress calculation procedure of all reviewed JPCP transverse cracking models.

- The model is the only existing JPCP transverse cracking model that accounts for such factors as PCC shrinkage, moisture warping, and construction curling.

- The model was calibrated using a very comprehensive database.

Even though the RPPR 1997 model was selected as the best available, the following drawbacks make it difficult for immediate incorporation into the current PRS methodology:

- The model requires that the ICM program be used to determine the distribution of hourly temperature gradients (through concrete slabs for an average year) for each pavement section. Running the ICM program may be time-consuming, as

the program requires the input of a substantial number of climatic and material parameters.

- The procedure for estimation of construction curling differential requires simplification for use in the current PRS methodology.

It should be noted that an attempt was made in the RPPR 1997 study to develop a more objective way to determine appropriate *temperature shift factors*. This attempt resulted in the suggestion to use the following mean shift factors specific to climatic regions: [16]

- Dry-Freeze: 6.1 °C (11.0 °F)
- Dry-Nonfreeze: 6.4 °C (11.5 °F)
- Wet-Freeze: 4.4 °C (8 °F)
- Wet-Nonfreeze: 4.7 °C (8.5 °F)

However, the use of these average shift factors (instead of individual section shift factors) resulted in a much worse predictive ability, even for the same RPPR 1997 database.

Figure 21 illustrates that the RPPR 1997 model predicts very well ($R^2 = 0.93$) when individual section temperature shift factors and individual temperature gradient distributions (i.e., temperature shift factors and gradient distributions determined specifically for each section independently) were applied. Figure 22 shows that the accuracy of the model decreases substantially ($R^2 = 0.52$) when individual section temperature shift factors are replaced with the suggested overall climatic zone means (note that for this case, the section specific temperature gradient distributions are still used). Finally, when climatic zone mean values were used for both temperature shift factors and gradient distributions, the model's predictive ability decreased even farther ($R^2 = 0.44$).

IMPROVEMENT OF THE RPPR 1997 JPCP TRANSVERSE CRACKING MODEL

Based on the results of the validation process, and the review of previously developed models, the transverse slab cracking model validation/improvement effort focused on improving the RPPR 1997 model so that it would be more applicable for use within the current PRS methodology. The specific procedure used in the improvement of the RPPR 1997 model includes:

- Preparation of the model improvement data set.
- Selection of appropriate statistical tools for regression and optimization.
- Recalibration of the final JPCP transverse cracking model.

These tasks are described in greater detail in the following sections.

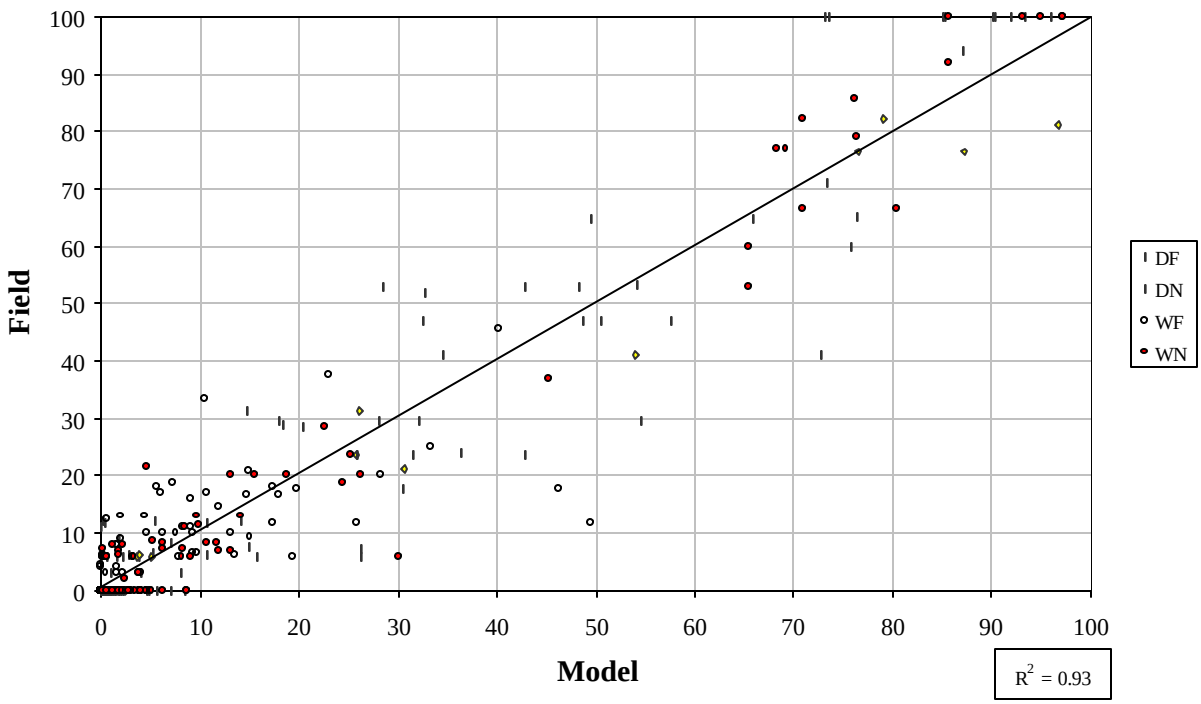

Figure 21. Actual (field) versus predicted (RPPR 97 model) slab cracking (using the section-by-section temperature shift factors and gradient distributions).[16]

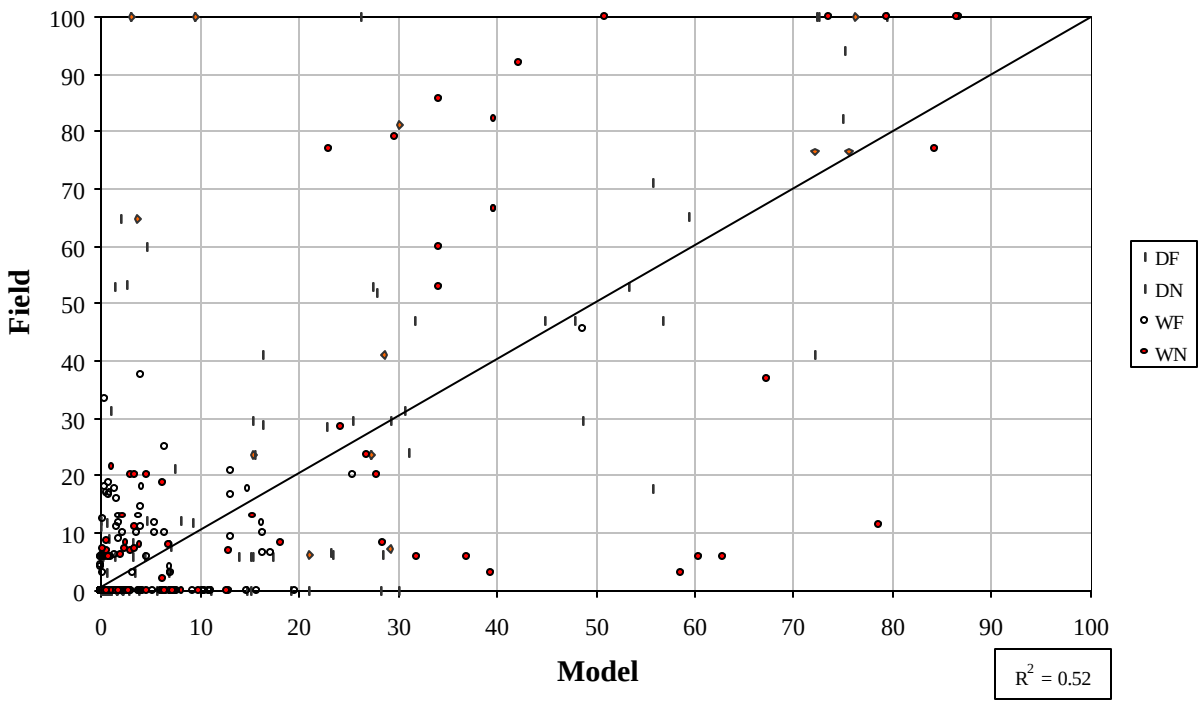

Figure 22. Actual (field) versus predicted (RPPR 97 model) slab cracking (regional temperature shift factors with section-by-section temperature gradient distributions).[16]

Data Preparation

The same data used in the validation of the current PaveSpec 2.0 model were used in the recalibration of the RPPR 1997 model. As discussed above, data from the RPPR database were combined with JPCP data from the LTPP study (GPS-3 data only) to develop a comprehensive model validation / development data set. This final data set consisted of a total of 815 observations for pavement test sections in 28 States and 3 Canadian Provinces. A detailed summary of this data was presented previously in table 24.

Statistical Tools for Regression and Optimization

The SAS nonlinear procedure (NLIN) was selected as the appropriate regression tool to be used in final model calibration because the procedure is versatile and allows for constraining model coefficients where required.[30] Other SAS procedures, such as STEPWISE, REG, RSQUARE, and RSREG, were used in preliminary model development for determining and selecting the most suitable variables for incorporation into the final model. The SAS NLIN Marquardt algorithm was used in the optimization of the transverse cracking model.

Final JPCP Transverse Cracking Model

The first step in the final calibration of the RPPR 1997 cracking model involved incorporating a simplified method for determining frequency distributions of temperature differentials between the PCC top and bottom surfaces. Specifically, the following approach was used:

1. The ICM model was used to generate the frequencies of temperature differentials between the PCC top and bottom surfaces for typical conditions associated with the four climatic regions (wet-freeze, wet-nonfreeze, dry-freeze, and dry-nonfreeze).[34] Within each climatic region, frequency distributions were generated for different PCC slab thicknesses (varied from 127 to 381 mm [5 to 15 in] at 6-mm [0.25-in] increments). Frequencies for other slab thicknesses were determined by linearly interpolating between these generated frequency distributions.

2. It was proposed to estimate construction temperature gradients based on the PCC slab thickness and the climatic region using the following equation:

$$T_s = \xi \frac{(h-2)}{h^3} + \psi \tag{53}$$

where:

h = Slab thickness, in.
ξ, Ψ = Climatic region specific parameters determined during the model calibration.

The same S-shaped functional form used in the RPPR 1997 model for the relationship between the cumulative damage and the percentage of cracked slabs was used in the recalibration procedures. Specifically, this model form is as follows:

$$\%CRACKED = \frac{100}{1 + a * FD^{-b}} \tag{54}$$

where %CRACKED is the percentage of cracked slabs, and a and b are regression coefficients that will be determined during the calibration.

A nonlinear regression was performed using performance data for 815 observations. The regression resulted in the temperature shift factor coefficients presented in table 25.

Table 25. Temperature shift factor coefficients by climatic zone.

Climatic Zone	>	R
Wet-Freeze	327.27	5.73
Wet-Nonfreeze	218.18	6.26
Dry-Freeze	436.36	6.78
Dry-Nonfreeze	436.36	7.37

Using these temperature shift coefficients in the regression analysis, the following equation was developed for the relationship between fatigue damage, FD, and percentage of cracked slabs, %CRACKED:

$$\%CRACKED = \frac{100}{1 + 1.16\ FD^{-1.3}} \tag{55}$$

The diagnostic statistics for this calibrated slab cracking model are as follows:

N = 815.
R^2 = 0.56.
SEE = 9.3 percent of slabs.

Plots of the predicted versus measured transverse cracking, and residuals versus predicted transverse cracking, are shown in figures 23 and 24, respectively. Figure 23 shows that crack prediction is low for higher amounts of measured cracking. However, it is important to note that this trend should have little effect when used within the PRS methodology since the actual percentage of cracked slabs on an in-service highway pavement is rarely allowed to reach such high levels. The diagnostic statistics and both

plots verify that the model is effective for predicting transverse cracking. The R^2 of 0.56 and SEE of 9.3 percent are very reasonable given the large number of RPPR and LTPP

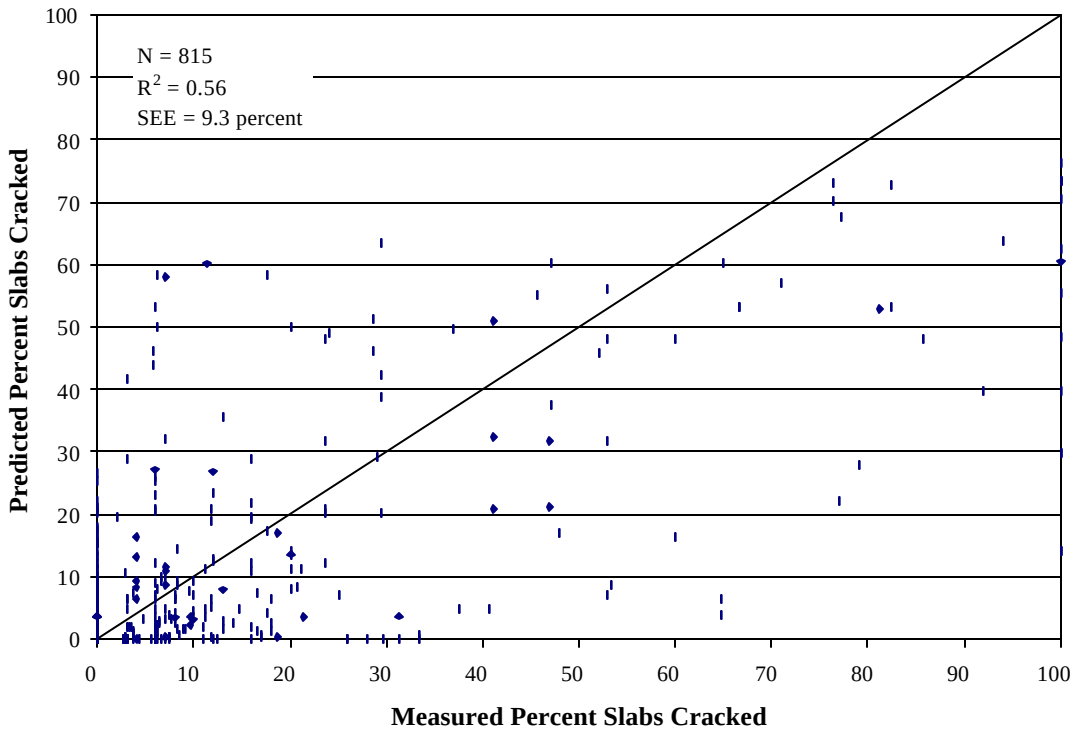

Figure 23. Predicted (equation 55) versus measured JPCP transverse cracking.

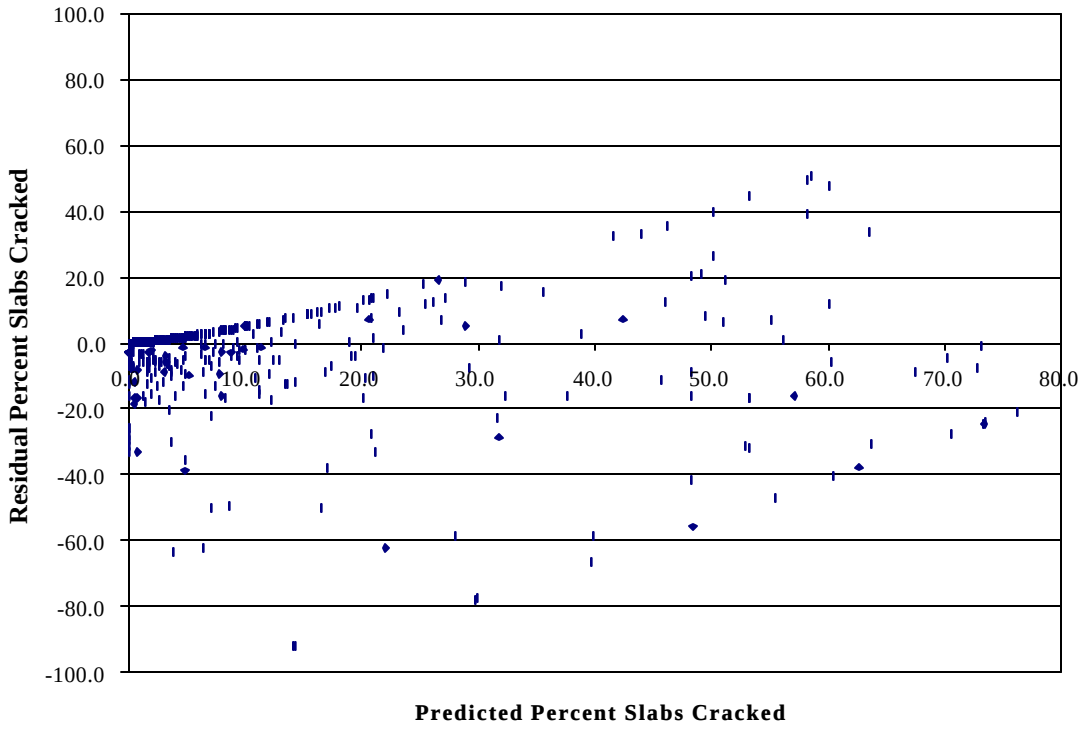

Figure 24. Residual versus predicted (equation 55) JPCP transverse cracking.

field data observations (N=815) and the likelihood that some transverse cracking was caused by other factors (such as late joint sawing).

Procedure Used to Predict Fatigue Damage

The detailed step-by-step procedure used to compute fatigue damage is presented in this section. This procedure is very similar to that used in the original RPPR 1997 model.

Step 1—Find the Effective Slab Thickness

If the pavement has a base layer, the structural contribution of the base is accounted for by replacing the original two-layered slab (PCC and base layer) with an equivalent slab that has the same deflection profile as the original two-layered slab. The maximum stresses in the PCC layer and the equivalent slab are related to each other. Depending on the interface condition between the slab and the PCC layer, the thickness of the equivalent slab, h_e, is defined using the following equations:

If an *unbonded* interface is chosen:

$$h_e = \sqrt[3]{h_{PCC}^3 + \frac{E_{base}}{E_{PCC}} h_{base}^3} \tag{56}$$

If a *bonded* interface is chosen:

$$h_e = \sqrt[3]{h_{PCC}^3 + \frac{E_{base}}{E_{PCC}} h_{base}^3 + 12\left[h_{PCC}\left(x - \frac{h_{PCC}}{2}\right)^2 + \frac{E_{base}}{E_{PCC}}\left(h_{PCC} - x + \frac{h_{base}}{2}\right)^2 h_{base}\right]} \tag{57}$$

where x is a distance from the top surface of the PCC layer to the neutral axis:

$$x = \frac{\frac{h_{PCC}^2}{2} + \frac{E_{base}}{E_{PCC}} h_{base}\left(h_{PCC} + \frac{h_{base}}{2}\right)}{h_{PCC} + \frac{E_{base}}{E_{PCC}} h_{base}} \tag{58}$$

where:

h_{PCC} = PCC slab thickness, in.
h_{base} = Base thickness, in.
E_{PCC} = Elastic modulus of PCC, psi.
E_{base} = Elastic modulus of base material, psi.

Step 2—Calculate Load Stresses

To calculate maximum bending stresses in the effective slab, load and curling stresses should be determined. Calculation of load stresses involves the following steps:

Step 2.1. Calculate the radius of relative stiffness (*l*) (currently used for the faulting model):

$$\ell = \sqrt[4]{\frac{E_{PCC} h_e^3}{12(1-\mu_{PCC}^2)k}} \tag{59}$$

where:

E_{PCC} = Elastic modulus of PCC, psi.
h_e = Effective thickness computed in step 1.
μ_{PCC} = Poisson's ratio for PCC (assumed to be 0.15).
k = Modulus of subgrade reaction (k-value), psi/in.

Step 2.2. Calculate the effective wheel radius (a_{eff}) using the following equation:

$$a_{eff} = a * \left[\begin{array}{l} 0.909 + 0.339485\left(\frac{s}{a}\right) + 0.103946\left(\frac{a}{l}\right) - 0.017881\left(\frac{s}{a}\right)^2 \\ - 0.045229\left(\frac{a}{l}\right)\left(\frac{s}{a}\right)^2 + 0.000436\left(\frac{s}{a}\right)^3 - 0.301805\left(\frac{s}{a}\right)\left(\frac{a}{l}\right)^3 \\ + 0.034664\left(\frac{s}{l}\right)^2 + 0.001\left(\frac{s}{a}\right)^3\left(\frac{a}{l}\right) \end{array} \right] \tag{60}$$

where:

a_{eff} = Computed effective wheel radius, in.
a = $\sqrt{\frac{18{,}000}{4 * p * 95}}$ = 3.883019 in.
s = Assumed tire spacing of 12 in.
l = Radius of relative stiffness computed in step 2.1.

Step 2.3. Compute the nondimensional wheel radius, a_R.

$$a_\ell = \frac{a_{eff}}{\ell} \tag{61}$$

Step 2.4. Calculate free edge stress, σ_{fe}.

$$\sigma_{fe} = \frac{3(1+\mu_{PCC})\frac{P}{2}}{\pi(3+\mu_{PCC})h_e^2}\left[\begin{array}{l} Ln\left(\frac{E_{PCC}h_e^3}{100ka_e^4}\right)+1.84-\frac{4\mu_{PCC}}{3}+\frac{1-\mu_{PCC}}{2} \\ +1.18*(1+2\mu_{PCC})*a_\ell \end{array}\right] \tag{62}$$

Step 2.5. Calculate edge support reduction factor, f_{LTE}.

This calculation is dependent on the type of edge support present. The following apply:

If *No Edge Support*, then:

$$f_{LTE} = 1 \tag{63}$$

If *Tied PCC Shoulder*, then:

$$f_{LTE} = \frac{1}{1+LTE_\sigma} \tag{64}$$

where:

LTE_σ = A chosen stress load transfer efficiency (value between 0.05 and 0.30).

If *Widened Lane*, then:

$$f_{LTE} = 0.454147 + \frac{0.013211}{D_\ell} + 0.386201\frac{a_\ell}{D_\ell} - 0.24565\left(\frac{a_\ell}{D_\ell}\right)^2 + 0.053891\left(\frac{a_\ell}{D_\ell}\right)^3 \tag{65}$$

where:

a_l = Nondimensional wheel radius (computed in step 2.3).
D_l = $42/l$.
l = Radius of relative stiffness computed in step 2.1.

Step 2.6. Compute the stress due to load, σ_{LOAD}.

$$\sigma_{LOAD} = f_{LTE}\sigma_{fe} \tag{66}$$

where:

σ_{LOAD} = Computed stress due to load, psi.
f_{LTE} = Edge support reduction factor (computed in step 2.5).
σ_{fe} = Free edge stress (computed in step 2.4).

Step 3—Compute Array of Temperature Stresses

Step 3.1. Compute the curling stress coefficient, C:

$$C = 1 - \frac{2\cos l * \cosh l}{\sin 2l + 2\sinh l * \cosh l}(\tan l + \tanh l) \tag{67}$$

where:

$$\lambda = \frac{L}{\ell\sqrt{8}} \tag{68}$$

L = Joint spacing expressed in inches.
l = Radius of relative stiffness computed in step 2.1.

Step 3.2. Compute the temperature shift factor, T_S.

$$T_s = \xi\frac{(h_e - 2)}{h_e^3} + \psi \tag{69}$$

where:

h_e = Effective thickness computed in step 1.
>, R = Temperature shift factor coefficients presented in table 25.

Step 3.3. Compute an array of temperature stresses.

For each temperature gradient (ΔT) throughout the slab thickness (from $\Delta T = -8$ °F to 34 °F in increments of 2 °F), calculate corresponding curling stress due to temperature, $(F_{TEMPERATURE})_i$.

$$(\sigma_{TEMPERATURE})_i = \frac{CE_{PCC}\alpha_{PCC}(\Delta T - T_S)_i}{2} \tag{70}$$

where:

$(F_{TEMPERATURE})_I$ = Computed curling stress (due to temperature) associated with the ith entry in the array of $\Delta T - T_S$ values.
i = Array index number equal to 1 to 22; the original ΔT array has 22 values (–8 °F to 34 °F in increments of 2 °F).
$\Delta T - T_S$ = Temperature difference.
ΔT = Temperature gradient through the slab.
T_S = Temperature shift factor computed in step 3.2, °F.
C = Curling stress coefficient computed in step 3.1.
E_{PCC} = Elastic modulus of PCC, psi.

α_{PCC} = PCC coefficient of thermal expansion, 1/°F (assumed to be 5.5 E-06).

Step 4—Compute Array of Combined Temperature and Load Stresses

Step 4.1. Compute a curling stress reduction factor (R) associated with each value in the temperature difference ($\Delta T - T_S$) array (for i = 1 to 22 values).

$$
\begin{aligned}
R_i = {} & 1.062 - 1575.68\alpha(\Delta T - T_S)_i - 0.0000876k - 0.01068\frac{L}{\ell} \\
& +387.317\alpha_{PCC}(\Delta T - T_S)_i\frac{L}{\ell} + 1.17*10^{-6}E_{PCC}k\alpha_{PCC}(\Delta T - T_S)_i \\
& -0.0181E_{PCC}k\left(\alpha_{PCC}(\Delta T - T_S)_i\right)^2 \\
& -1.051*10^{-8}E_{PCC}k\alpha_{PCC}(\Delta T - T_S)_i\left(\frac{L}{\ell}\right)^2 \\
& +1.84*10^{-3}E_{PCC}k\left(\alpha_{PCC}(\Delta T - T_S)_i\right)^2\frac{L}{\ell} - 17.487\left(\frac{L}{\ell}\right)^2\alpha_{PCC}(\Delta T - T_S)_i \\
& +3.4351*10^{10}\left(\alpha_{PCC}(\Delta T - T_S)_i\right)^3 + 8.697*10^{-5}\left(\frac{L}{\ell}\right)^3 \\
& -816396\left(\frac{L}{\ell}\right)\left(\alpha_{PCC}(\Delta T - T_S)_i\right)^2
\end{aligned}
\tag{71}
$$

where:

R_i = Computed curling stress reduction factor associated with the ith entry in the array of $\Delta T - T_S$ values.
i = Array index number equal to 1 to 22; the original ΔT array has 22 values (–8 °F to 34 °F in increments of 2 °F).
$\Delta T - T_S$ = Each value in the temperature difference array (determined in step 3).
ΔT = Temperature gradient through the slab. As stated above, there is an array of these values that goes from –8 °F to 34 °F in increments of 2 °F.
T_S = Temperature shift factor computed in step 3.2, °F.
k = Modulus of subgrade reaction (k-value), psi/in.
L = Joint spacing expressed in inches.
l = Radius of relative stiffness computed in step 2.1.
α_{PCC} = PCC coefficient of thermal expansion, 1/°F (assumed to be 5.5 E-06).
E_{PCC} = Elastic modulus of PCC, psi.

If R < 0.42 then R = 0.42 should be used.

Step 4.2. Calculate an array of combined stresses (not adjusted for presence of a base layer).

Using the arrays of temperature stresses ($\sigma_{TEMPERATURE}$ computed in step 3.3) and curling stress reduction factors (R determined in step 4.1), compute an array of associated combined stresses using the following equation (note: these combined stresses are not adjusted for the presence of the base layer):

$$(\sigma_{COMB-NOADJUST})_i = \sigma_{LOAD} + R_i(\sigma_{TEMPERATURE})_i \tag{72}$$

where:

$(F_{COMB\text{-}NOADJUST})_i$ = Computed combined load and temperature stresses (not adjusted for the presence of the base layer) associated with the ith entry in the array of $\Delta T - T_S$ values.

σ_{LOAD} = Stress due to load, psi (computed in step 2.6).

$(F_{TEMPERATURE})_i$ = Curling stress (due to temperature) associated with the ith entry in the array of $\Delta T - T_S$ values (computed in step 3.3).

R_i = Computed curling stress reduction factor associated with the ith entry in the array of $\Delta T - T_S$ values.

i = Array index number equal to 1 to 22; the original ΔT array has 22 values (–8 °F to 34 °F in increments of 2 °F).

$\Delta T - T_S$ = Each value in the temperature difference array (determined in step 3).

ΔT = Temperature gradient through the slab. As stated above, there is an array of these values that goes from –8 °F to 34 °F in increments of 2 °F.

T_S = Temperature shift factor computed in step 3.2, °F.

Step 4.3. Adjust the combined stresses (computed in step 5.2) for the presence of a base layer). The maximum PCC bending stresses should be calculated using the following relationship between the PCC and effective slab stresses:[37]

For the *unbonded* case,

$$(\sigma_{COMB})_i = \frac{h_{pcc}}{h_e}(\sigma_{COMB-NOADJUST})_i \tag{73}$$

For the *bonded* case,

$$(\sigma_{COMB})_i = \frac{h_{pcc} - x}{h_e}(\sigma_{COMB-NOADJUST})_i \tag{74}$$

where:

$(F_{COMB})_i$ = Combined load and temperature stresses (adjusted for the presence of the base layer) associated with the ith entry in the array of $\Delta T - T_S$ values.

$(F_{COMB\text{-}NOADJUST})_i$ = Combined load and temperature stresses (not adjusted for the presence of the base layer) associated with the ith entry in the array of $\Delta T - T_S$ values.

i = Array index number equal to 1 to 22; the original ΔT array has 22 values (–8 °F to 34 °F in increments of 2 °F).

$\Delta T - T_S$ = Each value in the temperature difference array (determined in step 3).

ΔT = Temperature gradient through the slab. As stated above, there is an array of these values that goes from –8 °F to 34 °F in increments of 2 °F.

T_S = Temperature shift factor computed in step 3.2, °F.

x = Distance from the top surface of the PCC layer to the neutral axis (computed in step 1).

h_{PCC} = PCC slab thickness, in.

h_e = Effective slab thickness, in (computed in step 1).

Step 5—Compute an Array of Allowable Load Repetitions

For i = 1 to 22, the following equation is used to get an array of allowable load repetitions (expressed as $Log_{10}(N)$):

$$(Log\ N)_i = 2.13\left(\frac{(\sigma_{COMB})_i}{MR_{28}}\right)^{-1.2} \tag{75}$$

where:

$(Log\ N)_i$ = *Allowable* load repetitions (expressed as a base 10 log value) associated with the ith entry in the array of $\Delta T - T_S$ values.

$(F_{COMB})_i$ = Combined load and temperature stresses (adjusted for the presence of the base layer) associated with the ith entry in the array of $\Delta T - T_S$ values (computed in step 4.3).

i = Array index number equal to 1 to 22; the original ΔT array has 22 values (–8 °F to 34 °F in increments of 2 °F).

MR_{28} = PCC modulus of rupture at 28 days, psi.

Step 6—Compute Array of Pass-to-Coverage Ratios

For i = 1 to 22, the following equations are used to get an array of pass-to-coverage (pc) ratios. The particular equation used to compute pc ratios is dependent on a computed stress ratio, SR.

Step 6.1. Compute the stress ratio, SR.

$$SR = MR_{28} / (F_{COMB})_I \tag{76}$$

where:

SR = Stress ratio.
MR_{28} = PCC modulus of rupture, psi.
$(F_{COMB})_i$ = Combined load and temperature stresses (adjusted for the presence of the base layer) associated with the ith entry in the array of $\Delta T - T_S$ values (computed in step 4.3).

Step 6.2. Compute the pass-to-coverage ratios using one of the following equations:

Case 1: If $SR_i < 0$, then:

$$pc_i = 10{,}000. \tag{77}$$

Case 2: If $SR_i > 1$, then:

$$pc_i = \left[\begin{array}{l} 416.3 - 1148.6 \dfrac{(s_{COMB})_i}{MR_{28}} + 1259.9 \left(\dfrac{(s_{COMB})_i}{MR_{28}} \right)^2 \\ - 491.55 \left(\dfrac{(s_{COMB})_i}{MR_{28}} \right)^3 \end{array} \right] (1 - WL) + 2.6 \tag{78}$$

Case 3: If $0 <= SR_i <= 1$, then:

$$pc_i = \left[\begin{array}{l} 140.2 - 172.3 \dfrac{(s_{COMB})_i}{MR_{28}} + 77.94 \left(\dfrac{(s_{COMB})_i}{MR_{28}} \right)^2 \\ - 12.04 \left(\dfrac{(s_{COMB})_i}{MR_{28}} \right)^3 \end{array} \right] (1 - WL) + 2.6 \tag{79}$$

where:

pc_i = Computed pc ratio associated with the ith entry in the array of $\Delta T - T_S$ values.
$(F_{COMB})_i$ = Combined load and temperature stresses (adjusted for the presence of the base layer) associated with the ith entry in the array of $\Delta T - T_S$ values (computed in step 4.3).
MR_{28} = PCC modulus of rupture at 28 days, psi.
WL = Presence of widened lane. If widened lanes are present, WL = 1; otherwise WL = 0.
i = Array index number equal to 1 to 22; the original ΔT array has 22 values (–8 °F to 34 °F in increments of 2 °F).

Step 7—Select the Appropriate Frequency Distribution

Step 7.1. Round the effective thickness (h_e, computed in step 1) to the nearest 0.25 in.

Step 7.2. Based on climatic region and rounded effective thickness, select the appropriate frequency distribution of temperature gradients from tables 26 through 29. Note, the selected array contains i = 1 to 22 entries that are associated with the other previously computed arrays.

Step 8—Compute Array of Actual Traffic Coverage Values

The traffic coverage of 80-kN (18-kip) ESAL load application is determined from the following equation:

$$n_i = \frac{f_i * CESAL}{pc_i} \tag{80}$$

where:

n_i = *Actual* traffic value associated with the ith entry in the array of $\Delta T - T_S$ values.
pc_i = Computed pc ratio associated with the ith entry in the array of $\Delta T - T_S$ values.
CESAL = Cumulative ESAL's.
i = Array index number equal to 1 to 22; the original ΔT array has 22 values (–8 °F to 34 °F in increments of 2 °F).

Step 9—Compute Cumulative Damage

Finally, cumulative damage is determined using the following equation:

$$FD = \sum_{i=1to22} \frac{n_i}{N_i} \tag{81}$$

where:

FD = Cumulative fatigue damage.
n_i = *Actual* traffic value associated with the ith entry in the array of $\Delta T - T_S$ values (computed in step 9).
N_i = *Allowable* load repetitions (computed as 10^[Log N]$_i$ where [Log N]$_i$ was computed in step 6) associated with the ith entry in the array of $\Delta T - T_S$ values.

This computed fatigue damage is then used in the final model (equation 55) for predicting slab cracking.

Table 26. Frequency distributions of temperature gradients for the wet-freeze region (based on rounded effective thickness).

	Rounded Effective Thickness, in																			
DT	**5.00**	**5.25**	**5.50**	**5.75**	**6.00**	**6.25**	**6.50**	**6.75**	**7.00**	**7.25**	**7.50**	**7.75**	**8.00**	**8.25**	**8.50**	**8.75**	**9.00**	**9.25**	**9.50**	**9.75**
-8	0.211	0.189	0.168	0.146	0.125	0.123	0.121	0.120	0.118	0.117	0.115	0.114	0.112	0.109	0.105	0.101	0.098	0.096	0.094	0.093
-6	0.159	0.146	0.132	0.118	0.104	0.103	0.101	0.100	0.098	0.097	0.095	0.094	0.092	0.094	0.095	0.096	0.098	0.095	0.093	0.091
-4	0.103	0.104	0.105	0.107	0.108	0.106	0.103	0.100	0.098	0.095	0.093	0.090	0.087	0.083	0.079	0.075	0.071	0.073	0.076	0.078
-2	0.085	0.079	0.073	0.067	0.061	0.061	0.061	0.062	0.062	0.062	0.062	0.062	0.062	0.063	0.064	0.065	0.067	0.067	0.067	0.068
0	0.064	0.064	0.065	0.066	0.066	0.065	0.064	0.063	0.063	0.062	0.061	0.060	0.059	0.058	0.058	0.058	0.057	0.056	0.054	0.052
2	0.053	0.050	0.047	0.044	0.041	0.040	0.040	0.039	0.038	0.037	0.037	0.036	0.035	0.035	0.035	0.035	0.035	0.036	0.036	0.036
4	0.046	0.045	0.045	0.044	0.043	0.043	0.043	0.043	0.043	0.043	0.043	0.043	0.043	0.042	0.040	0.039	0.037	0.038	0.039	0.040
6	0.064	0.060	0.057	0.053	0.050	0.048	0.046	0.045	0.043	0.041	0.040	0.038	0.036	0.037	0.038	0.038	0.039	0.037	0.034	0.032
8	0.041	0.039	0.037	0.035	0.033	0.033	0.033	0.033	0.033	0.033	0.033	0.034	0.034	0.033	0.033	0.032	0.032	0.033	0.035	0.036
10	0.056	0.053	0.049	0.045	0.041	0.041	0.040	0.039	0.039	0.038	0.038	0.037	0.036	0.036	0.035	0.035	0.034	0.033	0.032	0.031
12	0.079	0.068	0.058	0.047	0.036	0.035	0.034	0.033	0.032	0.031	0.029	0.028	0.027	0.028	0.028	0.028	0.029	0.028	0.028	0.028
14	0.010	0.021	0.032	0.043	0.054	0.052	0.051	0.049	0.048	0.046	0.045	0.043	0.042	0.039	0.037	0.035	0.033	0.033	0.033	0.034
16	0.000	0.013	0.026	0.038	0.051	0.049	0.047	0.045	0.042	0.040	0.038	0.036	0.033	0.034	0.034	0.034	0.035	0.032	0.030	0.028
18	0.000	0.001	0.002	0.002	0.003	0.008	0.013	0.018	0.023	0.028	0.033	0.038	0.043	0.042	0.041	0.040	0.039	0.039	0.039	0.039
20	0.000	0.000	0.000	0.000	0.000	0.003	0.006	0.009	0.012	0.016	0.019	0.022	0.025	0.028	0.031	0.035	0.038	0.038	0.038	0.037
22	0.000	0.000	0.000	0.000	0.000	0.000	0.000	0.000	0.000	0.000	0.000	0.000	0.000	0.001	0.003	0.004	0.005	0.009	0.013	0.017
24	0.000	0.000	0.000	0.000	0.000	0.000	0.000	0.000	0.000	0.000	0.000	0.000	0.000	0.000	0.000	0.000	0.000	0.000	0.000	0.000
26	0.000	0.000	0.000	0.000	0.000	0.000	0.000	0.000	0.000	0.000	0.000	0.000	0.000	0.000	0.000	0.000	0.000	0.000	0.000	0.000
28	0.000	0.000	0.000	0.000	0.000	0.000	0.000	0.000	0.000	0.000	0.000	0.000	0.000	0.000	0.000	0.000	0.000	0.000	0.000	0.000
30	0.000	0.000	0.000	0.000	0.000	0.000	0.000	0.000	0.000	0.000	0.000	0.000	0.000	0.000	0.000	0.000	0.000	0.000	0.000	0.000
32	0.000	0.000	0.000	0.000	0.000	0.000	0.000	0.000	0.000	0.000	0.000	0.000	0.000	0.000	0.000	0.000	0.000	0.000	0.000	0.000
34	0.000	0.000	0.000	0.000	0.000	0.000	0.000	0.000	0.000	0.000	0.000	0.000	0.000	0.000	0.000	0.000	0.000	0.000	0.000	0.000

Table 26. Frequency distributions of temperature gradients for the wet-freeze region (based on rounded effective thickness) (continued).

DT	Rounded Effective Thickness, in																				
	10.00	**10.25**	**10.50**	**10.75**	**11.00**	**11.25**	**11.50**	**11.75**	**12.00**	**12.25**	**12.50**	**12.75**	**13.00**	**13.25**	**13.50**	**13.75**	**14.00**	**14.25**	**14.50**	**14.75**	**15.00**
-8	0.091	0.090	0.088	0.086	0.084	0.083	0.081	0.079	0.077	0.077	0.076	0.075	0.075	0.074	0.073	0.072	0.072	0.072	0.072	0.073	0.073
-6	0.088	0.089	0.090	0.091	0.092	0.093	0.094	0.095	0.096	0.096	0.096	0.097	0.097	0.098	0.098	0.098	0.099	0.099	0.099	0.099	0.100
-4	0.081	0.081	0.081	0.081	0.081	0.081	0.081	0.081	0.081	0.081	0.081	0.080	0.080	0.080	0.079	0.079	0.079	0.079	0.079	0.079	0.079
-2	0.068	0.068	0.068	0.068	0.068	0.067	0.067	0.067	0.067	0.068	0.069	0.069	0.070	0.071	0.072	0.073	0.074	0.073	0.073	0.073	0.073
0	0.051	0.050	0.050	0.050	0.049	0.049	0.049	0.048	0.048	0.048	0.048	0.048	0.048	0.047	0.047	0.047	0.047	0.047	0.047	0.048	0.048
2	0.037	0.037	0.037	0.037	0.037	0.037	0.037	0.037	0.037	0.037	0.038	0.038	0.038	0.038	0.038	0.038	0.039	0.039	0.039	0.039	0.040
4	0.040	0.040	0.040	0.040	0.040	0.040	0.040	0.040	0.040	0.039	0.038	0.038	0.037	0.036	0.036	0.035	0.034	0.034	0.033	0.033	0.033
6	0.030	0.029	0.029	0.029	0.029	0.029	0.029	0.029	0.029	0.029	0.030	0.030	0.031	0.031	0.032	0.032	0.033	0.034	0.035	0.035	0.036
8	0.038	0.037	0.036	0.036	0.035	0.034	0.034	0.033	0.033	0.032	0.032	0.031	0.031	0.031	0.030	0.030	0.030	0.030	0.029	0.029	0.029
10	0.029	0.030	0.030	0.031	0.031	0.032	0.032	0.033	0.033	0.032	0.032	0.031	0.030	0.029	0.028	0.028	0.027	0.026	0.025	0.024	0.022
12	0.027	0.027	0.026	0.025	0.024	0.024	0.023	0.022	0.022	0.022	0.023	0.024	0.024	0.025	0.026	0.027	0.027	0.028	0.028	0.029	0.029
14	0.034	0.034	0.034	0.034	0.033	0.033	0.033	0.033	0.033	0.032	0.032	0.031	0.030	0.030	0.029	0.028	0.028	0.027	0.027	0.027	0.027
16	0.026	0.026	0.026	0.025	0.025	0.025	0.024	0.024	0.024	0.024	0.025	0.026	0.026	0.027	0.028	0.028	0.029	0.028	0.027	0.026	0.026
18	0.039	0.038	0.037	0.037	0.036	0.036	0.035	0.035	0.034	0.033	0.032	0.031	0.030	0.029	0.028	0.027	0.027	0.028	0.029	0.030	0.031
20	0.037	0.037	0.036	0.036	0.035	0.035	0.034	0.034	0.034	0.034	0.034	0.034	0.034	0.034	0.034	0.034	0.035	0.034	0.033	0.032	0.031
22	0.021	0.022	0.024	0.025	0.026	0.027	0.029	0.030	0.031	0.031	0.030	0.030	0.029	0.028	0.028	0.027	0.027	0.027	0.027	0.027	0.027
24	0.000	0.001	0.003	0.004	0.005	0.007	0.008	0.009	0.010	0.012	0.014	0.015	0.017	0.018	0.020	0.021	0.023	0.023	0.023	0.024	0.024
26	0.000	0.000	0.000	0.000	0.000	0.000	0.000	0.000	0.000	0.000	0.000	0.000	0.000	0.000	0.000	0.000	0.001	0.001	0.001	0.001	0.001
28	0.000	0.000	0.000	0.000	0.000	0.000	0.000	0.000	0.000	0.000	0.000	0.000	0.000	0.000	0.000	0.000	0.000	0.000	0.000	0.000	0.000
30	0.000	0.000	0.000	0.000	0.000	0.000	0.000	0.000	0.000	0.000	0.000	0.000	0.000	0.000	0.000	0.000	0.000	0.000	0.000	0.000	0.000
32	0.000	0.000	0.000	0.000	0.000	0.000	0.000	0.000	0.000	0.000	0.000	0.000	0.000	0.000	0.000	0.000	0.000	0.000	0.000	0.000	0.000
34	0.000	0.000	0.000	0.000	0.000	0.000	0.000	0.000	0.000	0.000	0.000	0.000	0.000	0.000	0.000	0.000	0.000	0.000	0.000	0.000	0.000

Table 27. Frequency distributions of temperature gradients for the wet-nonfreeze region (based on rounded effective thickness).

	Rounded Effective Thickness, in																			
DT	**5.00**	**5.25**	**5.50**	**5.75**	**6.00**	**6.25**	**6.50**	**6.75**	**7.00**	**7.25**	**7.50**	**7.75**	**8.00**	**8.25**	**8.50**	**8.75**	**9.00**	**9.25**	**9.50**	**9.75**
-8	0.211	0.188	0.164	0.141	0.118	0.116	0.114	0.112	0.110	0.107	0.105	0.103	0.101	0.098	0.095	0.092	0.089	0.086	0.083	0.079
-6	0.145	0.134	0.123	0.113	0.102	0.099	0.096	0.093	0.090	0.087	0.084	0.081	0.078	0.077	0.075	0.073	0.071	0.072	0.073	0.075
-4	0.106	0.095	0.083	0.071	0.059	0.059	0.059	0.058	0.058	0.057	0.057	0.056	0.056	0.055	0.054	0.053	0.053	0.052	0.052	0.051
-2	0.041	0.039	0.037	0.035	0.034	0.034	0.034	0.034	0.034	0.034	0.033	0.033	0.033	0.035	0.036	0.037	0.038	0.040	0.041	0.043
0	0.037	0.039	0.040	0.042	0.043	0.041	0.039	0.037	0.035	0.033	0.031	0.029	0.027	0.026	0.026	0.026	0.026	0.026	0.025	0.025
2	0.051	0.046	0.040	0.035	0.029	0.029	0.030	0.030	0.030	0.030	0.030	0.030	0.030	0.030	0.030	0.030	0.030	0.031	0.031	0.031
4	0.029	0.029	0.028	0.028	0.028	0.029	0.030	0.031	0.032	0.034	0.035	0.036	0.037	0.038	0.038	0.038	0.039	0.037	0.035	0.033
6	0.047	0.046	0.044	0.043	0.042	0.039	0.037	0.035	0.032	0.030	0.027	0.025	0.023	0.022	0.022	0.021	0.020	0.022	0.023	0.024
8	0.048	0.041	0.034	0.028	0.021	0.021	0.020	0.020	0.020	0.020	0.020	0.019	0.019	0.019	0.019	0.019	0.018	0.019	0.019	0.020
10	0.069	0.062	0.054	0.047	0.040	0.040	0.041	0.041	0.042	0.042	0.042	0.043	0.043	0.041	0.039	0.037	0.035	0.034	0.033	0.031
12	0.064	0.060	0.056	0.052	0.048	0.045	0.042	0.039	0.037	0.034	0.031	0.028	0.026	0.027	0.028	0.029	0.031	0.030	0.030	0.029
14	0.071	0.066	0.061	0.056	0.052	0.050	0.049	0.048	0.046	0.045	0.044	0.042	0.041	0.039	0.037	0.035	0.033	0.034	0.035	0.036
16	0.000	0.012	0.025	0.037	0.050	0.049	0.049	0.048	0.048	0.047	0.046	0.046	0.045	0.045	0.044	0.044	0.044	0.041	0.039	0.036
18	0.000	0.016	0.032	0.047	0.063	0.060	0.057	0.055	0.052	0.049	0.046	0.044	0.041	0.041	0.041	0.040	0.040	0.041	0.043	0.044
20	0.000	0.002	0.004	0.007	0.009	0.013	0.018	0.022	0.027	0.031	0.036	0.040	0.045	0.043	0.042	0.040	0.039	0.038	0.036	0.035
22	0.000	0.000	0.000	0.000	0.000	0.006	0.011	0.017	0.022	0.028	0.033	0.039	0.044	0.045	0.046	0.046	0.047	0.046	0.045	0.044
24	0.000	0.000	0.000	0.000	0.000	0.000	0.000	0.000	0.000	0.000	0.000	0.000	0.000	0.005	0.011	0.016	0.021	0.025	0.029	0.033
26	0.000	0.000	0.000	0.000	0.000	0.000	0.000	0.000	0.000	0.000	0.000	0.000	0.000	0.000	0.000	0.000	0.000	0.001	0.001	0.002
28	0.000	0.000	0.000	0.000	0.000	0.000	0.000	0.000	0.000	0.000	0.000	0.000	0.000	0.000	0.000	0.000	0.000	0.000	0.000	0.000
30	0.000	0.000	0.000	0.000	0.000	0.000	0.000	0.000	0.000	0.000	0.000	0.000	0.000	0.000	0.000	0.000	0.000	0.000	0.000	0.000
32	0.000	0.000	0.000	0.000	0.000	0.000	0.000	0.000	0.000	0.000	0.000	0.000	0.000	0.000	0.000	0.000	0.000	0.000	0.000	0.000
34	0.000	0.000	0.000	0.000	0.000	0.000	0.000	0.000	0.000	0.000	0.000	0.000	0.000	0.000	0.000	0.000	0.000	0.000	0.000	0.000

Table 27. Frequency distributions of temperature gradients for the wet-nonfreeze region (based on rounded effective thickness) (continued).

DT	Rounded Effective Thickness, in																				
	10.00	**10.25**	**10.50**	**10.75**	**11.00**	**11.25**	**11.50**	**11.75**	**12.00**	**12.25**	**12.50**	**12.75**	**13.00**	**13.25**	**13.50**	**13.75**	**14.00**	**14.25**	**14.50**	**14.75**	**15.00**
-8	0.076	0.076	0.076	0.077	0.077	0.077	0.078	0.078	0.078	0.079	0.080	0.081	0.082	0.083	0.084	0.085	0.085	0.085	0.085	0.085	0.084
-6	0.076	0.075	0.074	0.073	0.072	0.071	0.070	0.069	0.069	0.068	0.067	0.066	0.066	0.065	0.064	0.064	0.063	0.064	0.065	0.066	0.067
-4	0.051	0.051	0.051	0.051	0.051	0.052	0.052	0.052	0.052	0.052	0.051	0.050	0.050	0.049	0.048	0.048	0.047	0.046	0.045	0.044	0.043
-2	0.045	0.043	0.042	0.041	0.040	0.039	0.038	0.037	0.036	0.038	0.039	0.041	0.042	0.044	0.045	0.047	0.048	0.049	0.051	0.052	0.053
0	0.024	0.027	0.029	0.031	0.034	0.036	0.038	0.041	0.043	0.043	0.042	0.042	0.042	0.042	0.041	0.041	0.041	0.039	0.037	0.035	0.033
2	0.031	0.031	0.031	0.030	0.030	0.030	0.029	0.029	0.029	0.030	0.030	0.031	0.032	0.033	0.034	0.034	0.035	0.037	0.039	0.041	0.043
4	0.031	0.031	0.030	0.030	0.029	0.028	0.028	0.027	0.027	0.027	0.027	0.027	0.027	0.027	0.027	0.027	0.027	0.028	0.028	0.028	0.029
6	0.026	0.025	0.023	0.022	0.021	0.020	0.019	0.018	0.017	0.017	0.017	0.016	0.016	0.016	0.016	0.016	0.016	0.016	0.017	0.017	0.017
8	0.020	0.022	0.023	0.025	0.027	0.029	0.030	0.032	0.034	0.033	0.033	0.032	0.031	0.031	0.030	0.029	0.029	0.028	0.028	0.027	0.027
10	0.030	0.029	0.028	0.028	0.027	0.026	0.026	0.025	0.024	0.025	0.026	0.027	0.028	0.029	0.030	0.030	0.031	0.030	0.029	0.029	0.028
12	0.029	0.028	0.027	0.025	0.024	0.023	0.022	0.021	0.020	0.020	0.020	0.020	0.020	0.020	0.020	0.020	0.020	0.021	0.022	0.023	0.024
14	0.037	0.037	0.038	0.038	0.039	0.039	0.039	0.040	0.040	0.040	0.039	0.039	0.038	0.038	0.037	0.037	0.036	0.036	0.036	0.036	0.036
16	0.034	0.034	0.034	0.034	0.034	0.033	0.033	0.033	0.033	0.033	0.033	0.032	0.032	0.032	0.031	0.031	0.031	0.030	0.030	0.030	0.029
18	0.045	0.044	0.042	0.040	0.038	0.037	0.035	0.033	0.032	0.032	0.032	0.032	0.033	0.033	0.033	0.034	0.034	0.034	0.035	0.035	0.036
20	0.034	0.035	0.036	0.038	0.039	0.040	0.041	0.042	0.044	0.043	0.042	0.041	0.041	0.040	0.039	0.039	0.038	0.037	0.037	0.037	0.036
22	0.043	0.041	0.040	0.038	0.037	0.035	0.034	0.032	0.031	0.031	0.032	0.033	0.033	0.034	0.035	0.035	0.036	0.036	0.035	0.035	0.035
24	0.036	0.037	0.038	0.039	0.040	0.040	0.041	0.042	0.043	0.041	0.040	0.039	0.037	0.036	0.035	0.034	0.032	0.033	0.033	0.033	0.034
26	0.003	0.005	0.007	0.010	0.012	0.015	0.017	0.020	0.022	0.024	0.025	0.026	0.027	0.028	0.029	0.031	0.032	0.032	0.033	0.033	0.033
28	0.000	0.000	0.000	0.000	0.000	0.000	0.000	0.000	0.000	0.001	0.002	0.003	0.004	0.005	0.006	0.006	0.007	0.008	0.008	0.008	0.009
30	0.000	0.000	0.000	0.000	0.000	0.000	0.000	0.000	0.000	0.000	0.000	0.000	0.000	0.000	0.000	0.000	0.000	0.000	0.000	0.000	0.000
32	0.000	0.000	0.000	0.000	0.000	0.000	0.000	0.000	0.000	0.000	0.000	0.000	0.000	0.000	0.000	0.000	0.000	0.000	0.000	0.000	0.000
34	0.000	0.000	0.000	0.000	0.000	0.000	0.000	0.000	0.000	0.000	0.000	0.000	0.000	0.000	0.000	0.000	0.000	0.000	0.000	0.000	0.000

Table 28. Frequency distributions of temperature gradients for the dry-freeze region (based on rounded effective thickness).

	Rounded Effective Thickness, in																			
DT	**5.00**	**5.25**	**5.50**	**5.75**	**6.00**	**6.25**	**6.50**	**6.75**	**7.00**	**7.25**	**7.50**	**7.75**	**8.00**	**8.25**	**8.50**	**8.75**	**9.00**	**9.25**	**9.50**	**9.75**
-8	0.205	0.188	0.172	0.156	0.140	0.135	0.130	0.125	0.121	0.116	0.111	0.106	0.101	0.098	0.095	0.092	0.088	0.088	0.088	0.088
-6	0.170	0.150	0.130	0.110	0.090	0.089	0.089	0.089	0.089	0.088	0.088	0.088	0.088	0.089	0.090	0.091	0.092	0.091	0.090	0.090
-4	0.124	0.121	0.118	0.116	0.113	0.109	0.105	0.102	0.098	0.095	0.091	0.087	0.084	0.081	0.079	0.077	0.074	0.074	0.075	0.075
-2	0.073	0.067	0.061	0.055	0.048	0.049	0.050	0.051	0.052	0.053	0.054	0.055	0.056	0.056	0.056	0.057	0.057	0.056	0.055	0.054
0	0.070	0.068	0.066	0.064	0.062	0.062	0.062	0.062	0.061	0.061	0.061	0.061	0.061	0.061	0.061	0.061	0.061	0.060	0.059	0.058
2	0.051	0.050	0.049	0.047	0.046	0.045	0.043	0.042	0.040	0.039	0.038	0.036	0.035	0.034	0.033	0.032	0.031	0.032	0.033	0.034
4	0.053	0.048	0.043	0.038	0.033	0.033	0.034	0.034	0.034	0.034	0.034	0.034	0.035	0.035	0.035	0.035	0.036	0.036	0.037	0.037
6	0.061	0.060	0.059	0.058	0.057	0.055	0.053	0.052	0.050	0.048	0.046	0.045	0.043	0.043	0.043	0.043	0.043	0.040	0.037	0.035
8	0.043	0.040	0.037	0.034	0.031	0.031	0.031	0.031	0.032	0.032	0.032	0.032	0.032	0.032	0.031	0.030	0.029	0.031	0.033	0.034
10	0.055	0.052	0.048	0.045	0.041	0.041	0.042	0.042	0.042	0.042	0.043	0.043	0.043	0.042	0.040	0.039	0.037	0.036	0.035	0.034
12	0.080	0.070	0.060	0.049	0.039	0.037	0.034	0.032	0.029	0.026	0.024	0.021	0.019	0.020	0.022	0.024	0.026	0.025	0.024	0.023
14	0.003	0.013	0.023	0.034	0.044	0.045	0.045	0.045	0.045	0.046	0.046	0.046	0.047	0.044	0.041	0.039	0.036	0.036	0.037	0.037
16	0.000	0.016	0.032	0.048	0.064	0.060	0.055	0.051	0.046	0.042	0.037	0.033	0.028	0.029	0.029	0.029	0.030	0.028	0.026	0.024
18	0.000	0.001	0.001	0.002	0.003	0.008	0.013	0.017	0.022	0.027	0.032	0.037	0.042	0.039	0.037	0.034	0.032	0.032	0.033	0.033
20	0.000	0.000	0.000	0.000	0.000	0.004	0.009	0.013	0.017	0.022	0.026	0.030	0.034	0.039	0.043	0.047	0.051	0.049	0.046	0.044
22	0.000	0.000	0.000	0.000	0.000	0.000	0.000	0.000	0.000	0.000	0.000	0.000	0.000	0.002	0.004	0.005	0.007	0.013	0.018	0.024
24	0.000	0.000	0.000	0.000	0.000	0.000	0.000	0.000	0.000	0.000	0.000	0.000	0.000	0.000	0.000	0.000	0.000	0.000	0.000	0.000
26	0.000	0.000	0.000	0.000	0.000	0.000	0.000	0.000	0.000	0.000	0.000	0.000	0.000	0.000	0.000	0.000	0.000	0.000	0.000	0.000
28	0.000	0.000	0.000	0.000	0.000	0.000	0.000	0.000	0.000	0.000	0.000	0.000	0.000	0.000	0.000	0.000	0.000	0.000	0.000	0.000
30	0.000	0.000	0.000	0.000	0.000	0.000	0.000	0.000	0.000	0.000	0.000	0.000	0.000	0.000	0.000	0.000	0.000	0.000	0.000	0.000
32	0.000	0.000	0.000	0.000	0.000	0.000	0.000	0.000	0.000	0.000	0.000	0.000	0.000	0.000	0.000	0.000	0.000	0.000	0.000	0.000
34	0.000	0.000	0.000	0.000	0.000	0.000	0.000	0.000	0.000	0.000	0.000	0.000	0.000	0.000	0.000	0.000	0.000	0.000	0.000	0.000

Table 28. Frequency distributions of temperature gradients for the dry-freeze region (based on rounded effective thickness) (continued).

DT	Rounded Effective Thickness, in																				
	10.00	**10.25**	**10.50**	**10.75**	**11.00**	**11.25**	**11.50**	**11.75**	**12.00**	**12.25**	**12.50**	**12.75**	**13.00**	**13.25**	**13.50**	**13.75**	**14.00**	**14.25**	**14.50**	**14.75**	**15.00**
-8	0.088	0.086	0.085	0.083	0.081	0.080	0.078	0.077	0.075	0.075	0.074	0.074	0.074	0.074	0.073	0.073	0.073	0.073	0.074	0.075	0.076
-6	0.089	0.090	0.091	0.092	0.093	0.094	0.095	0.096	0.097	0.096	0.096	0.096	0.095	0.095	0.094	0.094	0.094	0.093	0.092	0.091	0.090
-4	0.076	0.075	0.074	0.073	0.073	0.072	0.071	0.071	0.070	0.070	0.071	0.071	0.071	0.072	0.072	0.073	0.073	0.073	0.073	0.073	0.073
-2	0.053	0.054	0.056	0.057	0.058	0.060	0.061	0.062	0.064	0.063	0.063	0.063	0.063	0.062	0.062	0.062	0.061	0.062	0.063	0.064	0.065
0	0.058	0.057	0.056	0.055	0.054	0.053	0.052	0.051	0.051	0.052	0.053	0.054	0.055	0.056	0.057	0.058	0.059	0.059	0.059	0.059	0.058
2	0.035	0.035	0.036	0.036	0.036	0.036	0.036	0.036	0.037	0.036	0.035	0.034	0.034	0.033	0.032	0.032	0.031	0.031	0.030	0.030	0.030
4	0.038	0.038	0.038	0.037	0.037	0.037	0.037	0.037	0.037	0.036	0.036	0.036	0.036	0.036	0.036	0.036	0.036	0.037	0.037	0.037	0.038
6	0.032	0.032	0.032	0.032	0.032	0.033	0.033	0.033	0.033	0.033	0.033	0.033	0.034	0.034	0.034	0.034	0.034	0.034	0.034	0.033	0.033
8	0.036	0.035	0.035	0.034	0.033	0.032	0.031	0.030	0.030	0.029	0.029	0.029	0.029	0.029	0.029	0.029	0.029	0.030	0.032	0.034	0.035
10	0.033	0.034	0.034	0.034	0.035	0.035	0.035	0.036	0.036	0.035	0.035	0.034	0.033	0.032	0.031	0.031	0.030	0.028	0.026	0.023	0.021
12	0.022	0.022	0.021	0.021	0.020	0.020	0.019	0.019	0.018	0.019	0.020	0.021	0.021	0.022	0.023	0.024	0.024	0.025	0.026	0.027	0.028
14	0.037	0.037	0.036	0.036	0.036	0.035	0.035	0.035	0.034	0.034	0.033	0.033	0.033	0.032	0.032	0.032	0.031	0.030	0.030	0.029	0.028
16	0.023	0.023	0.023	0.023	0.023	0.023	0.023	0.023	0.023	0.022	0.022	0.022	0.022	0.022	0.022	0.021	0.021	0.021	0.021	0.020	0.020
18	0.033	0.033	0.033	0.033	0.032	0.032	0.032	0.032	0.032	0.031	0.031	0.031	0.031	0.031	0.031	0.030	0.030	0.031	0.031	0.031	0.032
20	0.042	0.040	0.039	0.037	0.036	0.034	0.032	0.031	0.029	0.029	0.028	0.027	0.027	0.026	0.025	0.025	0.024	0.023	0.022	0.021	0.021
22	0.030	0.031	0.032	0.034	0.035	0.037	0.038	0.040	0.041	0.040	0.038	0.037	0.036	0.034	0.033	0.032	0.030	0.031	0.032	0.033	0.034
24	0.000	0.002	0.004	0.005	0.007	0.009	0.011	0.013	0.014	0.017	0.020	0.023	0.026	0.028	0.031	0.034	0.037	0.037	0.036	0.036	0.036
26	0.000	0.000	0.000	0.000	0.000	0.000	0.000	0.000	0.000	0.000	0.000	0.000	0.000	0.000	0.000	0.000	0.000	0.001	0.001	0.001	0.001
28	0.000	0.000	0.000	0.000	0.000	0.000	0.000	0.000	0.000	0.000	0.000	0.000	0.000	0.000	0.000	0.000	0.000	0.000	0.000	0.000	0.000
30	0.000	0.000	0.000	0.000	0.000	0.000	0.000	0.000	0.000	0.000	0.000	0.000	0.000	0.000	0.000	0.000	0.000	0.000	0.000	0.000	0.000
32	0.000	0.000	0.000	0.000	0.000	0.000	0.000	0.000	0.000	0.000	0.000	0.000	0.000	0.000	0.000	0.000	0.000	0.000	0.000	0.000	0.000
34	0.000	0.000	0.000	0.000	0.000	0.000	0.000	0.000	0.000	0.000	0.000	0.000	0.000	0.000	0.000	0.000	0.000	0.000	0.000	0.000	0.000

Table 29. Frequency distributions of temperature gradients for the dry-nonfreeze region (based on rounded effective thickness).

	Rounded Effective Thickness, in																			
DT	**5.00**	**5.25**	**5.50**	**5.75**	**6.00**	**6.25**	**6.50**	**6.75**	**7.00**	**7.25**	**7.50**	**7.75**	**8.00**	**8.25**	**8.50**	**8.75**	**9.00**	**9.25**	**9.50**	**9.75**
-8	0.128	0.121	0.113	0.105	0.098	0.095	0.093	0.090	0.088	0.085	0.083	0.080	0.078	0.079	0.081	0.083	0.085	0.083	0.080	0.078
-6	0.125	0.116	0.108	0.099	0.091	0.088	0.085	0.082	0.079	0.075	0.072	0.069	0.066	0.065	0.064	0.063	0.062	0.062	0.063	0.063
-4	0.092	0.086	0.080	0.073	0.067	0.067	0.067	0.067	0.067	0.067	0.067	0.067	0.067	0.064	0.061	0.058	0.055	0.056	0.057	0.058
-2	0.057	0.051	0.044	0.038	0.032	0.033	0.034	0.035	0.036	0.037	0.038	0.039	0.040	0.041	0.042	0.043	0.045	0.043	0.042	0.041
0	0.035	0.035	0.036	0.037	0.038	0.037	0.036	0.035	0.033	0.032	0.031	0.030	0.028	0.029	0.029	0.029	0.030	0.030	0.031	0.031
2	0.044	0.041	0.039	0.037	0.034	0.033	0.032	0.030	0.029	0.028	0.026	0.025	0.024	0.024	0.024	0.024	0.024	0.024	0.024	0.025
4	0.031	0.028	0.025	0.022	0.019	0.021	0.022	0.023	0.024	0.025	0.026	0.028	0.029	0.028	0.027	0.026	0.025	0.025	0.026	0.026
6	0.039	0.037	0.036	0.035	0.033	0.032	0.031	0.031	0.030	0.029	0.028	0.027	0.026	0.027	0.028	0.028	0.029	0.026	0.024	0.021
8	0.044	0.040	0.036	0.032	0.028	0.026	0.024	0.023	0.021	0.019	0.018	0.016	0.014	0.014	0.014	0.014	0.014	0.017	0.020	0.022
10	0.050	0.044	0.038	0.032	0.026	0.027	0.027	0.028	0.028	0.028	0.029	0.029	0.030	0.029	0.027	0.026	0.025	0.024	0.024	0.023
12	0.064	0.060	0.056	0.052	0.047	0.046	0.045	0.044	0.043	0.041	0.040	0.039	0.038	0.037	0.036	0.035	0.035	0.033	0.031	0.029
14	0.069	0.061	0.053	0.045	0.037	0.036	0.034	0.033	0.031	0.030	0.028	0.027	0.025	0.026	0.027	0.028	0.028	0.030	0.032	0.034
16	0.035	0.037	0.039	0.042	0.044	0.044	0.044	0.044	0.044	0.044	0.044	0.045	0.045	0.043	0.041	0.039	0.038	0.037	0.036	0.035
18	0.000	0.013	0.026	0.039	0.052	0.049	0.047	0.045	0.042	0.040	0.038	0.035	0.033	0.034	0.036	0.037	0.039	0.035	0.032	0.028
20	0.000	0.015	0.030	0.045	0.060	0.057	0.055	0.052	0.050	0.047	0.044	0.042	0.039	0.038	0.036	0.035	0.033	0.035	0.037	0.039
22	0.000	0.000	0.000	0.000	0.000	0.005	0.011	0.016	0.022	0.027	0.033	0.038	0.044	0.040	0.036	0.032	0.028	0.028	0.028	0.028
24	0.000	0.000	0.000	0.000	0.000	0.005	0.010	0.015	0.019	0.024	0.029	0.034	0.039	0.040	0.040	0.041	0.042	0.043	0.044	0.045
26	0.000	0.000	0.000	0.000	0.000	0.000	0.000	0.000	0.000	0.000	0.000	0.000	0.000	0.007	0.014	0.021	0.028	0.030	0.032	0.034
28	0.000	0.000	0.000	0.000	0.000	0.000	0.000	0.000	0.000	0.000	0.000	0.000	0.000	0.000	0.000	0.000	0.000	0.000	0.000	0.000
30	0.000	0.000	0.000	0.000	0.000	0.000	0.000	0.000	0.000	0.000	0.000	0.000	0.000	0.000	0.000	0.000	0.000	0.000	0.000	0.000
32	0.000	0.000	0.000	0.000	0.000	0.000	0.000	0.000	0.000	0.000	0.000	0.000	0.000	0.000	0.000	0.000	0.000	0.000	0.000	0.000
34	0.000	0.000	0.000	0.000	0.000	0.000	0.000	0.000	0.000	0.000	0.000	0.000	0.000	0.000	0.000	0.000	0.000	0.000	0.000	0.000

Table 29. Frequency distributions of temperature gradients for the dry-nonfreeze region (based on rounded effective thickness) (continued).

	Rounded Effective Thickness, in																				
DT	**10.00**	**10.25**	**10.50**	**10.75**	**11.00**	**11.25**	**11.50**	**11.75**	**12.00**	**12.25**	**12.50**	**12.75**	**13.00**	**13.25**	**13.50**	**13.75**	**14.00**	**14.25**	**14.50**	**14.75**	**15.00**
-8	0.076	0.075	0.074	0.072	0.071	0.070	0.069	0.068	0.066	0.066	0.065	0.064	0.063	0.062	0.062	0.061	0.060	0.061	0.063	0.064	0.065
-6	0.063	0.064	0.064	0.065	0.066	0.066	0.067	0.067	0.068	0.069	0.070	0.071	0.072	0.073	0.074	0.075	0.076	0.074	0.072	0.071	0.069
-4	0.059	0.059	0.059	0.059	0.059	0.058	0.058	0.058	0.058	0.057	0.055	0.054	0.052	0.051	0.049	0.048	0.046	0.046	0.046	0.045	0.045
-2	0.039	0.039	0.039	0.038	0.038	0.038	0.038	0.038	0.037	0.038	0.038	0.039	0.040	0.040	0.041	0.041	0.042	0.044	0.046	0.048	0.051
0	0.032	0.032	0.032	0.032	0.032	0.032	0.032	0.032	0.032	0.032	0.033	0.033	0.034	0.034	0.034	0.035	0.035	0.034	0.034	0.033	0.032
2	0.025	0.026	0.028	0.029	0.030	0.032	0.033	0.034	0.036	0.036	0.036	0.036	0.036	0.035	0.035	0.035	0.035	0.036	0.037	0.037	0.038
4	0.026	0.025	0.025	0.024	0.023	0.023	0.022	0.021	0.021	0.021	0.022	0.022	0.023	0.023	0.024	0.024	0.025	0.025	0.026	0.026	0.026
6	0.018	0.017	0.017	0.016	0.015	0.014	0.014	0.013	0.012	0.012	0.013	0.013	0.013	0.013	0.013	0.014	0.014	0.014	0.014	0.014	0.014
8	0.025	0.025	0.025	0.025	0.025	0.025	0.025	0.025	0.025	0.024	0.024	0.024	0.024	0.023	0.023	0.023	0.023	0.023	0.023	0.023	0.023
10	0.022	0.024	0.026	0.027	0.029	0.030	0.032	0.034	0.035	0.034	0.033	0.032	0.031	0.030	0.029	0.028	0.027	0.027	0.026	0.026	0.026
12	0.027	0.025	0.024	0.022	0.021	0.019	0.018	0.016	0.015	0.016	0.017	0.019	0.020	0.021	0.022	0.024	0.025	0.024	0.024	0.023	0.023
14	0.036	0.035	0.034	0.033	0.032	0.031	0.030	0.029	0.028	0.028	0.028	0.028	0.027	0.027	0.027	0.027	0.026	0.027	0.028	0.029	0.030
16	0.034	0.034	0.034	0.034	0.034	0.035	0.035	0.035	0.035	0.034	0.034	0.033	0.032	0.032	0.031	0.031	0.030	0.030	0.030	0.030	0.030
18	0.025	0.025	0.025	0.026	0.026	0.026	0.027	0.027	0.027	0.027	0.027	0.027	0.026	0.026	0.026	0.026	0.026	0.025	0.024	0.024	0.023
20	0.041	0.040	0.039	0.038	0.036	0.035	0.034	0.033	0.031	0.032	0.033	0.034	0.035	0.036	0.037	0.038	0.039	0.039	0.040	0.041	0.041
22	0.027	0.029	0.031	0.032	0.034	0.036	0.037	0.039	0.041	0.039	0.037	0.035	0.033	0.032	0.030	0.028	0.026	0.026	0.025	0.025	0.024
24	0.046	0.044	0.042	0.040	0.038	0.035	0.033	0.031	0.029	0.030	0.031	0.032	0.033	0.034	0.036	0.037	0.038	0.037	0.037	0.037	0.036
26	0.036	0.036	0.035	0.035	0.035	0.034	0.034	0.033	0.033	0.032	0.031	0.029	0.028	0.027	0.026	0.024	0.023	0.023	0.024	0.024	0.024
28	0.000	0.004	0.007	0.011	0.015	0.018	0.022	0.025	0.029	0.030	0.031	0.032	0.033	0.034	0.035	0.036	0.037	0.037	0.036	0.036	0.036
30	0.000	0.000	0.000	0.000	0.000	0.000	0.000	0.000	0.000	0.001	0.002	0.003	0.005	0.006	0.007	0.008	0.009	0.010	0.011	0.011	0.012
32	0.000	0.000	0.000	0.000	0.000	0.000	0.000	0.000	0.000	0.000	0.000	0.000	0.000	0.000	0.000	0.000	0.000	0.000	0.000	0.000	0.000
34	0.000	0.000	0.000	0.000	0.000	0.000	0.000	0.000	0.000	0.000	0.000	0.000	0.000	0.000	0.000	0.000	0.000	0.000	0.000	0.000	0.000

MODEL VERIFICATION (SENSITIVITY ANALYSIS)

A sensitivity analysis was conducted on the final transverse cracking model to determine its reliability for predicting cracking within and outside of the inference space of the development database. This was accomplished by studying the effects of the various input parameters on the output generated by the cracking model. Note that the sensitivity analyses were accomplished by investigating the effects of changing one variable at a time, while holding all other variables constant.

Effect of Material- and Design-Related Factors

The material- and design-related factors that were incorporated into the final slab cracking model included PCC slab thickness, PCC flexural strength, PCC modulus of elasticity, PCC joint spacing, base type and thickness, and PCC slab edge support (shoulder type and presence of a widened lane). The sensitivity of the final cracking model to each of these variables is discussed separately in the following sections.

Effect of PCC Slab Thickness

Figure 25 shows that transverse slab cracking increases as slab thickness decreases. This trend is expected because a thicker slab exhibits much lower stresses than a thinner slab under the same site conditions assuming that all other design parameters are the same. This sensitivity indicates that PCC slab thickness is one of the most important parameters that should be controlled during construction.

Effect of PCC Flexural Strength

Figure 26 illustrates the sensitivity of the final JPCP transverse slab cracking model to changes in PCC compressive strength. The figure clearly shows that an increase in PCC flexural strength represented by the modulus of rupture results in a reduction in slab cracking. This trend is in agreement with the mechanistic principle that a concrete slab with higher flexural strength has lower fatigue damage than a corresponding slab with lower strength under the same level of bending stresses. However, it should be noted that in some cases, increased slab cracking has been associated with increased concrete strength due to an increase in drying shrinkage from additional cement in the mix. Mix design must be done properly to avoid high shrinkage for higher strengths.

Effect of PCC Modulus of Elasticity

Figure 27 shows that transverse slab cracking increases as PCC modulus of elasticity increases. Although this trend is expected because an increase in PCC modulus leads to an increase in maximum PCC bending stresses, this figure is somewhat misleading. An increase in PCC modulus will also increase PCC flexural strength. Figure 28 presents a comparison of predicted slab cracking for different values of PCC modulus

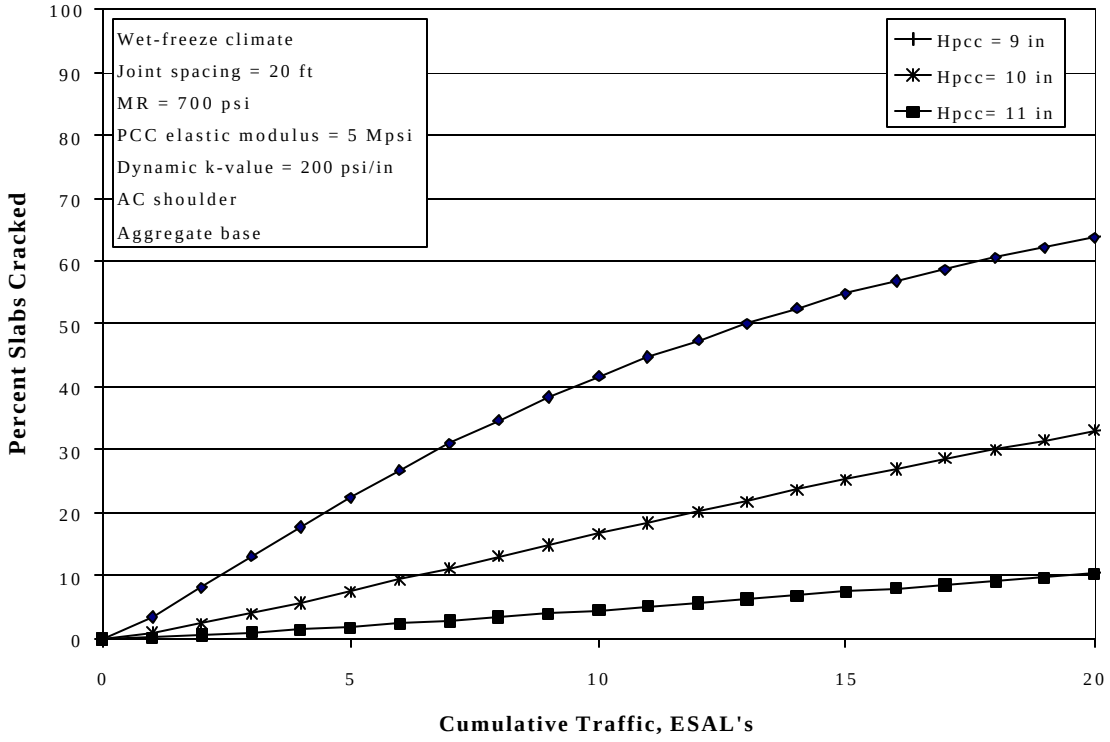

Figure 25. Sensitivity of the final JPCP transverse slab cracking model to changes in PCC slab thickness.

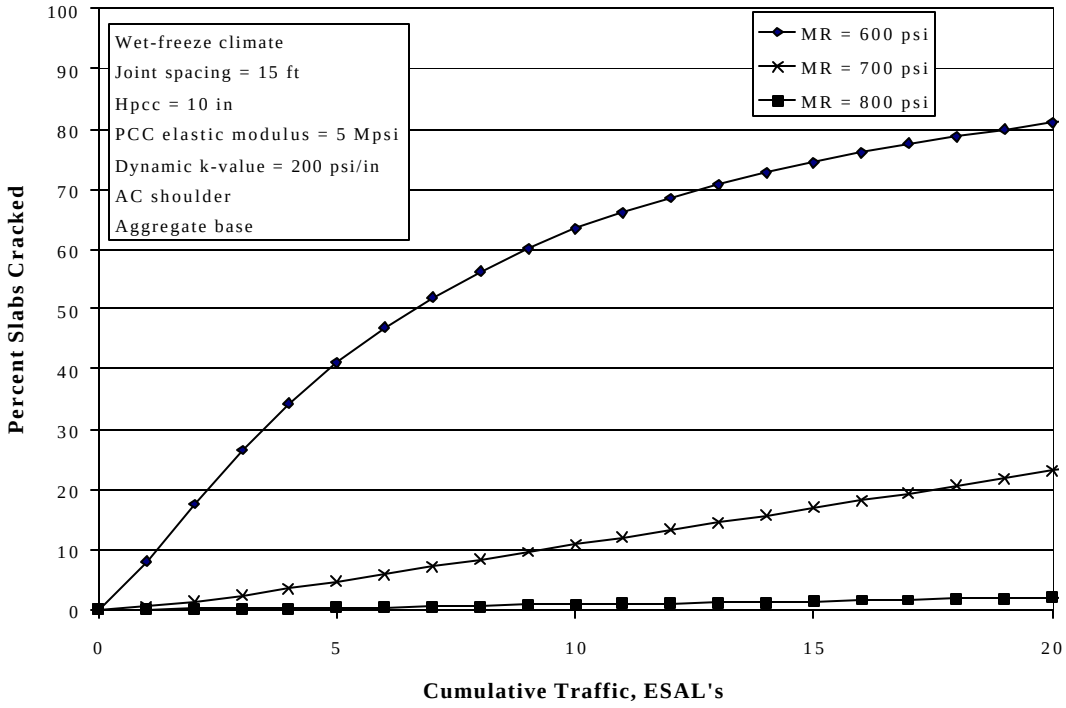

Figure 26. Sensitivity of the final JPCP transverse slab cracking model to changes in PCC flexural strength.

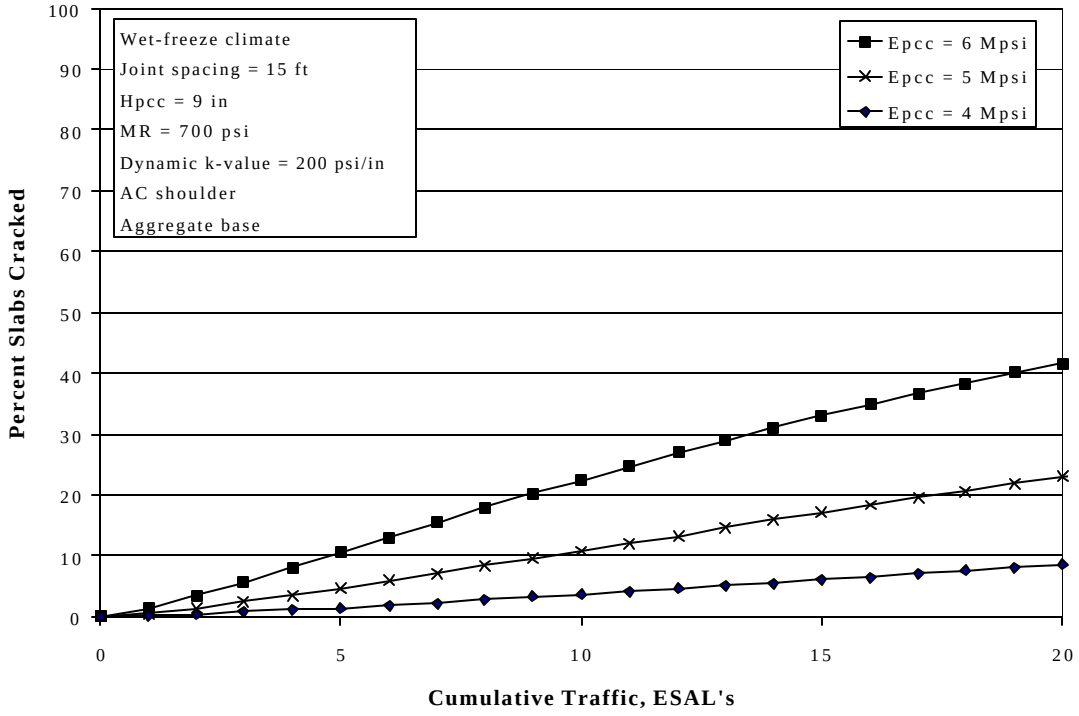

Figure 27. Sensitivity of the final JPCP transverse cracking model to changes in modulus of elasticity.

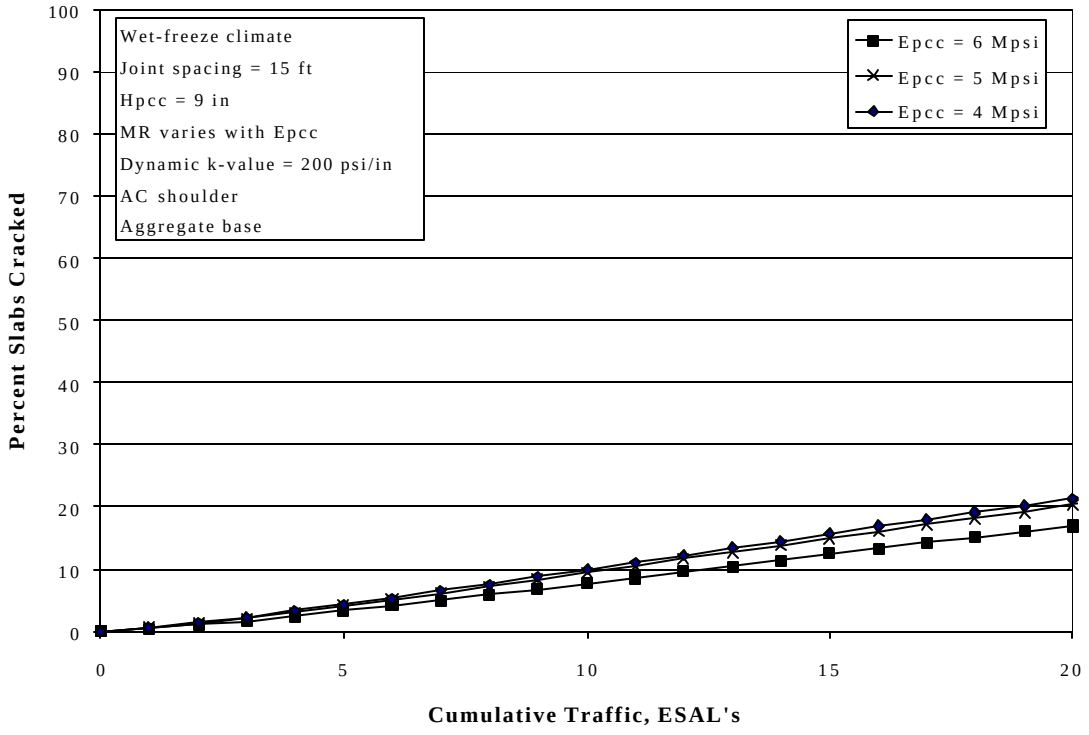

Figure 28. Sensitivity of the final JPCP transverse cracking model to changes in modulus of elasticity and corresponding changes in PCC flexural stiffness.

of elasticity assuming that the PCC flexural strength is related to PCC modulus of elasticity as predicted by Foxworthy's equation:

$$MR = 43.5\frac{E}{10^6} + 488.5 \qquad (82)$$

where MR is the PCC modulus of rupture, (psi) and E is the PCC modulus of elasticity (psi).[38] An analysis of figure 28 shows that PCC slab cracking decreases slightly when the PCC modulus of elasticity and modulus of rupture increase together.

Effect of PCC Transverse Joint Spacing

Figure 29 illustrates the sensitivity of the final JPCP transverse slab cracking model to changes in PCC transverse joint spacing. The figure clearly shows that an increase in joint spacing results in a dramatic increase in slab cracking. This trend agrees with numerous field observations that longer slabs crack much earlier than shorter slabs in pavements with variable joint spacing. This trend also means that if joint sawing is not done on time and proper joints are not formed, large "effective" joint spacing will be developed, which can cause random slab cracking.

Effect of PCC Slab Edge Support

Figure 30 shows that a tied PCC shoulder and widened slabs can significantly reduce the amount of slab cracking compared with an asphalt shoulder. The tied PCC shoulders improve cracking performance by reducing stresses at the pavement edge. The effectiveness of the tied PCC shoulder depends on the load transfer efficiency across the lane-shoulder joint. Widened slabs effectively move the traffic away from the pavement edges, thus allowing the interior stresses (rather than much higher edge stresses) to control fatigue cracking.

Effect of Base Type

The presence of a stabilized base can have a significant effect on slab cracking if the base is bonded to the pavement slab; however, the effect is negligible if the bonded response cannot be obtained. These trends are illustrated in figure 31. In reality, there is most often a partial bond with some slippage.

Effect of Site-Related Factors

In addition to being sensitive to the numerous material- and design-related factors discussed above, the final slab cracking model is also very sensitive to site-related factors. Two site condition factors that affect the development of JPCP cracking include climate (climatic zone) and subgrade support (dynamic k-value). The effects of these factors are described separately below.

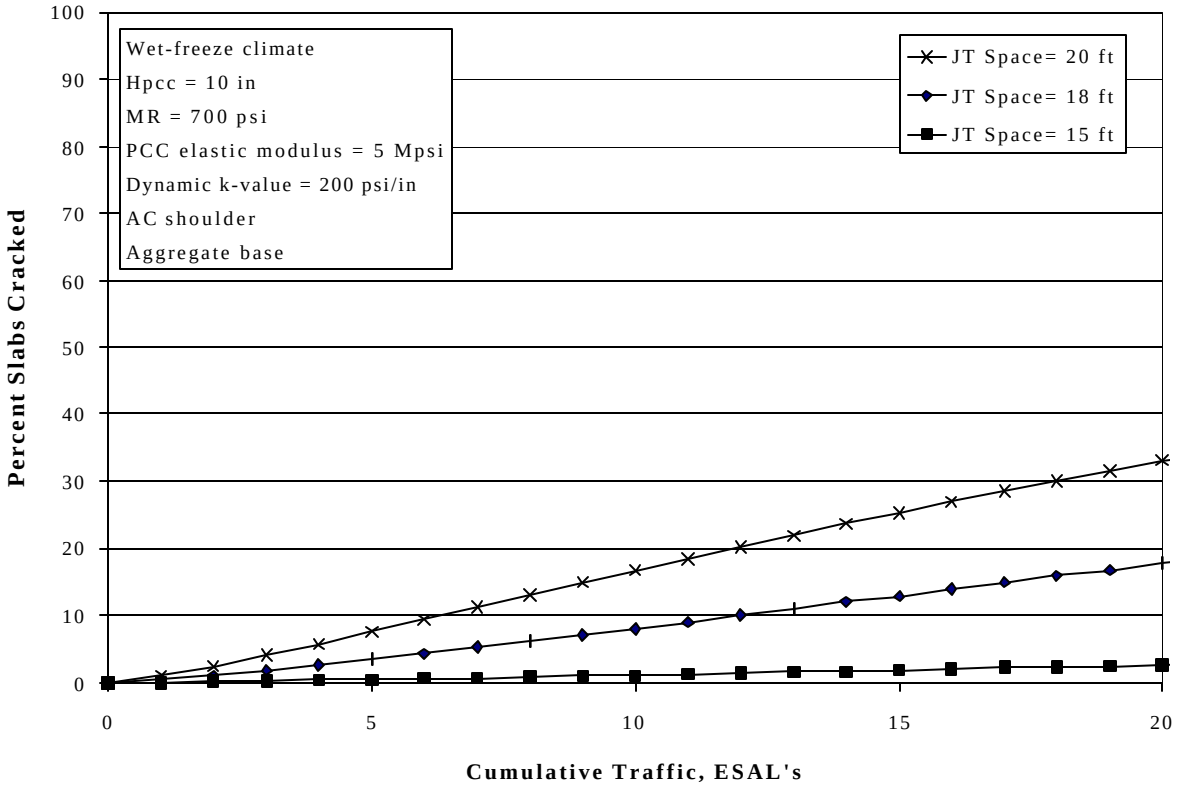

Figure 29. Sensitivity of the final JPCP transverse slab cracking model to changes in PCC slab joint spacing.

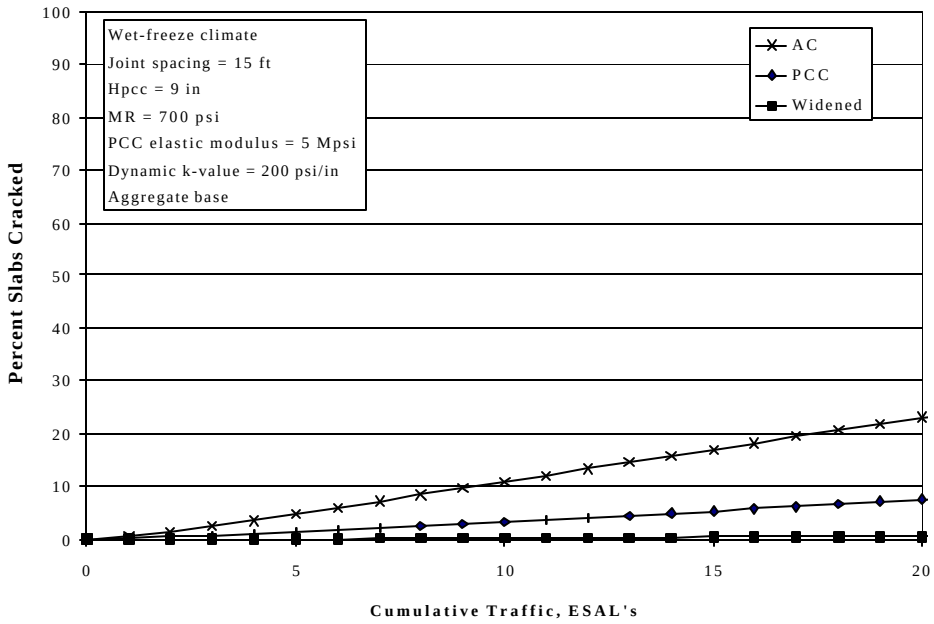

Figure 30. Sensitivity of the final JPCP transverse slab cracking model to changes in edge support.

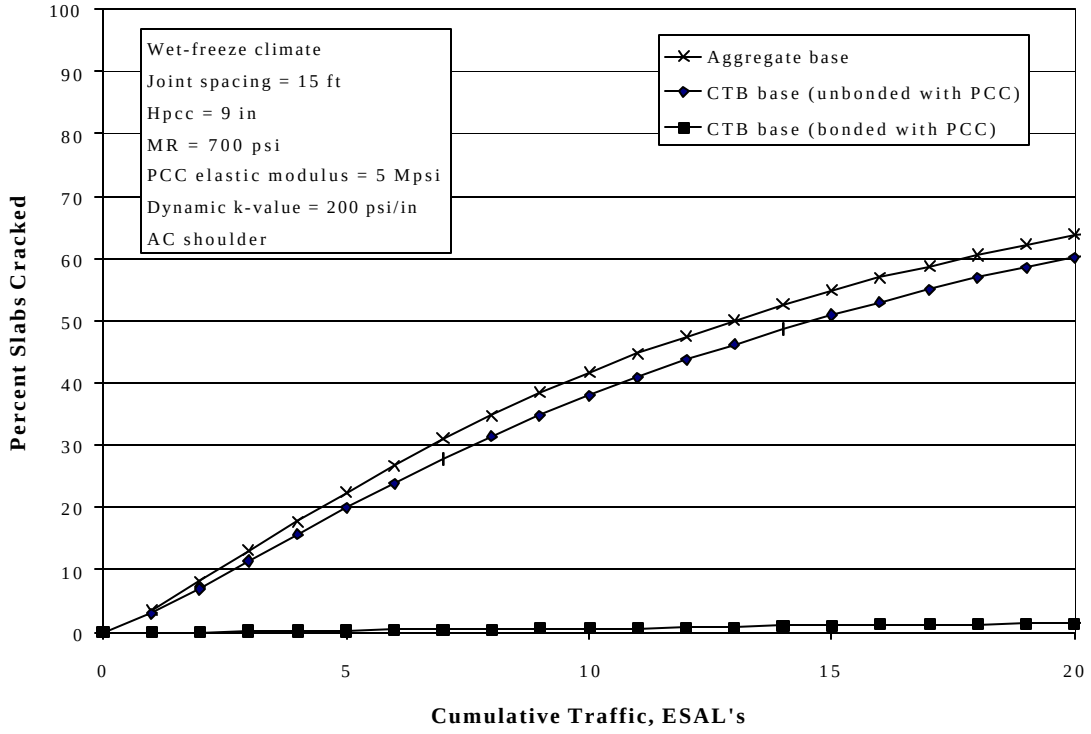

Figure 31. Sensitivity of the final JPCP transverse slab cracking model to changes in base type and bond condition.

Effect of Climate

Figure 32 illustrates that climatic conditions can have a significant effect on slab cracking. The conditions in the hotter climates generally lead to more slab cracking because of the higher temperature differentials. For top-down cracking, moisture conditions may also be important; drier conditions cause greater amounts of cracking because of the greater differential shrinkage.

Effect of Subgrade Support

Figure 33 contains a plot that illustrates the sensitivity of the final JPCP transverse cracking model to changes in subgrade support conditions (dynamic k-value backcalculated from FWD tests). This plot shows that the subgrade modulus of reaction has a relatively minor effect at lower levels, but the difference between the extreme conditions can be significant. For reference, the mean dynamic k-value of all LTPP GPS-3 sections has been found to be approximately 54 kPa/mm (200 psi/in). The static k-value, which is the traditional k-value used in pavement design for the past 75 years, is approximately one-half of the dynamic k-value. To avoid confusion since most engineers are familiar with the static k-value, the PaveSpec 3.0 software requires the input of a static k-value.

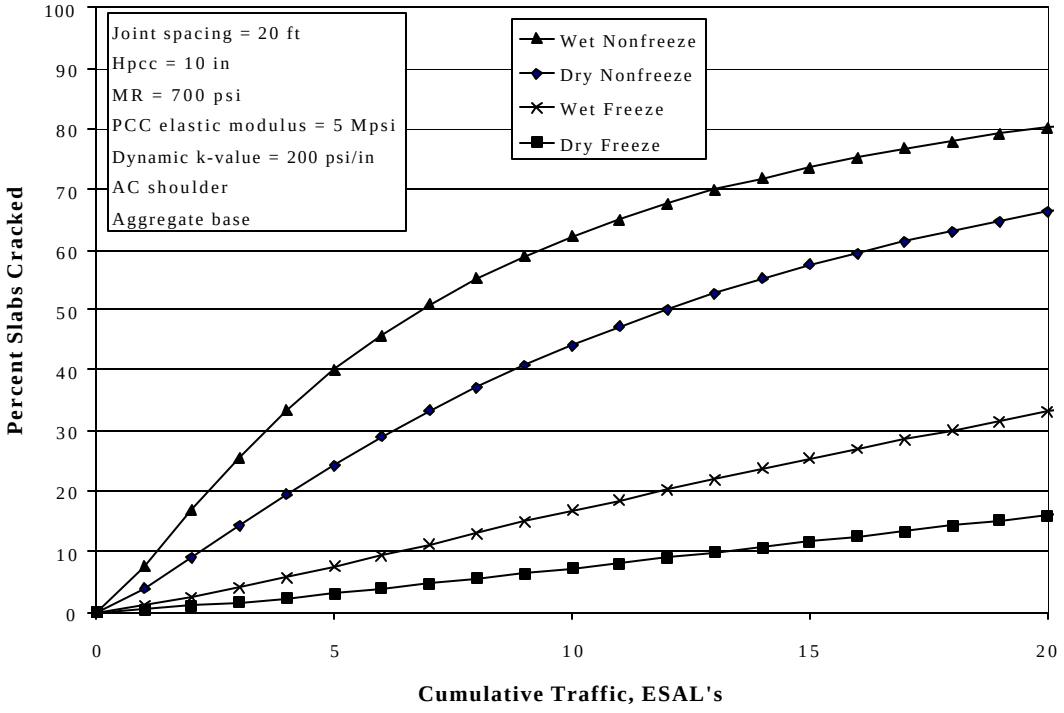

Figure 32. Sensitivity of the final JPCP transverse slab cracking model to changes in climate.

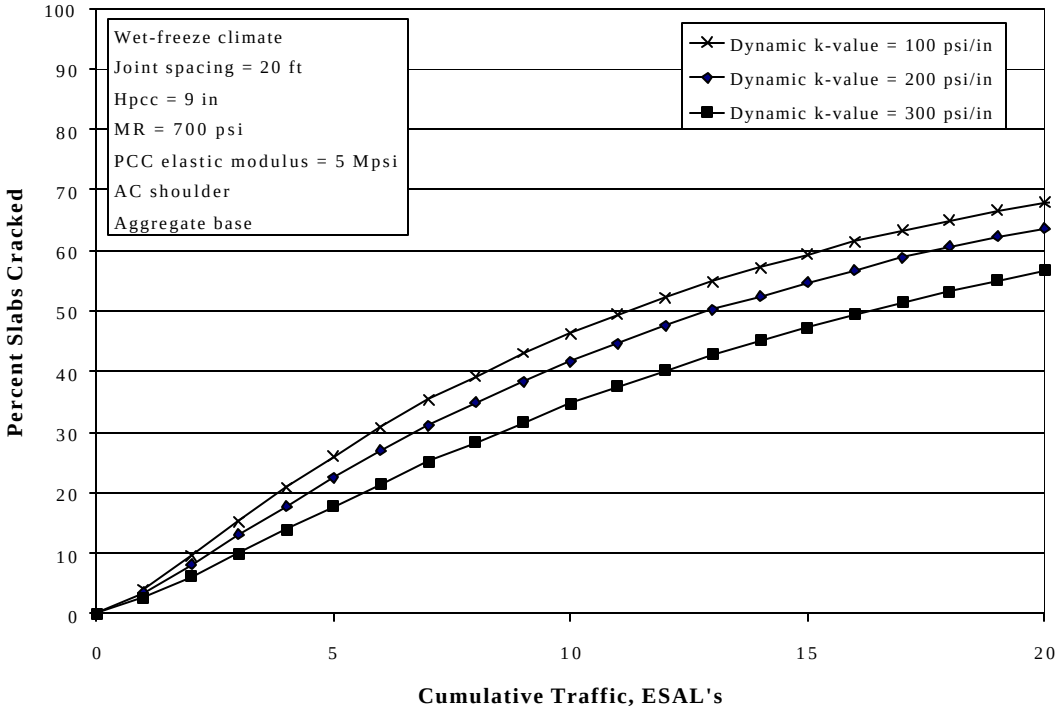

Figure 33. Sensitivity of the final JPCP transverse slab cracking model to changes in dynamic k-value.

SUMMARY

The RPPR 1997 JPCP transverse cracking model was recalibrated under this study. The recalibrated model is deemed suitable for use with the current PRS procedure because it incorporates PRS-related AQC's (PCC concrete strength and slab thickness) as well as other design-, material-, and site-related variables that significantly influence slab cracking. The model has reasonable statistics for being calibrated with such a large number of data points. Specific improvements to the new model include the following:

- Direct consideration of the characteristics of the base layer.
- Direct consideration of the effects of a tied PCC shoulder.
- Incorporation of improved procedures for computing load and thermal curling stresses.
- Incorporation of the influence of built-in construction curling on slab cracking.
- Recalibration of the model was accomplished using a much improved database (in both quality and quantity).

As mentioned previously, this model only considers the development of bottom-up cracking. However, both slab thickness and PCC strength will affect top-down cracking and bottom-up cracking similarly. Thus, the two AQC's important to the prediction of transverse cracking in PRS will have a significant effect on both bottom-up and top-down cracking. Once procedures for predicting top-down cracking are developed (they are under development at this time under other research), it is strongly recommended that they be incorporated into the transverse cracking prediction procedures used in the PRS.

CHAPTER 6: TRANSVERSE JOINT SPALLING MODEL

INTRODUCTION

Spalling is defined as the breakdown or disintegration of a PCC slab's edges at transverse joints and is generally categorized by its quantity (number of spalled joints or total length of joint spalled) and severity (low, medium, or high).[13,39] Joint spalling may be caused by infiltration of incompressibles into pavement joints, deterioration of the concrete material because of environmental factors, problems with load transfer devices, or the exposure of the slab's joint to a sudden and massive tensile stress. Spalling caused by a sudden force is usually of low severity and does not progress or deteriorate with time. However, spalling caused by incompressibles, repeated high tensile stress at the slab edges (fatigue), load transfer devices, or concrete deterioration is more significant. Spalling generally increases in amount and severity over time and eventually causes significant pavement joint deterioration and a need for associated repairs. An increase in pavement roughness, associated with developing spalling, typically results in a decrease in pavement serviceability and the need for costly rehabilitation.[10,13,39,40,41]

This chapter describes the researchers' initial attempt to validate the chosen best-available transverse joint spalling model (that used in PaveSpec 2.0), as well as the development of a new, improved spalling model for use in PaveSpec 3.0.

CURRENT PRS JPCP TRANSVERSE JOINT SPALLING MODEL

The transverse joint spalling model selected as the best available was that used in the PaveSpec 2.0 software. It is a combination of a spalling model developed by Yu et al. for the 1997 FHWA RPPR project and an adjustment ratio developed in 1993 by ERES and CTL.[10,16] The adjustment ratio was included in the process to incorporate the effects of two PRS-related AQC's (concrete strength and air content). Currently, no single model predicts transverse joint spalling based on both the AQC variables essential for PRS analysis and other significant climate, site, and design variables.

The transverse joint spalling model included in PaveSpec 2.0 consists of a multi-step procedure that adjusts a predicted *baseline* spalling (spalling predicted only as a function of various site, design, and climatic inputs) to account for changes in PRS-related AQC's. The following paragraphs summarize the details of this spalling model as they were presented in a 1999 report by Hoerner et al.[10]

Two different procedures are used to estimate transverse joint spalling, depending on whether air content is considered. If air content is not considered, transverse joint spalling is predicted directly using the baseline model. If air content is considered, the transverse joint spalling (predicted using the baseline model) is then adjusted based on

a comparison of as-constructed to as-designed mean air content and compressive strength. Both model procedures are presented separately below. (Note: The model outputs and inputs are presented in English units.)

Transverse Joint Spalling Baseline Model (Not Including Air Content)

$$\%SPALL = AGE^2 * 10^{-6} * JTSPACE * [551.6 - 847.3 * (LIQSEAL + PREFSEAL) + (0.936 * (DAYS90)^3 * 10^{-3}) + (364 * DOWELCOR) + (2.783 - 1.40 * LIQSEAL - 2.368 * PREFSEAL - 0.676 * SILSEAL) * FI] \quad (83)$$

where:

%SPALL = Percentage of medium- and high-severity spalled joints where air content is not considered (LTPP definition).
AGE = Number of years since original construction.
DOWELCOR = Dowel corrosion potential.
= 0, if no dowels exist or dowels are protected from corrosion.
= 1, if dowels are not protected from corrosion.
JTSPACE = Mean transverse joint spacing, ft.
LIQSEAL = 1, if liquid sealant exists in joint; otherwise, 0.
PREFSEAL = 1, if preformed sealant exists in joint; otherwise, 0.
SILSEAL = 1, if silicone sealant exists in joint; otherwise, 0.
FI = Mean annual freezing index, °F-days.
DAYS90 = Number of days with temperature greater than 90 °F.

Statistics:
N = 164.
R^2 = 0.76.
SEE = 5.4 percent of joints.

Transverse Joint Spalling Model and Procedure (Including Air Content)

If air content is included, a four-phased procedure is used to predict transverse joint spalling. The details of each phase are defined below.

<u>Phase 1—Calculate the As-Designed Transverse Joint Spalling</u>

The first step in computing the estimated yearly as-constructed transverse joint spalling is to determine the yearly as-designed transverse joint spalling values. The as-designed transverse joint spalling is assumed to be equal to the baseline spalling computed using equation 83.

Phase 2—Calculate the Relative Difference Between the As-Designed and As-Constructed Spalling (due to the effects of air content and compressive strength)

This relative difference between as-constructed and as-designed spalling is computed based on the differences between as-constructed and as-designed air content and concrete strength. This as-constructed to as-designed ratio (AC-AD RATIO) is computed based on equations that are functions of air content, compressive strength, freeze-thaw cycles (in the pavement), and age. Different equations are used depending on whether deicing salt is present. Each of these scenarios is described separately below.

Case 1—Salt is Present

If salt is present, an AC-AD RATIO is computed using the results of equations 84 and 85.

$$\text{AC-SPALL} = 115 - (9.29 * \text{AIR}_{\text{AS-CON}}) - (0.0114 * f'c_{\text{AS-CON}}) + (0.118 * \text{FTC}_3) \quad (84)$$

$$\text{AD-SPALL} = 115 - (9.29 * \text{AIR}_{\text{AS-DES}}) - (0.0114 * f'c_{\text{AS-DES}}) + (0.118 * \text{FTC}_3) \quad (85)$$

where:

AC-SPALL = As-constructed joint spalling (function of as-constructed air content and compressive strength), percentage of joint length.
AD-SPALL = As-designed joint spalling (function of as-designed air content and compressive strength), percentage of joint length.
FTC_3 = Cumulative number of estimated in-pavement freeze-thaw cycles (at 76 mm [3 in] below the pavement surface).
$\text{AIR}_{\text{AS-CON}}$ = Measured as-constructed air content, percent.
$\text{AIR}_{\text{AS-DES}}$ = As-designed air content, percent.
$f'c_{\text{AS-CON}}$ = Measured as-constructed 28-day compressive strength, psi.
$f'c_{\text{AS-DES}}$ = As-designed 28-day compressive strength, psi.

Finally, the AC-AD RATIO is computed as a function of AC-SPALL and AD-SPALL using equation 86.

$$\text{AC-AD RATIO} = \frac{\text{AC - SPALL}}{\text{AD - SPALL}} \quad (86)$$

Case 2—Salt is Not Present

If salt is not present, equation 87 (developed under a previous PRS project) is used.[5,6,7]

$$\text{SPALL} = 22.6 + 75.1 * \text{SALT} * \log(\text{FTC}_3) - 78.0 * \text{SALT} - \quad (87)$$

$$11.7 * AIR * SALT - 0.00478 * f'c$$

where:

SPALL = Joint spalling, percentage of joint length.
SALT = 0 if no calcium chloride is present, 1 if calcium chloride is present.
FTC_3 = Cumulative number of estimated freeze-thaw cycles in the pavement (at 76 mm [3 in] below the pavement surface).
AIR = Measured air content of the fully consolidated specimen, percent.
f'c = Measured 28-day compressive strength mean, psi.

Without the presence of salt, equation 87 simplifies to be a function of compressive strength only. Therefore, the effects of air content are no longer considered directly, but instead are considered indirectly through compressive strength. The equation is calculated for both the as-constructed and as-designed pavements (using representative as-constructed and as-designed compressive strength means), as shown in equations 88 and 89, respectively.

$$AC\text{-}SPALL = 22.6 - 0.00478 * f'c_{AS\text{-}CON} \quad (88)$$

$$AD\text{-}SPALL = 22.6 - 0.00478 * f'c_{AS\text{-}DES} \quad (89)$$

where:

AC-SPALL = As-constructed joint spalling (function of as-constructed compressive strength only), percentage of joint length.

AD-SPALL = As-designed joint spalling (function of as-designed compressive strength only), percentage of joint length.

$f'c_{AS\text{-}CON}$ = Measured as-constructed 28-day compressive strength, psi.

$f'c_{AS\text{-}DES}$ = As-designed 28-day compressive strength, psi.

Finally, the AC-AD RATIO is again computed using equation 86.

Phase 3—Determine the As-Constructed Spalling Values Using the Phase 2 AC-AD RATIO

The phase 3 as-constructed yearly spalling values are calculated by multiplying the phase 1 as-designed spalling values by the computed phase 2 AC-AD yearly ratios.

Phase 4—Adjustment of Phase 3 Spalling Values to the Assumed Boundary Conditions

Finally, the phase 3 as-constructed spalling values are adjusted to comply with the set of assumed boundary conditions presented in this section. The following general assumptions are used to define the boundary conditions:

- The as-designed and as-constructed curves are never allowed to cross.
- As-designed and as-constructed transverse joint spalling values are both equal to zero at an age equal to zero (i.e., at time of construction).
- The predicted transverse joint spalling value must increase (or stay constant) as time increases.
- If the as-constructed curve is above the as-designed curve (poorer quality than the as-designed), the as-constructed curve is assumed to go through the origin at an age of zero.

The following step-by-step procedure is used to determine the as-constructed spalling curve values required to match the boundary conditions. The values in question are near an age of zero. The procedure differs depending on whether the as-constructed values are greater than or less than the as-designed values. The as-designed and as-constructed values at the end of the analysis period are used to determine which scenario is used. Each scenario is explained in detail below.

Scenario 1: The as-constructed value is less than the as-designed value at the end of the analysis period.

Scenario 1 represents the case where the as-constructed pavement is constructed with better quality than specified for the as-designed pavement. When this occurs, the following procedure is used to ensure boundary conditions:

1. Calculate the yearly slope changes starting at the last year of the analysis period.
2. Compare year-to-year slopes starting at the last year of the analysis period and working backwards (i.e., moving toward an age of zero).
3. Identify the first yearly interval (trigger interval) where the slope stops decreasing and begins increasing (Trigger Interval = $SLOPE_{(n)} = SPALL_{YEAR(n)} - SPALL_{YEAR(n-1)}$).
4. If the slopes begin increasing, use the last decreasing slope in the series ($SLOPE_{(n+1)}$) as the assumed slope for the early age slopes (SLOPE = 0 to n).

5. One final check is to make sure that the as-constructed values are less than or equal to the as-designed values.

Scenario 2: The as-constructed value is greater than the as-designed value at the end of the analysis period.

Scenario 2 represents the case where the as-constructed pavement is constructed with poorer quality than that specified for the as-designed pavement. When this occurs, the following procedure is used to ensure boundary conditions:

1. Calculate the yearly slope changes starting at the last year of the analysis period.

2. Determine the projected y-intercept associated with each calculated slope.

3. Compare year-to-year projected y-intercepts starting at the last year of the analysis period and working backwards (i.e., moving toward an age of zero).

4. Identify the first yearly interval (trigger interval) where the y-intercept becomes greater than or equal to zero (Trigger Interval = $SLOPE_{(n)} = SPALL_{YEAR(n)} - SPALL_{YEAR(n-1)}$).

5. Determine the difference between the as-constructed and as-designed values at year n ($DIFFERENCE_{(n)} = AC\text{-}SPALL_{(n)} - AD\text{-}SPALL_{(n)}$).

6. As (n) moves toward zero, the difference between the spalling values decreases linearly. For example, if the difference is determined to be 6 (100 percent of the observed difference) at a time of n=10 years, 50 percent of the observed difference will be applied at a time of n / 2 (therefore, difference = 3 at 5 years). This difference progresses until a difference of zero is applied at a time equal to zero.

ATTEMPTED VALIDATION OF THE CURRENT PRS TRANSVERSE JOINT SPALLING MODEL

Before any new model development or calibration techniques were undertaken, the research team attempted to validate the current PRS transverse joint spalling model with a new independent data set. The validity of the current spalling model was assessed by:

- Reviewing plots of predicted versus measured spalling.
- Reviewing plots of residuals versus predicted spalling.
- Analyzing diagnostic statistics such as the R^2 and the SEE to determine the goodness-of-fit of the models when the independent data set is used.
- Identifying any general observed weaknesses in the model.

The independent data used in the initial model validation process consisted of JPCP data from the LTPP experiment database (GPS-3 data only). It consisted of 61 pavement test sections located in 17 States. A summary of the validation data is presented in table 30.

Table 30. Summary of LTPP data used in the initial validation of the PaveSpec 2.0 JPCP transverse joint spalling model.

Climatic Region	Variable	Range		Mean	Standard Deviation
		Min.	Max.		
Nonfreeze	Age, years	2	24	11.6	5.6
	Joint spacing, ft	14	30	19	4
	Liquid sealant	0 data points		-	-
	Preformed sealant	11 data points		-	-
	Silicone sealant	36 data points		-	-
	Other sealant	12 data points		-	-
	Days with temperature above 90 °F	15	99	60	24
	Load transfer mechanism	42 data points used dowels and 16 used aggregate interlock as the load transfer mechanism			
	Freezing index, °F days	0	147	60	56
	Air content, percent	3.8	9.8	5.4	1.8
	Core 28-day compressive strength, psi	3,700	6,000	4,800	884
	Air freeze-thaw cycles	2	80	42	28
Freeze	Age, years	0	25	10	5.6
	Joint spacing, ft	12.5	20	15.7	0
	Liquid sealant	30 data points		-	-
	Preformed sealant	26 data points		-	-
	Silicone sealant	50 data points		-	-
	Other sealant	3 data points		-	-
	Days with temperature above 90 °F	3	56	24	17.2
	Load transfer mechanism	21 data points used dowels and 87 used aggregate interlock as the load transfer mechanism			
	Freezing index, °F days	160	2,815	1,087	604
	Air content, percent	2.1	7	5.7	0.76
	Core 28-day compressive strength, psi	3,110	6,780	5,000	704
	Air freeze-thaw cycles	63	172	110	26.6

- The models used for estimating AD-AC RATIO were developed with laboratory-generated data with a limited inference space.

- A key input variable, freeze-thaw cycles at 76 mm (3 in) below the pavement surface, is a subjective variable that is difficult to estimate and is not present in national databases.

- A comparison of the measured and predicted spalling (using the independent LTPP data) showed a low R^2 value of 0.37 percent and an SEE of 3.2 percent.

Figures 34 and 35 show plots of predicted versus measured spalling, and residuals versus predicted spalling, respectively. The diagnostic statistics and both plots indicate that the predicted transverse joint spalling is random in nature and does not have a very strong correlation with the measured transverse joint spalling. Because of the lack of a strong correlation between the predicted and measured spalling values, it was decided that a simple calibration of the existing model would not significantly improve the model's prediction ability. Therefore, it was decided that the only way to obtain a transverse joint spalling model that would be truly suitable for use within the current PRS methodology was to develop a new model based on the data available in the newly compiled PRS national database.

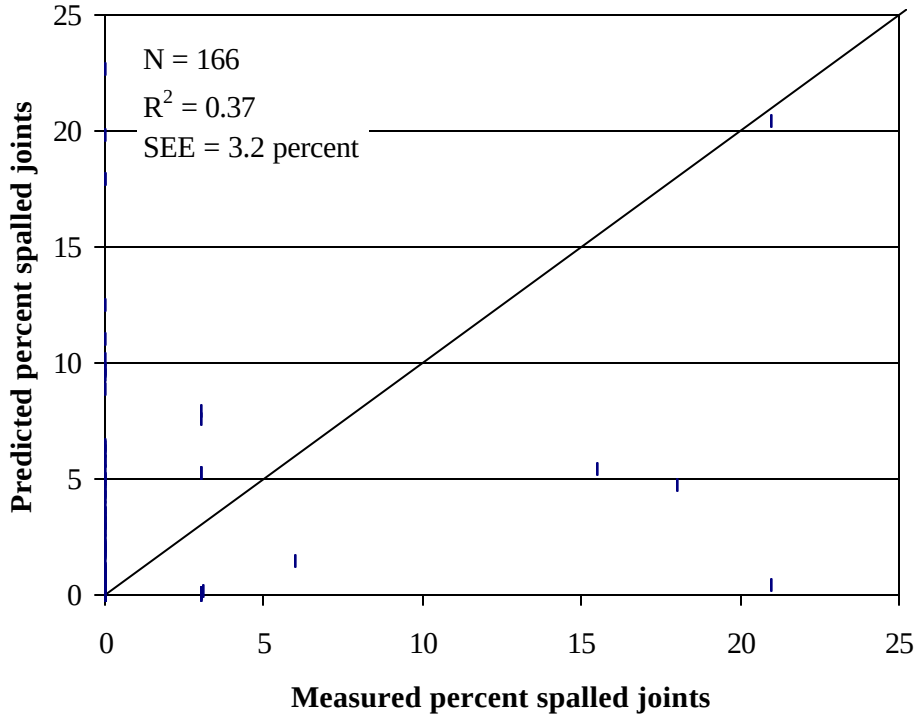

Figure 34. Predicted (equation 83) versus measured JPCP transverse joint spalling (using the LTPP validation data set).

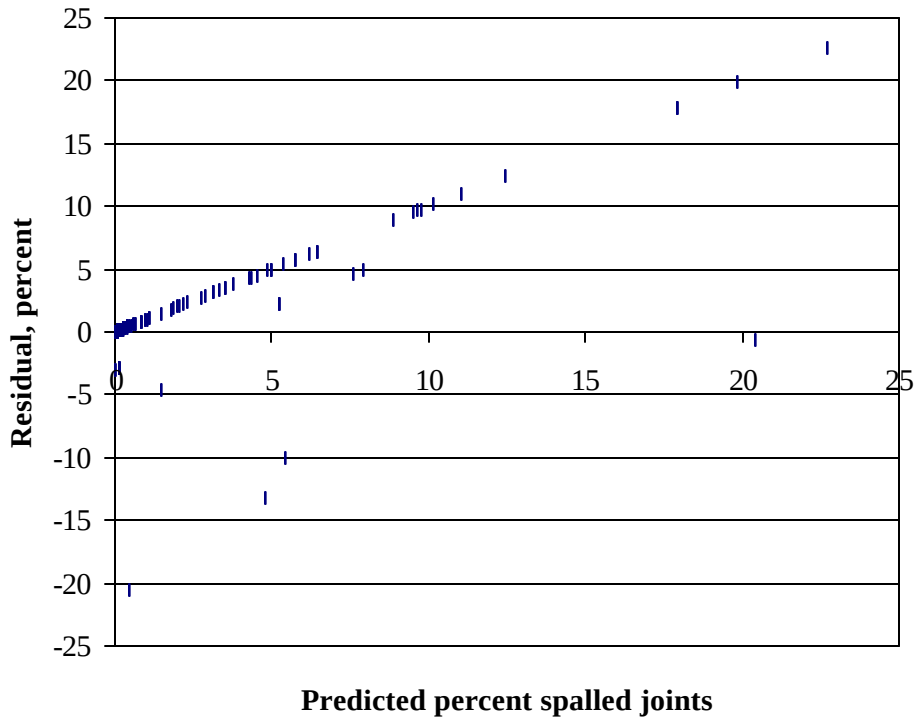

Figure 35. Residual versus predicted (equation 83) transverse joint spalling (using the LTPP validation data set).

EXISTING JPCP TRANSVERSE JOINT SPALLING MODELS

The first step in the model development process was to review transverse spalling models developed under previous research efforts. Reviewing previous studies not only provided guidance as to what variables should be considered for inclusion in the new model, but also added expert knowledge into the model development process at an early stage. During the review process, specific attention was paid to the engineering significance of the variables. The specific models reviewed were from the SHRP P-020, LTPP Data Analysis, CTL, and RPPR studies.[5,14,15, 16] The details of each of these models are described separately in the following sections.

SHRP P-020 JPCP Transverse Joint Spalling Model[14]

In a SHRP study conducted by Simpson et al. in 1994, titled *Early Analysis of LTPP General Pavement Studies Data*, the following JPCP joint spalling model was developed using LTPP data:[14]

$$\%SPALL = 9.79 + 10.09 * [-1.227 + 0.0022 * (0.9853 * AGE + 0.1709 * FTCYC)^2] \quad (90)$$

where:

%SPALL = Predicted mean percentage of transverse joint spalling (all severities), percentage of the total number of joints.
AGE = Age since construction, years.
FTCYC = Mean annual air freeze-thaw cycles.

Statistics:
N = 56.
R^2 = 0.335.
SEE = 11.05 percent of joints.

This model relates spalling to the pavement age and the mean annual number of air freeze-thaw cycles. This model suggests that joint spalling increases with age, and that stress cycles generated within the pavement while undergoing freezing and thawing contribute to spalling. Freezing and thawing of concrete also result in the expansion of water in the pores of the concrete, creating additional stresses that weaken the concrete.

The age variable in this model could represent several factors, such as cyclic slab curling and warping, and temperature cycles due to daily and seasonal temperature variations that result in joint movements and the generation of stresses within the PCC slab concrete. Cyclic joint movements ultimately increase joint openings and damage the joint sealant, allowing for the infiltration of incompressibles into the joints. Age also represents the amount of repeated traffic loading, since older pavements are expected to have carried more traffic.

The SHRP P-020 model indicates that spalling generally increases slowly during the first few years of the pavement's life and then increases more rapidly after several years. This is logical because it takes some time for incompressibles in the pavement's joints or cracks to accumulate and increase the stress concentrations at the joint. It also takes time for pavement damage to accumulate.

LTPP Data Analysis JPCP Transverse Joint Spalling Model[15]

In 1999, Titus-Glover et al. developed a JPCP transverse joint spalling model under a FHWA LTPP data analysis contract.[15] This model, based solely on LTPP data, is as follows:

$$\%SPALL = \frac{100 * Damage^{2.1}}{Damage^{2.5}}(0.34 * TRANGE - 0.42 * RH + 0.0318 * FTCYC) \qquad (91)$$

where:

%SPALL = Percentage of JPCP joints with spalling (all severities).
TRANGE = Average daily temperature range, °C.

RH = Average daily range of relative humidity during the month of construction (can be obtained from the National Oceanic and Atmospheric Administration [NOAA] tables, percent.
FTCYC = Number of air freeze-thaw cycles.
Damage = Damage from traffic and environmental stresses.

Statistics:
N = 52.
R^2 = 0.61.
SEE = 12 percent of joints.

Damage is calculated as follows: [15]

$$\text{Damage} = \frac{\text{KESAL}}{N_T} + \left(\frac{\text{AGE}}{N_E}\right)^{0.145} \tag{92}$$

where:

KESAL = Number of 80-kN (18-kip) ESAL's, in thousands.
AGE = Pavement age in years.
N_T = Allowable number of cycles due to traffic stresses.
N_E = Allowable number of cycles due to environmental stresses.

The allowable numbers of cycles, N_T and N_E, used to calculate damage are obtained from tensile stresses generated at the slab joint from traffic and environmental stress cycles. The specific variables of which N_T and N_E are functions are defined as follows:

N_T = f(height of sealant, modulus of subgrade reaction [k-value], transverse joint sealant type, PCC slab thickness, elastic modulus of PCC slab).

N_E = f(transverse joint sealant type, transverse joint spacing, thermal gradient in the slab, indirect tensile strength, concrete coefficient of thermal expansion, subbase friction factor).

The LTPP data analysis model identified three key groups of factors that influence JPCP spalling: environmental effects, traffic loading, and sealants and incompressibles. The key environmental variables that were found to influence joint spalling were the average daily temperature range, the mean monthly relative humidity during the month of construction, and the number of annual freeze-thaw cycles. The model also shows the influence of the type of sealant, or lack thereof, in relation to all these factors.

A large daily temperature range results in more spalling regardless of the type of sealant used. It is believed that a larger temperature range may result in higher restrained thermal stresses at the slab joint. Preformed sealants seem to decrease these stresses and cause less spalling, whereas joints without any sealants (most likely filled

with incompressibles) experience more spalling. A high relative humidity during the period of construction reduces the occurrence of spalling. A possible explanation of this trend is that, by aiding the curing process because of the reduced rate at which moisture leaves the PCC slab, a high relative humidity may increase strength gain and concrete durability and reduce shrinkage, causing early age delaminations and microcracks that lead to spalling.

CTL JPCP Transverse Joint Spalling Model[5]

Under a previous PRS study, CTL conducted a laboratory materials study that evaluated the effects of presence of salt, freeze-thaw cycles in the pavement, PCC air content, and 28-day compressive strength on transverse joint spalling.[5] The detailed CTL model is as follows:

$$SPALL_LEN = 22.6 + 75.1 * SALT * \log(FTC_3) - 78.0 * SALT - 11.7 * AIR * SALT - 0.00478 * f'c \quad (93)$$

where:

SPALL_LEN = Joint spalling, percentage of joint length.
SALT = 0 if no calcium chloride is present, 1 if calcium chloride is present.
FTC_3 = Cumulative number of estimated freeze-thaw cycles at 76 mm (3 in) below the pavement surface.
AIR = Air content of the fully consolidated specimen, percent.
f'c = 28-day compressive strength mean, psi.

Statistics:
R^2 = 0.855.
SEE = 9.0 percent of joint length.

This model shows a decrease in predicted spalling with an increase in air content and PCC compressive strength. However, there was a significant increase in spalling as the total number of in-pavement freeze-thaw cycles increased (especially when deicing salt was present).

Equation 93 was calibrated using field data obtained from in-service pavements in a subsequent PRS study.[7] This calibrated model was the basis of the spalling adjustment factor (AC-AD RATIO) used in the transverse spalling prediction procedure currently used in PaveSpec 2.0. In general, a good correlation was observed between the field data and the calibrated model, indicating that the variables in the CTL models significantly influence spalling.

FHWA RPPR JPCP Transverse Joint Spalling Model[16]

The FHWA RPPR study (completed by Yu et al. in 1997) undertook a detailed examination of several past models.[16] It resulted in the following comprehensive list

of explanatory variables that can be used in the exploratory analysis for model development:

- Pavement age (time since construction).
- Cumulative 80-kN (18-kip) ESAL's in the traffic lane.
- Mean transverse joint spacing.
- PCC slab thickness.
- AASHTO drainage coefficient (C_d).
- Transverse joint opening.
- Mean transverse joint width.
- Transverse joint sealant type.
- Elastic modulus of the PCC slab.
- Mean backcalculated modulus of subgrade reaction (k-value).
- Thornthwaite moisture index.
- Number of days in which temperature was greater than 90 °F.
- Mean monthly temperature range.
- Mean annual freezing index.
- Mean annual air freeze-thaw cycles.
- Potential of dowel corrosion.

Under the RPPR study, Yu et al. considered all of these potential variables in the development of the following JPCP transverse joint spalling model:[16]

$$\%SPALL = AGE^2 * 10^{-6} * JTSPACE * [551.6 - 847.3 * (LIQSEAL + PREFSEAL) + (0.936 * (DAYS90)^3 * 10^{-3}) + (364 * DOWELCOR) + (2.783 - 1.40 * LIQSEAL - 2.368 * PREFSEAL - 0.676 * SILSEAL) * FI] \quad (94)$$

where:

%SPALL = Percentage of medium- and high-severity spalled joints where air content is not considered.
AGE = Number of years since original construction.
DOWELCOR = Dowel potential corrosion (assumed to be equal to 0).
= 0, if no dowels exist or dowels are protected from corrosion.
= 1, if dowels are not protected from corrosion.
JTSPACE = Mean transverse joint spacing, ft.
LIQSEAL = 1, if liquid sealant exists in joint; otherwise, 0.
PREFSEAL = 1, if preformed sealant exists in joint; otherwise, 0.
SILSEAL = 1, if silicone sealant exists in joint; otherwise, 0.
FI = Mean annual freezing index, °F-days.
DAYS90 = Number of days with temperature greater than 90 °F.

Statistics:
N = 164.
R^2 = 0.76.

SEE = 5.4 percent of joints.

This RPPR spalling model is the baseline model used in the transverse spalling prediction procedure currently included in PaveSpec 2.0.

The variables in this model can be divided into two groups—environment-related and design-related variables. The environment-related variables include age (cycles of climate changes, such as opening and closing of joints), annual number of days with temperature above 32 °C (90 °F) (Days 90), and freezing index. DAYS90 is indicative of the magnitude of repeated high compressive stresses to which the joint is subjected in the summer. Since pavements located in areas with high DAYS90 values generally undergo a great amount of compression, this can result in the generation of high stresses in the PCC slab and joint that lead to a greater amount of spalling, especially if incompressibles are present in the joints.

Pavements located in areas with a high freezing index are subjected to prolonged cycles of frozen water within the pores of the PCC slab and deterioration of the concrete material. This situation generally results in the disintegration of the concrete slab material at the slab surfaces and joints and, hence, leads to the development of spalling.

The design-related variables in the model include transverse joint spacing, sealant type, and dowel corrosion potential. The joint spacing is highly correlated to the degree of joint movement. Longer slabs expand more when subjected to cyclic temperature variations and create higher stresses at the joint when restrained by the presence of incompressibles. Spalling can be caused by dowel corrosion produced as a result of the dowel's exposure to chlorides and other chemicals that infiltrate the joint; therefore, applying a protective coating (epoxy, plastic, stainless steel) to the dowels will typically reduce the amount of spalling.

The role of joint sealants in minimizing spalling is to prevent the intrusion of incompressible material into the joint. Incompressibles restrain the slab joints from moving which, therefore, causes an increase in the stresses around the pavement joint. This increase in stresses around the joint generally leads to an increase in the spalling at the joint. The results of the RPPR study suggested that the use of preformed sealants in JPCP resulted in the lowest level of spalling for all sealed and unsealed joints. Preformed sealants are particularly effective in minimizing the intrusion of incompressibles into pavement joints.

Overview of JPCP Transverse Joint Spalling Models

The review of past spalling model development efforts indicates that, even though research has been ongoing since the early 1960's, the mechanism of spalling is yet to be fully understood. This is mainly due to the fact that most of the previously developed models are empirical. Empirical models typically have no mechanistic structural

inputs and draw entirely on statistical analysis of measured real-life data to arrive at models that predict distress or damage.

Although the new transverse spalling model developed under this project will be strongly based on empirical data, it is nonetheless important to identify the mechanistic relationships that influence transverse joint spalling. Spalling can be attributed to several interacting mechanisms caused by tensile stresses imposed on the pavement by environmental forces and inadequate quality control during construction. Some mechanistic-based causes of spalling identified in previous research include the following:

- The combination of repeated temperature cycles and entrapped incompressibles in a joint. A buildup of compressive stress is created when a joint with incompressibles is subjected to high temperatures.
- Poor consolidation of the concrete at the joint resulting from poor construction practices.
- The use of poor quality construction materials (e.g., reactive aggregates, D-cracking aggregates, and non-coated dowels).
- PCC with low entrained air content.
- Severe climatic conditions that cause frequent freezing and thawing and wetting and drying of the PCC slab, along with use of deicing salts.
- Inaccurate placement of load transfer devices, resulting in breakup of the joint.

The review of the recently developed transverse joint spalling models also identified a number of variables that significantly influence spalling. A summary of the significant variables used in past model development (for those models reviewed in this section) is summarized in table 31. This collective list of variables (or variables related to these) will be considered in the transverse spalling model development procedures conducted under this project.

DEVELOPMENT OF A NEW JPCP TRANSVERSE JOINT SPALLING MODEL

Based on the results of the validation process, the transverse joint spalling validation/improvement effort focused on replacing the current spalling model with a new empirical model that was not only a function of significant site, design, and

Table 31. Summary of variables found to significantly affect JPCP transverse joint spalling.

Variable	SHRP P-020[14]	LTPP Data Analysis[15]	CTL[5]	RPPR[16]
Age	✓	✓	✓	✓
80-kN (18-kip) ESAL's		✓		✓
Annual temperature range		✓		
Mean annual air freeze-thaw cycles	✓	✓	✓*	
Thermal gradient in PCC slab		✓		
Relative humidity		✓		
Freezing index				✓
Presence of salt			✓	
Average annual number of days with maximum temperature > 32°C (90 °F)				✓
Transverse joint spacing		✓		✓
Transverse joint sealant type		✓		✓
Height of sealant material		✓		
PCC slab thickness		✓		
PCC slab elastic modulus		✓		
PCC air content			✓	
PCC compressive strength			✓	
PCC indirect tensile strength		✓		
PCC coefficient of thermal expansion		✓		
Modulus of subgrade reaction (k-value)		✓		
Subbase friction factor		✓		
Dowel corrosion potential				✓

* The CTL model was based on in-pavement (76 mm [3 in] below the surface) freeze-thaw cycles rather than air freeze-thaw cycles.

climatic variables, but a function of PRS-related AQC's as well. The specific procedures used in the development and calibration of a new JPCP transverse joint spalling model suitable for use within the current PRS methodology included the following:

- Preparation of the model development data set.
- Selection of a suitable model form.
- Selection of appropriate statistical tools for regression and optimization.
- Development of the final IRI model.

The tasks are described in greater detail in the following sections.

Data Preparation

In preparation for the calibration steps of the model development process, all pertinent GPS-3 data from the LTPP database were compiled into a spalling model development database. This compiled database was used to link LTPP time-series spalling data with all climatic- and design-related variables that were believed to influencing transverse joint spalling. In addition to the linked LTPP data, CTL

laboratory data (used in the development of the CTL model discussed previously in this chapter) were included in the database to ensure that the data for model development had a wide range of design properties, climatic properties, and distress. Data assembly was accomplished using Microsoft® Access, Microsoft® Excel, and the SAS statistical software.

The LTPP data consisted of 88 pavement sections in 28 States and 2 Canadian Provinces. A summary of the data making up the final data set, its inference space, and other statistical characteristics are presented in table 32. The assembled data were thoroughly evaluated to identify any missing data elements and possible problem spots in the database (e.g., time-series data with a significant decrease in spalling over time). Attempts were made to obtain replacements for missing data where possible. The data set was also checked for anomalies and gross data errors.

Table 32. Summary of GPS-3 JPCP data and CTL laboratory data used in model development and calibration.

Data Source	Variable	Range		Mean	Standard Deviation
		Min.	Max.		
LTPP (146 records)	Medium- and high-severity spalling, percent joints	0.0	26.1	1.3	3.8
	Age, years	2.0	27.4	13.7	5.2
	PCC thickness, in	7.0	14.3	9.8	1.3
	Water cement ratio	0.27	0.72	0.45	0.09
	Air content, percent	3.8	9.8	5.7	1.1
	Compressive strength, psi	3,840	12,488	6,335	1,937
	Air freeze-thaw cycles	15	3102	1101	653
	Sealant type	33 records had preformed sealants			
CTL (33 records)	Medium- and high-severity spalling, percent joints[1]	0.0	84.0	28.7	27.5
	Age, years[2]	3.3	28.1	11.7	8.1
	PCC thickness, in	6.0	6.0	6.0	0
	Water cement ratio	0.42	0.50	0.45	0.04
	Air content, percent	2.5	4.8	3.7	0.9
	Compressive strength, psi	2,720	7,150	4,984	1,595
	Total air freeze-thaw cycles[3]	262	2,250	942	653
	Sealant type	No records had a preformed sealant			

Notes:

1. CTL data were measured as average length of spalling per joint, percent. This was converted to percent joint spalled using the assumption that average length of spalling per joint (in percent) is approximately equal to percentage of spalled joints.
2. An average air freeze-thaw cycle of 80 per year was assumed and used to estimate age for the CTL data.
3. The CTL laboratory study measured the total in-pavement freeze-thaw cycles at a depth of 76 mm (3 in) from the slab surface. The cumulative number of in-pavement freeze-thaw cycles was converted to total air freeze-

thaw cycles by multiplying the measured in-pavement cycles by a factor of 7.5. The 7.5 multiplying factor was obtained by determining the ratio of air and pavement base freeze-thaw cycles in Illinois.[42]

Selection of a Suitable JPCP Transverse Joint Spalling Prediction Model Form

An S-shaped curve was selected to be the characteristic model form for the new JPCP transverse joint spalling model because it is representative of the development and progression of spalling observed when plotting field observations versus time. The S-shaped curve is constrained to ensure that the predicted percentage of joints spalled ranges between 0 and 100. The specific chosen model form is the following:

$$\%SPALL = \left[\frac{AGE}{AGE + 0.01}\right]\frac{C1}{C2 + C3^{(\text{á}*AGE+SF)}} \tag{95}$$

where:

%SPALL = Percentage joints spalled (medium and high severities).
", C1, C2, C3 = Regression constants.
AGE = Time since construction, years.
SF = A scaling factor based on site-, design-, and climate-related variables that significantly influence spalling.

The scaling factor, SF, in equation 95 accounts for the effect of variables that significantly influence the development of spalling, including sealant type, PCC mix properties, PCC air content, air freeze-thaw cycles, precipitation, and PCC slab thickness. The following model form was selected for defining the scaling factor:

$$SF = C_0 + 8_1A_1 + 8_2A_2 + \ldots + 8_nA_n + :_1D_1 + :_2D_2 + \ldots + :_nD_n \tag{96}$$

where:

SF = Scaling factor.
A_i = Climate-related variable.
D_i = Design- and material- related variable.
C_0, 8_i, $:_i$ = Regression constants.

Statistical Tools for Regression and Optimization

Equation 95 is nonlinear; therefore, nonlinear statistical techniques were utilized for calibration. The SAS NLIN procedure was selected as the appropriate regression tool to be used in model development and calibration.[30] Other SAS procedures, such as STEPWISE, REG, RSQUARE, and RSREG, were used in selecting the most suitable variables for incorporation into the model. The SAS NLIN procedure utilized the Marquardt iterative method to optimize the developed spalling model. Further details on the Marquardt procedure can be obtained from the SAS/STAT User's Guide.[30]

Final JPCP Transverse Joint Spalling Model

The final step in the development of the JPCP transverse joint spalling model was the calibration of equations 95 and 96 (using the nonlinear optimization procedure) to obtain specific values for the required regression coefficients. Optimization techniques and regression analysis were used to determine regression coefficients that minimized the error between the predicting and measured spalling values. The specific procedure used was as follows:

1. Assign initial values to the variables and parameters in equations 95 and 96.

2. For those assigned values, perform nonlinear regression analysis to find the values of the spalling prediction model parameters that minimize the error vector, ,.

3. Repeat step 2 for different values of $ until the error vector is minimized and the conversion criteria are met (i.e., error is within acceptable limits).

Based on the successful completion of the iterative optimization process, the final spalling model was determined to be the following:

$$\%SPALL = \left[\frac{AGE}{AGE + 0.01}\right]\left[\frac{100}{1 + 1.005^{(-12*AGE+SF)}}\right] \tag{97}$$

where:

%SPALL = Percentage joints spalled (medium and high severities).
AGE = Time since construction, years.
SF = Scaling factor based on site-, design-, and climate-related variables.

The scaling factor is defined as the following:

$$SF = -1400 + 350 * AIR\% * (0.5 + PREFORM) + 43.4 * f'c^{0.4} - 0.2 * (FTCYC * AGE) + 43 * h_{PCC} - 536 * WC_Ratio \tag{98}$$

where:

AIR% = PCC air content, percent.
AGE = Time since construction, years.
PREFORM = 1 if preformed sealant is present, 0 if other sealant types or no sealant.
f'c = PCC slab compressive strength, psi.
FTCYC = average annual number of air freeze-thaw cycles.
h_{PCC} = PCC slab thickness, in.
WC_Ratio = PCC water/cement ratio.

The diagnostic statistics for the spalling model are as follows:

N = 179.
R^2 = 0.78.
SEE = 6.8 percent of joints.

Plots of the predicted versus measured spalling, and residuals versus predicted spalling, are shown in figures 36 and 37, respectively. The diagnostic statistics and both plots verify that the model is effective for predicting JPCP transverse joint spalling. The R^2 of 78 percent and SEE of 6.8 percent are very reasonable given the large number of LTPP GPS-3 field data (N=146) and CTL laboratory data (N= 33) used in model development.

MODEL VERIFICATION (SENSITIVITY ANALYSIS)

A sensitivity analysis was conducted on the final spalling model to determine its reliability for predicting spalling within and outside of the inference space of the development database. This was accomplished by studying the effects of the various input parameters on the output generated by the spalling model. The ranges of the input values used are presented in table 33. Note that the sensitivity analyses were accomplished by investigating the effects of changing one variable at a time, while holding all other variables at their mean values. The results obtained were compared with past empirical data and theoretical observations.

Table 33. Range of values of data used in sensitivity analysis.

Variable	Range		Mean
	Min.	Max.	
Age, years	0	30	—
PCC thickness, in	8	12	10
Water/cement ratio	0.38	0.50	0.44
Air content, percent	2	7	5.5
Compressive strength, psi	2,500	7,500	5,000
Avg. annual air freeze-thaw cycles	0	160	80
Sealant type	Preformed = 1, No sealant or other type = 0		

Effect of Air Content

Figure 38 shows a significant reduction in predicted joint spalling corresponding to an increase in air content from 2 to 7 percent. This trend clearly agrees with past laboratory observations and other studies that show that increased air content (up to < 12 percent) increases concrete durability and, therefore, reduces durability-related distresses such as spalling.[5]

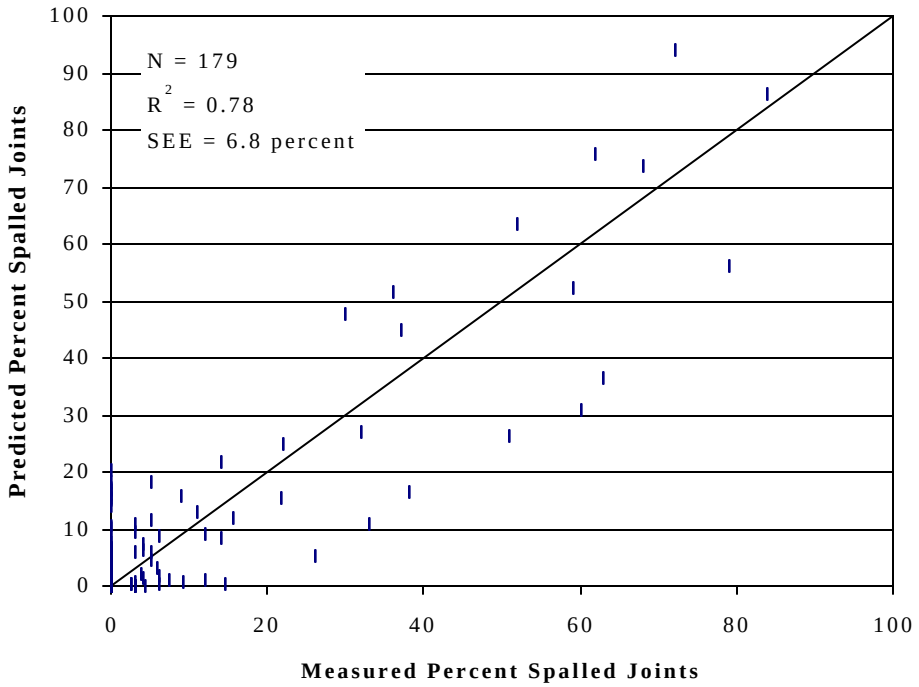

Figure 36. Predicted (equation 97) versus measured spalling for the final JPCP transverse joint spalling model.

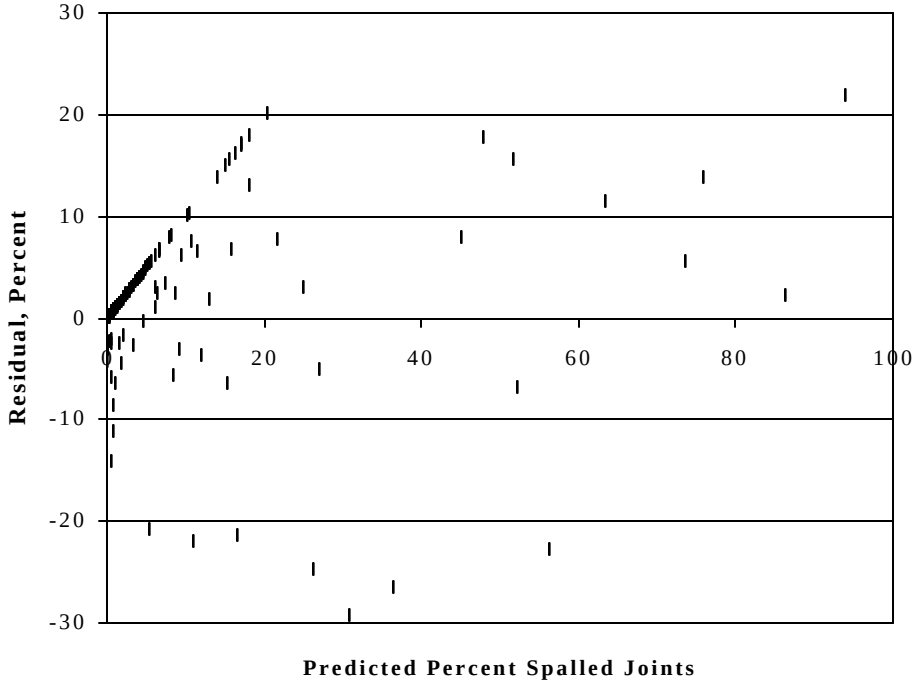

Figure 37. Residual versus predicted (equation 97) spalling for the final JPCP transverse joint spalling model.

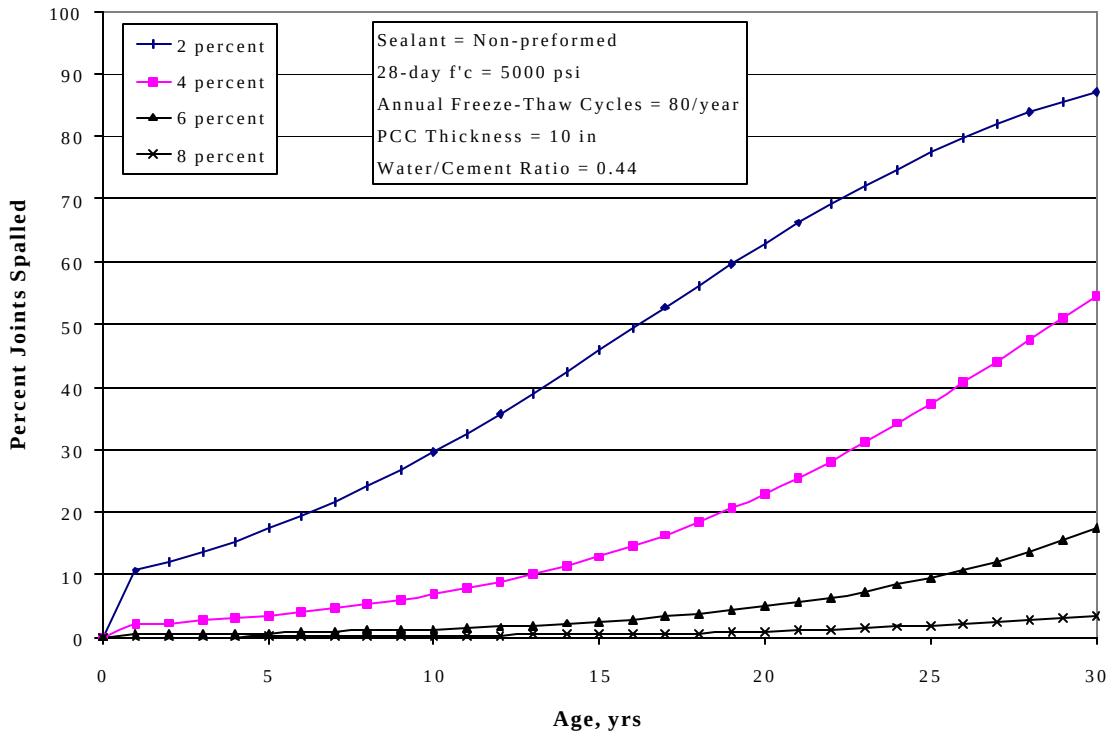

Figure 38. Sensitivity of final JPCP joint spalling model to changes in PCC concrete air content (measured with air pressure meter).

Effect of PCC Compressive Strength

Figure 39 illustrates the sensitivity of the final spalling model to changes in PCC compressive strength. The figure clearly shows that an increase in PCC compressive strength results in a reduction in spalling. This trend is in agreement with observations from the CTL materials study and the trends of the CTL joint spalling model. This also agrees with the mechanistic principle that concrete slabs with high compressive strength have a correspondingly high tensile strength and a reduced potential for spalling.[5]

Effect of Joint Sealant Type

Examination of figure 40 shows the influence of preformed sealants on joint spalling. The figure shows that preformed sealants were better at reducing joint spalling than other types of sealants (or no sealant). The most likely explanation for this benefit is the fact that preformed sealants are effective at preventing incompressibles from infiltrating into the slab joints.[15,16] This effect has been found in several previous studies.

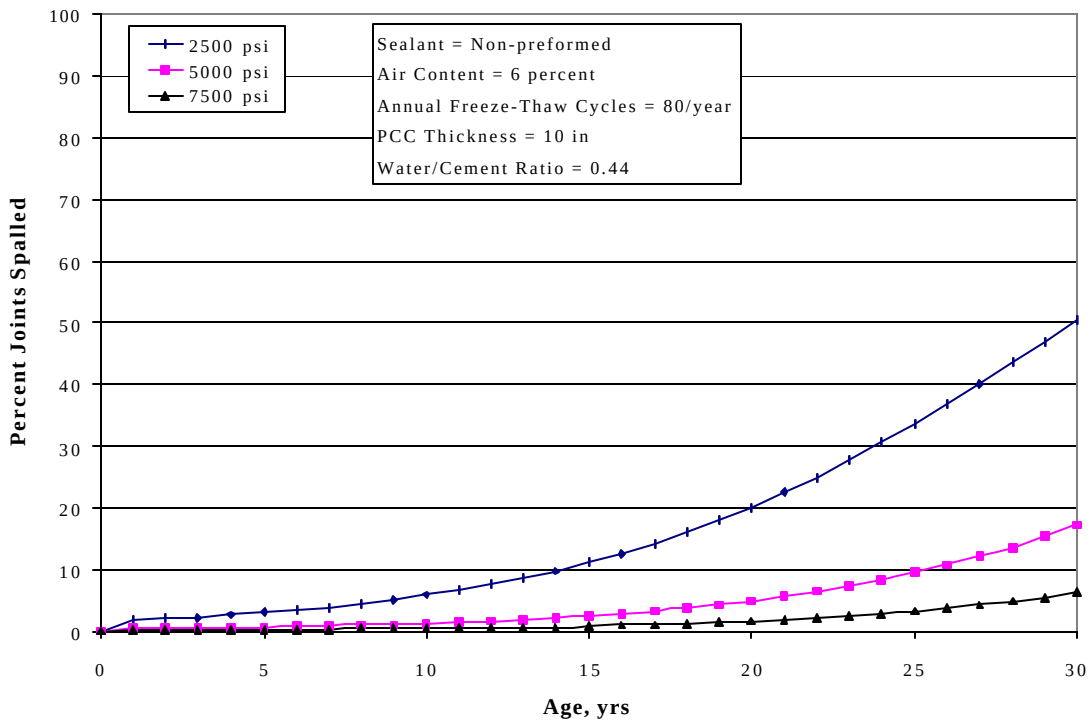

Figure 39. Sensitivity of final JPCP joint spalling model to changes in PCC 28-day compressive strength.

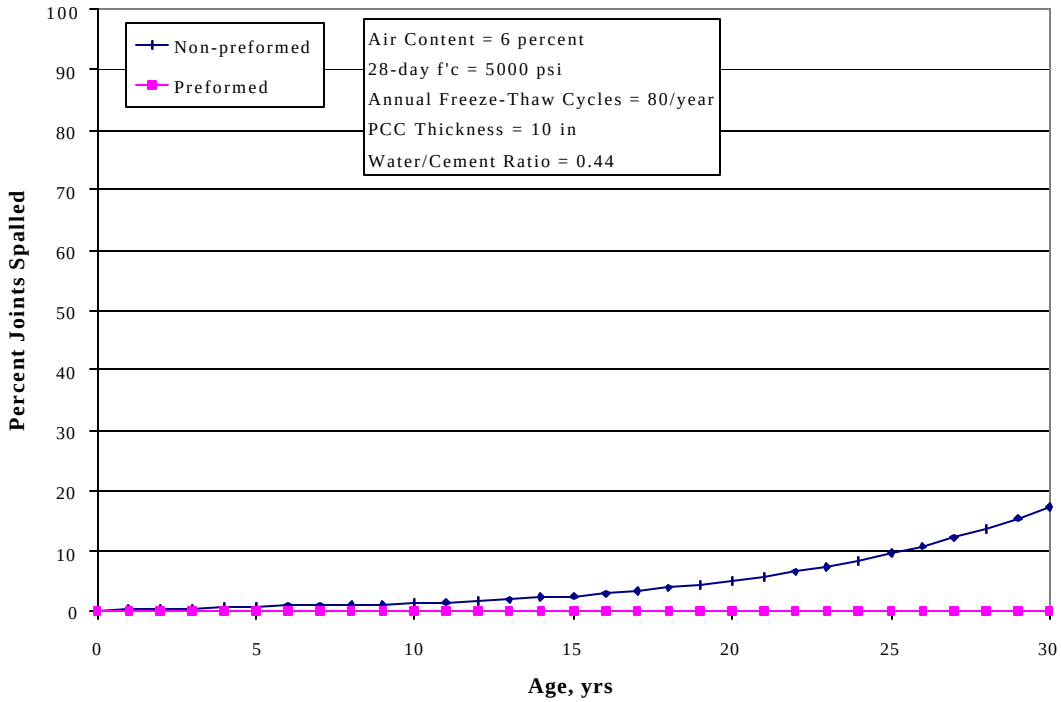

Figure 40. Sensitivity of final JPCP joint spalling model to changes in joint sealant type.

Effect of PCC Slab Thickness

Figure 41 shows that transverse joint spalling increases as slab thickness decreases. This trend is most likely explained by the fact that thicker slabs generally result in stiffer pavements that are less susceptible to excessive deflections and strains under loads.

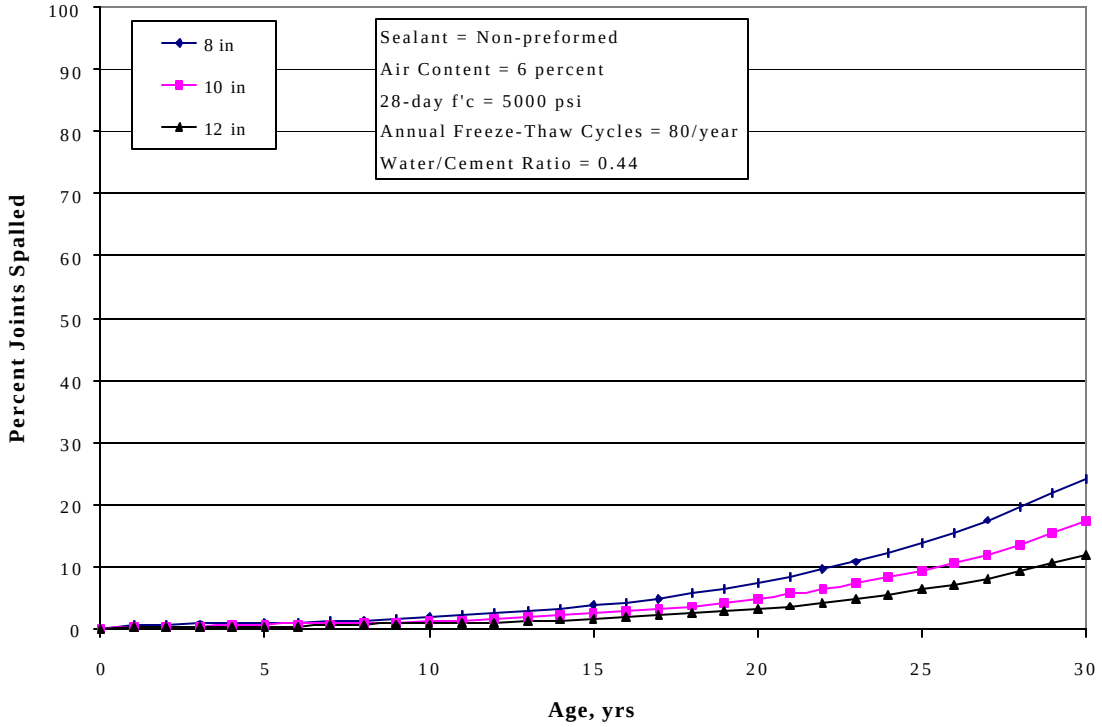

Figure 41. Sensitivity of final JPCP joint spalling model to changes in PCC slab thickness.

Effect of Total Air Freeze-Thaw Cycles

The climate-related variable found to have a significant effect on the prediction of joint spalling for JPCP was the cumulative number of air freeze-thaw cycles. Figure 42 shows the effect of air freeze-thaw cycles on predicted transverse joint spalling. Pavements in the freeze regions exhibited more spalling than those in the nonfreeze regions. Explanations for this trend include the fact that pavements in freeze regions are subjected to repeated freezing and thawing conditions. When water is present in the pores of the concrete, this repeated freezing and thawing typically causes the concrete slab to deteriorate, especially for concrete with lower entrained air contents. In addition, the typical presence of deicing salts on pavements in freeze regions has been found to accelerate the concrete scaling and the subsequent development of spalling.[10,13,15,16]

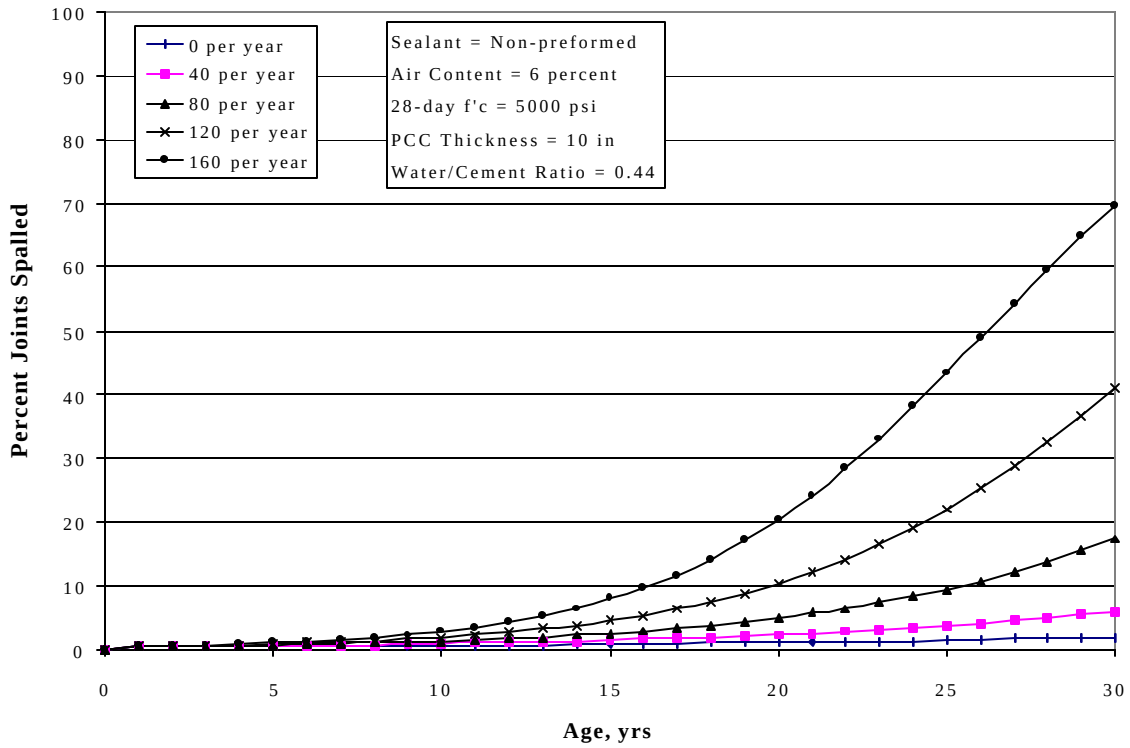

Figure 42. Sensitivity of final JPCP joint spalling model to changes in cumulative air freeze-thaw cycles.

Effect of Water/Cement Ratio

The effect of water / cement ratio on JPCP joint spalling is shown in figure 43. The trends illustrate that as water / cement ratio increases, so does spalling. However, in comparison with other input variables, the sensitivity of the spalling model to changes in water / cement ratio is relatively small.

SUMMARY

A new nonlinear empirical JPCP transverse joint spalling model was developed under this study for use within the current PRS procedure. The model is deemed suitable for use with the current PRS procedure because it incorporates PRS-related AQC's (PCC concrete strength, slab thickness, and air content) and other design-, materials-, and climatic-related variables that were found to significantly influence spalling. The model has a good correlation ($R^2 = 0.78$) and a low SEE (6.8 percent) for a large number of data points (N = 179).

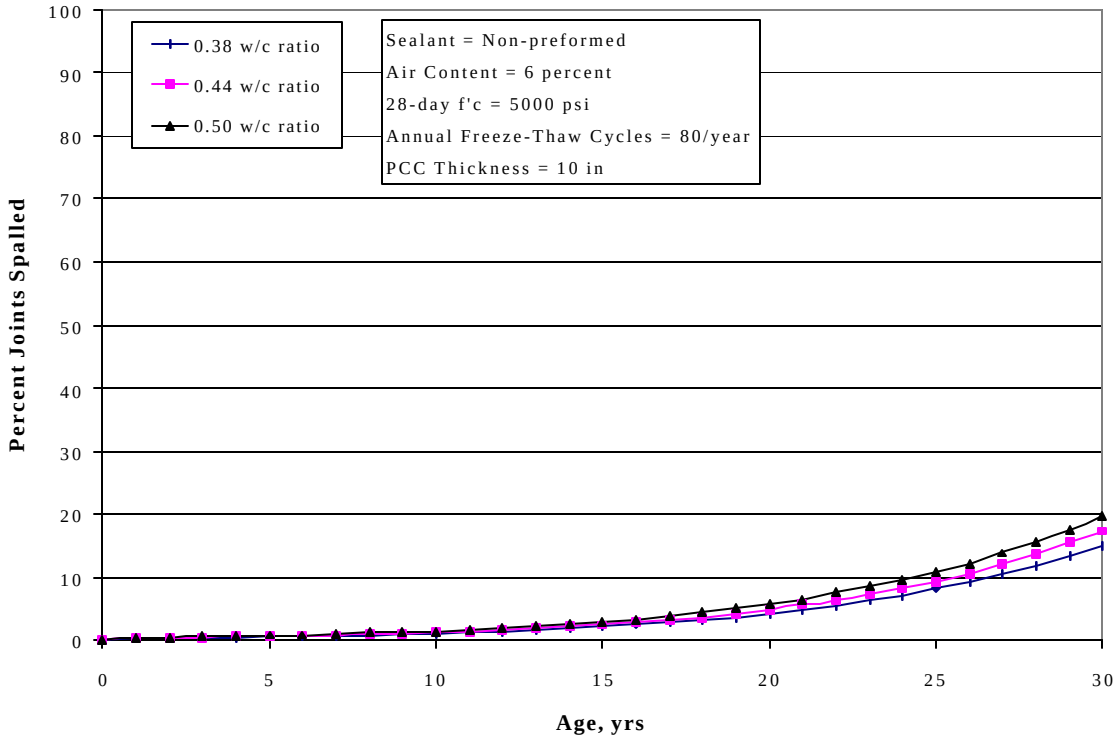

Figure 43. Sensitivity of final JPCP joint spalling model to changes in water-cement ratio.

CHAPTER 7: IRI MODEL

INTRODUCTION

Road roughness has been defined as "the variation in surface elevation that induces vibrations in traversing vehicles."[43] Previous studies have shown that rough roads lead to user discomfort, increased travel times, and higher vehicle operating costs that can lead to millions of dollars in losses to the general economy. Although the structural performance of a pavement is most important to highway designers, users' complaints about rough roads are often a key factor in the rehabilitation decisions that are made by State highway agencies.

Although many objective methods for measuring pavement smoothness have been developed since the AASHO Road Test, the most widely accepted index used today is IRI.[44] IRI is defined as the accumulated suspension vertical motion divided by the distance traveled as obtained from a mathematical model of a simulated quarter-car traversing a measured profile at 80 km / h.[44] Since the World Bank first published guidelines for conducting and calibrating pavement smoothness measurements, IRI has been adopted as a standard for the FHWA Highway Performance Monitoring System (HPMS).[45]

Because of the widespread usage and acceptance of IRI as the smoothness measurement standard for construction and pavement management, the IRI was incorporated into the current PRS methodology (both as a measurement of initial smoothness and for prediction over time). This chapter describes the attempted validation of the chosen best-available IRI model (identified in chapter 2), as well as the specific procedures used in the development of a new IRI model suitable for use within the current PRS methodology (and inclusion into PaveSpec 3.0).

CURRENT PRS IRI MODEL

The selected best-available IRI model was that developed in 1999 by Hoerner et al. and used in the previously developed PaveSpec 2.0 software.[10] This particular model was selected for validation / improvement as it was a function of both initial IRI and key distress indicators. The model was developed using distress data and backcasted initial IRI's (backcasted from time-series IRI data) from the LTPP database. (Note: The model outputs and inputs are presented in English units.)

$$IRI = INITIRI + (4.8389 * Age) - (0.047 * Age * INITIRI) + (0.7165 * \%CRACKED) + (359.956 * FAULT) + (0.3828 * \%SPALL) \quad (99)$$

where:

IRI = International roughness indicator, in / mi.
INITIRI = Initial IRI, in / mi.
Age = Number of years since construction, years.
%CRACKED = Percentage of slabs cracked due to transverse fatigue cracking (expressed as a number between 0 and 100).
FAULT = Average joint faulting per joint, in.
%SPALL = Percentage of medium- and high-severity spalled joints (expressed as a number between 0 and 100).

Statistics:
N = 122.
R^2 = 0.51.
SEE = 28.35 in / mi.

ATTEMPTED VALIDATION OF THE CURRENT PRS IRI MODEL

Before any new model development or calibration techniques were tried, the research team attempted to validate the current PRS IRI model with a new independent data set. The validity of the current IRI model was assessed by:

- Reviewing plots of predicted versus measured IRI.
- Reviewing plots of residuals versus predicted IRI.
- Analyzing diagnostic statistics such as the R^2 and the SEE to determine the goodness-of-fit of the model when the independent data set is used.
- Identifying any general observed weaknesses in the model.

The independent data used in the initial model validation process consisted of JPCP data from the LTPP experiment database (GPS-3 data only). It consisted of 184 time-series points from 81 pavement test sections located in 26 States and 3 Canadian Provinces. A summary of the validation data is presented in table 34.

Table 34. Summary of JPCP LTPP data used in the initial validation of the current IRI model.

Variable	Range		Mean	Standard Deviation
	Min.	Max.		
Initial IRI, in / mi	27.2	164.1	74.9	27.6
Pavement age, years	2.4	33.7	14.1	6.0
Cracked slabs, percent	0.0	65.1	5.3	11.9
Average joint faulting per joint, in	0.00	0.35	0.05	0.07
Spalled joints, percent	0.0	100.0	19.6	30.3

The validation data set was used in the current IRI model to obtain predicted IRI values for each section, while associated measured IRI values were obtained directly from the LTPP database. Figures 44 and 45 show plots of predicted versus measured IRI, and residuals versus predicted IRI, respectively. The key results obtained from the initial validation process were as follows:

- The model form is suitable for inclusion in the PRS methodology as it is a function of both initial IRI and other predicted distress indicators.
- A comparison of the measured and predicted spalling (using the independent LTPP data) showed a low R^2 value of 0.40 percent and a SEE of 27.5 in / mi.
- The plot of residuals versus predicted IRI shows a definite trend, indicating that one or more significant variables are not being considered in the current model.

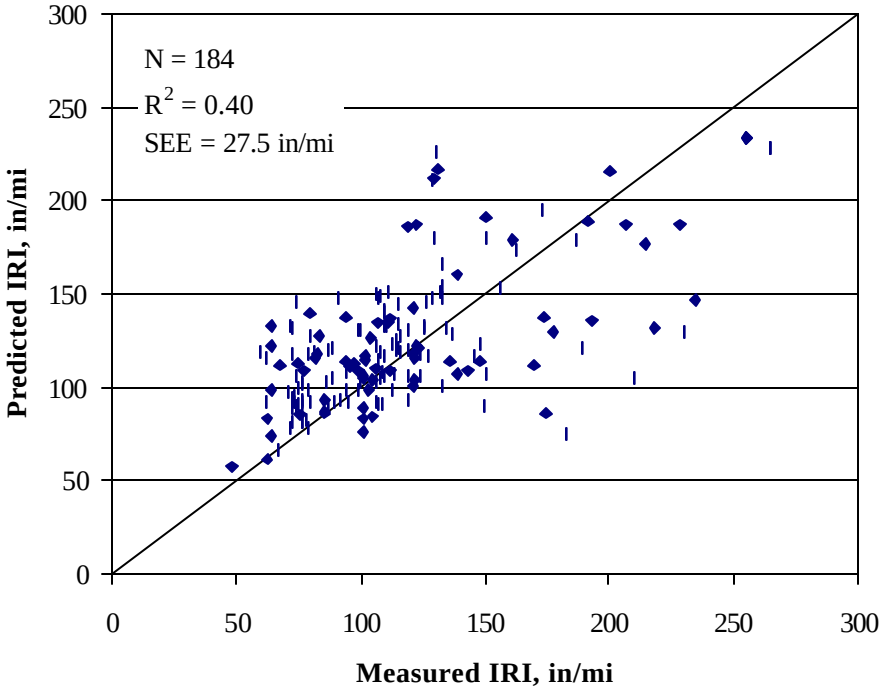

Figure 44. Predicted (equation 99) versus measured JPCP IRI (using the LTPP validation data set).

Given the relatively poor diagnostic statistics and the observed trend in the plot of residuals versus predicted IRI, it was concluded that a simple calibration of the existing model would not significantly improve the model's prediction ability. Therefore, the IRI model improvement effort focused on developing a new IRI model that is a function of initial IRI, other key pavement distress indicators, and additional site and climatic variables. The model was developed using the data available in the newly

compiled PRS national database. The details of the IRI model development effort are described in the following sections.

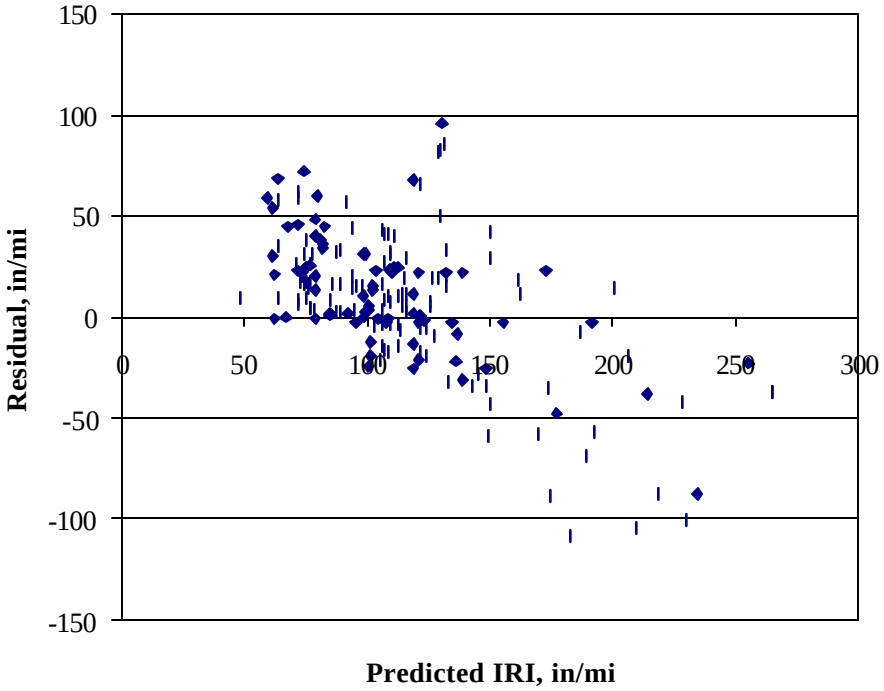

Figure 45. Residual versus predicted (equation 99) JPCP IRI (using the LTPP validation data set).

EXISTING JPCP IRI MODELS

In preparation for the model development process, a number of similar IRI models, developed under previous research studies, were reviewed. A review of previous models not only provided guidance as to what variables should be considered for inclusion in the new model, but also added expert knowledge into the model development process at an early stage. During the review process, specific attention was paid to the engineering significance of the variables. The details of each of these reviewed models are described separately in the following sections.

SHRP P-020 JPCP IRI Models[14]

In a SHRP study conducted by Simpson et al. in 1994, titled *Early Analysis of LTPP General Pavement Studies Data*, two different IRI models were developed—one for doweled JPCP and one for non-doweled JPCP.[14] Each of these models is presented below:

SHRP P-020 IRI Model for JPCP With Dowels

$$IRI = 105.9 + 159.1 * \left(\frac{AGE}{KSTATIC}\right) + 2.167 * JTSPACE - 7.127 * THICK + 13.49 * EDGESUP \quad (100)$$

where:

IRI = International roughness index, in / mi.
AGE = Age since construction, years.
KSTATIC = Mean backcalculated static k-value, psi / in.
JTSPACE = Mean transverse joint spacing, ft.
THICK = Concrete slab thickness, in.
EDGESUP = Edge support (1 = tied PCC shoulder, 0 = any other shoulder type).

Statistics:
N = 21.
R^2 = 0.55.
SEE = 19.06 in / mi.

An analysis of the P-020 doweled IRI model showed that increases in AGE and JTSPACE caused an increase in IRI, whereas increases in KSTATIC and THICK resulted in a decrease in IRI. The only variable that appeared to have a trend that was opposite of what was expected is EDEGSUP. The model indicates that a pavement with a tied PCC shoulder will exhibit higher IRI than a similar pavement with no edge support. No climatic variables were found to be significant enough for inclusion in the model.

SHRP P-020 IRI Model for JPCP Without Dowels

$$IRI = 38.85 + 12.89 * CESAL + 0.2217 * FTCYC + 1.498 * PRECIP - 10.96 * BASE - 13.69 * SUBGRADE \quad (101)$$

where:

IRI = International roughness index, in / mi.
CESAL = Cumulative 80-kN (18-kip) ESAL's in traffic lane, millions.
FTCYC = Mean annual air freeze-thaw cycles.
PRECIP = Mean annual precipitation, in.
BASE = Base type (1 = treated granular material [with asphalt cement] or lean concrete, 0 = untreated granular material).
SUBGRADE = AASHTO subgrade classification (0 = coarse grained [A-1, A-2, A-3], 1 = fine grained [A-4, A-5, A-6, A-7]).

Statistics:

$N = 28.$
$R^2 = 0.64.$
$SEE = 31.29$ in / mi.

The non-doweled IRI model indirectly relates IRI to other distress indicators by making use of the CESAL's variable (other distress indicators typically increase with age or ESAL applications). The model indicates that IRI increases linearly with an increase in CESAL's. The climatic influence on IRI is addressed with the inclusion of FTCYC and PRECIP. Specifically, IRI increases with increases in both FTCYC and PRECIP. The effect of slab support conditions on IRI is accounted for with the inclusion of the BASE and SUBGRADE variables into the model. An investigation of the model shows that pavements with treated base materials will have lower IRI values than pavements with untreated bases, when all other variables are held constant. In addition, the model indicates that pavements constructed on fine-grained subgrades will develop higher IRI values over time than similar pavements constructed on coarse-grained subgrades.

As evidenced by the diagnostic statistics, there is "considerable room for improvement of this model."[14] In addition, several other variables (e.g., transverse joint spacing) that had been identified in previous research studies as having a significant influence on IRI were absent from this model.

LTPP Data Analysis JPCP IRI Model[15]

In 1999, Titus-Glover et al. developed an IRI model for JPCP under an FHWA LTPP data analysis contract.[15] This model is the following:

$$IRI = 82.56 + KESAL^{0.4} * (0.01 * WETDAYS + 0.72 * ZONE) + AGE^{0.4} * (0.00506 * FI + 1.57 * 10^{-6} * E_{PCC} - 3.5 * SUBGRADE - 3.07 * DOWELDIA) \quad (102)$$

where:

IRI = International roughness index, in / mi.
KESAL = Cumulative 80-kN (18-kip) ESAL's in traffic lane, thousands.
WETDAYS = Number of days precipitation is greater than 0.5 in.
ZONE = LTPP climatic zone (1 = freezing climate, 0 = nonfreezing climate).
AGE = Age since construction, years.
FI = Freezing index, °F-days.
E_{PCC} = PCC elastic modulus, psi.
SUBGRADE = Subgrade type (1 = coarse grained, 0 = fine grained).
DOWELDIA = Dowel diameter, in.

Statistics:

N = 155.
R^2 = 0.50.
SEE = 22.0 in / mi.

The review of this IRI model showed that it was a function of traffic and age, as well as many climatic, site, and support condition variables. For the continuous variables, the model showed that increases in KESAL, WETDAYS, AGE, FI, and E_{PCC} caused an increase in IRI, whereas an increase in DOWELDIA resulted in a decrease in IRI. For the ZONE variable, the model indicated that pavements experiencing a freezing climate showed higher IRI values than similar pavements in nonfreeze climates. Similarly, pavements constructed on a fine-grained subgrade had higher IRI values than pavements with coarse-grained subgrades.

FHWA RPPR JPCP IRI Model[16]

The FHWA RPPR study investigated the direct effects of distress on IRI.[16] This model, based on data in the RPPR database, is as follows:

$$IRI = 99.59 + 2.6098 * TFAULT + 2.2802 * TCRACK^3 + 1.8407 * \%SPALL \quad (103)$$

where:

IRI = International Roughness Index, in / mile.
TFAULT = Total cumulated joint faulting per mile, in / mile.
TCRACK = Total number of transverse cracks, number of cracks per mile.
%SPALL = Percentage of joints spalled (medium and high severity), expressed as a number between 0 and 100.

Statistics:
N = 144.
R^2 = 0.61.
SEE = 64.11 in / mile.

A model such as this one is ideal for inclusion in a PRS because of its direct dependence on other developed distress indicators. However, one very serious limitation of the RPPR IRI model is that initial IRI is not included as a direct variable.

Overview of JPCP IRI Models

A review of past JPCP IRI models indicated that increasing quantities and severities of JPCP distress such as faulting, transverse cracking, and joint spalling will greatly contribute to a loss of pavement smoothness (increase in IRI) over time. Each of the reviewed models considers the influence of these distresses directly or indirectly

through the inclusion of many design, site, and climatic variables that influence the development of these other distresses.

One key factor that is especially significant in the prediction of IRI over time is the initial IRI measured at the time of construction.[41,45] Results from the NCHRP 1-31 project showed that future smoothness is significantly related to initial smoothness for all pavement types and AC overlays.[41,45] For PCC pavements, the study found that the initial smoothness significantly affected future smoothness on more than 80 percent of the projects evaluated. This finding suggests that pavements that are constructed smoother will typically stay smoother over time. Other more recent studies have confirmed these results.[46,47]

The review of the previously developed IRI models identified many different variables that influence the occurrence and progression of JPCP distress, and therefore IRI. A summary of those distresses and variables used in past model development efforts (for those models reviewed in this section) is included in table 35. This collective list of variables (or variables related to these) will be considered in the IRI model validation / development procedures.

Table 35. Summary of distresses and variables identified in previous research as significantly affecting JPCP IRI.

Distress/Variable	SHRP P-020[14]	LTPP Data Analysis[15]	RPPR[16]
DISTRESS			
Transverse joint faulting			✓
Transverse slab cracking			✓
Transverse joint spalling			✓
DISTRESS-RELATED VARIABLES			
Age	✓		
Cumulative 80-kN (18-kip) ESAL's	✓	✓	
Mean annual air freeze-thaw cycles	✓		
Mean annual precipitation	✓		
Average annual number of wetdays		✓	
LTPP climatic zone		✓	
Freezing index		✓	
Transverse joint spacing	✓		
PCC slab thickness	✓		
PCC slab elastic modulus		✓	
Base type	✓		
Mean backcalculated modulus of subgrade reaction (k-value)	✓		
Subgrade type	✓	✓	
Presence of tied PCC shoulder	✓		
Dowel diameter		✓	

DEVELOPMENT OF A NEW JPCP IRI MODEL

The specific procedure used in the development and calibration of a new IRI model suitable for use within the current PRS methodology involved the following:

- Preparation of the model development data set.
- Selection of a suitable model form.
- Selection of appropriate statistical tools for regression and optimization.
- Development of the final IRI model.

The tasks are described in greater detail in the following sections.

Data Preparation

The first step in the IRI model development process was the creation of the required model development database. Data preparation and assembly procedures for the development of the IRI model consisted of the following tasks:

1. Identify and retrieve all variables potentially related to the development of JPCP IRI.

2. Identify missing/erroneous data elements and merge LTPP design, climatic, and profile data sets.

3. Backcast initial IRI values from existing IRI time-series data.

4. Explore and clean data.

The details of these steps are described in the following sections.

Database Assembly

In preparation for the calibration steps of the model development process, all pertinent GPS-3 data from the LTPP database were compiled into an IRI model development database. The GPS pavements are existing JPCP sections nominated by State and provincial departments of transportation (DOT) and selected by SHRP and the FHWA's Pavement Performance Division for inclusion into the LTPP data collection program. To meet the experimental criteria, pavement section materials and structural designs must reflect standard engineering practices in the United States and Canada.[48,49,50]

For the data collected and recorded in the LTPP Information Management System (IMS), clear procedures and standards were established and are observed. These procedures help guarantee the consistency and the quality of the data collected. Information is also available showing the data reliability for a set of data. Throughout

the selection, gathering, and recording process, the basic philosophy of the LTPP program has been to provide high-quality data collected in a statistically correct and consistent manner.[48,49,50]

The data sets from the LTPP IMS used in model development are automated/manual distress and longitudinal profile. Automated and manual distress data provide a measure of pavement condition, primarily on the surface. The data include the frequency and severity of distresses such as cracking (longitudinal, transverse, durability), pumping, faulting, joint damage, surface deformation, and surface defects. Maintenance activities such as patching are also recorded.[48,49,50] The primary means used to obtain the surface distress data stored in the LTPP IMS is visual inspection of the pavement surface or visual interpretation of high-resolution 35-mm photographic images of the pavement surface.[48,50] The guidelines for distress data collection are contained in the *Distress Identification Manual for the Long-Term Pavement Performance Project*.[51] The surface distress data are collected every 1 to 2 years.[50]

Longitudinal profile data show the relative elevation of the pavement along the wheel path. The IRI, Mays Index, Root Mean Square Vertical Acceleration (RMSVA), and an approximation of slope variance are also computed from the data. The raw data include the X-Y profile data for at least five repeat runs for each wheelpath. It is stored separately from the statistics.[48,49,50] LTPP regional offices are responsible for collecting longitudinal profile data using profilometers or dipsticks.[51] The longitudinal profile of each LTPP test section is measured approximately once per year. Sections for the detailed study of seasonal effects are tested quarterly every other year.[50]

Data assembly was accomplished using Microsoft Access©, Microsoft Excel©, and the SAS/STAT statistical software.

Identification of Missing/Erroneous Data Elements and Merging of LTPP Data Sets

The second step of the data preparation procedure involved merging the LTPP section design and climatic data with corresponding profile and distress values. Prior to merging, the individual data sets were examined thoroughly to identify missing or erroneous data. As a result of this data review effort, the following were observed:

- The majority of distress and profile survey dates did not coincide (i.e., distress surveys were not conducted on the same days as profile surveys).
- The LTPP profile database contained no initial IRI information.
- The profile data had only minimal errors since they had recently been cleaned as part of the ongoing LTPP data analysis project.
- The faulting data had minimal errors since they had recently been cleaned as part of the ongoing LTPP data analysis project.

- Distress data had some errors, depending on which data set was used (manual or automated). The most reliable distress data for JPCP distress were in the MON_DIS_JPCC_REV table, so this information was used for model development.

Based on these observed results, it was determined that two issues needed to be resolved before a successful merger of the data sets could be accomplished. First, reasonable estimates of initial IRI needed to be determined, and second, discrepancies between survey and profile dates had to be resolved. Two methods were proposed for resolving these issues:

- Assuming that there are no significant changes in measured profile or distress within 120 days of data collection, profile and distress data collected during this period can be merged with minimal error.

- Models could be developed based on the pavement age and measured IRI for each pavement section with time-series IRI data, then used to estimate IRI corresponding to distress survey dates by interpolation or extrapolation. The models developed may also be used for obtaining estimates of initial IRI by extrapolating to age = 0 years.

The second method was adopted for use in estimating initial IRI, as well as IRI at the time of distress surveys.

Backcasting of Initial IRI Values

As noted, the LTPP database did not contain initial IRI values. Therefore, initial IRI had to be backcasted from IRI time-series data. The specific process chosen to backcast initial IRI values was as follows:

1. Determine a suitable model form for backcasting initial IRI.

2. Backcast initial IRI values for each pavement section using available time-series IRI data.

3. Evaluate the reasonableness of backcasted initial IRI values by reviewing trends and slopes of time-series data, comparing backcasted values with measured initial IRI from LTPP SPS pavement sections, and reviewing diagnostic statistics from the fitted model.

4. Compare the distribution (mean and variance) of backcasted initial IRI to typical initial IRI values measured from newly constructed LTPP SPS pavement sections.

Various model forms (e.g., linear, exponential, logarithmic, and polynomial) were evaluated for backcasting initial IRI with pavement age as the independent variable and measured IRI as the dependent variable. The functional form was thus:

$$IRI = f(age) \tag{104}$$

Initial IRI was therefore the IRI at age = 0 years. The typical pavement section used in the analysis was more than 10 years old and had three or more time-series data points. Using a linear model for backcasting initial smoothness was found to be the most practical since there were no available data close to the construction date (less than 3 years). The linear model form used for interpolating and extrapolating smoothness values was as follows:

$$IRI = \text{"}AGE + \$ \tag{105}$$

where:

" = Slope.
AGE = Pavement age, in years.
$ = Regression constant equivalent to initial smoothness.

Figure 46 shows an example of a linear model fitted to IRI time-series data for the purpose of backcasting an initial IRI value.

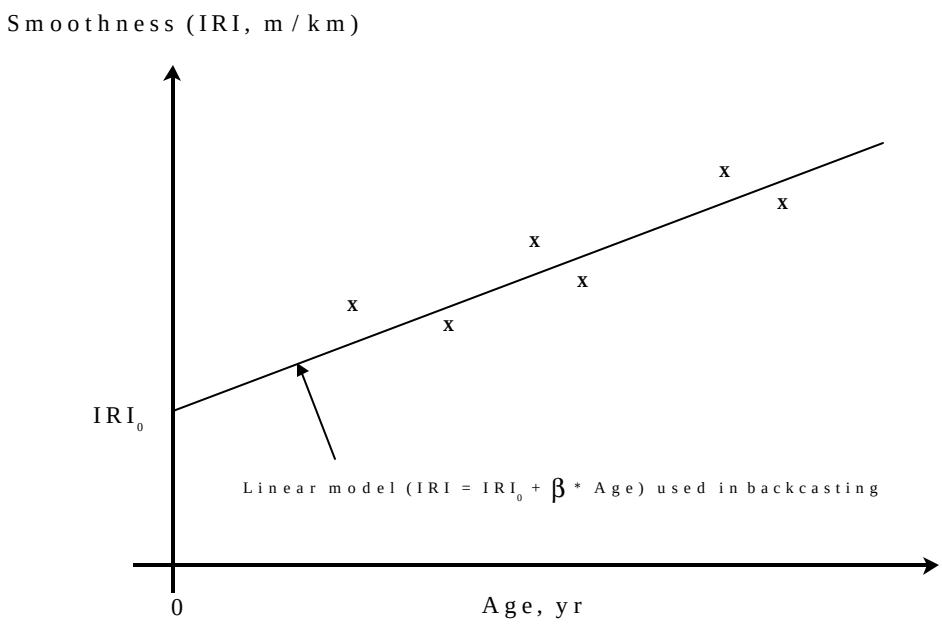

Figure 46. Example of the linear model method used to backcast an initial IRI from time-series data.

The reasonableness of the backcasted initial IRI values was evaluated by determining:

- If there was a significant difference in mean initial IRI values for the backcasted JPCP data and reference-measured initial IRI data.

- If there was a significant difference in variance in the backcasted and measured data sets.
- If the diagnostic statistics of the linear models used in interpolating or extrapolating IRI values are reasonable.

The reference-measured initial IRI values used for comparison were obtained from the LTPP SPS database. IRI values measured within the first 12 months of pavement construction were used. Analysis of variance (ANOVA) and t-test comparisons were used in determining if there were significant differences in the means and variance from the reference-measured and backcasted initial IRI values. The results are presented in table 36. The t-test results for comparison of the mean initial IRI and variance values show that there are no significant differences between measured initial IRI (from SPS pavements) and backcasted initial IRI for JPCP. Backcasted initial IRI for JPCP showed a higher variance than that of the measured SPS data; however, the variance was not excessive (as shown in figure 47).

Table 36. Summary of t-test results for the comparison of measured and backcasted initial IRI for JPCP.

Data Set	N	Mean IRI	Std. Dev. IRI	Std. Error IRI	Min. IRI	Max. IRI
Backcasted (GPS-3)	73	1.227	0.39	0.0465	0.389	2.246
Measured (SPS)	97	1.252	0.28	0.0288	0.758	2.094
Variances	T		DF		Prob> |T|	
Unequal	-0.4608		124.2		0.6457	
Equal	-0.4826		168.0		0.6300	
For H_0: variances are equal, F' = 1.96 DF = (72,96) Prob>F' = 0.0021						

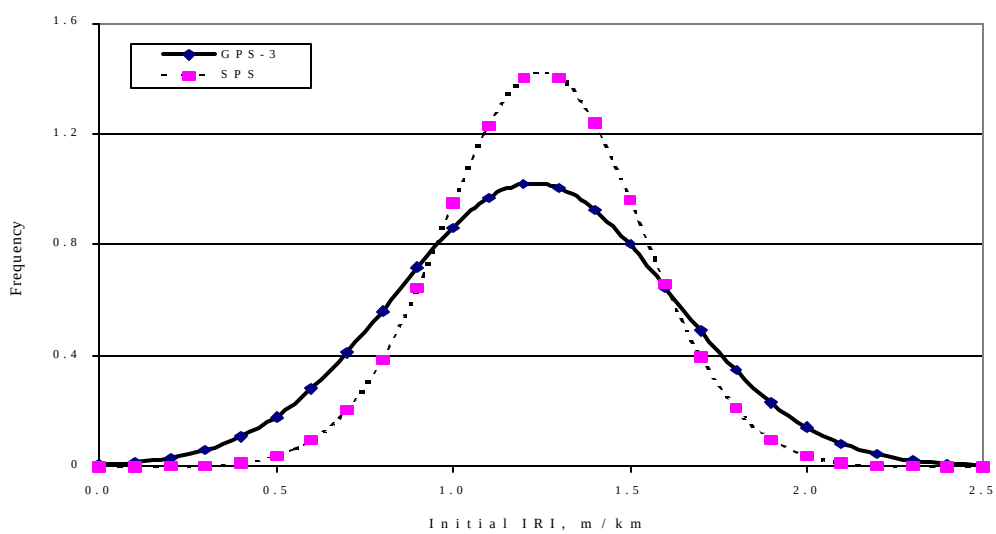

Figure 47. Initial IRI distribution for measured (SPS) and backcasted JPCP (GPS-3) data.

Measured initial IRI for SPS sections generally ranged from 0.5 to 2.0 m/km. This range of values was adopted as the reasonable range for backcasted values, and values out of this range were assumed to be outliers.

The final step in evaluating the quality of the backcasted initial smoothness values was to determine if there was any correlation between the backcasted initial IRI values and the current age of pavement sections. Bivariate plots of initial smoothness versus age were developed for the LTPP GPS-3 data to determine if there was any correlation. Figure 48 shows no significant trends between initial IRI and age for JPCP. The backcasted data were therefore determined to be suitable for model development.

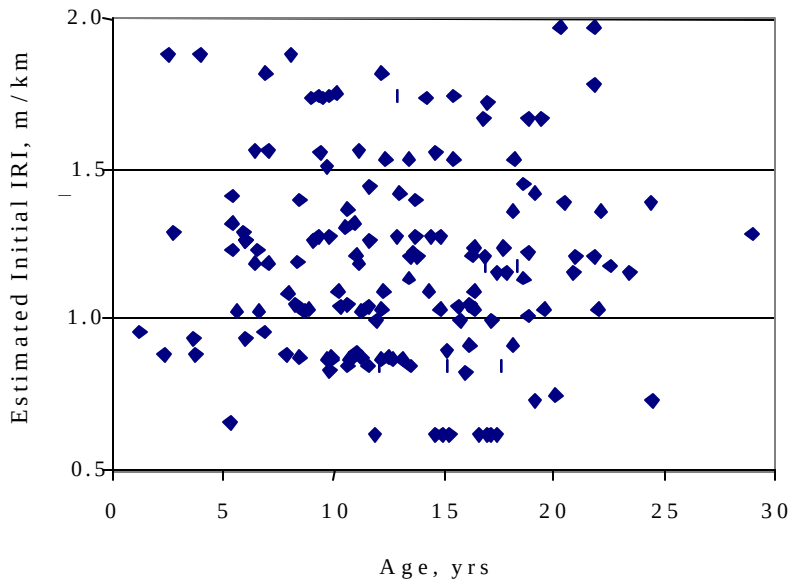

Figure 48. Plot of estimated initial backcasted IRI versus section age for JPCP.

After the data were merged, the assembled database was evaluated to identify possible problem spots (such as time-series data with a significant decrease in IRI with time). Attempts were made to obtain replacements for missing data where possible. The data set was also checked and cleaned for anomalies and gross data error. A summary of the variables initially considered for inclusion into the new IRI model, and their statistical characteristics, is presented in table 37.

Selection of a Suitable JPCP IRI Prediction Model Form

Clearly, several pavement distresses have a significant effect on IRI and should be used in modeling and predicting IRI over time. The general hypothesis to be used in the proposed IRI model is that the various distresses resulting in significant changes in IRI should be represented by separate components within the model. The chosen structure for the IRI model is the following:

Table 37. Summary of GPS-3 JPCP data considered in the IRI model development and calibration procedures.

Distress/Variable	Range		Mean
	Min.	Max.	
Transverse cracking,[1] percent slabs	0	42	3
Corner cracks,[1] percent slabs	0	20	1
Transverse joint spalling,[2] percent joints	0	100	16
Total transverse joint faulting, mm/km	0	1367	230
Annual mean temperature, °C	5.1	21.8	10.2
Freezing index, °C days	0	1862	301
Percent subgrade passing 0.075-mm sieve	1	98	39.5
Annual mean precipitation, mm	142	1542	897
IRI (estimated initial), m/km	0.4	1.8	1.2
IRI (measured overtime), m/km	0.8	3.6	1.7

[1] Transverse cracking and corner cracks (all severities) were combined to estimate total cracking.

[2] Only medium- and high-severity spalling were considered.

$$IRI(t) = IRI_0 + a_1 D(t)_1 + a_2 D(t)_2 + \ldots\ldots\ldots\ldots + a_n D(t)_n + b_n SITE(t) \quad (106)$$

where:

$IRI(t)$ = Pavement IRI over time, in m/km.
IRI_0 = Initial IRI, in m/km.
a_i, b_j = Regression constants.
$D(t)_I$ = i^{th} distress at a given time.
$SITE(t)$ = Site factor at a given time.

The general model form proposed was based on existing smoothness models that show an additive combination of initial smoothness and the development of distresses over time.

Empirical studies have identified several pavement site conditions (climate, subgrade, and traffic) that affect smoothness. Such identified variables can be used as the basis for developing mechanistic clusters for improving smoothness predicted from distress alone. Some of the site condition variables that affect smoothness are as follows:

- Traffic.
- Age.
- Freezing index.
- Subgrade soil type.
- Annual mean temperature.
- Number of air freeze-thaw cycles.

- Mean annual precipitation.
- Number of wet days.

The general hypothesis to be used in the proposed smoothness models is that a site factor (SITE) defined by the properties of the pavement location (e.g., age, freezing index, subgrade soil type) will significantly improve on the prediction capability of the models. The proposed structure of the site factor is as follows:

$$SITE = \$ * AGE * (A_1 * A_2 * \ldots A_n) \quad (107)$$

where:

SITE = Site factor.
AGE = Pavement age, years.
A_i = Variables representing the temperature, moisture, and subgrade properties at the pavement location.

Statistical Tools for Regression and Optimization

The SAS NLIN was selected as the appropriate regression tool to be used in final model calibration because the procedure is versatile and allows for constraining model coefficients where required (e.g., initial IRI should always have a coefficient of 1.0).[30] Other SAS procedures, such as STEPWISE, REG, RSQUARE, and RSREG, were used in preliminary model development for determining and selecting the most suitable variables for incorporation into the final model. The SAS NLIN Marquardt algorithm was used in the optimization of the IRI model.

Final JPCP IRI Model

The assembled JPCP data were explored to learn more about the suitability of individual distresses (at different levels of severity) for model development. The final model form was determined by conducting a comprehensive stepwise regression analysis of the cleaned data in order to evaluate the preliminary relationships between the measured smoothness, backcasted initial smoothness, and distress. A site factor (SITE) was included in the model as a method of incorporating the effects of age, freezing index, and percent subgrade passing 0.075-mm (#200) sieve. The final JPCP IRI model is as follows (Note: the final IRI model is expressed in metric units):

$$IRI = IRI_0 + 0.013 * \%CRACKED + 0.007 * \%SPALL + 0.001 * TFAULT + 0.03 * SITE \quad (108)$$

where:

IRI_0 = Initial smoothness measured as IRI, m/km.

%CRACKED = Percentage of slabs with transverse cracking and corner cracks (all severities) (expressed as a number between 0 and 100).

%SPALL = Percentage of joints with spalling (medium and high severities) (expressed as a number between 0 and 100).

TFAULT = Total joint faulting cumulated per km, mm.

SITE = Site factor = $AGE * (1 + FI)^{1.5} * (1+P_{0.075}) * 10^{-6}$.

AGE = Pavement age since construction, years.

FI = Freezing index, °C-days.

$P_{0.075}$ = Percentage of subgrade material passing the 0.075-mm (#200) sieve (expressed as a number between 0 and 100).

Statistics:

N = 183.

R^2 = 0.70.

SEE = 0.35 m / km.

Additional model development statistics are presented in table 38. Plots of predicted versus actual IRI and residuals versus predicted IRI are presented in figures 49 and 50, respectively. The R^2 and other diagnostic statistics for the model are reasonable and verify that the model provides reasonable predictions of IRI for JPCP.

Table 38. Diagnostic statistics for JPCP IRI model.

Distress Variable	Severities	t_{calc} for H_0: Parameter = 0	Probability $t_{calc} > t_{0.05}$	Is Distress/Site Variable Significant?*
Initial IRI	—	9.569	0.0001	Yes
Cracking	(L, M, H)	1.99	0.0481	Yes
Transverse joint spalling	(M, H)	2.955	0.0036	Yes
Faulting	—	13.836	0.0001	Yes
Site factor	—	10.735	0.0001	Yes
* Significance level = 5 percent.				

MODEL VERIFICATION (SENSITIVITY ANALYSIS)

A sensitivity analysis was conducted on the final IRI model to determine its reliability for predicting IRI within and outside of the inference space of the database used in model development. This was accomplished by studying the effects of the various input parameters on the output generated by the final IRI model.

Effect of Initial IRI

Initial IRI is not only an indicator of overall quality of construction, but all other things being equal, new pavements constructed with a lower IRI (smoother profile) will last longer than those constructed with a higher IRI. An analysis of the JPCP data

contained in the LTPP database shows that initial IRI typically ranges from 0.5 to 2.0 m/km.[47] Figure 51 illustrates the sensitivity of the final IRI model to changes in initial IRI and percent cracked slabs.

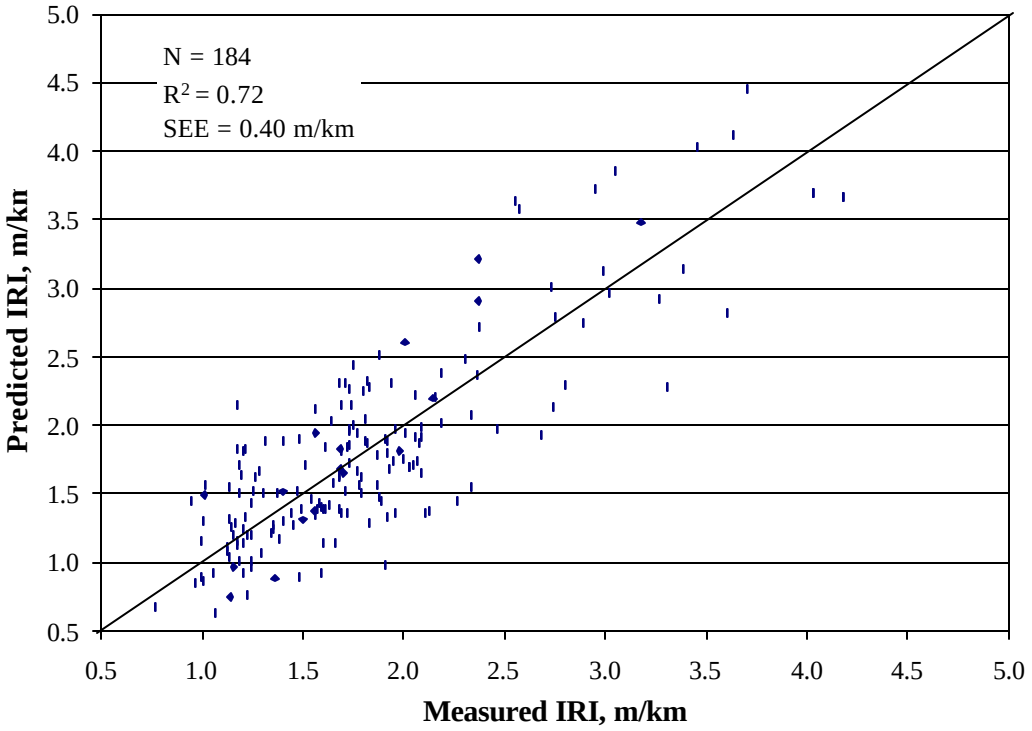

Figure 49. Predicted (equation 108) versus measured IRI for the final JPCP IRI model.

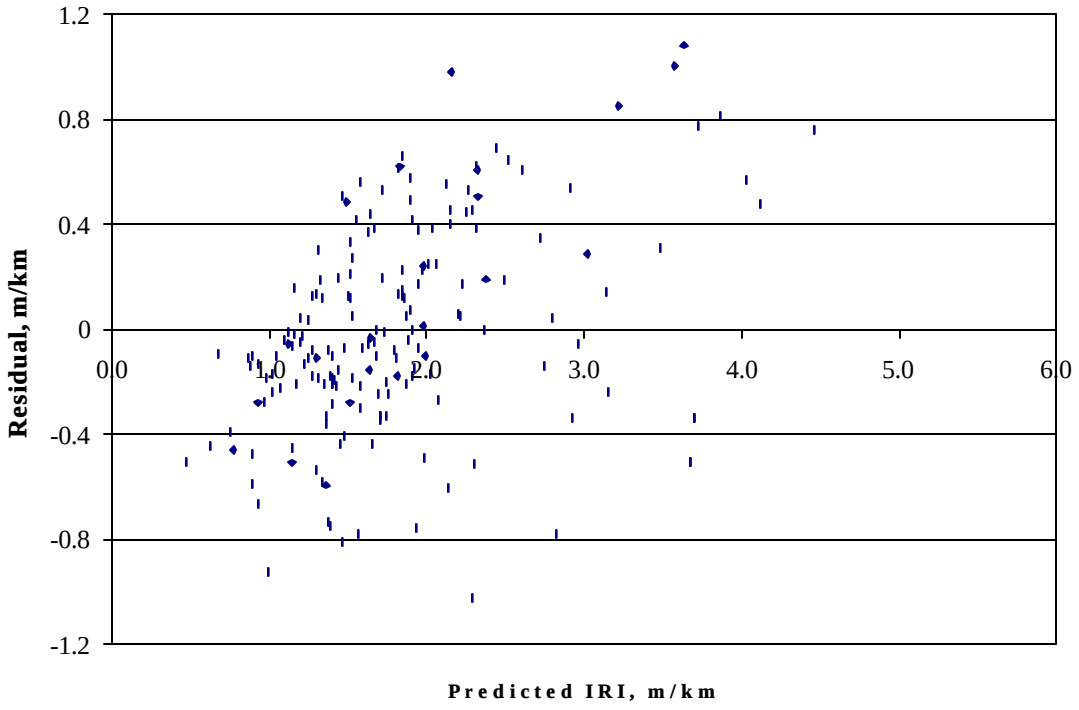

Figure 50. Residuals versus predicted (equation 108) IRI for the final JPCP IRI model.

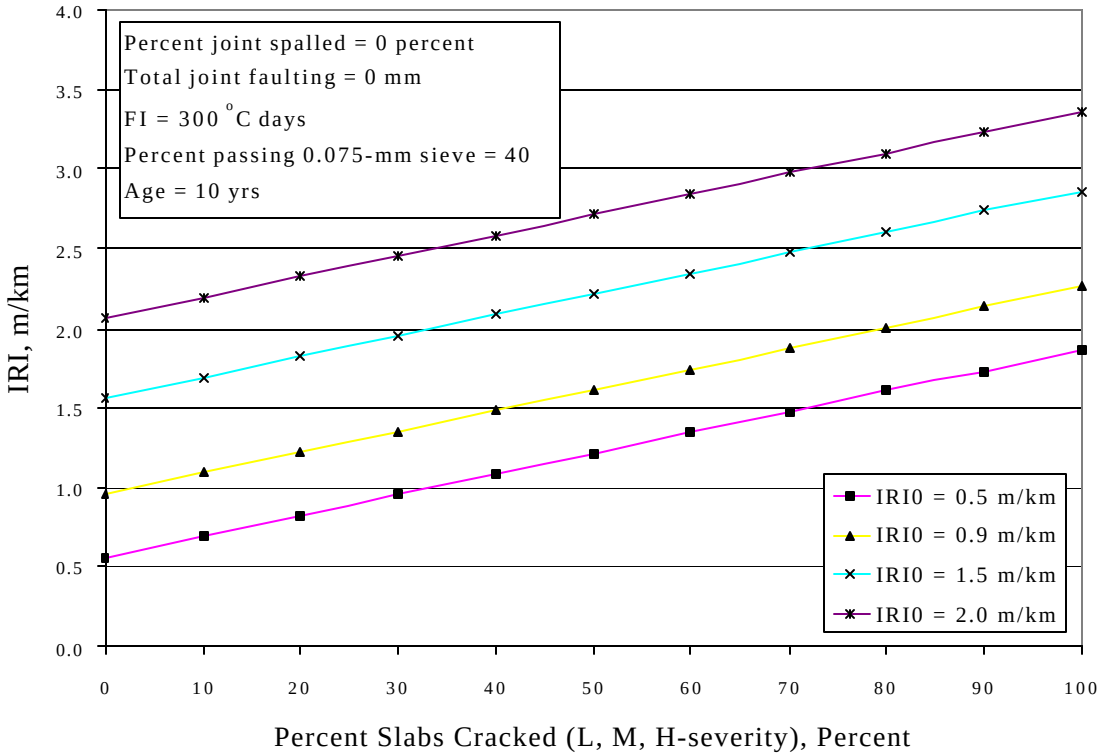

Figure 51. Sensitivity of the final JPCP IRI model to changes in initial IRI and percent cracked slabs.

Effect of Transverse Slab Cracking

Transverse cracks can occur at the midslab of JPCP slabs parallel to the joint. Typically, midslab cracks begin as a single crack at the edge of the slab that propagates through the entire slab as traffic is applied to the pavement.[15,52] Transverse cracks increase pavement roughness as the cracks fault and spall and there is a general breakup of the pavement.[15,52] This decreases serviceability and results in costly rehabilitation. Transverse cracks, especially when they are badly spalled, also cause surface runoff from rainfall to infiltrate the pavement structure, which normally results in erosion of the base and faulting, increasing deflections and resulting in an additional increase in IRI.[52]

Cracks are not always perpendicular to the centerline of the pavement but can occur close to the joint, diagonally from the slab shoulder edge of the pavement to the joint. This form of cracking is called corner cracks.[51] Corner cracks normally are initiated from the top of the PCC slab and progress downward (i.e., top-down cracking) as the pavement foundation erodes, load transfer across the joint is poor, the slab is curled up at the corner, and the pavement corners are subjected to heavy wheel loads.[13] This results in excessive deflection of the slab corners and a corresponding increase in the

tensile stresses at the top of the PCC slab. The tensile stresses cause the initiation of micro-cracks, and repeated loading propagates these cracks through the PCC slab.

The occurrence of corner cracks results in an increase in IRI because the developed cracks typically fault and spall, leading to a general breakup and deterioration of the pavement. This decreases serviceability and user comfort and results in costly rehabilitation. Once corner cracks become badly spalled, they contribute to joint deterioration, resulting in joint seal damage, infiltration of water into the pavement foundation, pumping, and faulting.

The effect of percent slabs cracked (transverse and corner) on IRI over time was shown previously in figure 51. Specifically, this plot shows that IRI increases as the percentage of slabs with cracking increases for any given age. This plot confirms the trends observed in previous research.[16]

Effect of Transverse Joint Spalling

As was stated in chapter 6, spalling is the breakdown or disintegration of a PCC slab's edges at transverse joints, usually resulting in the removal of sound concrete.[15,41] Several field studies have observed that joint spalling may be due to the deterioration of the concrete material from environmental factors and from infiltration of incompressibles.[16,19]

Spalling (medium and high severity) eventually causes a decrease in the smoothness of the pavement, resulting in a need for costly rehabilitation. Figure 52 shows the effect of the percentage of joints spalled (and initial IRI) on the development of IRI over time.

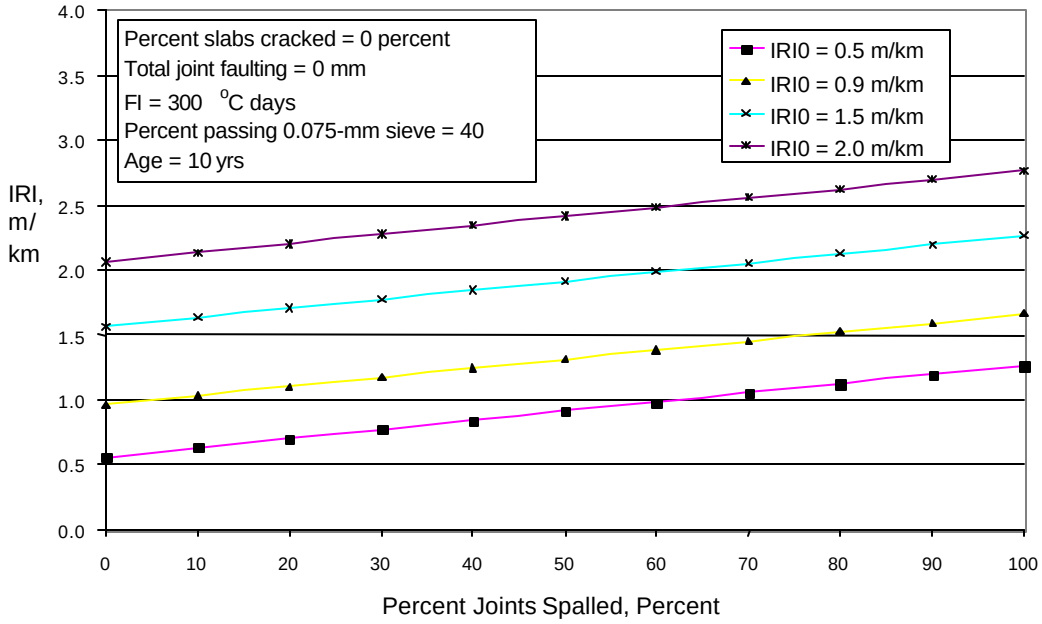

Figure 52. Sensitivity of the final JPCP IRI model to changes in percent joints spalled and initial IRI.

Effect of Transverse Joint Faulting

As was discussed in chapter 4, faulting is the result of a combination of poor load transfer across a joint or crack, heavy axle loads, free moisture beneath the pavement, and pumping of the supporting base, subbase, or subgrade material from underneath the slab.[15,53] It is primarily caused by the erosion of the supporting material from underneath the leave slab or treated base and a buildup of the loose material under the approach slab at a joint or crack. It is the difference in elevation between the adjacent slabs across a transverse joint or crack. Excessive faulting will greatly reduce the smoothness of a JPCP and will appreciably increase user discomfort. The influence of pavement joint faulting on smoothness of JPCP, as depicted by the model, is shown in figure 53.

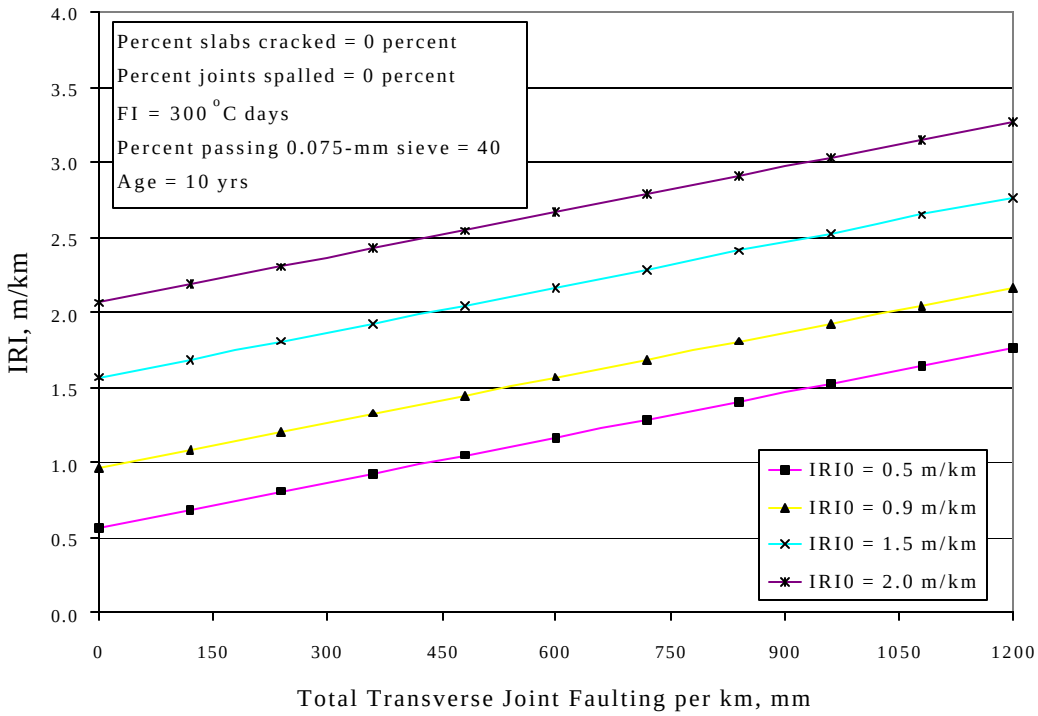

Figure 53. Sensitivity of the final JPCP IRI model to changes in total joint faulting per km and initial IRI.

Effect of Pavement Site Conditions

The influence of pavement site conditions on JPCP IRI is depicted by including a cluster of site-related variables in the IRI prediction model. Freezing index and percent subgrade material passing the 0.075-mm (#200) sieve were found to be two site-related variables that significantly influence IRI.

Freezing index was multiplied by pavement age to provide a cumulative freezing index experienced by the pavement. Age can also be assumed to account for the

presence of distresses such as settlement, frost heave, swelling soils, scaling, and durability problems that are not included in the smoothness model. Pavement age is therefore an alias variable accounting for the effects of hidden factors that influence pavement smoothness.

Figures 54 and 55 show that IRI increases with increases in freezing index and amount of subgrade fines (percent passing the 0.075-mm sieve), respectively.

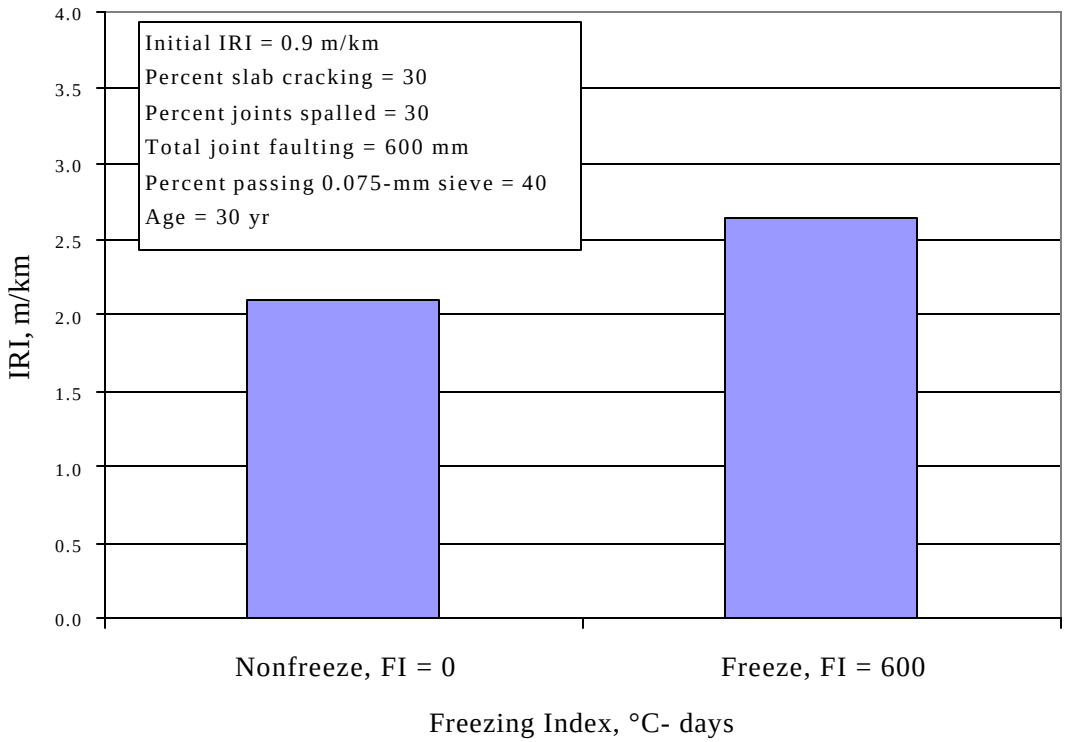

Figure 54. Effect of freezing index on JPCP IRI after 30 years.

SUMMARY

A new distress-based empirical JPCP IRI model was developed under this study for use within the current PRS procedure. The model is deemed suitable for use because it directly incorporates initial smoothness (a PRS AQC) and other JPCP distresses and variables that were found to significantly influence the development of IRI over time. The JPCP model was evaluated and verified using statistical techniques and by performing comprehensive sensitivity analyses. The sensitivity analyses confirm that the final IRI model is in agreement with sound engineering principles and judgment. The model has a good fit ($R^2 = 0.72$) and a low SEE of 0.40 m/km for a large number of data points (N=184).

One aspect of this new IRI model is that initial smoothness is expressed as an initial IRI. Many SHA's are currently in the process of adopting the use of lightweight

profilers that measure initial IRI directly on newly constructed PCC pavements; however, the majority of SHA's continue to use other types of more traditional equipment (e.g., California profilograph) to accomplish this task. The research team recognizes this potential difficulty and, therefore, has included information on

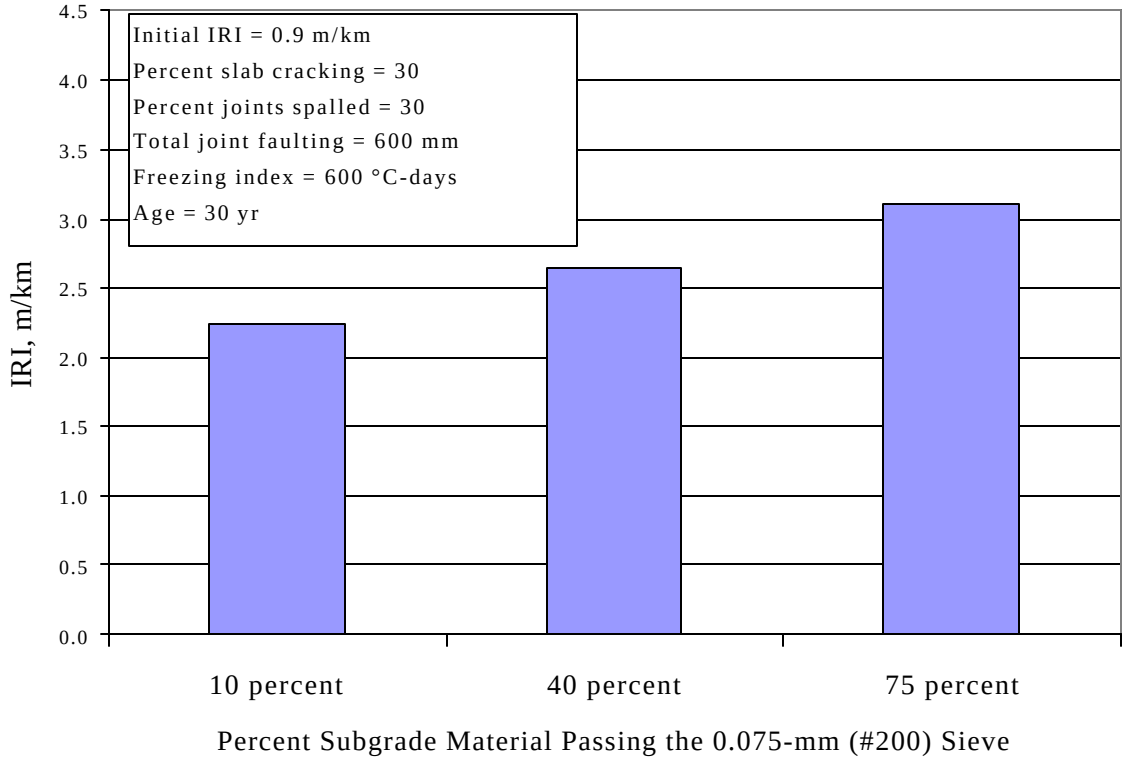

Figure 55. Effect of subgrade percent passing 0.075-mm sieve on JPCP IRI after 30 years.

relationships that can be used to estimate initial IRI based on some of the more common construction smoothness indices (see chapter 8, Development of Initial Smoothness Relationships).

CHAPTER 8: DEVELOPMENT OF INITIAL SMOOTHNESS RELATIONSHIPS

INTRODUCTION

The pavement smoothness model to be incorporated into the PRS process is based upon IRI. The model asserts that the IRI at any given time in a pavement's life is a function of its as-constructed or initial IRI, age and predicted key distresses at that time, and certain site factors.

Some SHA's are now using IRI directly to measure the smoothness of newly built PCC pavements, due to the introduction of inertial profilers, particularly lightweight systems, into the construction acceptance arena. However, many agencies still use profilographs to measure initial smoothness and assess compliance with profile index (PI)-based smoothness specifications. For these agencies, there is a real need to include in the updated PRS a reliable set of PI-to-IRI conversion equations. Such equations will enable the PaveSpec program user to quickly transform sublot PI values collected in the field to closely approximated IRI values, which will then be used to predict service lives and subsequently influence pay factors.

The relationship between PI and IRI can be somewhat clouded because the equipment and processes used to produce the two values are quite different. As will be discussed later, the most significant differences relate to 1) the reference profiles from which the two indexes are computed, 2) the type of sensors used, and 3) the degree and type of wavelength filtering done to produce PI and IRI values.

Although both indexes relate fairly well to user response to roughness, their correlation to each other is not as strong because different roughness components (i.e., short bumps, long dips) are amplified or attenuated in computing each index.[54] As various studies have indicated, the correlation of PI and IRI becomes progressively higher with the application of smaller and smaller blanking band widths (i.e., from 5-mm [0.2-in] blanking band to 0-mm [0.0-in] blanking band).[55,56,57] The larger blanking band widths have the obvious effect of masking more roughness.

In recognition of the problems described above, a concerted effort was made to establish practical relationships that link the commonly used initial smoothness statistic PI with the IRI statistic used in the PRS pavement smoothness-over-time model. Specifically, the following relationships were sought in this work effort:

- IRI as a function of PI determined using a 5-mm (0.2-in) blanking band (herein denoted as $PI_{5\text{-mm}}$ ($PI_{0.2\text{-in}}$).

- IRI as a function of PI determined using a 2.5-mm (0.1-in) blanking band (herein denoted as $PI_{2.5\text{-mm}}$ ($PI_{0.1\text{-in}}$).

- IRI as a function of PI determined using a zero blanking band (herein denoted as $PI_{0.0}$).

The approach toward accomplishing these objectives was twofold. First, a preliminary investigation was staged, consisting of a detailed literature search/review and the collection and correlation analysis of actual smoothness data. Next, a comprehensive analysis of LTPP smoothness data was performed, whereby profile data on many GPS-3, SPS-2, and SPS-4 test sections were transformed into PI values using commercial profilograph simulation software. The resulting PI values were then compared with the IRI values previously computed and recorded in the LTPP database.

The details of each IRI–PI investigation are presented in this chapter, following a short discussion of the current state of the practice for initial smoothness testing and subsequent smoothness monitoring. Based on the overall results of both investigations, recommended PI-to-IRI conversion equations are offered that can be used in the absence of more reliable agency-derived formulas.

BACKGROUND

Initial Smoothness Testing

For four decades, the profilograph has served as a construction quality control tool for highway pavements.[56] First developed by Francis Hveem in 1940 and first implemented into a specification by the California Department of Highways in 1960, it became one of the benchmark pieces of pavement smoothness testing equipment in the 1970's, and remains so to this day. Though predominantly used by highway agencies to test the initial smoothness of concrete pavements, many agencies have also used the profilograph for new asphalt pavements and asphalt overlays.

Past national surveys on the practice of measuring initial pavement smoothness indicated a significant trend toward the use of profilographs. While a 1987 AASHTO survey showed that 11 and 69 percent of all States used a profilograph to test asphalt and concrete pavements, respectively, a similar 1994 NCHRP survey showed these percentages increased to 36 and 75 percent.[45,58] Both surveys also showed overwhelming use of the California-type profilograph and the calculation of $PI_{5\text{-mm}}$.

The widespread use of the profilograph over the years is living testimony to its success, and its success is due in large part to the following factors:

- Relatively inexpensive to purchase and operate.

- Portability.
- Accuracy in identifying localized bumps.
- Ability to reasonably assess ride quality.
- Computerized profile measurement and trace reduction and analysis (beginning in the mid-1980's).

In essence, the profilograph has provided agencies with a tool to quantify and specify pavement smoothness. This, in turn, has helped fuel the drive for smoother and smoother pavements.

In recent years, new demands from the pavement community have perhaps begun to foreshadow the use of profilographs as construction quality control devices. Key among these demands are the following:[45]

- Accuracy—More restrictive smoothness specifications and specifications containing incentive / disincentive payment provisions have resulted in a need for greater accuracy (i.e., precision and bias) in the measurement of the pavement profile. Because profilographs have a short, fixed baselength (typically 7.6 m [25 ft]), the profile traces they generate represent somewhat skewed versions of the true profile.

- Speed—The need for quicker assessment of initial smoothness is making the slow operating speed (3 to 5 km / hr [2 to 3 mi / hr]) of the profilograph less tolerable. This is helping open the door to high-speed profilers capable of operating at speeds in excess of 50 km / hr (30 mi / hr).

- Relation to user response—Greater emphasis has been placed on correlating smoothness measurements with user response to roughness (i.e., the highway user's perception of ride quality). Because profilographs amplify and attenuate certain critical wavelengths in the pavement profile, there is concern about how well the profilograph output relates to the wavelengths that are felt by highway users.

- Compatibility with smoothness monitoring indexes—With thousands of lane-kilometers of pavement being evaluated annually or biennially for network-level pavement management system (PMS) purposes, high-speed measurement using sophisticated profiling equipment has become the norm. This has forced initial smoothness measurements to be made with the same type of high-speed profiling equipment used in pavement management, or to be made with a device that is highly correlated to the PMS high-speed profiler.

Although the AASHTO and NCHRP surveys showed increased use of the profilograph between 1987 and 1994, they also showed an increase in usage of inertial profilers (0 to 6 percent for asphalt pavements, 3 to 6 percent for concrete pavements).

More significantly, since the 1994 survey, the interest in inertial profilers for construction acceptance testing has skyrocketed. At least 15 States, including Arizona, Colorado, Florida, Kansas, Michigan, and South Dakota, have begun allowing the use of inertial profilers on new construction jobs; several others are either encouraging their use or are in the process of investigating their use.

Also of significance is the movement toward the reduction or elimination of blanking bands in the computation of PI. Many States, such as Louisiana and Missouri, have followed the lead of Kansas, which in 1992 implemented a $PI_{0.0}$ specification for its PCC pavements. This is considered a major improvement in smoothness specifications.

Though the trend of construction acceptance testing appears to be moving away from the use of profilographs and toward the use of inertial profilers and IRI, the up-front and operational expense of these inertial devices, as well as their complexities, may cause the trend to be somewhat gradual in the short term. Hence, profilographs should see continued use for at least a few years to come.

Smoothness Monitoring

Pavement smoothness over time is a vital component of the pavement management process. By knowing the smoothness trends of many individual pavement sections within a network, pavement managers can identify which pavements are approaching a maximum tolerance level for roughness and can reasonably predict the time until those pavements reach the established threshold. This information, in turn, helps in the development of a coherent, long-term maintenance and rehabilitation (M&R) program for the pavement network.

Key to the pavement smoothness monitoring process are the equipment and procedures used to collect and report smoothness data. Without accurate, time-stable smoothness measurements, the ability to predict future smoothness and develop a sound M&R program is seriously compromised. Although past methods of smoothness testing (e.g., Bureau of Public Roads [BPR] Roughometer, PCA Roadmeter, Mays Ride Meter) may have met the needs of their era, only the inertial-type profilers so common today are capable of providing the high-speed, quality measurements needed for pavement management.

A 1998 survey of State practices showed that a large majority of States (36 of 37 total respondents) used inertial profilers to collect smoothness data.[59] Of the 13 non-responding States, at least four had reported using inertial profilers in the 1994 NCHRP survey.[45]

Though many different profiler models are currently being used, the most popular are the International Cybernetics Corporation (ICC) profiler and the Roadware profiler,

each being used by 10 or more States.[59] IRI is the statistic of choice for computing and reporting pavement smoothness using the inertial profilers for nearly all of these agencies.

With respect to sensor types, profilers with laser sensors are the most popular. Two-thirds of the States responding to the 1998 smoothness survey indicated using this type of sensor over ultrasonic, infrared, or incandescent sensors. In the matter of profile filtering, most States use a 91.4-m (300-ft) filter—prior to roughness index calculation—to remove long wavelengths that do not cause discomfort to highway users.[59] And, lastly, in the calculation of the chosen roughness statistic, a majority of States use the profile data collected on both the left and right wheelpaths of a given travel lane.

It can be seen from these survey statistics that SHA's have set a course for the future that includes high-speed, inertial-based profiling and utilization of the IRI statistic. However, the fact that many different models of profilers are being used and are commercially available, and that each model uses different profile measurement instruments (e.g., sensors, accelerometers, distance measuring instruments [DMI's]) and profile filtering methods, may result in less consistency among States with respect to the measurement of smoothness.

PRELIMINARY INVESTIGATION—PAST STUDIES ON SMOOTHNESS RELATIONSHIPS

To begin this investigation, a fairly extensive literature search was performed focusing on National- and State-sponsored pavement smoothness studies conducted in the past 15 years. The search resulted in the collection of more than 50 reports, papers, or articles on the topic; however, only a small portion dealt specifically with the correlation of IRI and PI. Even fewer involved the correlation of these indexes based solely on the testing of JPCP.

Presented in this section are synopses of five documented studies and the PI-to-IRI correlations developed in those studies. Though some of the studies included examination of PI values obtained with a Rainhart profilograph, only the PI-to-IRI correlations associated with the California profilograph are featured, because of the California system’s predominant use.

Pennsylvania Transportation Institute Profilograph Calibration Study[58]

As part of a major effort to develop calibration procedures for profilographs and evaluate equipment for measuring the smoothness of new pavement surfaces, the Pennsylvania Transportation Institute (PTI) conducted a full-scale field testing program on behalf of the FHWA. Concrete and asphalt pavements at five different locations throughout Pennsylvania were selected for the experiment; each pavement was new or newly surfaced. Multiple 0.16-km- (0.1-mi-) long pavement sections were established at each location, resulting in 26 individual test sections over which 2 different types of profilographs (California and Rainhart), a Mays Meter, and an inertial profiler were operated. The resulting smoothness measurements were evaluated for correlation.

Figure 56 shows the relationship between the inertial profiler IRI and the $PI_{5\text{-mm}}$ ($PI_{0.2\text{-in}}$) determined manually from the California-type profilograph. As can be seen, the resulting linear regression equation had a coefficient of determination (R^2) of 0.57. Figure 57 shows the relationship between the inertial profiler IRI and the computer-

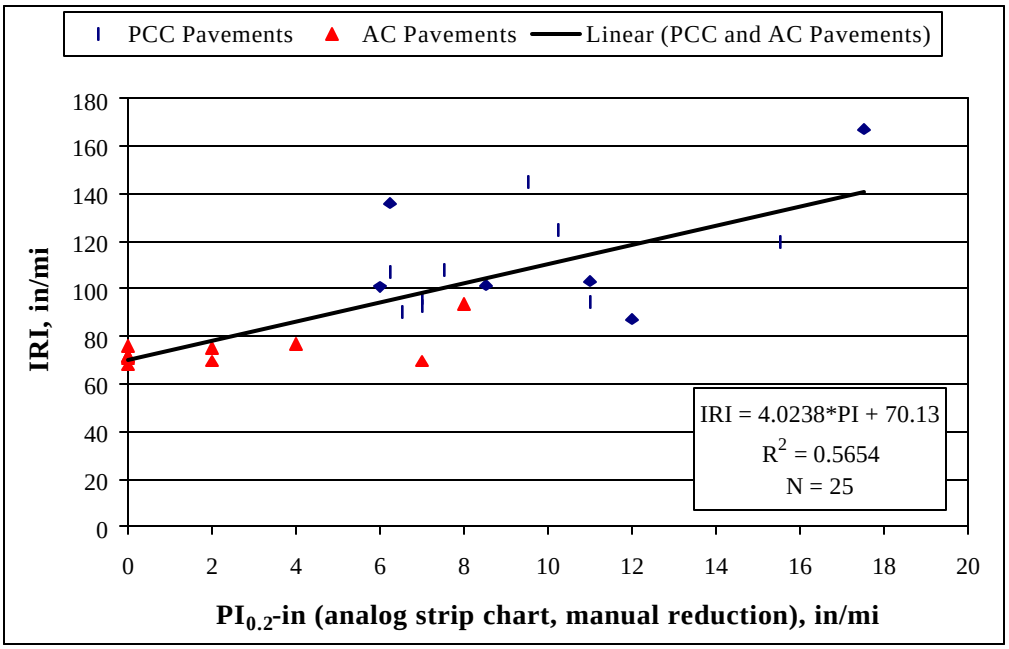

Figure 56. Relationship between IRI and manually generated PI in PTI profilograph calibration study.[58]

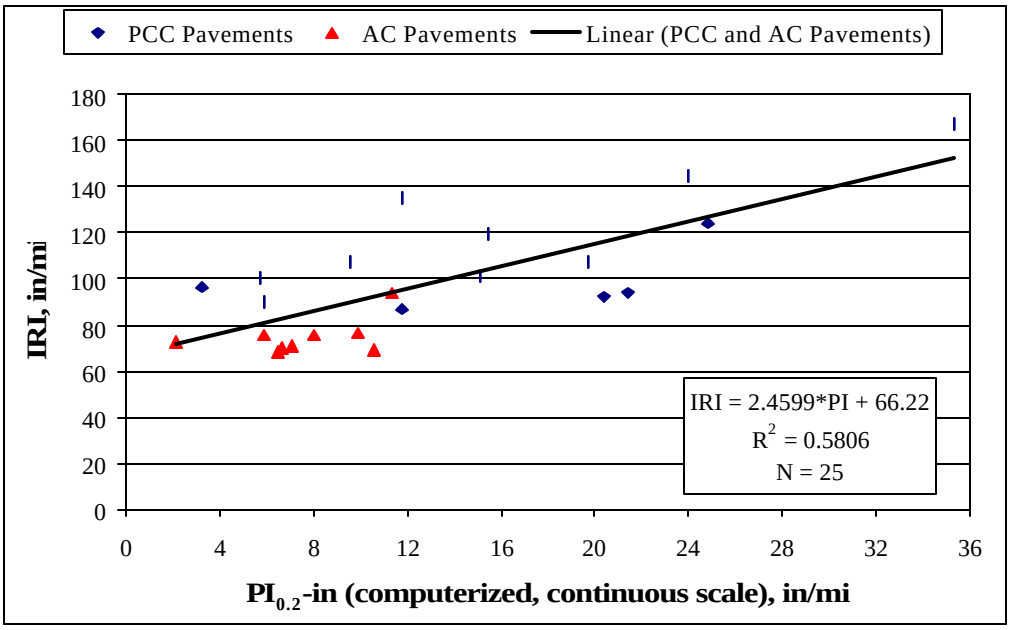

Figure 57. Relationship between IRI and computer-generated PI in PTI profilograph calibration study.[58]

generated $PI_{5\text{-mm}}$ from the California-type profilograph. Although the resulting linear regression equation had a similar coefficient of determination ($R^2 = 0.58$), its slope was considerably flatter. For any given IRI, the data show a wide range of $PI_{5\text{-mm}}$ ($PI_{0.2\text{-in}}$).

Although both of these relationships were based on measurements from both concrete and asphalt pavement sections, neither one is considerably different from regressions based solely on data from the concrete sections.

Arizona DOT Initial Smoothness Study[60]

In 1992, the Arizona DOT initiated a study to determine the feasibility of including their K.J. Law 690 DNC Profilometer (optical-based inertial profiler) as one of the principal smoothness measuring devices for measuring initial pavement smoothness on PCC pavements. At the time, the DOT used a Cox California-type profilograph to test newly constructed PCC pavements for compliance with construction smoothness standards.

To examine the correlative strength of the Profilometer outputs (IRI) and the profilograph (PI), a group of 12, 0.16-km (0.1-mi) pavement sections around the Phoenix area were selected for testing. The smoothness levels of the sections spanned a range that is typical of newly built concrete pavement—$PI_{5\text{-mm}}$ ($PI_{0.2\text{-in}}$) between 0 and 0.24 m/km (15 in/mi). A total of three smoothness measurements were made with the Profilometer over each wheelpath of each selected section, whereas a total of five measurements were made by the profilograph over each wheelpath of each section. The mean values of each set of three or five measurements were then used to correlate the IRI and PI values.

Simple linear regression analyses performed between the left wheelpath, right wheelpath, and both wheelpath sets of values indicated generally good correlation between the two indexes. Figure 58 shows the scatter plots of each group, as well as the regression line associated with the both wheelpath data group. As can be seen, the R^2 for the both wheelpath regression line was very high (0.93).

University of Texas Smoothness Specification Study[56]

In the course of developing new smoothness specifications for rigid and flexible pavements in Texas, researchers at the University of Texas conducted a detailed field investigation comparing the McCracken California-type profilograph and the Face Dipstick, a manual Class I profile measurement device. The two devices were used to collect smoothness measurements on 18 sections of roadway consisting of both asphalt and concrete pavements. For both devices, only one test per wheelpath was performed.

Results of linear regression analysis showed a strong correlation ($R^2 = 0.92$) between the IRI and $PI_{0.2\text{-in}}$ values. The resulting linear regression equation had a higher intercept

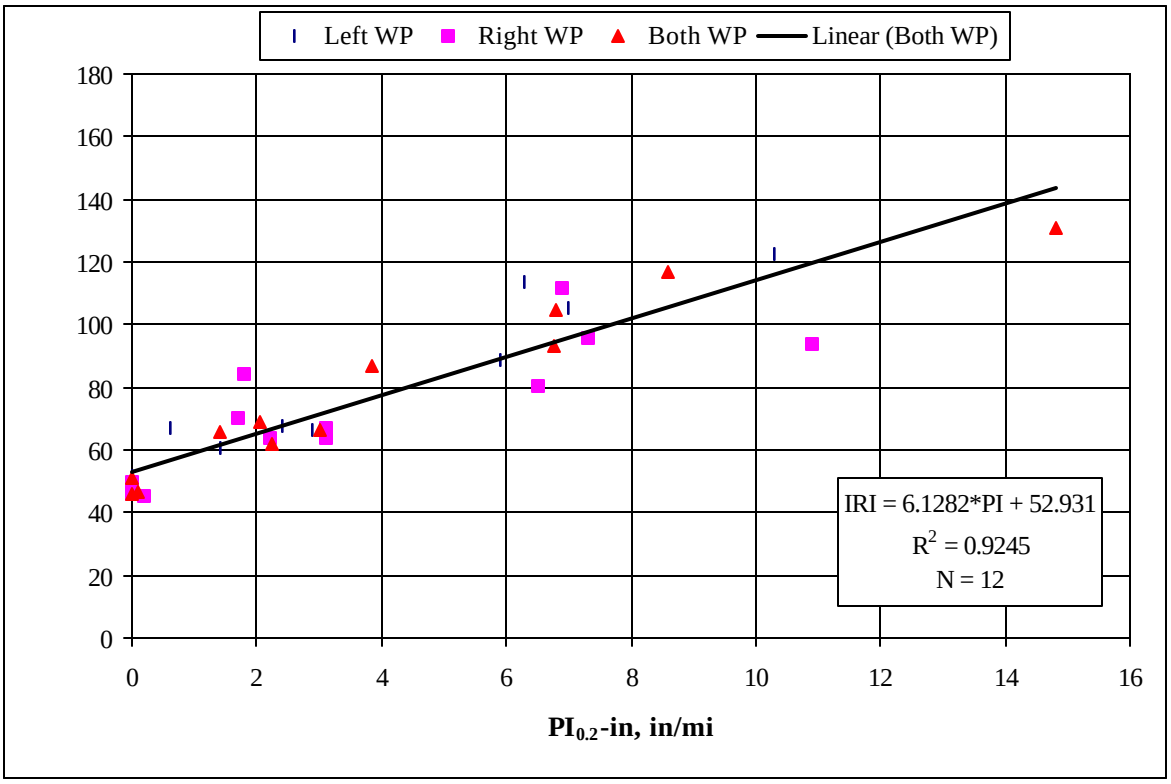

Figure 58. Correlation of IRI and PI in Arizona pavement smoothness study.[60]

value than those obtained in the PTI and Arizona DOT studies, while the slope of the equation was more in line with the slopes generated in the PTI study.

Florida DOT Ride Quality Equipment Comparison Study[61]

Looking to upgrade its smoothness testing and acceptance process for flexible pavements, the Florida DOT undertook a study designed to compare its current testing method (rolling straightedge) with other available methods, including the California profilograph and the high-speed inertial profiler. A total of 12, 0.81-km- (0.5-mi-) long pavement sections located on various Florida State highways were chosen for testing. All but one of the sections represented newly constructed or resurfaced asphalt pavements.

The left and right wheelpaths of each test section were measured for smoothness by each piece of equipment. The resulting smoothness values associated with each wheelpath were then averaged, yielding the values to be used for comparing the different pieces of equipment.

The inertial profiler used in the study was a model manufactured by ICC. Because one of the objectives of the study was to evaluate different technologies, the ICC inertial profiler was equipped with both laser and ultrasonic sensors. Separate runs were made with each sensor type, producing two sets of IRI data for comparison.

Figure 59 shows the relationships developed between the profilograph $PI_{5\text{-mm}}$ ($PI_{0.2\text{-in}}$) and the IRI values respectively derived from the laser and ultrasonic sensors. As can be seen, both correlations were fairly strong (R^2 values of 0.88 and 0.67), and the linear regression equations were somewhat similar in terms of slope. As is often the case, however, the ultrasonic-based smoothness measurements were consistently higher than the laser-based measurements, because of the added sensitivity to items such as surface texture, cracking, and temperature. This resulted in a higher y-intercept for the ultrasonic-based system.

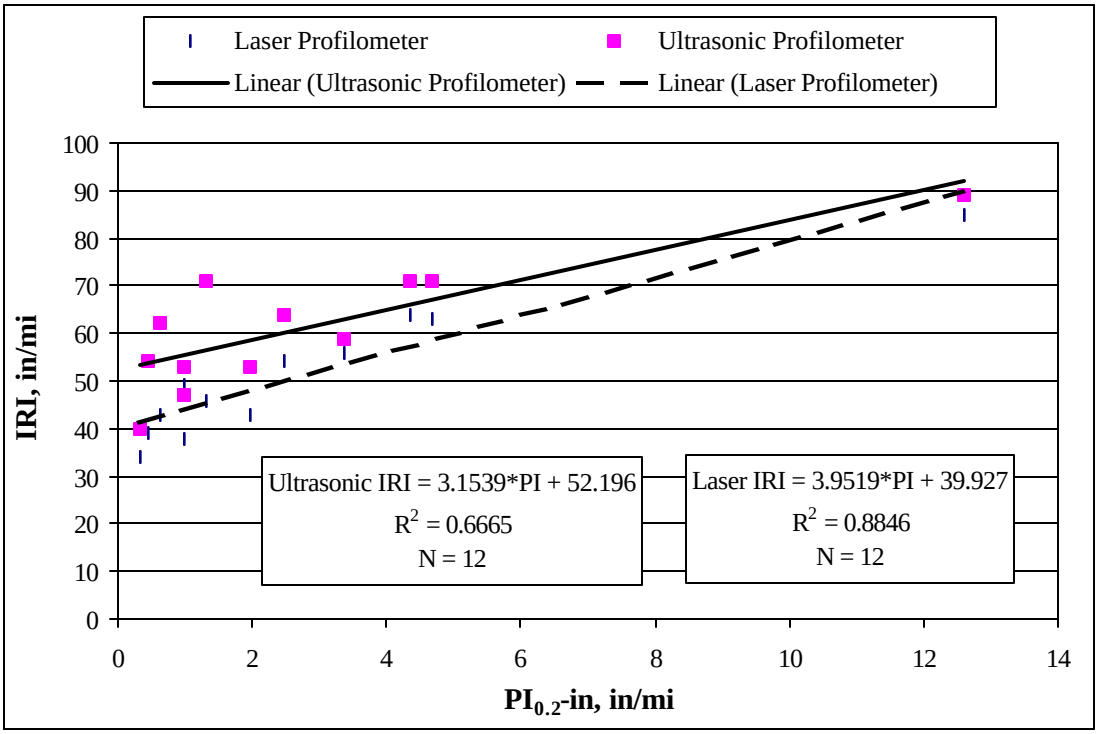

Figure 59. IRI–$PI_{5\text{-mm}}$ ($PI_{0.2\text{-in}}$) correlations established in Florida's ride quality equipment study.[61]

Figure 60 shows the correlations developed between IRI and $PI_{0.1\text{-in}}$ ($PI_{2.5\text{-mm}}$) and IRI and $PI_{0.0}$. It is quite clear from this and the previous figure that the application of smaller blanking bands results in higher PI values, since additional components of roughness are considered. More significant, however, is the fact that both the slopes and the y-intercept values in the resulting linear regression equations decrease with smaller blanking bands. This is, again, the result of additional profile roughness being considered.

It is reasonable to surmise from these observations that, if the $PI_{0.0}$ was computed from a more accurate pavement profile than the one generated by a profilograph, the y-intercept would be much closer to zero. This is because the roughness associated with long wavelengths (e.g., long dips or humps) is automatically filtered out as a result of the short baselength of profilographs.

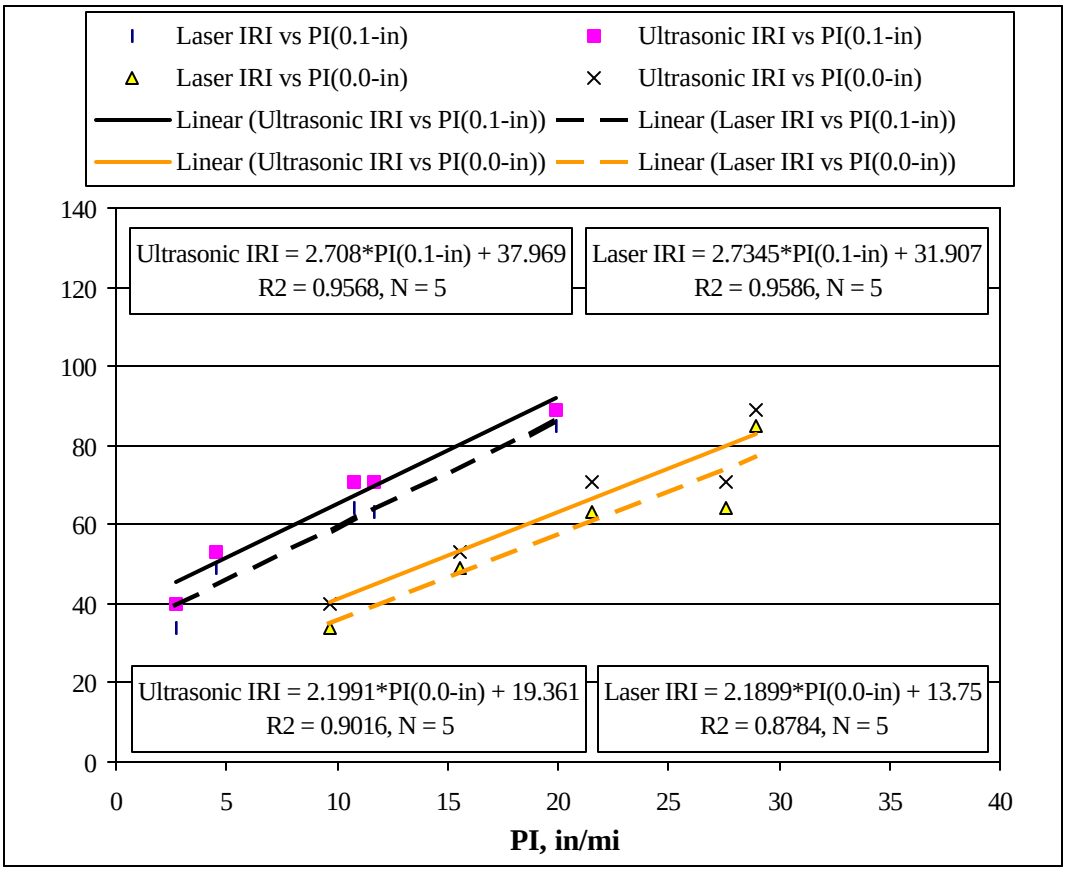

Figure 60. IRI–$PI_{2.5\text{-mm}}$ ($PI_{0.1\text{-in}}$) and IRI–$PI_{0.0}$ correlations established in Florida's ride quality equipment study.[61]

Texas Transportation Institute Smoothness Testing Equipment Comparison Study[57]

As part of a multi-staged effort to transition from a profilograph-based smoothness specification to a profile-based specification, the Texas Transportation Institute (TTI) was commissioned by the Texas DOT in 1996 to evaluate the relationship between IRI and profilograph PI. The study entailed obtaining longitudinal surface profiles (generated by one of the Department's high-speed inertial profiler) from 48 newly AC resurfaced pavement sections throughout Texas, generating computer-simulated profilograph traces from those profiles using a field-verified kinematic simulation model, and computing $PI_{5\text{-mm}}$ ($PI_{0.2\text{-in}}$) and $PI_{0.0}$ values using the Pro-Scan computer software.

A total of three simulated runs per wheelpath per section were performed, from which an average PI value for each section was computed. The resulting section PI values were then compared with the corresponding section IRI values, which had been computed by the inertial profiling system at the time the longitudinal surface profiles were produced in the field. Since both the PI and IRI values were based on the same

longitudinal profiles, potential errors due to differences in wheelpath tracking were eliminated.

Figure 61 illustrates the relationships between the IRI and the simulated PI response parameters. As can be seen, a much stronger trend was found to exist between IRI and $PI_{0.0}$ than between IRI and $PI_{5\text{-mm}}$ ($PI_{0.2\text{-in}}$). Again, this is not unexpected since the application of a blanking band has the natural effect of masking certain components of roughness.

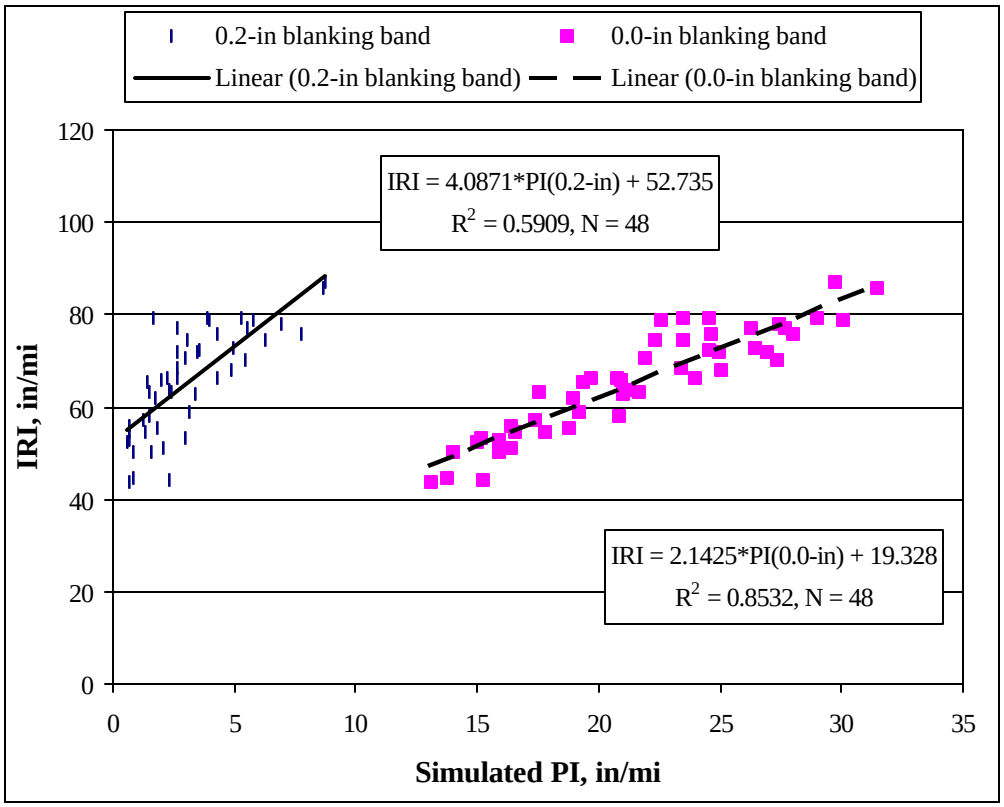

Figure 61. Relationship between IRI and computer-simulated PI values in TTI equipment comparison study.[57]

In comparison with the other IRI-$PI_{5\text{-mm}}$ (IRI–$PI_{0.2\text{-in}}$) correlations previously presented, the one developed in this study is quite typical. The linear regression equation includes a slightly higher slope but a comparable y-intercept value.

Summary of IRI–PI Relationships

Table 39 summarizes the various regression equations found in the literature relating IRI from an inertial profiling system with PI statistics ($PI_{5\text{-mm}}$ [$PI_{0.2\text{-in}}$], $PI_{2.5\text{-mm}}$ [$PI_{0.1\text{-in}}$], and $PI_{0.0}$) generated by California-type profilographs. How these various relationships compare visually with one another can be seen in figures 62 through 64. Generally speaking, there is considerable disparity in the vertical positioning of each

trend, but the slopes are rather similar. The fact that different pavement types, different roughness ranges, and different pieces of testing equipment are represented by the various trends is believed to account in large part for the disparities observed.

Table 39. Summary of documented IRI–PI relationships.

Study*	Pavement Types	No. Test Sections	Remarks	Linear Regression Equation, Metric (m/km)	Linear Regression Equation, English (in/mi)
IRI vs. $PI_{5\text{-mm}}$ ($PI_{0.2\text{-in}}$)					
PTI (1988)[58]	AC & PCC	26	Manually computed PI, Laser-type profiler	IRI = 4.02*PI + 1.11	IRI = 4.02*PI + 70.13
			Computer-generated PI, Laser-type profiler	IRI = 2.46*PI + 1.04	IRI = 2.46*PI + 66.22
Arizona DOT (1992)[60]	PCC	12	Computer-generated PI, Laser-type profiler	IRI = 6.1*PI + 0.83	IRI = 6.1*PI + 52.9
University of Texas (1992)[56]	AC & PCC	18	Manually computed IRI (Dipstick)	IRI = 2.83*PI + 1.16	IRI = 2.83*PI + 73.7
Florida DOT (1996)[61]	AC	12	Computer-generated PI, Laser-type profiler	IRI = 3.95*PI + 0.63	IRI = 3.95*PI + 39.93
			Computer-generated PI, Ultrasonic-type profiler	IRI = 3.15*PI + 0.82	IRI = 3.15*PI + 52.20
TTI (1996)[57]	AC overlays	48	Computer-simulated PI, Laser-type profiler	IRI = 4.09*PI + 0.83	IRI = 4.09*PI + 52.74
IRI vs. $PI_{2.5\text{-mm}}$ ($PI_{0.1\text{-in}}$)					
Florida DOT (1996)[61]	AC	12	Computer-generated PI, Laser-type profiler	IRI = 2.73*PI + 0.50	IRI = 2.73*PI + 31.91
			Computer-generated PI, Ultrasonic-type profiler	IRI = 2.71*PI + 0.60	IRI = 2.71*PI + 37.97
IRI versus $PI_{0.0}$					
TTI (1996)[57]	AC overlays	48	Computer-simulated PI, Laser-type profiler	IRI = 2.14*PI + 0.31	IRI = 2.14*PI + 19.33
Florida (1996)[62]	AC	12	Computer-generated PI, Laser-type profiler	IRI = 2.19*PI + 0.22	IRI = 2.19*PI + 13.75
			Computer-generated PI, Ultrasonic-type profiler	IRI = 2.20*PI + 0.31	IRI = 2.20*PI + 19.36

* The number in parentheses indicates the year in which the study was conducted.

DETAILED INVESTIGATION—LTPP CORRELATION ANALYSIS

To further examine the relationship of IRI and PI, a detailed evaluation of LTPP profile and smoothness data was performed. This evaluation consisted of the following three steps:

1. Processing time-series profile data on GPS-3, SPS-2, and SPS-4 JPCP test sections into $PI_{5\text{-mm}}$ ($PI_{0.2\text{-in}}$), $PI_{2.5\text{-mm}}$ ($PI_{0.1\text{-in}}$), and $PI_{0.0}$ values using commercial profilograph simulation software.

2. Developing scatter plots of the simulated PI values and corresponding IRI values recorded in the LTPP database.
3. Performing regression analysis on each scatter plot to establish the respective PI–IRI relationships.

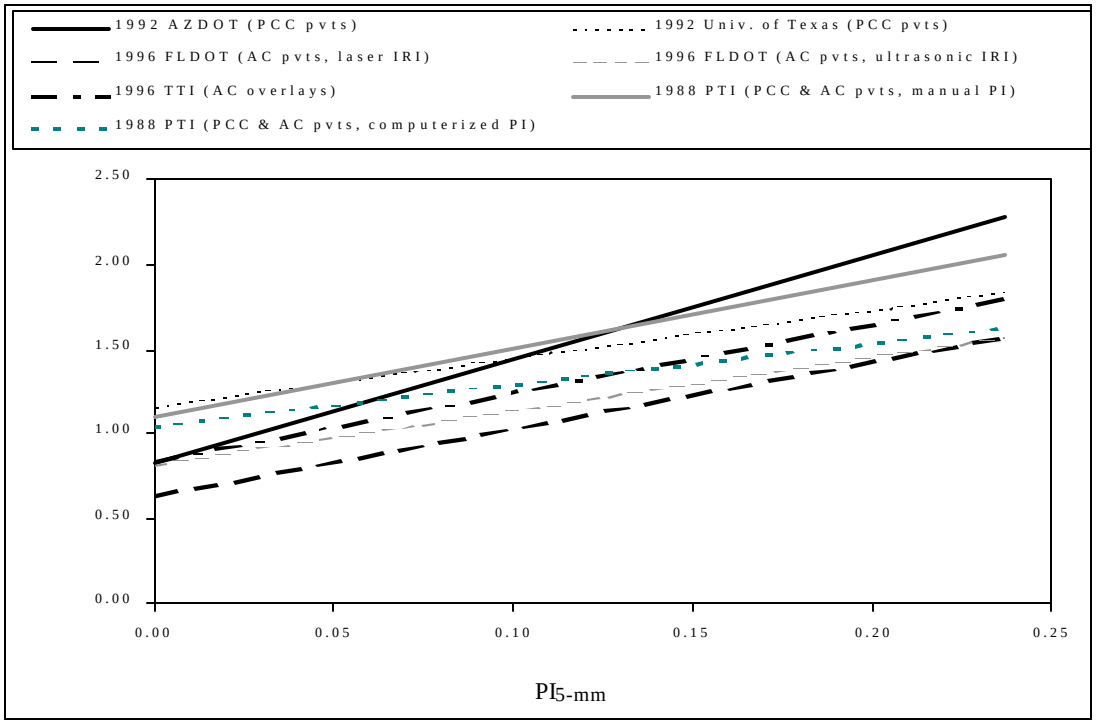

Figure 62. Graphical illustration of documented IRI–$PI_{5\text{-mm}}$ ($PI_{0.2\text{-in}}$) smoothness relationships.

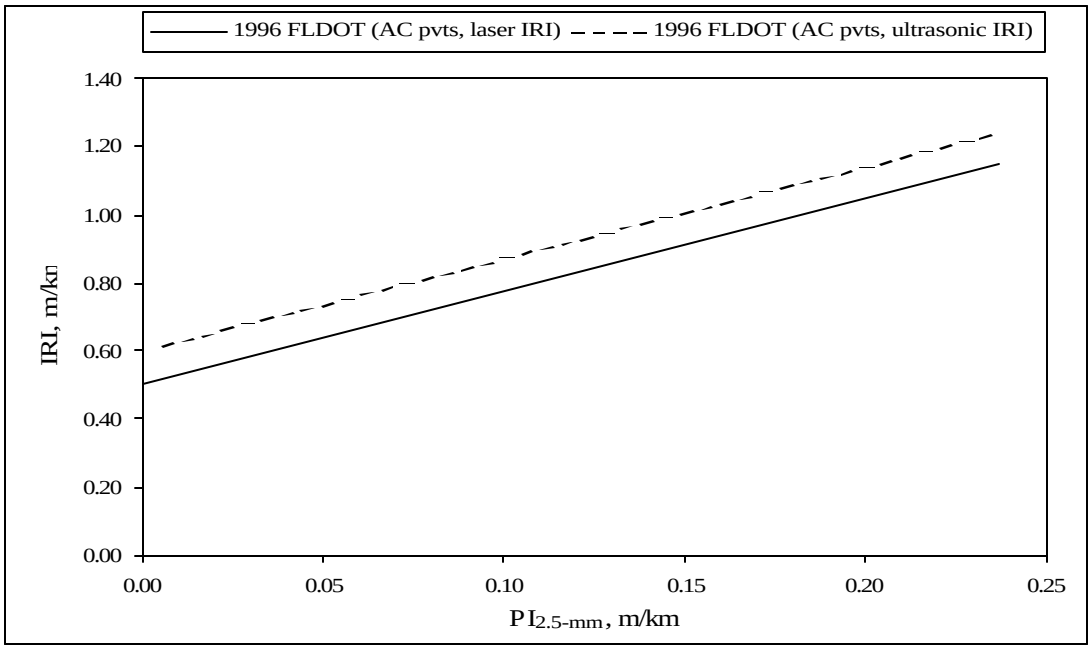

Figure 63. Graphical illustration of documented IRI–$PI_{2.5\text{-mm}}$ ($PI_{0.1\text{-in}}$) smoothness relationships.

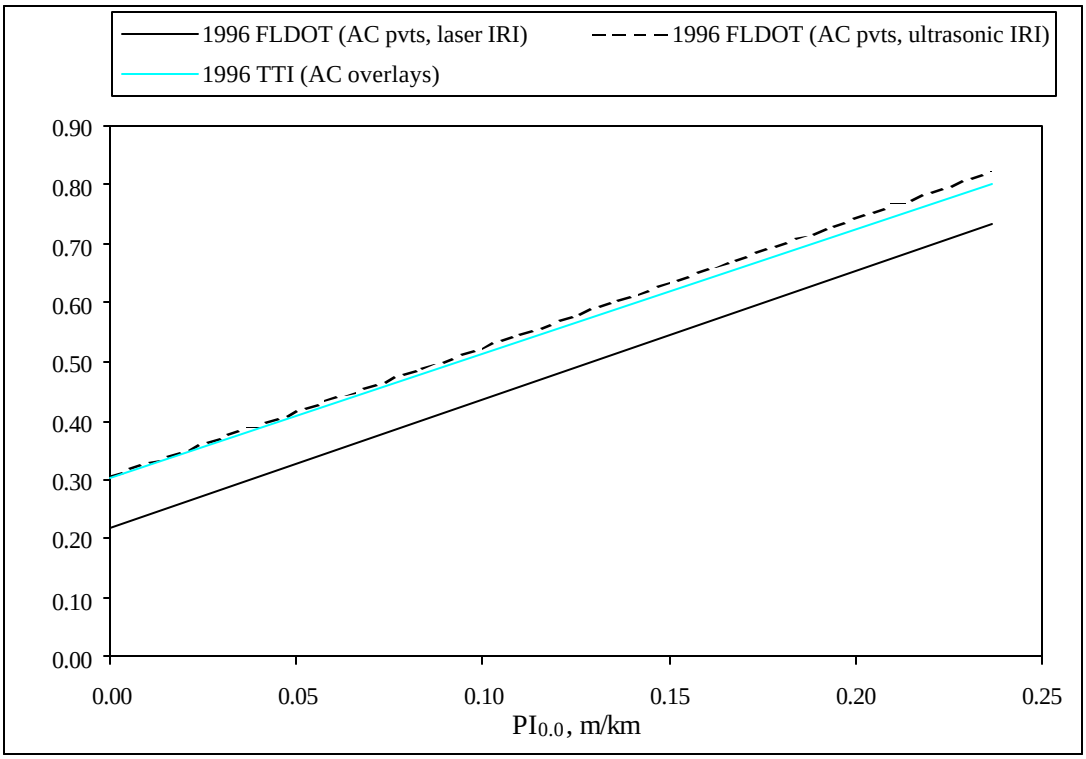

Figure 64. Graphical illustration of documented IRI–$PI_{0.0}$ smoothness relationships.

As seen in table 40, a total of 152 JPCP test sections located in 11 States and 1 Canadian Province formed the basis for this evaluation. It should be noted that all the States / Provinces in this table are located in the Midwest (comprehensive profile data were only immediately available from the LTPP North Central Region, which encompasses these and three other States / Provinces). In addition, the profile data analyzed represented data collected by the North Central Regional Contracting Office (NCRCO) since January 1997. Earlier data were not available due to the limitations of the profiling equipment used prior to that time.

In keeping with the PRS subject pavement type, the LTPP correlation analysis was limited to JPCP. In this way, the relationships developed between IRI and simulated PI would not be skewed by measurements taken on other pavement types. As table 40 shows, the evaluation centered on 36 GPS-3 sections, 96 SPS-2 sections, and 20 SPS-4 sections.

LTPP Profile and Smoothness Data

The profile and smoothness data used in the LTPP correlation analysis were collected using a K.J. Law T-6600 Profilometer from the North Central Region. This device is equipped with infrared sensors spaced 1,680 mm (66 in) apart, so as to measure the longitudinal profiles of the left and right wheelpaths of a travel lane. Profile data were recorded on 25-mm (1-in) intervals, which is similar to the 33-mm (1.25-in) interval currently used by computerized profilographs. This is also the

Table 40. Summary of JPCP test sections included in LTPP correlation analysis.

State/Province	LTPP Experiment			Total
	GPS-3[1]	SPS-2[2]	SPS-4[3]	
Indiana	2	0	0	2
Iowa	5	13	4	22
Kansas	3	13	0	16
Kentucky	1	0	2	3
Michigan	1	13	0	14
Minnesota	2	0	0	2
Nebraska	5	0	4	9
North Dakota	2	18	0	20
Ohio	0	20	3	23
South Dakota	6	0	7	13
Wisconsin	8	19	0	27
Manitoba	1	0	0	1
Total	36	96	20	152

Notes:

[1] Study of Jointed Plain Concrete Pavements.

[2] Study of Structural Factors for Rigid Pavements.

[3] Study of Preventive Maintenance Effectiveness of Rigid Pavements.

recording interval used by the K.J. Law lightweight inertial profiler. The T-6600 Profilometer is considered a class I accelerometer-established inertial profiling reference based on ASTM E-950-98. Its capabilities for good repeatability and compatibility with other LTPP Profilers are documented in several studies.[62,63]

The data used for the analysis were based on 2,795 individual profile runs (1,111 GPS-3, 1,443 SPS-2, and 241 SPS-4 runs), covering the full 152.4 m (500 ft) of each test section pavement. Each run included measurements of both the left and right wheelpaths. The average IRI based on all of these profile runs was 1.64 m/km (103.8 in/mi). The range in IRI was from 0.63 m/km (39.9 in/mi) to 5.56 m/km (352.5 in/mi), which is representative of new to very deteriorated JPCP. Individual data files were created using the LTPP archived profile data. These data files followed the Engineering Research Division (ERD) format developed for the RoadRuf software at the University of Michigan Transportation Research Institute (UMTRI).

Development and Application of Simulation Software

To model profilograph traces and generate PI values from the LTPP profile data, a software modeling system was needed. In 1995, K.J. Law developed software to model California-type profilograph traces and output PI values. This software is now used with their lightweight profilers to compute PI and IRI. K.J. Law's lightweight profilers use the same vertical elevation sensors that are mounted on the T-6600 Profilometer.

As of March 2000, K.J. Law lightweight profilers were approved for use in 12 States, including Pennsylvania, New York, Utah, Texas, Arizona, and Michigan. Approval of the system is pending in seven other States. The system has been calibrated against California-type profilographs in Kansas, Arkansas, Indiana, Idaho, Minnesota, Oklahoma, Utah, Arizona, and Georgia. Although there are several good lightweight profilers and PI modeling systems available, the K.J. Law modeling software was selected for this study to provide the most compatibility with the available LTPP profile data.

Using the modeling and index computation software currently installed on their commercial lightweight profilers, K.J. Law developed an interface for analysis of the LTPP data. Named "Indexer," the software computes PI, IRI, and ride number values using ERD format input files. The size of the blanking band can be set by the operator. Other factors that can be selected include:

- Blanking band filter (straight-line or selectable null filter).
- Smoothing filter (moving average or third-order Butterworth).
- Scallop filter (height, length, rounding).

Data Analysis

As discussed previously, the primary objective of the LTPP correlation analysis was to establish relationships between IRI and three different variations of the PI statistic—$PI_{5\text{-mm}}$ ($PI_{0.2\text{-in}}$), $PI_{2.5\text{-mm}}$ ($PI_{0.1\text{-in}}$), and $PI_{0.0}$. The established relationships would then be compared with the relationships identified and documented in past studies, in an attempt to satisfy the overall goal of identifying reasonable PI-to-IRI conversions for the PaveSpec user.

The analysis of data consisted of two parts. First, a baseline evaluation was done, in which simulated PI computations were made using filter settings that provide the best correlation with profilograph data from test track comparisons. These settings consisted of a moving average smoothing filter set at 0.76 m (2.5 ft) and minimum height, maximum height, and rounding scallop filters set at 0.9, 0.6, and 0.25 mm (0.035, 0.024, and 0.01 in), respectively. After modeling a California profilograph response to these filtered profiles, straight-line blanking band filters of 0, 2.5 mm (0.1 in), and 5 mm (0.2 in) were used to compute the associated values.

The second part of the analysis involved a look at the sensitivity effect of different filter types and filter settings on the IRI–PI relationships. In this sensitivity analysis, $PI_{0.0}$, $PI_{2.5\text{-mm}}$ ($PI_{0.1\text{-in}}$), and $PI_{5\text{-mm}}$ ($PI_{0.2\text{-in}}$) parameters were computed using profilograms from profile traces generated using moving average filters set at 0.31, 0.76, and 1.22 m (1.0, 2.5, and 4.0 ft). These same three parameters were also computed using a third-order Butterworth filter set at 0.76 m (2.5 ft). Minimum height, maximum height, and

rounding scallop filter settings in this analysis were kept at the same levels as in the baseline evaluation.

Baseline Evaluation

Figures 65 through 67 show the resulting IRI–PI scatter plots and linear regression equations corresponding to the baseline PI computations. Each plot consists of more than 5,000 data points, again spanning a range of IRI between 0.63 and 5.56 m / km (39.9 and 352.5 in / mi).

There is a strong fit among each data set (all R^2 values > 0.75) and an increasingly stronger correlation associated with PI values derived from smaller blanking-band sizes. In addition, as was observed with the Florida DOT and TTI smoothness study correlations, both the slope and y-intercept values given by the linear regression equations decreased with the application of smaller blanking bands.

Figures 68 through 70 provide for a direct visual comparison of the smoothness relationships developed in past studies with the LTPP-derived relationships. In each figure, a band width envelope centered one standard deviation around the LTPP-derived regression line has been transposed over the individual regression lines of the past documented smoothness studies. Though the LTPP relationships represent a wide range of smoothness, only the levels typical of new construction (IRI < 2.0 m / km [126.8 in / mi]) are illustrated in figures 68 through 70.

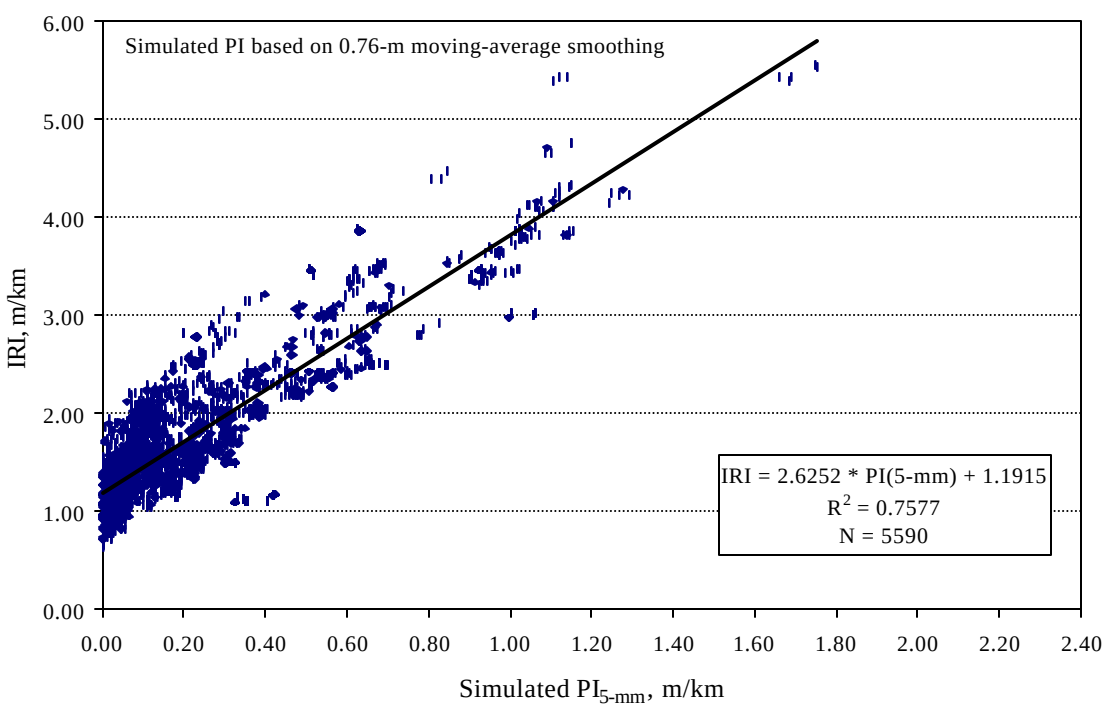

Figure 65. Graphical illustration of LTPP IRI–$PI_{5\text{-mm}}$ ($PI_{0.2\text{-in}}$) smoothness relationship.

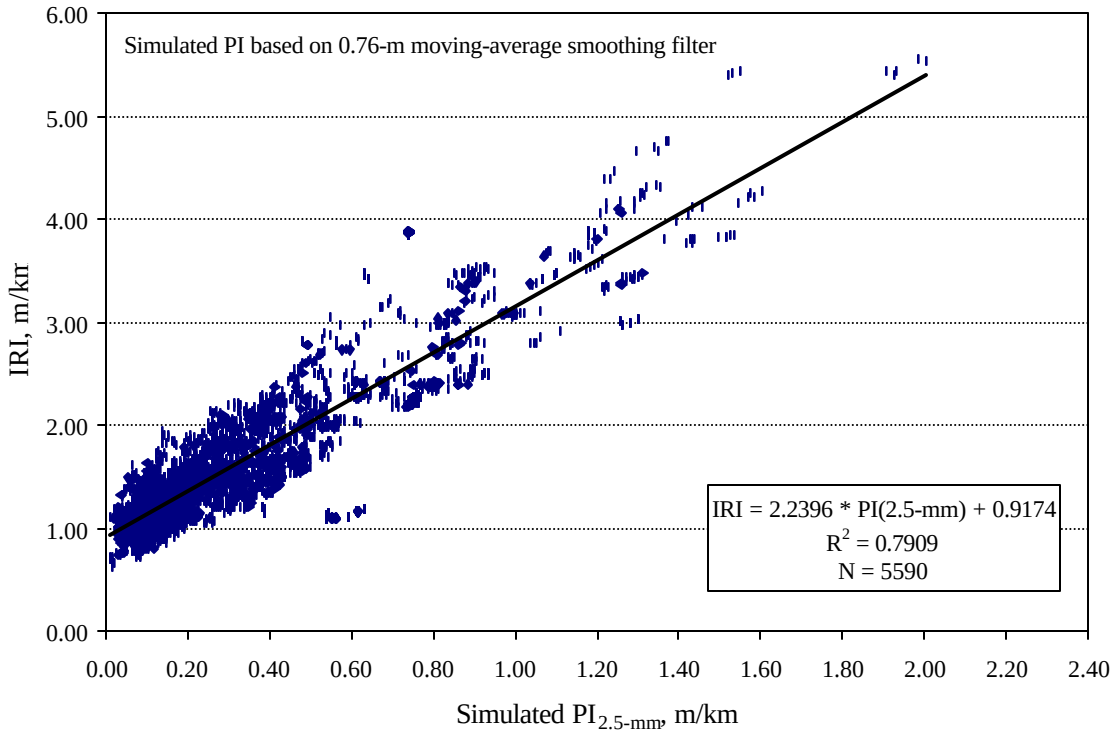

Figure 66. Graphical illustration of LTPP IRI–$PI_{2.5\text{-mm}}$ ($PI_{0.1\text{-mm}}$) smoothness relationship.

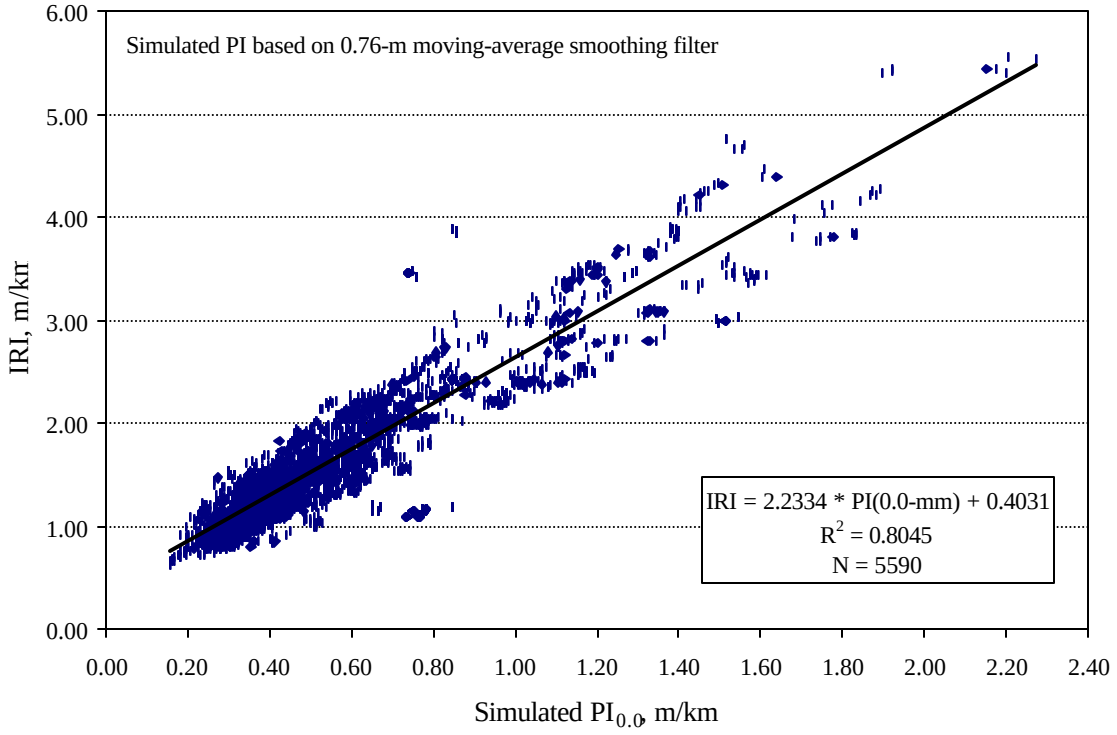

Figure 67. Graphical illustration of LTPP IRI–$PI_{0.0}$ smoothness relationship.

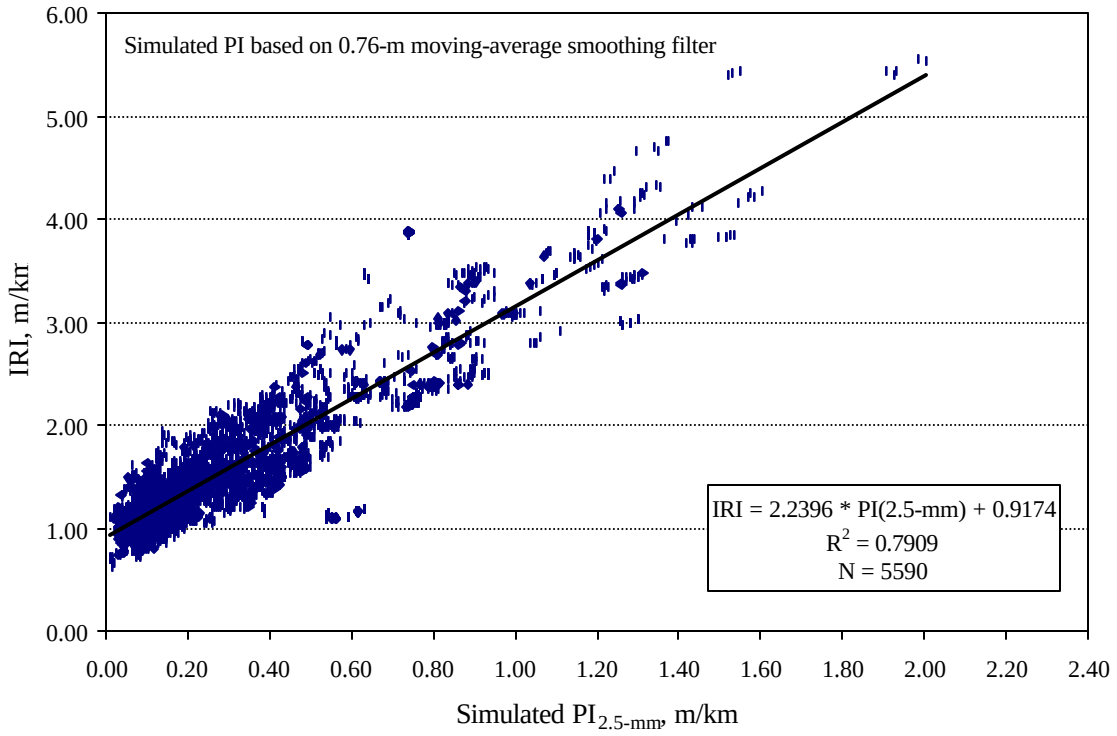

Figure 66. Graphical illustration of LTPP IRI–$PI_{2.5\text{-mm}}$ ($PI_{0.1\text{-mm}}$) smoothness relationship.

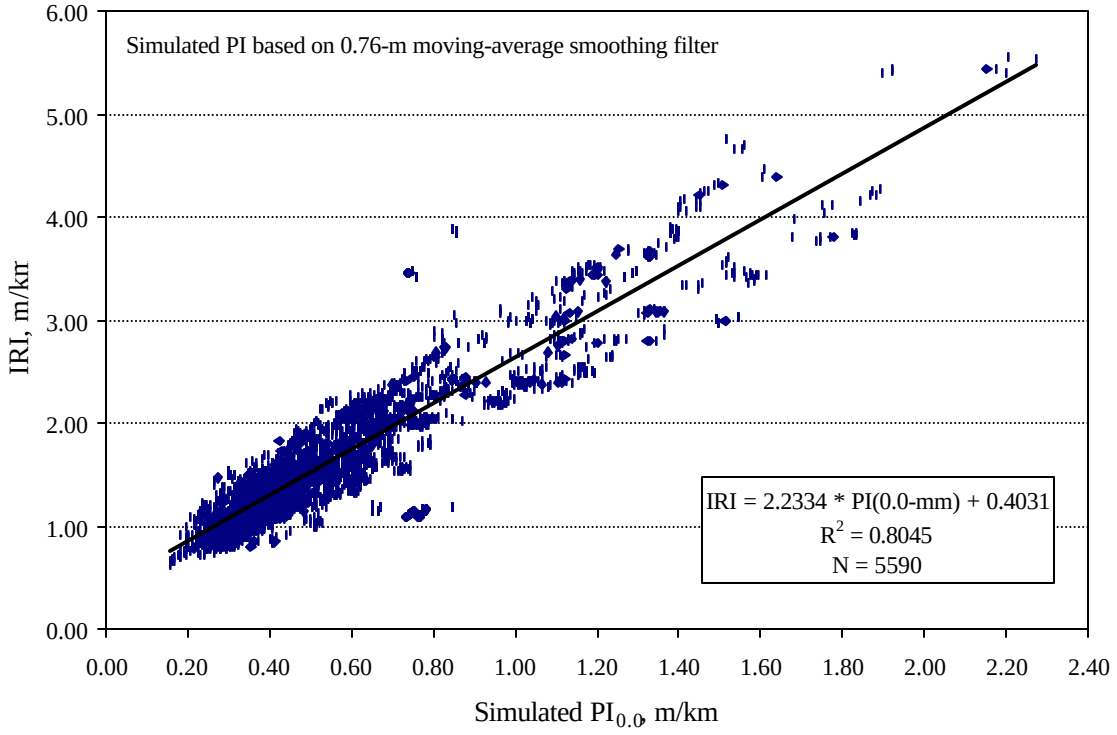

Figure 67. Graphical illustration of LTPP IRI–$PI_{0.0}$ smoothness relationship.

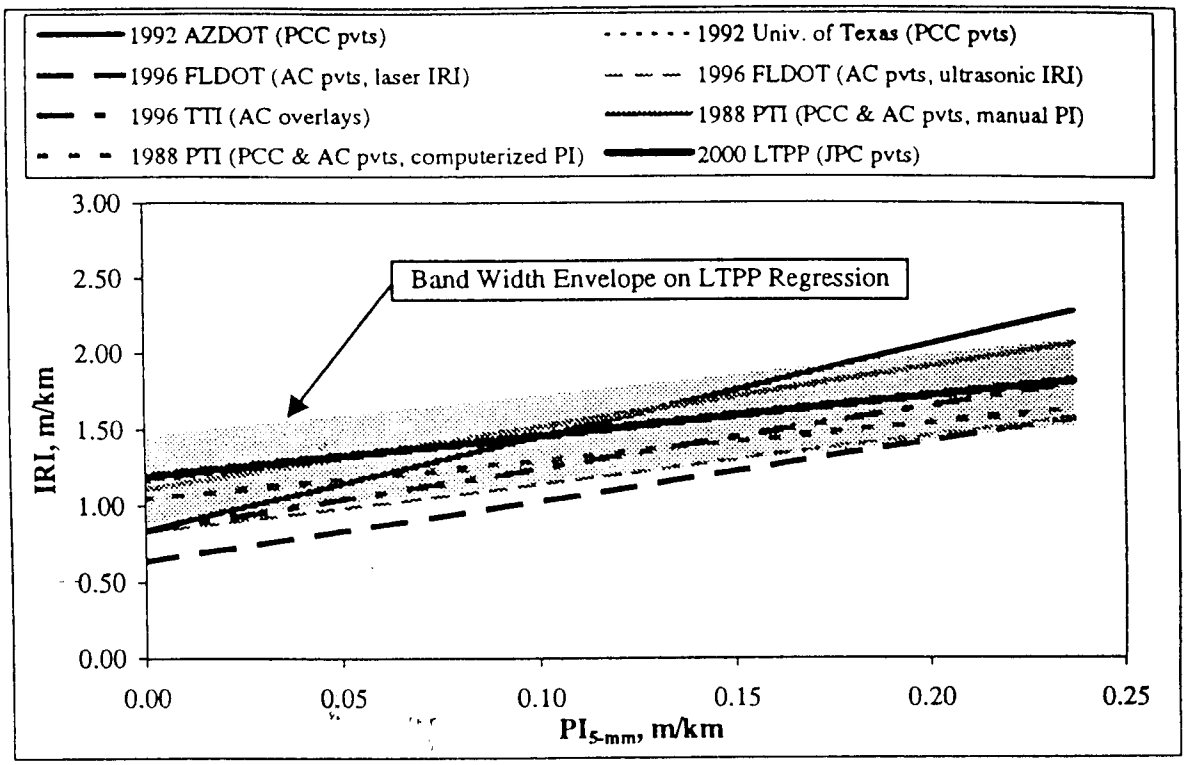

Figure 68. Graphical comparison of IRI–$PI_{5\text{-mm}}$ ($PI_{0.2\text{-in}}$) smoothness relationships.

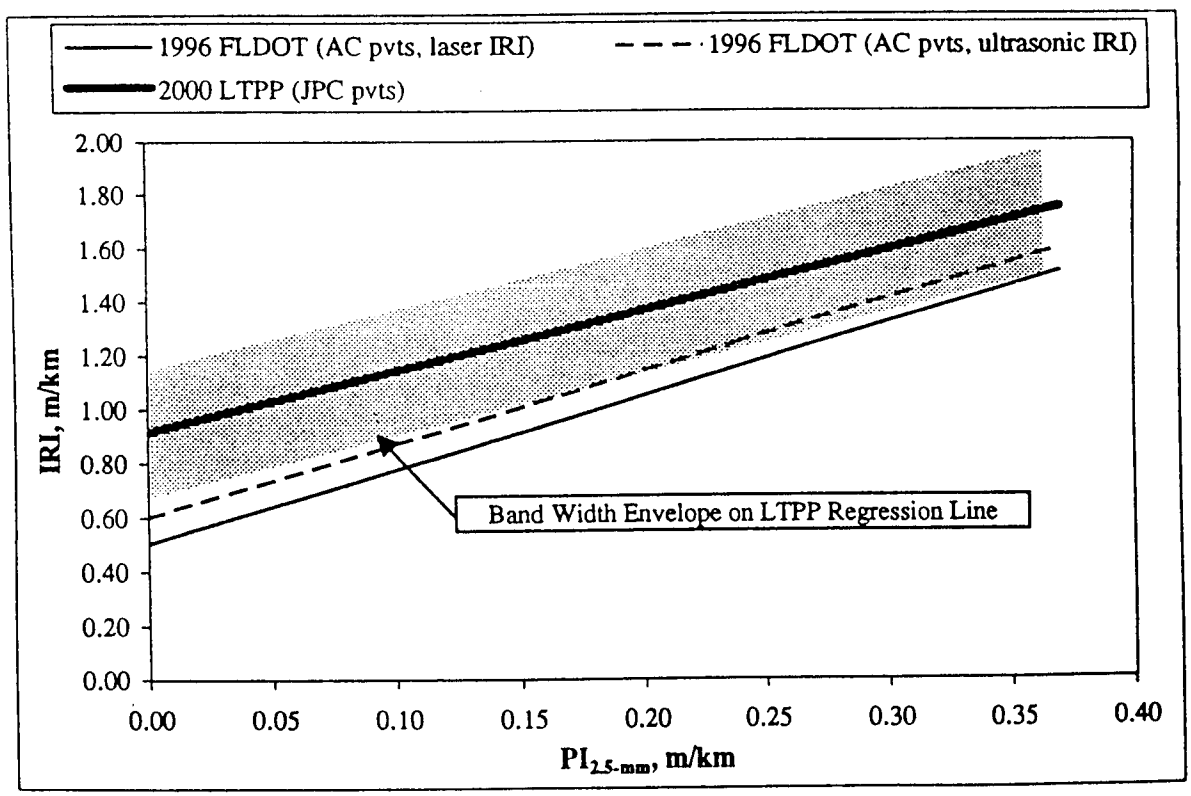

Figure 69. Graphical comparison of IRI–$PI_{2.5\text{-mm}}$ ($PI_{0.1\text{-in}}$) smoothness relationships.

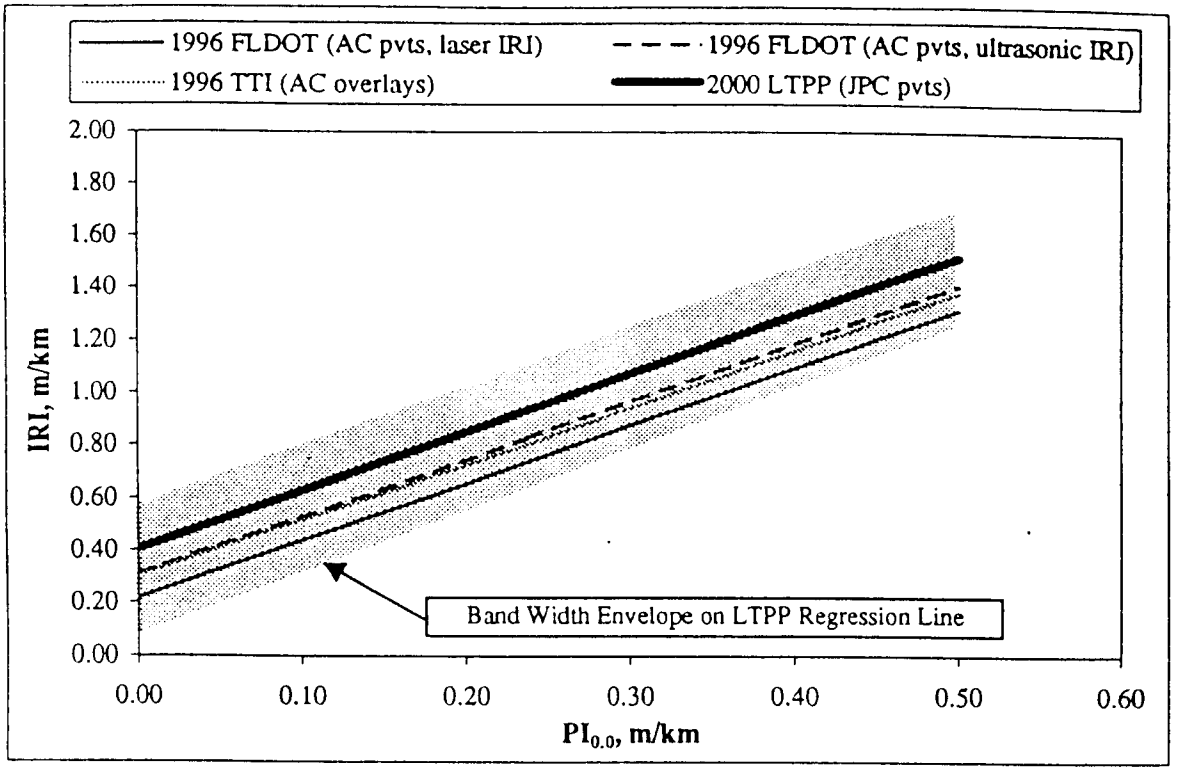

Figure 70. Graphical comparison of IRI–$PI_{0.0}$ smoothness relationships.

In figure 68, it can be seen that the LTPP regression envelope covers most of the other IRI–$PI_{5\text{-mm}}$ relationships. Moreover, with the exception of part of the 1992 Arizona DOT relationship, it coincides quite well with the relationships developed using smoothness measurements on PCC pavements. In fact, the 1992 University of Texas regression equation closely mimics the LTPP regression equation. The fact that the Arizona relationship was based on measurements from only 12 concrete pavement sections may help explain its departure from the LTPP-derived relationship. However, other factors, such as sensor type (Arizona used optical sensors, whereas LTPP used infrared sensors), are likely to have also contributed to this.

Figures 68 and 69 show only some similarities between the LTPP- and Florida DOT-derived IRI–PI relationships. In both cases, the Florida trends are substantially lower than the LTPP trends, but the slopes of the regression lines are similar. One explanation for these discrepancies is pavement type—the LTPP relationships are based on measurements of JPCP, whereas the Florida relationships are based on measurements of AC pavements. Another probable factor is equipment. As mentioned previously, the Florida study used ICC laser- and ultrasonic-type sensors, whereas the LTPP study used K.J. Law infrared sensors.

The LTPP and Florida IRI–$PI_{0.0}$ relationships appear to agree more closely, as depicted in figure 70. Though still somewhat lower than the LTPP trend, both Florida trends and the 1996 TTI trend are covered by the LTPP regression envelope. In addition, they all have very similar slopes. Though pavement type and equipment type

are still key factors in trend discrepancies, it appears that reducing the blanking band has the effect of producing more harmonious relationships.

Sensitivity Analysis

As discussed previously, PI can be computed from a longitudinal profile using various types of filters and filter settings. To examine the effects of some of the more commonly available filtering routines on the IRI–PI relationship, the following PI computations were performed on the LTPP profile data using the K.J. Law profilograph simulation software:

- $PI_{5\text{-mm}}$ ($PI_{0.2\text{-in}}$)
  - 0.31-m (1-ft) moving average filter.
  - 1.22-m (4-ft) moving average filter.
  - 0.76-m (2.5-ft) third-order Butterworth filter.
- $PI_{2.5\text{-mm}}$ ($PI_{0.1\text{-in}}$)
  - 0.31-m (1-ft) moving average filter.
  - 1.22-m (4-ft) moving average filter.
  - 0.76-m (2.5-ft) third-order Butterworth filter.
- $PI_{0.0}$
  - 0.31-m (1-ft) moving average filter.
  - 1.22-m (4-ft) moving average filter.
  - 0.76-m (2.5-ft) third-order Butterworth filter.

As with the baseline evaluation of IRI and PI derived using a 0.76-m (2.5-ft) moving average filter, the computed PI values were plotted against the corresponding actual IRI values, and linear regressions were performed. Table 41 lists all of the relationships developed between IRI and simulated $PI_{5\text{-mm}}$ ($PI_{0.2\text{-in}}$), $PI_{2.5\text{-mm}}$ ($PI_{0.1\text{-in}}$), and $PI_{0.0}$ values, along with the corresponding R^2 values. Note: PI is expressed in metric units of m / km and English units of in / mi.

Figures 71 through 73 show the series of trends for each blanking band PI, covering only the levels of smoothness typical of newly constructed pavement (again, IRI < 2.0 m / km [126.8 in / mi]). In each figure, it can be seen that the trends associated with the short wavelength (0.31-m [1-ft]) moving average filter and the third-order Butterworth filter are nearly identical, and both are a little lower than the corresponding baseline filter (0.76-m [2.5-ft] moving average) trends. The trends associated with the long wavelength (1.22-m [4-ft]) moving average filter, on the other hand, are a little higher than the corresponding baseline trends.

Table 42 summarizes the percent differences between the baseline filter IRI–PI trends and the alternative filter trends at discrete levels of initial smoothness. Though the percent differences are appreciable in some cases, they are, for the most part, considerably smaller than the percentages characterized by the IRI–PI relationships of

Table 41. Summary of IRI–PI relationships based on different filter types and settings.

Filter Type	Filter Setting	Linear Regression Equation (Metric, m/km)	Linear Regression Equation (English, in/mi)	R^2
IRI vs. $PI_{5\text{-mm}}$ ($PI_{0.2\text{-in}}$)				
Moving Average	0.31 m (1 ft)	IRI = 2.350*PI + 1.164	IRI = 2.350*PI + 73.823	0.77
	0.76 m (2.5 ft)	IRI = 2.625*PI + 1.192	IRI = 2.625*PI + 75.541	0.76
	1.22 m (4 ft)	IRI = 2.834*PI + 1.221	IRI = 2.834*PI + 77.437	0.73
Third-Order Butterworth	0.76 m (2.5 ft)	IRI = 2.367*PI + 1.151	IRI = 2.367*PI + 72.946	0.79
IRI vs. $PI_{2.5\text{-mm}}$ ($PI_{0.1\text{-in}}$)				
Moving Average	0.31 m (1 ft)	IRI = 2.021*PI + 0.875	IRI = 2.021*PI + 55.481	0.80
	0.76 m (2.5 ft)	IRI = 2.240*PI + 0.917	IRI = 2.240*PI + 58.163	0.79
	1.22 m (4 ft)	IRI = 2.407*PI + 0.953	IRI = 2.407*PI + 60.446	0.78
Third-Order Butterworth	0.76 m (2.5 ft)	IRI = 2.052*PI + 0.871	IRI = 2.052*PI + 55.233	0.82
IRI vs. $PI_{0.0}$				
Moving Average	0.31 m (1 ft)	IRI = 2.033*PI + 0.351	IRI = 2.033*PI + 22.279	0.81
	0.76 m (2.5 ft)	IRI = 2.233*PI + 0.403	IRI = 2.233*PI + 25.557	0.80
	1.22 m (4 ft)	IRI = 2.387*PI + 0.440	IRI = 2.387*PI + 27.915	0.79
Third-Order Butterworth	0.76 m (2.5 ft)	IRI = 2.135*PI + 0.319	IRI = 2.135*PI + 20.219	0.81

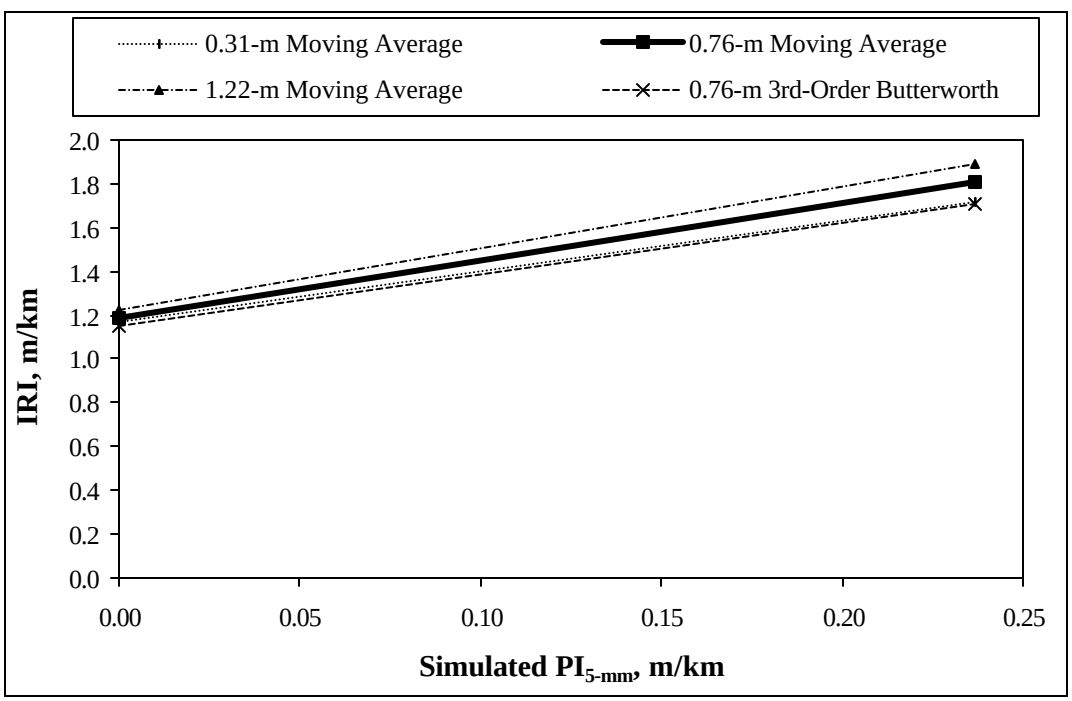

Figure 71. Comparison of IRI–$PI_{5\text{-mm}}$ ($PI_{0.2\text{-in}}$) relationships for different filter types and settings.

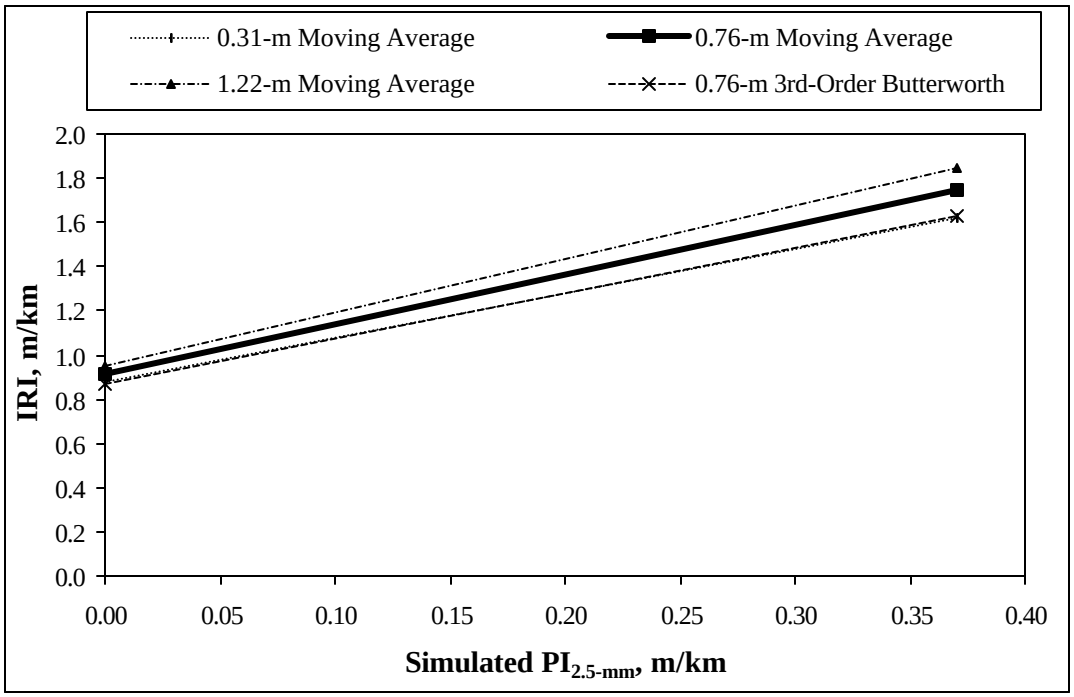

Figure 72. Comparison of IRI–$PI_{2.5\text{-mm}}$ ($PI_{0.1\text{-in}}$) relationships for different filter types and settings.

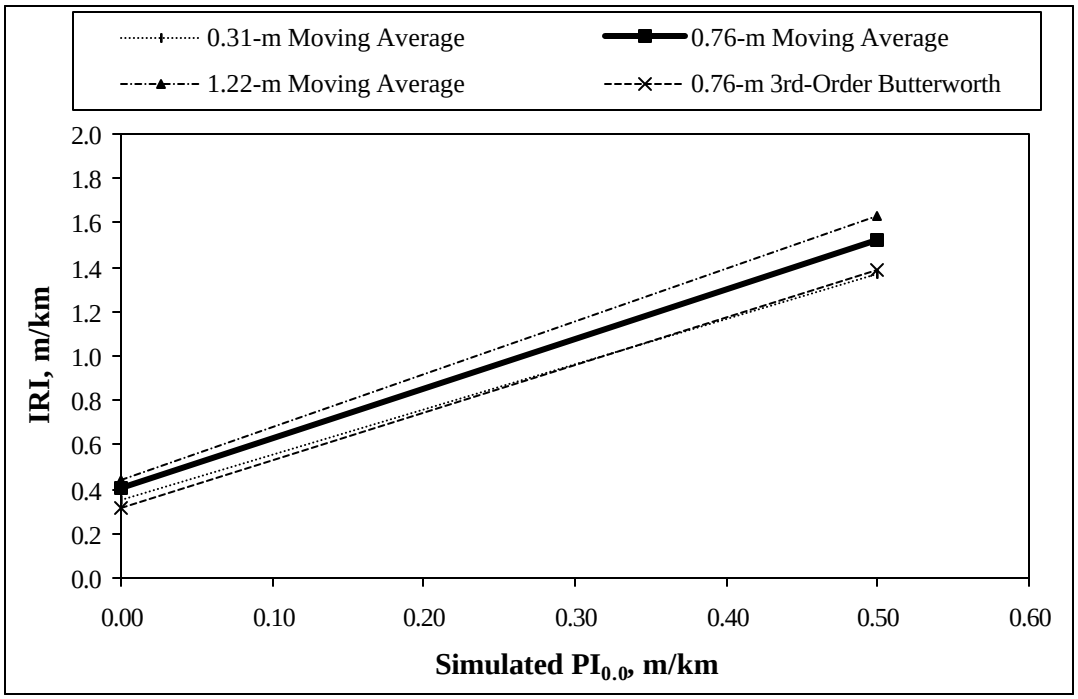

Figure 73. Comparison of IRI–$PI_{0.0}$ relationships for different filter types and settings.

Table 42. Effects of alternative filter types and settings on IRI–PI relationships.

PI Parameter	Filter Setting and Type	% Difference in IRI Between Baseline Filter Trend and Alternative Filter Trend at:			
		PI = 0.0 m/km	PI_{5mm} = 0.237 m/km	$PI_{2.5mm}$ = 0.37 m/km	$PI_{0.0}$ = 0.5 m/km
PI_{5-mm}	0.31-m (1-ft) Moving Avg.	2.27%	5.09%		
	0.76-m (2.5-ft) Moving Avg.	—	—		
	1.22-m (4-ft) Moving Avg.	-2.51%	-4.38%		
	0.76-m (2.5-ft) Third-Order Butterworth	3.43%	5.63%		
$PI_{2.5-mm}$	0.31-m (1-ft) Moving Avg.	4.61%		7.06%	
	0.76-m (2.5-ft) Moving Avg.	—		—	
	1.22-m (4-ft) Moving Avg.	-3.93%		-5.60%	
	0.76-m (2.5-ft) Third-Order Butterworth	5.04%		6.63%	
$PI_{0.0}$	0.31-m (1-ft) Moving Avg.	12.82%			9.98%
	0.76-m (2.5-ft) Moving Avg.	—			—
	1.22-m (4-ft) Moving Avg.	-9.23%			-7.51%
	0.76-m (2.5-ft) Third-Order Butterworth	20.89%			8.76%

past smoothness studies. Moreover, if the alternative filter trends were added to figures 68 through 70, they would easily fall within the band width envelopes centered one standard deviation around the LTPP baseline trends. Hence, it is reasonable to believe that the effects of profiler equipment characteristics and pavement types have a greater influence on the IRI–PI relationship than the PI simulation filter types and settings.

SUMMARY AND RECOMMENDATIONS

In the search for reasonable, practical relationships that link IRI with PI derived from different blanking bands, a comprehensive evaluation was made of trends documented in past pavement smoothness studies, as well as trends developed in this study from vast amounts of LTPP profile and smoothness data. The background and results of these studies were presented and discussed in this chapter.

Although past documented IRI–PI relationships were rather limited (particularly with respect to IRI–$PI_{2.5-mm}$ ($PI_{0.1-in}$) and IRI–$PI_{0.0}$ relationships) and showed varying degrees of disparity, factors such as pavement type, equipment characteristics, and filtering methods contributed significantly to those disparities.

A much broader and more controlled evaluation using more than 5,000 LTPP smoothness data points showed IRI–PI trends generally similar to the past study trends. The data points consisted of IRI and simulated PI values computed from the

same longitudinal profiles measured multiple times for 152 LTPP JPCP test sections. Based on a standard filtering routine (a 0.76-m [2.5-ft] moving average smoothing filter) and the application of 5-mm (0.2-in), 2.5-mm (0.1-in), and zero blanking bands, the following PI-to-IRI conversion equations (in metric units of m/km) were developed:

$$IRI = 2.6252*PI_{5\text{-}mm} + 1.1915 \qquad R^2 = 0.76 \qquad (109)$$

$$IRI = 2.2396*PI_{2.5\text{-}mm} + 0.9174 \qquad R^2 = 0.79 \qquad (110)$$

$$IRI = 2.2334*PI_{0.0} + 0.4031 \qquad R^2 = 0.80 \qquad (111)$$

These will be included as the default relationships in the new PaveSpec 3.0 software and will serve as practical alternatives for agencies that lack their own reliable conversion algorithms. However, it should be emphasized that these relationships are based on profile data collected by one distinct piece of inertial profiling equipment (K.J. Law T-6600 Profilometer) and on simulated PI values derived from those profile data. The use of other profiler models will likely result in slightly different relationships, because of the inherent differences in vehicle characteristics, profile measurement instruments (e.g., sensors, accelerometers), and profile filtering methods. Similarly, the use of actual PI data (i.e., data collected in the field using a profilograph) will likely produce slightly different relationships because of differences in the measured profile and the profile filtering methods used.

CHAPTER 9: GUIDELINES FOR MODEL CALIBRATION AND DEVELOPMENT

INTRODUCTION

Many SHA's are wary about using distress or smoothness prediction models that were not developed using data from their agency. This is a valid concern because local construction, materials, and specific design situations may vary significantly from national averages. Thus, there is a significant need for the capability to evaluate and tailor distress indicator models to better reflect local conditions and circumstances (remove bias and improve precision). Every construction project represents a unique combination of pavement type, pavement design, material properties, subgrade support, mix design, climatic variables, traffic, and construction quality. It is, therefore, naive to think that one set of performance prediction models based on national data will be completely accurate for all projects. To address this limitation, this chapter outlines guidelines that may be used by a SHA to either 1) calibrate a national distress indicator model to better reflect the specific local conditions associated with a project, or 2) develop a new distress indicator model using SHA data. These two methods of model improvement are discussed separately below.

GUIDELINES FOR CALIBRATING AN EXISTING DISTRESS INDICATOR MODEL

IF SHA's believe that the performance of their pavements is not being accurately predicted by the PRS performance models, they may want to consider calibrating the models to an actual data set in which they have confidence. This section describes all aspects of a procedure that a SHA may use to successfully complete such a calibration.

The model calibration approach chosen as the basis for these guidelines is similar to that used in the World Bank HDM4 software.[64] As expressed in the World Bank report, the calibration of a distress indicator model consists of finding adjustment factors that allow model predictions to best approximate measured data. Actual SHA performance data are plotted against the predicted performance data from the same pavement sections. A linear regression of the predicted versus actual plot is conducted, and linear regression coefficients (A and B) are determined. Regression coefficients are calculated in such a way as to minimize the total error between the calibrated model and actual observed distress for each pavement section. The results coming from the calibrated model are then computed using the following equation:

$$\text{Calibrated Distress Value} = A + B * (\text{Original Model Distress Value}) \quad (112)$$

where:

A and B = Calibration factors determined from regression of predicted distress vs. actual distress using actual SHA data to minimize the error in prediction.

A calibrated model will often remove bias present in the national model, as well as reduce some scatter in the results (i.e., improve precision). Figure 74 illustrates the results of a model calibration procedure in which a Condition Rating Survey (CRS—distress rating) model for the Illinois DOT was calibrated with a new data set.[65] The two plots shown in figure 74 show predicted versus actual data for both the *before* calibration (existing model) and *after* calibration (calibrated model) scenarios. The calibrated model corrects both bias and scatter about the one-to-one line. The detailed steps required to successfully calibrate a distress indicator model to an external data set are discussed in the following section.

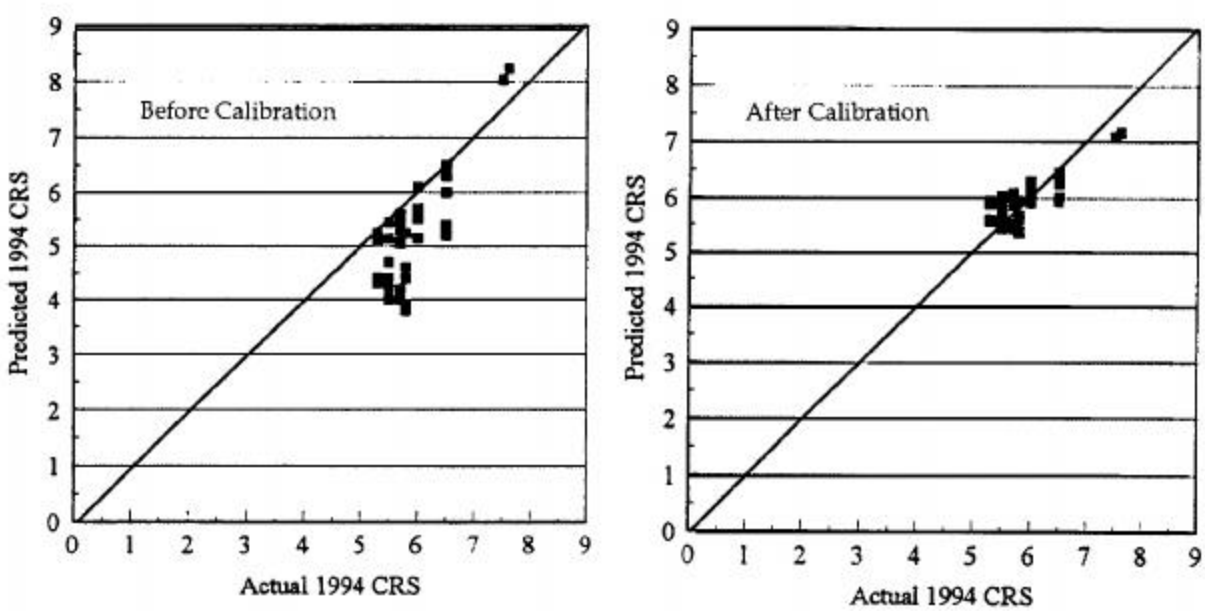

Figure 74. Illustration of predicted vs. actual CRS both before calibration and after calibration with new data.[65]

Step 1—Compile the Calibration Data Set

The first step in the model calibration process is to compile a data set that best represents current performance trends (distress versus time) for a chosen distress indicator model. This data set must include not only data representing all of the inputs required by the distress model in question, but also actual measured distress values at different points in time. The local conditions represented by the compiled data set should closely represent those local conditions expected at the project for which the

calibrated model will be used. Each data point within the calibration data set represents the unique combination of pavement section inputs and one measured distress value influenced by the associated *n* data input values. An example of the format for this calibration data set is shown in table 43. LTPP data from sections in the State should be adequate for this purpose.

Table 43. Format for a calibration data set.

Data Point	Input 1	Input 2	* * *	Input n	Measured Distress Value
1					
2					
3					
4					
*					
*					
*					
m					

Step 2—Compute Corresponding *Predicted* Values

The second step in the process involves computing predicted distress values using the original distress indicator model being investigated. Predicted distress values are computed for each of the *m* data points (reflecting the associated values identified for the *n* inputs) in the calibration data set. The comparison of these predicted distress indicator values to the actual measured distress values will become the basis of the calibration procedure. An example of the updated calibration data set (updated to include the predicted distress values) is shown in table 44.

Table 44. Example calibration data set table with predicted values included.

Data Point	Input 1	Input 2	* * *	Input n	Measured Distress Value	Predicted Distress Value
1						
2						
3						
4						
*						
*						
*						
m						

Step 3—Plot Predicted vs. Measured Distress Values

Predicted distress values are then plotted versus actual measured distress values. The construction of this predicted versus actual plot allows a user to visually evaluate the data by identifying any potential bias, lack of precision, or unwanted trends associated with the original model.

Step 4—Statistical Analysis of Predicted vs. Measured Distress Values

A simple statistical analysis (paired t-test) is performed to determine if there is a significant difference between the sets of predicted and actual distress values. The paired t-test is used to test the null hypothesis (Ho) that there is no difference between the means of the measured and predicted distress values (predicted using the original distress model). For this analysis, the null hypothesis being tested is that presented in equation 113.

$$\text{Ho: } \mu_{ACTUAL} - \mu_{PREDICTED} = 0 \tag{113}$$

where:

μ_{ACTUAL} = Mean of measured values.

$\mu_{PREDICTED}$ = Mean of values predicted using the original distress indicator model.

To run a paired t-test on the data set, the user first has to decide on chosen level of significance. Typically, a significance level of 5 or 10 percent (i.e., 95 or 90 percent confidence) is recommended. Thus, the null hypothesis is rejected if the determined p-value is less than 0.05 or 0.10, respectively. The p-value represents the smallest significance level at which a null hypothesis can be rejected.[65] A stand-alone statistical software package may be used to easily conduct the t-test. (Note: most spreadsheet software packages such as Microsoft Excel also have statistical tools for completing such analyses.)

If the null hypothesis is not rejected, there is no significant difference (for the chosen confidence interval) between the predicted and actual data; therefore, the agency may use the national distress indicator model with confidence. If the hypothesis is rejected, there is a significant difference between the predicted and actual data. For this case, it is recommended that the SHA complete the remaining steps of this calibration process.

Step 5—Determine Calibration Coefficients A and B

The calibration coefficients (A and B) are determined by running a linear regression on the predicted versus measured data values. A statistical or spreadsheet software package contains statistical tools to successfully complete a linear regression through a given data set. The coefficients (A and B) simply represent the y-intercept and slope of the determined best-fit regression line.

Step 6—Determine Calibrated Distress Values

Calibrated distress values are computed as a function of the original distress model predicted values and the calibration coefficients determined under step 5 of this process. Specifically, the calibrated values are determined using the previously

displayed equation 112. For convenience, equation 7 is displayed here again as equation 114.

$$\text{Calibrated Distress Value} = A + B * (\text{Original Model Distress Value}) \quad (114)$$

where:

Original Model Distress Value = Predicted value computed using the original distress indicator model (calculated in step 2 of this process).

A = Calibration coefficient that represents the y-intercept of the linear regression line fit through the predicted versus actual distress data.

B = Calibration coefficient that represents the slope of the linear regression line fit through the predicted versus actual distress data.

Step 7—Plot Calibrated vs. Measured Distress Values

Plotting the calibrated versus actual measured distress values allows the user to again visually evaluate the data. A side-by-side comparison of the original predicted versus actual plot (step 3) and calibrated versus actual plot gives an initial indication of the improved effectiveness of the calibrated model.

Step 8—Statistical Analysis of Calibrated vs. Measured Distress Values

The same paired t-test analysis discussed in step 4 is again used to determine if there is a significant difference between the sets of calibrated and actual measured distress values. For this case, the null hypothesis (Ho) is that there is no significant difference between the means of the measured and calibrated distress values (this null hypothesis is shown in equation 115). The paired t-test is used to determine if this null hypothesis can be rejected using a significance level of 5 or 10 percent.

$$\text{Ho: } \mu_{ACTUAL} - \mu_{CALIBRATED} = 0 \quad (115)$$

where

μ_{ACTUAL} = Mean of measured values.

$\mu_{CALIBRATED}$ =Mean of calibrated values (calibrated values are those determined using equatic

If the hypothesis is not rejected, there is no significant difference (for the chosen confidence interval) between the calibrated and actual data sets; therefore, the agency may use the calibrated model with confidence. If the hypothesis is rejected, there is a significant difference between the calibrated and actual data. This should not occur if calibration is properly performed. If this occurs, an evaluation of the data and

procedures used must be made to determine if any errors have been made. If no errors are identified, the SHA may want to proceed with the development of a new model.

GUIDELINES FOR DEVELOPING NEW DISTRESS INDICATOR MODELS

This section is provided as a general guide for those SHA's that are interested in developing *new* distress indicator models that are specific to a SHA data set. If a SHA is not satisfied with the performance of one of the national distress indicator models, it is strongly recommended that the SHA first try to calibrate existing national distress indicator models with a specific data set. If the SHA is still not satisfied with the performance of the calibrated model, a new distress indicator model can be developed using the general procedure outlined in this section.

Distress Indicator Prediction Model Types

Generally, two types of prediction models can be developed: empirical and mechanistic-empirical. The details of each of these are discussed below.

Empirical Models

Ideally, empirical models are developed using statistical regression methods *and* basic engineering principles and judgment; however, they do not model the basic mechanisms of the distress. They are simply the best relationship that allows prediction of an explanatory or dependent variable (i.e., a distress indicator) from a set of independent variables based on the available data. The model obtained does not necessarily signify a cause-and-effect relationship between the independent variables and the dependent variable; however, the analyst can use the engineering knowledge available and experimental results to improve this empirical aspect of the model.

One of the ways to improve empirical models is to include as independent variables one or more mechanistic parameters or clusters. These clusters are functions of independent variables and should be identified using engineering mechanics and dimensional analysis techniques. An example of a cluster variable used in many transverse joint faulting models is the radius of relative stiffness (l).

$$l = \sqrt[4]{\frac{E h^3}{12(1-\mu^2)k}} \tag{116}$$

where:

l = The cluster of terms that is appropriate to use in predicting the slab's radius of relative stiffness, in.
E = PCC modulus of elasticity, psi.
h = Slab thickness, in.

μ = PCC Poisson's ratio (assumed to be equal to 0.15).
k = Modulus of subgrade reaction, psi/in.

One of the advantages of using a cluster variable is that it accounts for the relative contribution of its components in a rational manner.

Mechanistic-Empirical Models

Mechanistic-empirical models attempt to incorporate mechanistic principles that account for the cause-and-effect relationship between the explanatory (dependent) variable and independent variables. Based on the mechanistic principles behind the cause of a particular distress, a model can be formulated that attempts to describe both the occurrence and progression of the distress. The model is then calibrated using field data (e.g., LTPP data) and standard statistical and optimization techniques. Perhaps the most important benefit of a mechanistic-empirical model is its potential to extrapolate beyond the limits of the data used in its development.

Basic Principles to Developing Improved Distress Indicator Prediction Models

When conducting any model development/improvement activities, a number of basic principles should be applied in order to optimize the development/improvement process. Some of these basic principles are as follows:

- Past efforts of predictive model building should be fully considered, including model functional forms, independent and dependent variables, interaction of variables, and model accuracy achieved.

- The results of the t-test and multivariate analysis should be accounted for in the process of selecting independent variables.

- The very best predictive models are those that are first formulated using principles of mechanics and then calibrated using the extensive new field database. An attempt should be made to identify the underlying mechanistic functional form of the model and variables prior to use of the database. Modern statistical model building techniques should also be utilized.[66]

- Comprehensive sensitivity analyses should be conducted for each model. This includes developing plots of each independent variable (X-axis) versus the dependent variable (distress on Y-axis) to show its relative effect. Sometimes, a statistical test will show that some X-variable is significant, but from an engineering standpoint its effect on the Y-variable is insignificant. This can be readily seen from these plots. Any interactions or colinearity between independent variables (such as age and traffic loads) should be directly considered in the sensitivity analysis.

- Both the direction of the effect and its magnitude should be examined for each X-variable in the model. A comparison of the general magnitude of each of these effects with the results obtained from the major experimental projects where direct comparisons can be made should be considered, as should current pavement engineering knowledge. For example, if a faulting model shows that a permeable base has no effect on joint faulting, but several of the major experimental sections show the opposite, a "red-flag" would be raised. Such an inconsistency should be fully explored to attempt to determine an explanation for the discrepancy.

- The performance of a new model should be compared with existing time-series performance data. The time-series data allow monitoring of the progression of distresses in individual pavement sections. The amount and accuracy of available time-series distress data will greatly influence the performance of the developed model.

Figure 75 shows a flow chart that incorporates the above-mentioned basic principles into an overall step-by-step procedure that can be used to develop pavement distress indicator prediction models.[14] More information regarding the specific methods used to develop pavement distress indicator models may be found in a number of sources, including those by Lee[66] and Simpson et al.[14]

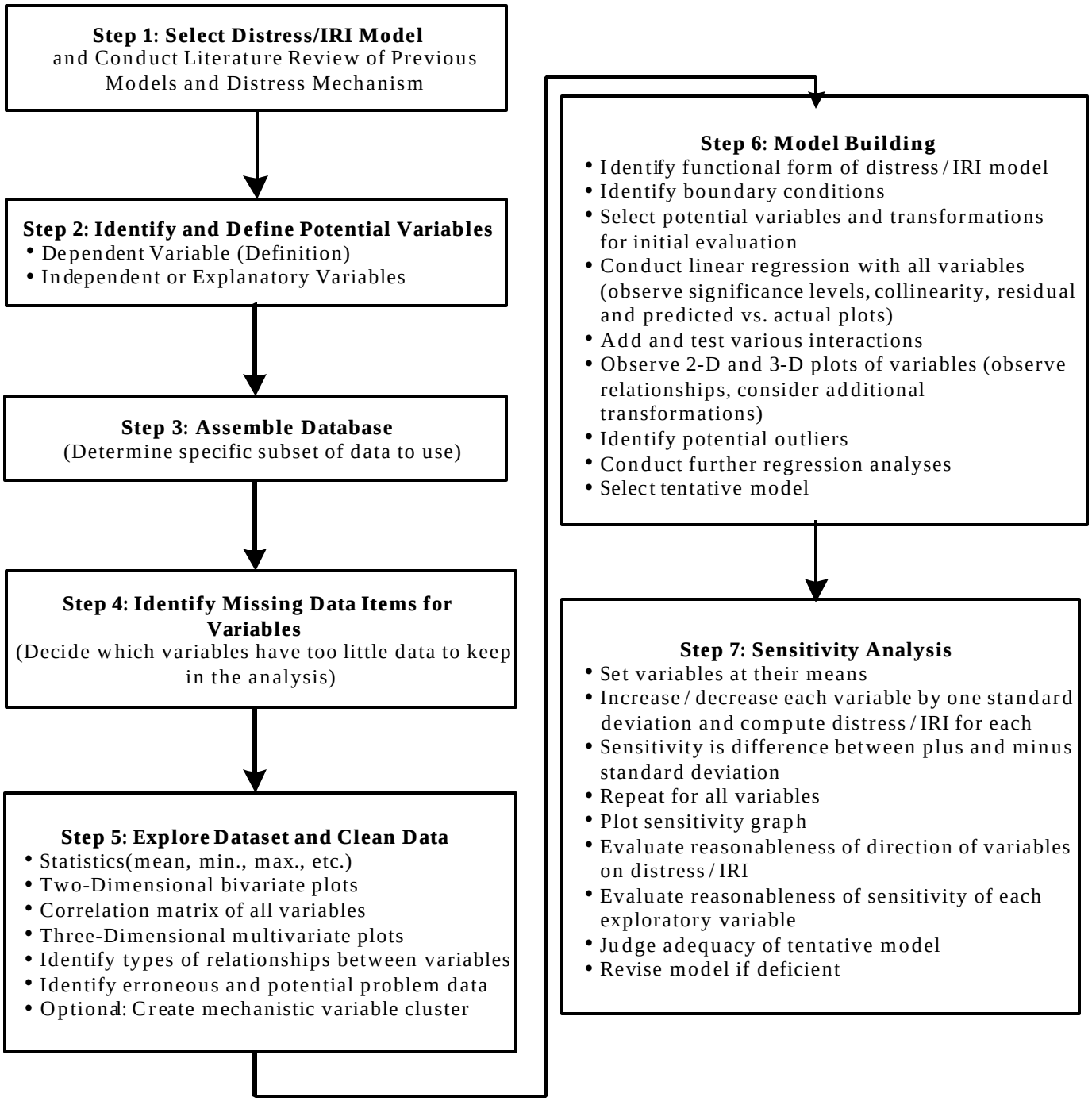

Figure 75. Flow chart for developing pavement distress models for rigid pavements.[14]

CHAPTER 10: SUMMARY AND RECOMMENDATIONS

SUMMARY

One of the key benefits of a PRS continues to be the identification of rational pay adjustments (incentives and disincentives) related to the predicted AQC-influenced future performance of an as-constructed pavement project. The continued focus on linking future pavement performance to the quality of the measured AQC's will lead to improved construction quality, reduced future maintenance and rehabilitation, and the subsequent reduction in LCC's (those incurred by both the agency and the user). The implementation of PRS is expected to improve construction quality, similar to the way in which incentives have improved smoothness over the past several years.

Under this research project, the prototype PRS (developed under previous FHWA research) was improved.[5,8,9,10,11] Specifically, this study focused on improving the key distress indicator and smoothness prediction models used in the prototype PRS for JPCP demonstrated in version 2.0 of the PaveSpec software. This report discussed all aspects of the research, including:

- Completed model improvement (validation / calibration) efforts, details of the improved models, and their associated sensitivity analyses.
- Results of a study that investigated relationships between different methods of measuring initial smoothness and initial IRI.
- Development of guidelines that can be used to calibrate national distress prediction models to reflect local conditions.

The PaveSpec 2.0 PRS demonstration software was also improved under this study. Specific improvements in the PaveSpec 3.0 software include:

- Incorporation of the improved distress indicator models.
- Capability to calibrate or modify a national distress indicator model to better reflect a project's local conditions.
- Inclusion of sensitivity analysis capabilities.
- Ability to produce project-specific expected pay charts used to assess risks to both the contractor and agency.
- Incorporation of an online user's guide.

Based on the research conducted under this project, the following conclusions and recommendations were compiled.

Improved Performance Prediction Models

The PRS methodology has been under development by the FHWA for several years and has now reached a level at which it can be implemented by SHA's to improve the quality of their jointed concrete pavements. However, the adequacy of the key performance models included in the PRS has been of concern to SHA's. To resolve this issue, performance models included in the PaveSpec 2.0 software were evaluated and substantially improved under this project. Specifically, the models chosen to be improved include:

- Transverse joint faulting.
- Transverse slab cracking.
- Transverse joint spalling.
- IRI.

The evaluation and improvement of the above performance models were accomplished using JPCP performance data compiled from the following data sources:

- LTPP JPCP database (GPS-3) (134 sections).
- FHWA RPPR JPCP database (303 sections)
- NCHRP 1-19 (COPES) database (152 sections).
- Extended AASHO Road Test (25 sections).
- Mn/ROAD database (sections included in LTPP).

Combined, these data sources included more than 600 sections located in 40 different States and Canadian Provinces.

The improved performance prediction models are the most comprehensive and robust models developed to date and can be used with relative confidence to predict key distresses and smoothness of JPCP. Each improved distress indicator model is summarized below.

- *Transverse Slab Cracking.* Fatigue damage was accumulated at the slab edge on the basis of key pavement structural and climatic factors. This damage was then correlated with measured slab cracking from the many database sections. The final model included the following key variables: slab thickness (an AQC), slab concrete strength (an AQC), base type and subgrade support, joint spacing, longitudinal joint load transfer (widened lane or tied shoulder), thermal gradients in the slab, and built-in thermal gradient, which produces an upward curling of the slab.

- *Transverse Joint Faulting.* The erodibility of the base course along with key structural and climatic factors were directly considered in the development of the improved JPCP transverse joint faulting model. The database used to develop this model included data from LTPP, RPPR, NCHRP 1-19, and the extended AASHO Road Test. The final transverse joint faulting model included the following key variables: slab thickness (an AQC), slab concrete strength (an AQC), base type and subgrade support, transverse joint spacing, transverse joint load transfer, widened slab, temperature factors, and moisture factors.
- *Transverse Joint Spalling.* Transverse joint spalling was modeled empirically using LTPP data from GPS-3 supplemented by laboratory data obtained from a previous FHWA PRS contract.[5,6,7] The laboratory study specifically investigated the effects of materials properties (air content and PCC percent consolidation) and cumulative freeze-thaw cycles on the transverse joint spalling of PCC slabs.[5,6,7] The final transverse joint spalling model determined under this project was obtained from nonlinear regression and included the following key variables: age of the concrete, air content (an AQC), slab thickness (an AQC), compressive strength of the concrete (an AQC), type of joint sealant, average annual number of air freeze-thaw cycles, and concrete water/cement ratio.
- *International Roughness Index.* The prediction of IRI was based on the premise that the IRI over time was dependent on the initial IRI (measured immediately after construction), the other distress indicators that develop over time, and additional site factors. The final model included the following key variables: initial IRI after construction, transverse cracking, transverse joint spalling, transverse joint faulting, and specific site factors (fines content in the subgrade soil, freezing index, and age since construction).

Investigation of Initial Smoothness Relationships

The relationships between initial IRI and PI (using 0.0-, 2.5-, and 5.0-mm [0.0-, 0.1-, and 0.2-in] blanking band widths) were studied and subsequently greatly improved using LTPP data. This makes it possible to more accurately express initial smoothness in terms of an IRI that is then directly used in the prediction of IRI over time. These determined correlations are intended to give SHA's more confidence in using the IRI model (included in PRS) to predict smoothness over time.

The IRI versus PI correlations utilized data from LTPP that included more than 5,000 data points. Results showed that good correlations were obtained over a wide range of IRI and PI values; however, increasingly better correlations were obtained as the PI was computed with smaller and smaller blanking bands. The correlation between IRI and PI was best at a zero blanking band.

Distress Indicator Model Calibration Guidelines

Distress indicator model calibration guidelines were also developed so that a given State could calibrate any of these models to better reflect their pavement performance

data (local conditions). For example, a State could utilize its LTPP sections, other research test sections, or sections selected from its pavement management data to calibrate each of the performance models included in the PRS (faulting, spalling, cracking, IRI).

Development of PaveSpec 3.0

The PaveSpec PRS demonstration software was upgraded to version 3.0 under this project. The improved PaveSpec 3.0 software demonstrates all aspects of the current PRS methodology by providing the following general capabilities:

- *Development of a Specification.* The PaveSpec 3.0 *Specification Wizard* leads the user through the development of all aspects of the PRS (for JPCP) for a given project. The overall focus of the development process is to provide guidance on determining rational LCC-based pay factor curves associated with each AQC (concrete strength, slab thickness, concrete entrained air content, initial smoothness, and percent consolidation of concrete around dowel bars).

- *Evaluation of a Developed Specification.* PaveSpec provides two tools for evaluating a developed specification: sensitivity analysis and expected pay charts. A specification-dependent sensitivity analysis is used to investigate the effects of AQC changes on pay factors, while expected pay charts help analyze the risks for both the agency and the contractor.

- *Use of a Developed Specification.* Performance-related lot pay factors (and pay adjustments) may be computed based on actual AQC field data.

RECOMMENDATIONS FOR FUTURE RESEARCH

Although the current PRS methodology has been advanced over the past decade, many improvements to the existing PRS for JPCP are still needed. The implementation of the current PRS is anticipated to be a major effort, and obstacles are to be expected. To overcome these obstacles, the results of future research must continue to be incorporated into the current methodology. The following are identified areas of the existing PRS that could be addressed under future research efforts:

- *More Comprehensive User Cost Models.* The user cost models currently used in the PRS methodology are relatively simple. It is recommended that future PRS research strive to include a more robust user cost method.

- *Improved or Additional Distress Indicator Models.* Although the current PRS distress indicator models were greatly improved under this research project, continual

efforts are needed to develop improved mechanistic-based models for the prediction of key distress types and smoothness.

A specific example of ongoing model improvement work (under another research effort) is the development of a transverse slab cracking prediction model that predicts bottom-up and top-down cracking. Top-down cracking has recently been recognized as a very important distress for JPCP as it has occurred on several projects. PaveSpec 3.0 only includes bottom-up cracking of JPCP as a key performance indicator. The inclusion of top-down cracking would add a valuable construction curling variable to the PRS in that built-in curling would be directly controlled by the contractor.

- *Inclusion of Additional AQC's.* As researchers continue to develop distress indicator models that are more mechanistic, the possibility of identifying and including new AQC's into the PRS methodology increases. Influential AQC's that currently cannot be incorporated into the PRS include joint sawing depth, surface texture, concrete mixture components (e.g., cement, aggregates), base course quality, and subgrade quality. It is recommended that additional AQC's be incorporated into the PRS methodology as reliable and practical measurement methods of these potential AQC's become available, and as new distress indicator models are developed as a function of one or more of these potential AQC's.

- *PRS for Additional Pavement Types.* The current prototype PRS is only valid for JPCP. The same concepts could be applied in future research to develop PRS for pavement types such as continuously reinforced concrete pavement (CRCP) and unbonded concrete overlays.

- *Inclusion of Other Pavement Features.* Currently, the PRS methodology is applicable to the mainline pavement only. It is recommended that future research address the inclusion of the pavement shoulders.

- *Additional AQC Sampling and Testing Methods.* As new AQC sampling and testing methods become reliable and practical, they should be considered for use within the PRS. The PRS would benefit greatly from the incorporation of sampling and testing methods that are more rapid, nondestructive, and inexpensive.

- *Use of Pavement Management System Data to Support PRS Implementation.* Such aspects as calibration of distress models, validation of distress models, and validation and improvement of M & R life-cycle costing are important.

- *PRS Training.* Considerable training in PRS concepts and practice will be needed for SHA, contractor, and industry personnel.

REFERENCES

1. *Performance-Related Specifications (PRS): A Cooperative Effort to Improve Pavement Quality*. FHWA-SA-97-008. Washington, DC: Federal Highway Administration, 1997.

2. Weed, R.M. *Statistical Specification Development*. FHWA / NJ-88-017. Trenton, NJ: New Jersey Department of Transportation, 1989.

3. Anderson, D.A., D.R. Luhr, and C.E. Antle. *Framework for Development of Performance-Related Specifications for Hot-Mix Asphaltic Concrete*. NCHRP Report 332. Washington, DC: Transportation Research Board, 1990.

4. Irick, P.E., S.B. Seeds, M.G. Myers, and E.D. Moody. *Development of Performance-Related Specifications for Portland Cement Concrete Pavement Construction*. FHWA-RD-89-211. Washington, DC: Federal Highway Administration, 1990.

5. Darter, M.I., M. Abdelrahman, P.A. Okamoto, and K.D. Smith. *Performance-Related Specifications for Concrete Pavements: Volume I—Development of a Prototype Performance-Related Specification*. FHWA-RD-93-042, Washington, DC: Federal Highway Administration, June 1993a.

6. Darter, M.I., M. Abdelrahman, T. Hoerner, M. Phillips, K.D. Smith, and P.A. Okamoto. *Performance-Related Specifications for Concrete Pavements: Volume II—Appendixes A through C*. FHWA-RD-93-043. Washington, DC: Federal Highway Administration, June 1993b.

7. Okamoto, P.A., C.L. Wu, S.M. Tarr, M.I. Darter, and K.D. Smith. *Performance-Related Specifications for Concrete Pavements: Volume III—Appendixes D through E*. FHWA-RD-93-044. Washington, DC: Federal Highway Administration, June 1993.

8. Hoerner, T.E. and M.I. Darter. *Guide to Developing Performance-Related Specifications for PCC Pavements, Volume I: Practical Guide, Final Report and Appendix A*. FHWA-RD-98-155. Washington, DC: Federal Highway Administration, 1999.

9. Hoerner, T.E., M.I. Darter, S.M. Tarr, and P.A. Okamoto. *Guide to Developing Performance-Related Specifications for PCC Pavements, Volume II: Appendix B—Field Demonstrations*. FHWA-RD-98-156. Washington, DC: Federal Highway Administration, 1999.

10. Hoerner, T.E., S.M. Tarr, M.I. Darter, and P.A. Okamoto. *Guide to Developing Performance-Related Specifications for PCC Pavements, Volume III: Appendixes C Through F*. FHWA-RD-98-171. Washington, DC: Federal Highway Administration, 1999.

11. Hoerner, T.E. *Guide to Developing Performance-Related Specifications for PCC Pavements, Volume IV: Appendix G—PaveSpec 2.0 User Guide*. FHWA-RD-99-059. Washington, DC: Federal Highway Administration, 1999.

12. Byrum, C.R., W. Hansen, and S.D. Kohn. "The Effect of PCC Strength and Other Parameters on the Performance of PCC Pavements." *Proceedings: Sixth International Purdue Conference on Concrete Pavement Design and Materials for High Performance.* Purdue University, November 1997, pp. 373-393.

13. Owusu-Antwi, E.B., L. Titus-Glover, L. Khazanovich, and J.R. Roessler. *Development and Calibration of Mechanistic-Empirical Distress Models for Cost Allocation*. Final Report. Washington, DC: Federal Highway Administration, April 1997.

14. Simpson, A.L., J.B. Rauhut, P.R. Jordahl, E. Owusu-Antwi, M.I. Darter, and R. Ahmad. *Early Analysis of LTPP General Pavement Studies Data, Volume III: Sensitivity Analyses for Selected Pavement Distresses*. Report SHRP-P-393, Washington, DC: Strategic Highway Research Program, 1994.

15. Titus-Glover, L., E.B. Owusu-Antwi, and M.I. Darter, *Design and Construction of PCC Pavements, Volume III: Improved PCC Performance.* FHWA-RD-98-113. Washington, DC: Federal Highway Administration, January 1999.

16. Yu, H.T., K.D. Smith, M.I. Darter, J. Jiang, and L. Khazanovich. *Performance of Concrete Pavements, Volume III: Improving Concrete Pavement Performance.* FHWA-RD-95-111. Washington, DC: Federal Highway Administration, 1997.

17. Yu, H.T., L. Khazanovich, S.P. Rao, M.I. Darter, and H. Von Quintus. *Guidelines for Subsurface Drainage Based on Performance, Appendices*. Washington, DC: National Cooperative Highway Research Program, Project 1-34, August 1998.

18. Smith, K.D., A.L. Mueller, M.I. Darter, and D.G. Peshkin. *Performance of Jointed Concrete Pavements, Volume II—Evaluation and Modification of Concrete Pavement Design and Analysis Models*. FHWA-RD-89-137, Washington, DC: Federal Highway Administration, 1990.

19. Darter, M.I., J.M. Becker, and M.B. Snyder. *Development of a Concrete Pavement Evaluation System (COPES), Volume I—Research Report*. Washington, DC: National Cooperative Highway Research Program, Project 1-19, August 1984.

20. Hudson, S.B. *Handbook of Applications of Statistical Concepts to the Highway Construction Industry, Part I*. Report Number MAT-RES-DEV-WGAI-71-660-1. Washington, DC: Federal Highway Administration, June 1971.

21. Hoerner, T.E., M.I. Darter, and E. Owusu-Antwi. *Evaluation of the 1986 AASHTO Rigid Pavement Design Model Using the LTPP Database.* Prepared under PCA Contract 95-02a. Skokie, IL: Portland Cement Association, December 1996.

22. Hall, K.T., M.I. Darter, T.E. Hoerner, and L. Khazanovich. *LTPP Data Analysis—Phase I: Validation of Guidelines for k-Value Selection and Concrete Pavement Performance Prediction*. FHWA-RD-93-198. Washington, DC: Federal Highway Administration, January 1997.

23. Wu, C.L., J.W. Mack, P.A. Okamoto, and R.G. Packard. "Prediction of Faulting of Joints in Concrete Pavements," *Volume 2, Proceedings of the International Conference on Concrete Pavement Design*. Lafayette, IN: Purdue University, 1993.

24. Packard, R.G.. "Design Considerations for Control of Joint Faulting of Undoweled Pavements," *Proceedings of the International Conference on Concrete Pavement Design*. Lafayette, IN: Purdue University, 1977.

25. Permanent International Association of Road Congresses (PIARC). *Combatting Concrete Pavement Slab Pumping—State of the Art and Recommendations*. PIARC Technical Committee on Concrete Roads. 1987.

26. Ray, M. "A European Synthesis on Drainage, Subbase, Erodability, and Load Transfer in Concrete Pavements," *Proceedings, 2nd International Conference on Concrete Pavement Design*. Lafayette, IN: Purdue University, April 14-16, 1981.

27. Ray M. and J.P. Christory. "Combatting Concrete Pavement Slab Pumping—State of the Art and Recommendations," *Proceedings, 4th International Conference on Concrete Pavement Design and Rehabilitation*. Lafayette, IN: Purdue University, April 18-20, 1989.

28. Ray M., J.P. Christory, and J.P. Poilane. "Drainage and Erodibility: International Seminar Synthesis and New Research Results Related to Field Performance," *Proceedings, 3rd International Conference on Concrete Pavement Design and Rehabilitation*. Lafayette, IN: Purdue University, April 23-25, 1985.

29. Birmann, D. "Erosion of Cement Treated Subbases Below Concrete Pavement," *Theme III: Pavement Performance and Evaluation, Proceedings from the 8th International Symposium on Concrete Roads*. Lisbon-Portugal, September 1998.

30. SAS Institute Inc., SAS/STAT User's Guide, Version 6, Fourth edition, Volume 2. Cary, NC: SAS Institute Inc., 1989. 846 pp.

31. Darter, M.I. *Design of Zero-Maintenance Plain Jointed Concrete Pavement: Vol. I—Development of Design Procedures*. FHWA -RD-77-111. Washington, DC: Federal Highway Administration, June 1977.

32. Barenberg, E.J., and M.R. Thompson. *Calibrated Mechanistic Design Procedure for Pavements*, Phase 2 NCHRP 1-26. Washington, DC: National Cooperative Highway Research Program / Transportation Research Board, 1992.

33. Salsilli, R.A., E.J. Barenberg, and M.I. Darter. "Calibrated Mechanistic Design Procedure to Prevent Transverse Cracking of Jointed Plain Concrete Pavements," *Volume 2, Proceedings of the International Conference on Concrete Pavement Design*, Lafayette, IN: Purdue University, 1993.

34. Lytton, R.L., D.E. Pufahl, C.H. Michalak, H.S. Liang, and J. Dempsey. *An Integrated Model of the Climatic Effects on Pavements*. FHWA-RD-90-033. McLean, Virginia: Federal Highway Administration, 1993.

35. Eisenmann, J., and G. Leykauf. Simplified Calculation Method of Slab Curling Caused by Surface Shrinkage, *Proceedings, 2nd International Workshop on Theoretical Design of Concrete Pavements*. Madrid, Spain, 1990.

36. Eisenmann, J., and G. Leykauf. Effects of Paving Temperatures on Pavement Performance, *Proceedings, 2nd International Workshop on Theoretical Design of Concrete Pavements*. Madrid, Spain, 1990, pp. 419-428.

37. Ioannides, A.M., L. Khazanovich, and J.L. Becque. Structural Evaluation of Base Layers in Concrete Pavement Systems, *Transportation Research Record 1370*, Washington, DC: Transportation Research Board, National Research Council, 1992, pp. 20-28.

38. Foxworthy, P.T. *Concepts for the Development of a Nondestructive Testing and Evaluation System for Rigid Airfield Pavements*. Ph.D. thesis, Urbana, IL: University of Illinois at Urbana-Champaign, 1985.

39. Federal Highway Administration. *Data Collection Guide for Long-Term Pavement Performance Studies*, Operational Guide No. SHRP-LTPP-OG-001. Washington, DC: Strategic Highway Research Program (SHRP), January 1990 (Revised October 1993, FHWA LTPP Division).

40. Zollinger, D.G., and E.J. Barenberg. *Continuously Reinforced Pavements: Punchouts and Other Distresses and Implications for Design*. FHWA / IL / UI / 227. Springfield, IL: Illinois Department of Transportation, 1990.

41. Sanadheera, S.P., and D.G. Zollinger. *Influence of Coarse Aggregate in Portland Cement Concrete on Spalling of Concrete Pavements*. Research Report 1244-11. College Station, TX: Texas Transportation Institute, 1995.

42. Dempsey (original reference unknown at time of Draft submittal).

43. Sayers, M.W., and T.D. Gillespie. “The International Road Roughness Experiment: A Basis for Establishing a Standard Scale for Road Roughness Measurements.” *Transportation Research Record 1084*. Washington, DC: Transportation Research Board, 1986.

44. Queiroz, C.A.V., and W.R. Hudson.“A Stable, Consistent, and Transferable Roughness Scale for Worldwide Standardization.” *Transportation Research Record* 997. Washington, DC: Transportation Research Board, 1984.

45. Smith, K.L., K.D. Smith, L.D. Evans, T.E. Hoerner, and M.I. Darter. *Smoothness Specifications for Pavements*. Final Report. NCHRP Project 1-31. Washington, DC: Transportation Research Board, March 1997.

46. Khazanovich, L., M. Darter, R. Bartlett, and T. McPeak. *Common Characteristics of Good and Poorly Performing PCC Pavements*. FHWA-RD-97-131, Washington, DC: Federal Highway Administration, 1998.

47. Perera, R.W., C. Byrum, and S.D. Kohn. *Investigation of Development of Pavement Roughness*. FHWA-RD-97- 147, Washington, DC: Federal Highway Administration, May 1998.

48. Federal Highway Administration. *Long-Term Pavement Performance Information Management System Data User’s Reference Manual*, Washington, DC, January 1996.

49. Rowshan, S., and S. Harris. *Long Term Pavement Performance Information Management System*. FHWA-RD-93-094, Washington, DC: Federal Highway Administration, July 1993.

50. Strategic Highway Research Program. *SHRP Database Structure Reference Manual*. Washington, DC, April 1992.

51. Federal Highway Administration. *Distress Identification Manual for Long-Term Pavement Performance Project*. SHRP-P-338. Washington, DC: Strategic Highway Research Program (SHRP), 1993.

52. Darter, M.I. *Report on the 1992 U.S. Tour of European Concrete Highways*. FHWA-SA-93-012. Washington, DC: Federal Highway Administration, January 1993.

53. Christory, J.P. "Assessment of PIARC Recommendations on the Combating of Pumping in Concrete Pavements." *Sixth International Symposium on Concrete Roads*. Madrid, Spain, 1990.

54. Al-Omari, B., and M.I. Darter. *Relationships Between IRI and PSR*. Report Number UILU-ENG-92-2013. Springfield, IL: Illinois Department of Transportation, 1992.

55. Walker, R.S., and H.T. Lin. *Profilograph Correlation Study with Present Serviceability Index: Demonstration Project No. 72, Automated Pavement Data Collection Equipment*. FHWA-DP-88-072-002. Washington, DC: Federal Highway Administration, 1988.

56. Scofield, L. "Profilograph Limitations, Correlations, and Calibration Criteria for Effective Performance-Based Specifications." Project 20-7 Task 53 Draft Report. Washington, DC: National Cooperative Highway Research Program, 1993.

57. Fernando, E.G. "Evaluation of Relationship Between Profilograph and Profile-Based Roughness Indices," Paper Prepared for the 79th Annual Meeting of the Transportation Research Board. Washington, DC, 2000.

58. Kulakowski, B.T. and J.C. Wambold. "Development of Procedures for the Calibration of Profilographs." Final Report. University Park, PA: Pennsylvania Transportation Institute (PTI), Pennsylvania State University, 1989.

59. Ksaibati, K., R. McNamara, W. Miley, and J. Armaghani. "Pavement Roughness Data Collection and Utilization," *Transportation Research Record 1655*, Washington, DC: Transportation Research Board, 1999.

60. Kombe, E.M., and S.A. Kalevela. "Evaluation of Initial Pavement Smoothness for the Development of PCCP Construction Specifications." Phase I Final Report. Phoenix, AZ: Arizona Department of Transportation, 1993.

61. Florida Department of Transportation (DOT). "Comparison of Ride Quality Monitoring Equipment Used for New Construction." Draft Report, Pavement Systems Evaluation Study 97-2. Tallahassee, FL: Florida DOT State Materials Office, 1997.

62. Soil and Materials Engineers, Inc. (SME). Technical Memorandum on Acceptance Testing of Profiles, Plymouth, MI: SME, 1996.

63. SME. "Comparison Testing of FHWA-LTPP Profiles." Draft Report Prepared for Federal Highway Administration, Washington, DC, 1998.

64. Latin American Study Team. "Modeling Road Design and Maintenance Effects for Pavements in HDM4." Final Report, Santiago, Chile: Prepared for World Bank, September, 1996.

65. Gharaibeh, N.G., M.I. Darter, and L.B. Heckel. *Evaluation and Improvement of the CRS Prediction Models*. FHWA-IL-UI-267, Report IHR-540. Springfield, IL: Illinois Cooperative Highway Research Program, March 1999.

66. Lee, Y. *Development of Pavement Prediction Models*. Ph.D. thesis, Urbana, IL: University of Illinois at Urbana-Champaign, 1993.